MOLECULAR DYNAMICS STUDIES OF SUPERCOOLED WATER USING A MONATOMIC MODEL

by

Emily Brooke Moore

A dissertation submitted to the faculty of
The University of Utah
in partial fulfillment of the requirements for the degree of

Doctor of Philosophy

Department of Chemistry

The University of Utah

May 2012

The University of Utah Graduate School

STATEMENT OF DISSERTATION APPROVAL

The dissertation of **Emily Brooke Moore**

has been approved by the following supervisory committee members:

Valeria Molinero	, Chair	**12/15/2010** Date Approved
Michael D. Morse	, Member	**12/15/2010** Date Approved
Peter F. Flynn	, Member	**12/15/2010** Date Approved
Jack Simons	, Member	**12/15/2010** Date Approved
Thomas Cheatham	, Member	**12/15/2010** Date Approved

and by **Henry White**, Chair of the Department of **Chemistry**

and by Charles A. Wight, Dean of The Graduate School.

ABSTRACT

There remain many unanswered questions regarding the structure and behavior of water, particularly when cooled below the melting temperature into water's supercooled region. In this region, liquid water is metastable, and rapid crystallization makes it difficult to study experimentally the liquid and the crystallization process. Computational studies are hindered by the complexity of accurately modeling water and the computational cost of simulating processes such as crystallization.

In this work, the development and validation of mW, a monatomic water model, is presented. This model is able to quantitatively reproduce the structure, dynamic anomalies and phase behavior of water without hydrogen atoms or electrostatics by reproducing water's propensity to form locally tetrahedral structures. Using the mW water model in molecular dynamics simulations, we show the evolution of the local structure of water from 300 - 100 K. We find that the thermodynamic and structural properties studied, density, tetrahedrality and structural correlation length, change maximally or are maximum at 202 ± 2 K, the liquid-liquid transformation temperature.

Shifting to water confined within cylindrical nanopores, we present the development of a rotationally invariant method, the CHILL algorithm, to distinguish between liquid, hexagonal and cubic ice. We analyze the process of homogeneous nucleation, growth and melting within hydrophilic pores, as well as the effect of water-pore interaction strength on the melting of ice and liquid-ice coexistence within pores.

Crystallization within the nanopores results in cubic ice with hexagonal stacking faults in agreement with experiments.

We also investigate crystallization of bulk liquid within water's experimentally inaccessible "no man's land". Crystallization occurs through rapid development of ice nuclei that grow and consolidate, precluding the measurement of diffusion within the liquid. Analysis of how ice structure develops shows that hexagonal ice can exist in large fractions at times prior to what has been observed in experiments.

Finally, crystallization mechanism and timescales are studied over a range of temperatures above and below the liquid-liquid transformation temperature. It is just below the liquid-liquid transformation temperature we observe the change from nucleation-dominated to growth-dominated crystallization, providing evidence of a kinetic spinodal, the limit of stability of the supercooled water.

-- To Mother

for love in abundance and unlimited phone calls

-- To Noah

for all to come

“The hope is that if we do understand the ice crystal, we shall ultimately understand the glacier.”

- Richard Feynman, 1965

TABLE OF CONTENTS

ACKNOWLEDGMENTS

I would like to thank my advisor, Valeria Molinero, for her brilliant ideas, guidance and patience. To the members of my committee, thank you for your suggestions and encouragement. For help in many forms (laughter, listening, good suggestions and much more), thanks to my fellow group members: Diane Neff, Ly Le, Robert DeMille, Liam Jacobson and Jessica Johnston. A very special thanks to my computer guru and good friend, Irvin Allen, for the introduction to my first Macbook, and all of the conversations that came after. Thank you, Noah, for all of your support. I will do my best to return the favor. To Linda Kastelowitz and Victor Lieberman, thanks again for the long talks, hugs and the much appreciated vacations. To Brenda, Bob, Matthew, Courtney, Bobbie and Papa: you inspire me, believe in me, listen to me, make fun of me, keep me laughing and keep me going. With all of my heart, thank you.

Chapter 1

INTRODUCTION

Water has been the subject of research for centuries.[1] This is no doubt due to water's ubiquity, as well as its biological and atmospheric significance, but also for the shear complexity of behavior exhibited by a seemingly simple molecular substance. A popular website[2] devoted to water research lists 67 water anomalies. These anomalies range from water's unusually high melting point in comparison to other hydrides from the same group of the periodic table, to the uncommon increase in the speed of sound through water upon heating. Water research attracts scientists from many different backgrounds, from biochemists and physical chemists to condensed matter physicists and engineers, studying many aspects of water's behavior and interactions with other materials. With so many aspects of water behavior under study, it is important to specify the scope of this work up front: to elucidate the mechanism through which water undergoes the change from liquid to ice over a range of conditions.

Although water is one of the most well researched liquids, the mechanism through which homogeneous ice nucleation occurs, how pure liquid water forms ice, is not yet understood. Development of methods for controlling ice nucleation is needed in many areas, including fuel cells and biopreserved drugs and proteins. In atmospheric sciences, improved estimates of water/ice proportions in clouds would increase climate modeling accuracy, due to the very different radiative properties of liquid water and ice.[3]

In the process of studying such a richly complex substance, opportunities to expand this work into related areas appeared, resulting in a collection of studies that provide insight into a range of cold water behavior. These include studies on i) the local structure of water under conditions impossible to explore with current experiments, ii) the effect of confinement on liquid-ice coexistence, crystallization and melting, iii) the formation of a metastable ice structure different from the common hexagonal ice and iv) the relationship between temperature, liquid structure and the crystallization process. Though a variety of issues are addressed, the structure of water and how structure affects, or in some cases drives, the phase changes within the supercooled liquid will be the common thread linking the chapters of this work.

First, we begin broadly by introducing the metastable phase diagram of water from very hot to very cold temperatures. This allows for a specific region of the phase diagram, referred to as “no man’s land” and the focus of much of this work, to be highlighted before describing the main results to be presented. As each chapter includes a detailed introduction, only a brief summary of the main results is included here.

Figure 1.1 shows the phase diagram of water, including the metastable phases, at 1 atm of pressure. Starting in the stable region, upon cooling the liquid, a number of changes occur. We know from X-ray diffraction that the structure of the liquid becomes more similar to that of ice,[4] in which each molecule has four nearest neighbors. A number of response functions show unusual behavior,[5,6] including the compressibility (how the volume changes with a change in pressure), the coefficient of thermal expansion (how the volume changes with a change in temperature) and the heat capacity (the amount of heat required to raise the temperature a given amount). For each of these response functions, a typical liquid shows a monotonous decrease upon cooling. The compressibility of water decreases until 319 K, where a minimum is reached. Upon cooling further, there is a sharp increase in the compressibility. The heat capacity

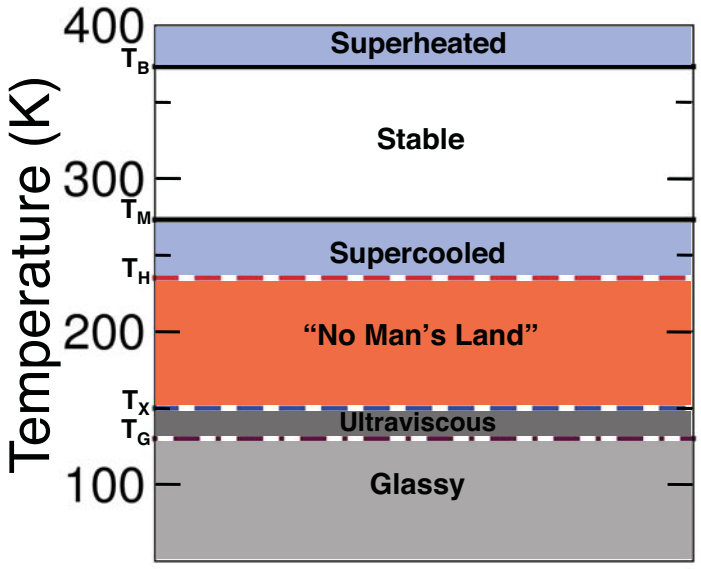

Figure 1.1 Water's Metastable Phase Diagram
The phases of water at 1 atm of pressure are shown. Above the boiling temperature T_B, liquid water is superheated, while below the melting temperature T_M, liquid water is supercooled.

behaves similarly, with a minimum at 308 K. The coefficient of thermal expansion is zero at 277 K, the temperature of maximum density of water, before decreasing rapidly.

Below the melting temperature, T_M = 273 K, ice I is the stable phase and liquid water is metastable.[7] The formation of an ice nucleus, necessary for the process of crystallization, requires the development of an ordered region within the disordered liquid. Since the process of nucleation requires overcoming an energy barrier, the result of a competition between the cost of creating a liquid/ice interface and the benefit of developing the stable phase, pure water does not freeze homogeneously upon reaching the melting temperature.[7] In fact, in the absence of impurities or interfaces that promote the nucleation of ice, liquid water can be supercooled down to T_H = 235 K, the homogeneous nucleation temperature, before crystallization becomes unavoidable on experimental timescales of about one second, nearly forty degrees below the melting temperature.[8] Much more detail on the specifics of homogeneous nucleation will be

detailed in chapters 4 and 6-8. It is in this supercooled region, between 273 K and 235 K in which many anomalies of water become more pronounced, including the previously mentioned response functions.[1,5,9]

If cooled rapidly, at a rate of more than 10^6 Ks^{-1}, to a temperature below the glass transition temperature, T_G = 136 K, crystallization of micron-sized droplets can be avoided and a glass is formed.[1] In the glassy state, water is an amorphous solid, characterized, like ice, by very slow dynamics, but lacking long-range order.[10] At a pressure of 1 atm (shown in Figure 1.1), water molecules that form the glassy water each have about four nearest neighbors, similar to the ice though, again, the glass lacks the long range order found in ice. The structure of the glass is made up of a collection of disordered tetrahedra, while in the ice the tetrahedra are aligned. Upon increasing the pressure to 0.6 GPa, the glass undergoes a sharp transition to a 20% denser glass, in which each molecule has five nearest neighbors.[11] This means that glassy water comes in two varieties, the low-density amorphous (LDA) and high-density amorphous (HDA) glass. Warming of the glassy water results in an ultraviscous liquid prior to crystallization at T_X = 150 K,[12,13] which is the lower bound of "no man's land." Thus, a complex picture of the physical properties of water emerges, resulting in a difficult task for those attempting to form a coherent theory of water capable of encompassing water's properties across its entire phase diagram.

The liquid-liquid phase transition[14] and the singularity free scenarios[15] are the two most prominent theories to explain the behavior of water currently being studied. The liquid-liquid critical point scenario proposes that the transition observed in glassy water, from LDA to HDA, has a corresponding liquid-liquid transition within "no man's land" that ultimately ends in a second critical point. In the singularity free scenario, no critical point within the metastable phase diagram is necessary. Regardless of where these theories disagree, all current scenarios attempting to describe water's physical

behavior can be related based on the relative weight they place on the directional strength and the cooperative strength of hydrogen bonding in water. This means that current theory places the determining factor for the physical properties of the liquid on water's preference for tetrahedral structure.

Each of these scenarios contain aspects that remain unproven by experiments, due to the difficulty of studying highly metastable liquid water.[1] More detail about the specific insights provided by, and the limitations of, current experiments are described within each chapter. Computer simulations provide an alternative way to probe water's properties in regions of the phase diagram beyond the current reaches of experiment. Development of an accurate computational model of water is notoriously difficult, requiring a balance between the addition of full atomistic detail and computational efficiency. Too much detail limits the size of simulations possible, in time and length scales. Not enough detail and the result is a qualitative description of water behavior at best. Prior to this work, the study of crystallization has been limited to simulations of less than 800 rigid water molecules (in which each molecule's oxygen-hydrogen bond lengths and angles are fixed) modeled using classical potentials.[16] Simulations large enough for comparison of ice structure to X-ray diffraction experiments require more than 30,000 water molecules.[13,17]

In chapter 2, the development of the model used throughout this dissertation, the mW model, is described. A summary of the current state of water modeling and the validation of the mW water model is provided. We show that it is possible to quantitatively reproduce properties of water, including the structure, dynamic anomalies and phase behavior, with a computationally very efficient model. This model contains no hydrogen atoms or electrostatics, yet reproduces the key feature central to the current theories of water, its propensity to form locally tetrahedral structures.

In chapter 3, we use this model to investigate the structure of liquid water from the stable liquid at 350 K to the glass at 100 K. Specific details of what is known from experiments up to the boundaries of "no man's land", along with the results of prior theoretical and simulation studies of the properties of water in this region are described and discussed. We find that the liquid continues its trend toward locally tetrahedral structure, transforming from predominately five-coordinated (molecules having exactly five neighboring molecules in its first neighbor shell) to four-coordinated at the liquid-liquid transformation temperature, T_{LL} = 202 ± 2 K. Upon approaching T_{LL}, regions of four-coordinated molecules form within the liquid, exhibiting power law growth in the correlation length between these regions as the liquid is cooled towards T_{LL}. This is the first determination from computer simulations of an increase in structural correlation length in supercooled water, providing evidence of the existence of a critical point consistent with the liquid-liquid critical point scenario described previously. Using small-angle X-ray scattering, Huang et al.[18] recently confirmed our predictions, observing increasing correlation lengths to down to 252 K that fit power law behavior.

In chapters 4 and 5, we shift from bulk water to water confined within cylindrical nanopores. Confinement can greatly effect water's phase changes, typically decreasing significantly the melting and freezing temperatures in comparison to bulk water. To study the process of melting and freezing within water, we must be able to distinguish between the liquid, which becomes increasingly ice-like on cooling, and the ice, which can have either cubic or hexagonal structure. We show in chapter 4 that the lack of long range order found in the liquid can be used to distinguish liquid from ice, even when both are locally tetrahedral, and that a subtle difference between the hexagonal and cubic ice structures can be exploited to differentiate the two structures. We developed the first rotationally invariant method distinguishing between the liquid and cubic and hexagonal ices. Our simulations, the first that involve nucleation and growth of ice in nanopores,

show the development of complex stacking patterns of the cubic and hexagonal ices upon crystallization from the confined liquid and the dissolution of the structure upon melting with molecular level resolution.

In the only simulation study of liquid-ice coexistence within nanopores to date, chapter 5 focuses on premelting within cylindrical nanopores and how the melting temperature of the ice is affected by the strength of interaction between confined ice and the pore walls. Our results show that the radius of the ice cylinder within the pores determines the melting temperature, the water-pore interaction is only significant to the extent it affects the amount of liquid in coexistence with the ice and correspondingly, the radius of the ice cylinder.

In chapters 6 and 7, we take the exploration of cubic and hexagonal ice formation to bulk supercooled liquid water, performing large-scale simulations of crystallization in bulk. Chapter 6 details the general crystallization process from the liquid, the first simulation study of crystallization within "no man's land." We find that the crystallization occurs through rapid ice development throughout the simulation cell, followed by consolidation of the individual ice clusters into larger crystallites. The onset of such rapid crystallization precludes the measurement of diffusion of liquid water within "no man's land", as the equilibration of the liquid is shorter than the onset of crystallization.

In chapter 7, we use the ability to distinguish liquid from cubic and hexagonal ices for closer analysis of the nucleation, growth and consolidation processes that occur during spontaneous crystallization within "no man's land." Upon comparison of the static structure factor obtained from our simulations to those obtained from diffraction experiments,[13,19] we find excellent agreement, both showing development of peaks characteristic with the cubic ice structure. With the molecular level detail afforded by the simulation studies, we find that while the static structure factors show the signatures of

cubic ice, significant amounts of 'silent' hexagonal ice, present as layers between the cubic ice, can be present prior to the appearance of characteristic hexagonal structure peaks in the static structure factor. We show that cubic ice is preferred at ice cluster sizes smaller than either the cubic or hexagonal unit cell, ruling out thermodynamic arguments based upon cubic ice having a lower interfacial energy than hexagonal ice.

In the final chapter, we compare the timescales and mechanisms of crystallization from hundreds of crystallization events over a range of temperatures. Above T_{LL}, crystallization times are dominated by the time required for nucleation with very short growth times. Below T_{LL}, nucleation is rapid and the time required for crystal growth is long. This result links the local structure of the liquid with the kinetics of crystallization and provides evidence for the existence of a kinetic spinodal, the limit of stability of the supercooled liquid.

References

1 O. Mishima and H. Stanley, Nature **396**, 329 (1998).

2 http://www.lsbu.ac.uk/water/.

3 M. D. Shupe, S. Y. Matrosov, and T. Uttal, J. Atmos. Chem. **63**, 697 (2006).

4 A. K. Soper, F. Bruni, and M. A. Ricci, J. Chem. Phys. **106**, 247 (1997).

5 R. J. Speedy and C. A. Angell, J. Chem. Phys. **65**, 851 (1976).

6 G. S. Kell, J. Chem. Eng. Data **20**, 97 (1975).

7 P. G. Debenedetti, *Metastable Liquids: Concepts and Principles*. (Princeton University Press, Princeton, 1996).

8 B. J. Murray, S. L. Broadley, T. W. Wilson, S. J. Bull, R. H. Wills, H. K. Christenson, and E. J. Murray, Phys. Chem. Chem. Phys. **12**, 10380 (2010); J. Huang and L. S. Bartell, J. Phys. Chem. **99**, 3924 (1995); G. Wood and A. Walton, J. Appl. Phys. **41**, 3027 (1970); B. Krämer, O. Hübner, H. Vortisch, L. Wöste, T.

Leisner, M. Schwell, E. Rühl, and H. Baumgärtel, J. Chem. Phys. **111**, 6521 (1999); B. J. Murray, D. A. Knopf, and A. K. Bertram, Nature **434**, 202 (2005).

[9] P. G. Debenedetti and H. E. Stanley, Phys. Today **56**, 40 (2003).

[10] J. Finney, A. Hallbrucker, I. Kohl, A. Soper, and D. Bowron, Phys. Rev. Lett. **88**, 225503 (2002).

[11] O. Mishima, L. D. Calvert, and E. Whalley, Nature **314**, 76 (1985).

[12] Y. Handa, O. Mishima, and E. Whalley, J. Chem. Phys. **84**, 2766 (1986).

[13] I. Kohl, E. Mayer, and A. Hallbrucker, Phys. Chem. Chem. Phys. **2**, 1579 (2000).

[14] P. H. Poole, F. Sciortino, U. Essmann, and H. E. Stanley, Nature **360** (6402), 324 (1992).

[15] S. Sastry, P. G. Debenedetti, and F. Sciortino, Phys. Rev. B: Condens. Matter **53**, 6144 (1996).

[16] M. Matsumoto, S. Saito, and I. Ohmine, Nature **416**, 409 (2002); L. Vrbka and P. Jungwirth, J. Phys. Chem. B **110**, 18126 (2006).

[17] P. Jenniskens and D. Blake, Science **265**, 753 (1994).

[18] C. Huang, T. Weiss, D. Nordlund, K. Wikfeldt, L. Petterson, and A. Nilsson, PNAS **133**, 134504 (2010).

[19] P. Jenniskens and D. Blake, Astrophys. J. **473**, 1104 (1996); T. Hansen, M. Koza, P. Lindner, and W. Kuhs, J. Phys. Condens. Matter **20**, 285105 (2008).

CHAPTER 2

WATER MODELED AS AN INTERMEDIATE ELEMENT BETWEEN CARBON AND SILICON

4008 *J. Phys. Chem. B* **2009,** *113,* 4008–4016

Water Modeled As an Intermediate Element between Carbon and Silicon†

Valeria Molinero* and Emily B. Moore

Department of Chemistry, University of Utah, 315 South 1400 East, Salt Lake City, Utah 84112

Received: June 13, 2008; Revised Manuscript Received: September 4, 2008

Water and silicon are chemically dissimilar substances with common physical properties. Their liquids display a temperature of maximum density, increased diffusivity on compression, and they form tetrahedral crystals and tetrahedral amorphous phases. The common feature to water, silicon, and carbon is the formation of tetrahedrally coordinated units. We exploit these similarities to develop a coarse-grained model of water (mW) that is essentially an atom with tetrahedrality intermediate between carbon and silicon. mW mimics the hydrogen-bonded structure of water through the introduction of a nonbond angular dependent term that encourages tetrahedral configurations. The model departs from the prevailing paradigm in water modeling: the use of long-ranged forces (electrostatics) to produce short-ranged (hydrogen-bonded) structure. mW has only short-range interactions yet it reproduces the energetics, density and structure of liquid water, and its anomalies and phase transitions with comparable or better accuracy than the most popular atomistic models of water, at less than 1% of the computational cost. We conclude that it is not the nature of the interactions but the connectivity of the molecules that determines the structural and thermodynamic behavior of water. The speedup in computing time provided by mW makes it particularly useful for the study of slow processes in deeply supercooled water, the mechanism of ice nucleation, wetting-drying transitions, and as a realistic water model for coarse-grained simulations of biomolecules and complex materials.

I. Introduction

Computer simulations play an important role in understanding the significance of microscopic interactions in water properties. The first model of liquid water was proposed in 1933 by Bernal and Fowler: an icelike disordered tetrahedral structure arising from the electrostatic interactions between close neighbors.[1] About hundred atomistic potentials of water have been developed since then. The apparent profligacy of atomistic potentials is not just a tribute to water's essential role in nature, but an admission of the difficulty in representing the complex physics of water with a simple and efficient to compute model. Atomistic models used in molecular simulations use long-ranged forces (electrostatics) to produce short-ranged tetrahedral structure (hydrogen bonds). The most popular models of water, SPC,[2] SPCE,[3] TIP3P,[4] TIP4P,[4] TIP5P,[5] and their polarizable cousins,[6–9] follow this modeling paradigm based on the electrostatic nature of the intermolecular interactions in real water.

In this article we address the question of what are the essential ingredients for a model to generate the thermodynamic, dynamic, and structural anomalies of water,[10] while quantitatively reproducing water's experimental structure, energetics, and phase behavior. Can a coarse-grained model without electrostatic interactions and hydrogen atoms reproduce the structure and phase behavior of water as accurately as all-atoms models?

The idea of developing a coarse-grained model of water, without hydrogen and electrostatics, is not new.[11–14] Here we make a distinction between coarse-grained and toy models of water: the former are parametrized to quantitatively reproduce some water properties, while the latter aim to qualitatively capture water's anomalous behavior without attempting to reproduce faithfully the properties of water. The phase change energetics and the structures of the condensed phases of waterlike toy models are not close to those of water, but the models provide insight on which microscopic interactions can produce waterlike anomalous behavior. Examples of waterlike toy models of water are the Mercedez-Benz model in two[15,16] and three dimensions,[17] isotropic potentials with two characteristic length-scales,[18–23] and modified van der Waals models.[24,25] All these models produce waterlike anomalies and most of them also produce liquid−liquid transitions.

Existing coarse-grained models of water without electrostatics and hydrogen atoms represent intermolecular interactions with a spherically symmetric potential. It has been proved that isotropic potentials cannot reproduce the energetics and structure of water simultaneously.[14] Isotropic models that reproduce the radial distribution function (rdf) of liquid water are unable to reproduce the oxygen−oxygen–oxygen angular distribution function (adf),[14] they underestimate the internal energy of the liquid by about 50%,[13] and they do not produce the most characteristic anomaly of water, the existence of a density maximum.[14] Moreover, isotropic monatomic models of water do not form a tetrahedral crystal or a low-density glass on cooling. They model a "normal" liquid, not water.

To investigate whether a coarse-grained model can reproduce the structures and phase behavior of water without using electrostatics and hydrogen atoms, we first shift our attention from water to simple monatomic systems that also form tetrahedral structures: silicon and germanium. Similar to water, these elements form tetrahedral crystals at room pressure and have two amorphous phases:[26,27] a low- and a high-density glass. The low-density glasses, low-density amorphous ice (LDA), a-Si and a-Ge, are disordered structures with tetrahedral coordination.[26–28] The high-density glasses of these three substances also have analogous structure.[29]

The similarities between water, Si, and Ge also encompass the phase diagram and anomalies. These three belong to a

† Part of the special section "Aqueous Solutions and Their Interfaces".

* To whom correspondence should be addressed. E-mail Valeria.Molinero@utah.edu. Phone: +1801-585-9618. Fax: +1801-581-4353.

10.1021/jp805227c CCC. $40.75
Published on Web 10/29/2008

handful of substances whose liquid is denser than the crystal, resulting in a decrease of the melting temperature with pressure. The density of "normal" liquids increases monotonously on cooling. The density of water, on the other hand, displays a maximum at 4 °C and sharply decreases in the supercooled region.[10] Silicon also displays a density maximum, deep in the supercooled regime.[30] The dynamics of these liquids are also anomalous: while the viscosity of "normal" liquids increases with pressure, liquid silicon and water become more fluid on compression.[10,31] This anomaly is more pronounced in the deeply supercooled regime, and disappears at higher temperatures.[10]

The similarities between these tetrahedral liquids suggest that water, as silicon, may be modeled as a single particle with only short-ranged interactions. This does not mean that electrostatic interactions or the hydrogen atoms are irrelevant in determining water structure and thermodynamics, but that their effect may be effectively produced with a monatomic short-ranged potential.

II. Model and Methods

A. The mW Monatomic Water Model. To "make water out of silicon", we start from the Stillinger−Weber (SW) silicon potential.[32] In the SW model, tetrahedral coordination of the atoms is favored by adding to a pairwise potential $v_2(r)$ a three-body term $v_3(r,\theta)$ that penalizes configurations with angles that are not tetrahedral, $v = v_2(r) + \lambda\, v_3(r,\theta)$. The parameter λ tunes the strength of the tetrahedral penalty.[33] The higher the value of λ, the more tetrahedral the model is.

The full expression of the SW potential as a function of the distances between pairs of atoms and the angles formed by triplets of atoms is given by

$$E = \sum_i \sum_{j>i} \varphi_2(r_{ij}) + \sum_i \sum_{j\neq i} \sum_{k>j} \varphi_3(r_{ij}, r_{ik}, \theta_{ijk})$$

$$\varphi_2(r) = A\varepsilon\left[B\left(\frac{\sigma}{r}\right)^p - \left(\frac{\sigma}{r}\right)^q\right]\exp\left(\frac{\sigma}{r - a\sigma}\right)$$

$$\varphi_3(r, s, \theta) = \lambda\varepsilon[\cos\theta - \cos\theta_o]^2\exp\left(\frac{\gamma\sigma}{r - a\sigma}\right)\exp\left(\frac{\gamma\sigma}{s - a\sigma}\right)$$

where[32] $A = 7.049556277$, $B = 0.6022245584$, $p = 4$ $q = 0$, and $\gamma = 1.2$ give the form and scale to the potential, the reduced cutoff $a = 1.8$ ensures that all terms in the potential and forces go to zero at a distance $a\sigma$, and the cosine quadratic term around $\theta° = 109.47°$ favors tetrahedral angles. The parameters λ scales the repulsive three-body term and determines the strength of the tetrahedral interaction in the model; its value for silicon is 21.[32] Two additional parameters set the energy scale ε (the depth of the two-body interaction potential) and the length scale σ (the particle diameter) of the model. Note that the SW potential can be written in a reduced form independent of the values of σ and ε. Only the tetrahedrality λ and the size and energy scale, σ and ε, are tuned to produce the monatomic water model mW that represents each molecule as a single atom with tetrahedral interactions.

B. Simulation Details. We carried out molecular dynamics (MD) simulations using LAMMPS, a massively parallel MD software developed by Plimpton et al.[34] A reduced time step of 0.025 was used for the parametrization and validation. For the final set of parameters we found that timesteps up to 10 fs (0.05 in reduced units) conserve the energy better than 1/10000 in microcanonical simulations of 10^6 steps. We used a 10 fs step for the simulations to validate the properties of the model, except for the high pressure simulations and those that involve an open interface, where a 5 fs step was used. Where indicated, the temperature and pressure were controlled with the Nose−Hoover thermostat and barostat with relaxation times 1 and 2.5 ps, respectively. All isobaric simulations were at $p = 0$. Except when otherwise is indicated, the system contained 4096 particles in a periodic box and the simulation time was 10 ns.

C. Property Computation. ***Melting Temperature.*** The structures of hexagonal (Ih) and cubic (Ic) ices without hydrogen atoms correspond to hexagonal and cubic diamond, respectively. Their melting temperatures (T_m) were determined through the phase coexistence method, as implemented and discussed in detail in ref 35. In this method, a perfect crystal and a liquid slab are put in contact to facilitate the growth of the stable phase on isobaric isothermal (NPT) MD run. Garcia Fernandez et al. applied this method to atomistic models of water and proved that it reproduces the melting temperatures obtained from free energy calculations.[35] We start from a periodic cell of dimensions approximately 50 Å × 30 Å × 30 Å, where half of it (~25 Å × 30 Å × 30 Å) is a perfect cubic or hexagonal diamond crystal and the other half is a liquid. In a NPT simulation starting from this system below T_m ice grows until it encompasses all the system, same for the liquid above T_m. We determine T_m as the mean value between the highest T for which does not melt at the lowest T for which it does, and report as the error bar half the difference between these two. In the case of the mW potential, we estimated the precision from five independent series of simulations for each of the two crystalline structures.

Density, Enthalpy, Heat Capacity, and Compressibility. The density was determined as $\rho = NM/(N_A\langle V\rangle)$, where where N is the number of particles in and V the volume of the simulation cell, $M = 18.015$ g is the molar weight of water, N_A is Avogadro's number and $\langle ...\rangle$ indicates a time average over an equilibrium simulation. The enthalpies of the condensed phases were computed as $\langle H\rangle = \langle E + pV\rangle$, where E is the total energy per mol, V the simulation volume per mol, and p the pressure of the system. We assumed the molar enthalpy of the vapor was that of an ideal gas with zero internal energy, $H_{gas} = 1.5\ RT + pV_{gas} = 2.5\ RT$. Relatively small systems, 512 or 576 particles, were used for the enthalpies calculation in the parameter search, while the results reported for the final mW potential were obtained with 4096 particles.

An isobaric quench simulation from 320 to 205 K in 230 ns (rate 0.5 Kns^{-1}) was used to compute (i) the temperature dependence of the density and the location of its maximum, and (ii) the enthalpy of the liquid, and its temperature derivative, Cp. The rate of change of the temperature is slow compared with the equilibration time of the liquid, and we assume that the liquid is in local equilibrium. $H(T)$ and $\rho(T)$ were computed from a rolling average over one nanosecond-length intervals. The assumption of local equilibrium was verified by computing the average density and enthalpy for 5 to 10 ns isothermal simulations at several temperatures along the whole temperature range; the average values are indistinguishable from those of the slow ramp. The use of the slow ramp is advantageous in determining the position of the density maximum without the need of interpolation. The enthalpy was fitted to an equation of the form[36] $H_{liquid}(T) = A + BT + C(T/T_o - 1)^\gamma$ (correlation coefficient 0.999824) from which the isobaric heat capacity was obtained by analytical derivation, $Cp = dH/dT)_{p,N}$.

The isothermal compressibility of mW liquid at 300 K around $\rho_o = 1$ g·cm^{-3} was calculated by a finite difference approximation[37] as

$$\kappa_T = -\frac{1}{V}\left(\frac{\partial V}{\partial p}\right)_T \approx \left(\frac{\ln(\rho_2/\rho 1)}{p_2 - p_1}\right)_T$$

where ρ_2 and ρ_1 are 1% above and below ρ_o. The average pressures p_2 and p_1 were computed from a 10 ns NVT simulation at $T = 300$ K.

Radial and Angular Distribution Functions. The pair distribution function between two water sites in the coarse-grained model was computed as an ensemble average over pairs of water particles

$$g(r) = \frac{V}{N^2}\left\langle \sum_{i=1} \sum_{j \neq i} \delta(r - r_{ij}) \right\rangle$$

The average number of neighbors in the liquid up to a distance Rc is given by

$$n_c = 4\pi \frac{N}{V} \int_o^{R_c} r^2 g(r)\, dr$$

The adf was computed as an ensemble average over the angles between each water and its closest n_c neighbors

$$P(\theta) = \frac{1}{N n_\theta}\left\langle \sum_{k=1}^{N} \sum_{i=1}^{n_c} \sum_{j \neq i}^{n_c - 1} \delta(\theta - \theta_{ikj}) \right\rangle$$

where n_θ is the number of angles subtended by the n_c neighbors around the central molecule k. We selected $n_c = 8$ to compare with the neutron scattering results of Strassle et al.[38]

Self-Diffusion Coefficient. The diffusion coefficient of liquid water was computed from the slope of the mean square displacement with time using Einstein's relation

$$D = \lim_{t \to \infty} \frac{1}{6t} \langle |r(t) - r(0)|^2 \rangle$$

At room pressure, statistics were collected at temperatures ranging from 363 to 243 K. To study the density dependence of the diffusion coefficient, NVT simulations were performed at 243 and 220 K at densities from 0.94 to 1.20 g·cm^{-3}.

Surface Tension. The liquid−vapor surface tension was determined as in ref 39: a periodic liquid slab containing 1024 particles was placed between two empty regions, with its two interfaces perpendicular to the z axis. The dimensions of the periodic cell containing the slab and the vacuum region is $Lx = Ly = 30$ Å and $Lz = 100$ Å. The surface tension was obtained from the average over 20 ns NVT simulation at 300 K of the components of the pressure tensors tangential and perpendicular to the liquid-vacuum interface, $\langle p_T \rangle$ and $\langle p_N \rangle$, respectively:[39]

$$\gamma = \frac{L_z}{2}[\langle p_N \rangle - \langle p_T \rangle]$$

The error was propagated from the uncertainties in $\langle p_T \rangle$ and $\langle p_N \rangle$.

D. Parameterization of mW. To find the optimum values of λ, ε, and σ we implemented a noniterative procedure. First, we computed the melting temperature for *Ih* in the range $22 < \lambda < 27$ in reduced units, $T_m^*(\lambda)$. Second, for each value of tetrahedral parameter λ, we found the energy scale $\varepsilon(\lambda)$ that yields the experimental T_m of water: 273.15 K $= T_m^*(\lambda)\varepsilon(\lambda)/k_b$, where k_b is Boltzmann's constant. Third, the phase change enthalpies were computed as a function of λ. The value $\lambda = 23.15$ was selected as the one that best reproduce water's vaporization enthalpy (see Figure 1). Finally, the value of σ was scaled to reproduce the density of the liquid at 298 K.

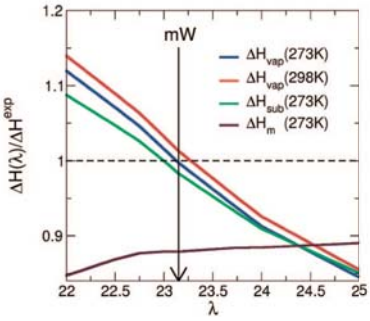

Figure 1. Optimization of the tetrahedral parameter λ for the monatomic water. The ratio between the enthalpies of vaporization, sublimation, and melting in SW potentials and the experiment shows best agreement for a tetrahedrality $\lambda = 23.15$. The energy scale for each of these potentials is obtained by requiring that the computed melting point agrees with the experimental values for hexagonal ice.

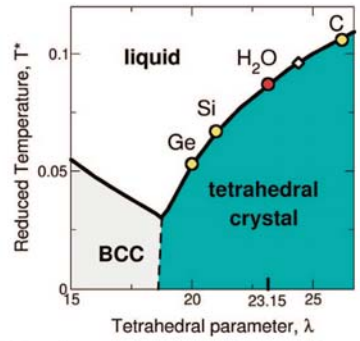

Figure 2. Phase diagram of modified SW potential as a function of the strength of the tetrahedral repulsive parameter λ at zero pressure. The stable crystal is tetrahedral for $\lambda > 18.75$; for less tetrahedral potentials an 8-coordinated BCC crystal is more stable.[33] Carbon, water, silicon, and germanium can be considered as members of this family with different tetrahedral strength: $\lambda_C = 26.2$,[40] $\lambda_{water} = 23.15$ (this work), $\lambda_{Si} = 21$,[32] and $\lambda_{Ge} = 20$.[26] Their reduced melting points, $T_m k_b/\varepsilon$, are indicated by circles on the coexistence curve. The hollow rhomboid signals the tetrahedrality ($\lambda = 24.4$ at $p = 0$) for which the coexisting crystal and liquid have the same density. Carbon with $\lambda > 24.4$ is the only one of these substances for which the crystal (both diamond and the most stable graphite) is denser than the liquid.[41]

The interaction parameters of mW are $\lambda = 23.15$, $\varepsilon = 6.189$ Kcal/mol and $\sigma = 2.3925$ Å; all other parameters are identical to silicon in ref 32. The potential is very short ranged: all forces between atoms farther than 4.32 Å are zero. The parametrization of mW places water as an element with tetrahedrality intermediate between silicon and carbon: Figure 2 shows that the tetrahedral strength of water, $\lambda = 23.15$ is higher than that of silicon $\lambda = 21$[32] and germanium $\lambda = 20$[26] and lower than that of carbon, $\lambda = 26.2$.[40] The tetrahedral ordering C > water > Si > Ge is supported by an increasing number of first neighbors in the liquids: carbon (<4)[41] < water (5.2−5.3)[42] < Si (~5.5−6)[43] < Ge(~6−7).[44]

TABLE 1: Comparison of Water Models and Experiment[a]

	$T_{m\ HEX.\ ICE}$ (K)	ΔH_m (T_m) (kcal·mol^{-1})	ρ_{liquid} (T_m) (g·cm^{-3})	ρ_{ice} (T_m) (g·cm^{-3})	ρ_{liquid}(298 K) (g·cm^{-3})	ΔH_{vap} (298 K) (kcal·mol^{-1})	D (298 K) (10^{-5} cm^2·s^{-1})	γ_{LV} (300 K) mJ·m^{-2}	*TMD* (K)	$\rho_{liquid,\ MAX}$ (TMD) (g·cm^{-3})
exp	273.15	1.436	0.999	0.917	0.997	10.52	2.3	71.6	277	0.99997
mW	**274.6**	**1.26**	**1.001**	0.978	**0.997**	10.65	6.5	**66.0**	250	**1.003**
SPC	(191)	0.62	0.991	**0.934**	0.977	**10.56**	4.0	53.4	228	1.008
SPCE	(215)	0.74	1.007	0.950	0.999	10.76	**2.4**	61.3	241	1.012
TIP3P	(146)	0.30	1.017	0.947	0.986	10.17	5.3	49.5	182	1.038
TIP4P	232	1.05	1.002	0.940	1.001	10.65	3.9	54.7	253	1.008
TIP5P	(274)	1.75	0.987	0.982	0.999	10.46	2.6	52.3	**285**	0.989

[a] Melting temperatures of hexagonal ice, densities of liquid, and crystal phase at coexistence and enthalpy of melting are from ref 71. Parentheses enclosing a T_m signal that the stable crystal is ice II, not hexagonal ice, for these models.[72] Diffusion coefficients D and density at 298 K are from refs 73 and 74. Liquid-vacuum surface tensions are from ref 75. TMD and its corresponding liquid density $\rho_{liquid,MAX}$ are from ref 76. Bold numbers signal the closest agreement with the experiment.

We benchmarked mW against SPCE, the least expensive atomistic model, in simulations with 1600 molecules. mW is 180 times faster than SPCE. The speedup arises from the smaller number of particles (1 versus 3) the longer timesteps (10 versus 1.5 fs) and shorter range of interactions (cutoff at 4.32 Å versus Ewald sums).

III. Results

Energetics, Density and Surface Tension. The melting temperature T_m, enthalpy of sublimation of ice at T_m, enthalpy of vaporization of the liquid computed with molecular dynamics simulations of mW are within 2% of the experimental values, as shown in Table 1. In agreement with experiment, the mW model predicts that hexagonal ice ($T_m = 274.6 \pm 1$ K) is more stable than cubic ice ($T_m = 271.5 \pm 1$ K). The density of mW liquid is within 1% of the experimental value in the temperature range 250 to 350 K.

How well a water model reproduces the liquid−vapor surface tension is of the highest relevance for the study of water at the vacuum and hydrophobic interfaces, wetting-drying transitions and hydrophobic attraction. The liquid-vacuum surface tension of mW at 300 K is $\gamma_{lv} = 66 \pm 2$ mJ/m^2, which is in very good agreement with the experimental value, 71.6 mJ/m^2.

Structure. Simple liquids, such as molten metals, typically have an average of ~11 first neighbors. At 25 °C, water has an average of 5.1 to 5.3 molecules in the first coordination shell and characteristically short-ranged radial ordering.[42,45] The radial distribution function was not considered in the parametrization of mW. Nevertheless, Figure 3 shows that the structure of the mW liquid is in excellent agreement with the one derived from X-ray and neutron diffraction experiments for water[45,42] (Figure 3b). The number of water neighbors up to a distance of 3.5 Å is between 5.1 and 5.3 for the neutron/X-ray refined structures of Soper[42] and is 5.1 for the monatomic water (mW has 4.25 neighbors within the first 3.3 Å).

The adf provides a more stringent validation for the quality of a water model. The monatomic model quantitatively reproduces the experimental OOO adf of liquid water[38] (Figure 3a). The intermolecular forces in the mW model vanish at just 4.3 Å, so we conclude that long-range forces are not needed to reproduce the characteristically short-ranged structure of the liquid.

Density Anomaly. Among water thermodynamic anomalies, the best known is the density maximum at 4 °C. Most atomistic models of water reproduce the existence of a density maximum with varied success in predicting the temperature of maximum density (TMD). Figure 4 shows the liquid density as a function of temperature at room pressure for water, mW, and atomistic

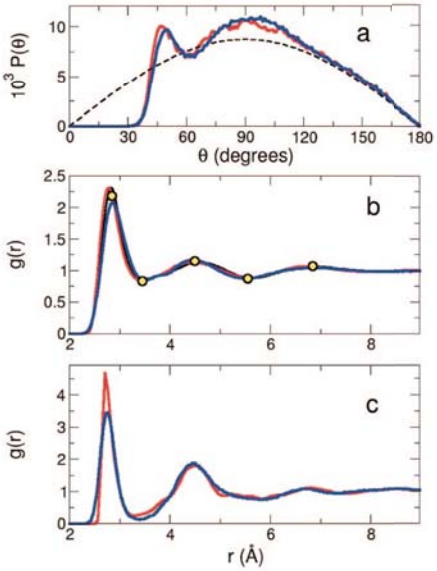

Figure 3. The tetrahedral monatomic model without electrostatic interactions reproduces the structure of water. (a) Angular distribution function of eight closest oxygen neighbors in water at 298 K in experiment[38] (red) and mW simulation (blue). Dashed line is the random distribution. (b) Radial distribution function of liquid water at 298K in mW (blue line) and experiment: X-ray diffraction is from ref 45 (yellow circles) and refined structure from Advanced Light Source X-ray and neutron data is from ref 42 (red and black lines). (c) The experimental radial structure of LDA[77] (red) is well reproduced by the mW model (blue).

models; Table 1 summarizes the TMD and maximum densities, $\rho_{liquid,MAX}$. The density maximum of mW is 1.003 g·cm^{-3}, which is in excellent agreement with the experimental value of 0.99997 g·cm^{-3}.[46] The temperature of maximum density (TMD) of mW is 250 K, which is below the melting temperature and the experimental value of 277 K.[46] While the TMD is an intrinsic property of the liquid, the melting point depends on the relative enthalpy and entropy of liquid and crystal. mW was parametrized to reproduce the experimental melting temperature, but it can be argued that monatomic water should have a melting point higher than molecular water, because there is no contribution from the rotational entropy to the melting of the monatomic liquid. We interpret that the location of the TMD in mW below T_m (as also observed in silicon[30]) is a consequence of the monatomic character of the model.

Heat Capacity Anomaly. Another consequence of mW being monatomic is a low heat capacity. mW has one-third of the

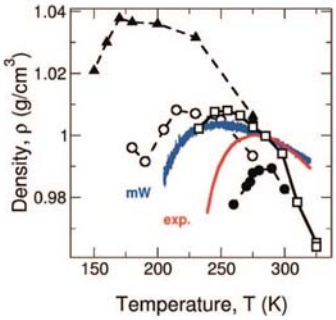

Figure 4. Temperature dependence of the density of liquid water at p = 1 atm. The experimental (labeled exp) density maximum is qualitatively reproduced by all atomistic models of water and the monatomic model with tetrahedral interactions mW but not by isotropic pair potentials that reproduce the radial distribution function of water.[14] Atomistic data from ref : TIP5P (black circles), TIP4P (white squares), TIP3P (black triangles), SPC (white circles). Experimental density from ref 46.

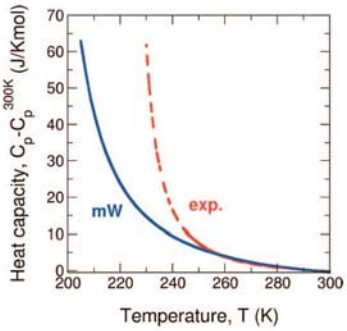

Figure 5. The constant pressure heat capacity of liquid water shows a marked increase in the supercooled region, coincident with the expansion of the density (Figure 4). Experimental data, available down to 245 K, is well represented by $C_p(T) = 0.44(T/222\text{-}1)^{-1.5} + 74.3$.[36] The dotted line extrapolates the fit into the temperature range experimentally inaccessible due to ice crystallization. The heat capacity of monatomic water mW is well described by $C_p(T) = 2.36\ (T/185\text{-}1)^{-1.5} + 28.25$ in the temperature range 205 to 320 K.

degrees of freedom of atomistic water, and a constant pressure heat capacity C_p at 25 °C that is 44% of the experimental value (33 versus 75.3 J/Kmol[46]). The low value should be mainly due to the loss of the rotational contribution to the liquid's heat capacity.

In Figure 5, we present the heat capacity of liquid water and mW, with respect to their values at 300 K. There is a sharp increase in the C_p of supercooled liquid water[47] that correlates with the dramatic volume expansion shown in Figure 4. The coarse-grained model mW reproduces this thermodynamic anomaly associated to the transformation of the liquid to a low-density almost perfectly tetrahedral amorphous phase (see below). The experimental heat capacity, available down to 245 K, is well represented by $C_p(T) = 0.44(T/222\text{-}1)^{-1.5} + 74.3$.[36] The heat capacity of monatomic water mW is well described by $C_p(T) = 2.36\ (T/185\text{-}1)^{-1.5} + 28.25$ in the temperature range 205 to 320 K. The temperature of the transformation is shifted to lower temperatures with respect to the experiment for the same reasons discussed above for the density maximum.

Diffusion Anomaly. The diffusion coefficient of mW at 298 K is $D = 6.5 \times 10^{-5}$cm^2/s, almost three times the experimental value (see Table 1). The mobility in mW is faster because the molecules are not slowed down by the reorientation of hydrogen atoms. The effect of the lack of hydrogens is not only an increase in the magnitude of the mobility but also a lower activation energy than the experiment: Figure 6 shows that D of mW is less sensitive to temperature than that of the experimental substance. The consequence is that mW reaches the deeply supercooled state where the liquid transforms to a low-density structure, with relatively high mobility.

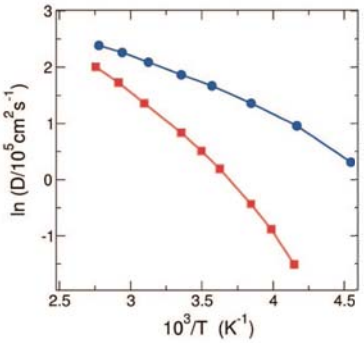

Figure 6. Diffusion coefficient of mW and experimental water as a function of temperature. The diffusion coefficient of monatomic water (blue circles) is higher and less sensitive to temperature than the experimental one (red diamonds).

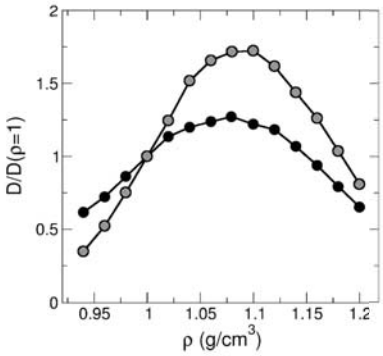

Figure 7. The monatomic water reproduces water's diffusivity anomaly. Relative diffusion with respect to that at $\rho = 1$ g/cm^3 at 243 K (black circles) and 220 K (gray circles).

Experimentally and in atomistic simulations with the SPC/E model, water diffusivity attains a maximum when the liquid is compressed to a density of about 1.1 g·cm^{-3}.[48,49] The coarse-grained model reproduces this anomalous density dependence: the diffusivity passes through a maximum for a density of 1.1 and 1.08 g·cm^{-3} at $T = 243$ and 220 K, respectively (Figure 7). The ratio $D_{max}/D(\rho = 1\ \text{g·cm}^{-3})$ (the strength of the anomaly) is comparable in the experiment and coarse-grained simulations if the temperature is measured from the TMD; at 25 K below the TMD, the enhancement in diffusivity is 1.8[50] and 1.75, respectively.

Phase Transformations of Supercooled Water. The existence of a density maximum and a heat capacity that dramatically increases in supercooled liquid silicon[33] and water is related to the stabilization of low-density amorphous structures (a-Si and LDA) at low temperatures. Computer simulations of Si with the Stillinger-Weber potential reveal a first order liquid−liquid transition at room pressure.[51] It is still debated whether (and in which pressure range) a first order transition separates the high- and low-density liquids in water.[28] On the one hand, experi-

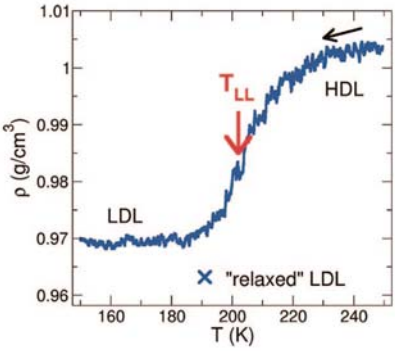

Figure 8. (color online) Liquid−liquid transformation in supercooled liquid water. The density of liquid water through a linear temperature quench at a 10 K/ns rate displays a sharp transition at $T_{LL} = 202$ K from a high-density structure (HDL) to a low-density one (LDL). Relaxation of the liquid below T_{LL} produces a liquid of lower density, indicated with a red cross. The liquid−liquid transformation competes with ice crystallization, that occurs around T_{LL} for quenching rates 1 K/ns.

mental studies are hindered by the crystallization of the metastable liquid when it approaches the putative location of the liquid−liquid coexistence line. The easy crystallization makes it difficult to study the characteristics of deeply supercooled water and the process of vitrification or ice nucleation in experiments. On the other hand, the slow dynamics of the supercooled liquid hinders its study through atomistic simulations. The monatomic model, with its low computational cost and higher mobility, is adequate to fill in this gap in the study of phase transitions and properties of supercooled water.

As observed in the experiments, the product, ice or glass, of a fast quenching of the monatomic liquid water at room pressure depends on the cooling rate; we find that mW forms ice for cooling rates 10^9 K/s or slower. At higher quenching rates, mW water transforms to a low-density liquid (LDL) that vitrifies to LDA (see Figure 8). It is interesting to note that crystallization in the quenching simulations happens always around the temperature where the high-density liquid transforms into the low-density one, $T_{LL} = 202$ K for the mW model at 1 atm. More studies are needed to determine whether the liquid−liquid transformation is continuous or first order.

The cooling rate needed to bypass crystallization in a system with 4096 mW is $\sim 10^3$ faster than in experiments involving micron-sized droplets; ice nucleation in mW is several orders of magnitude faster than in real water. The reasons are probably two-fold: (i) the lack of hydrogens that reduce the search in configurational space to produce ice nuclei, and (ii) the higher diffusivity of the liquid, also due to a lack of hydrogen atoms. The highest rate makes feasible the collection of the thousands of crystallization trajectories needed to characterize the stochastic process of ice nucleation. It should be noted that the ice nucleation times are a strongly varying function of the temperature, and a system with 4096 mW can be equilibrated down to 205 K without interference of crystallization. In this condition, the characteristic time for ice nucleation is 30 ns while the relaxation time of the monatomic liquid is less than one nanosecond.[52] The study of the mechanism of ice nucleation in bulk and in nanopores and its relationship to water polyamorphism will be presented in separate communications.

If crystallization is bypassed it is possible (but difficult!) to partially relax the low density liquid at a temperature below T_{LL}. The relaxed density for a system of 512 molecules after 130 ns NPT simulation at 190 K is shown as a cross in Figure 8. The structure of mW's LDL is an amorphous tetrahedral network with an average of 4.04 first neighbors and rdf in excellent agreement with the one for LDA measured by neutron diffraction (Figure 3c). The formation of amorphous ice, not considered in the parametrization of mW, supports the hypothesis that a monatomic model with short-ranged tetrahedral interactions is enough the produce the main features of water's phase behavior at room pressure.

IV. Discussion

Can a coarse-grained model without electrostatic interactions and hydrogen atoms reproduce water properties as accurately as all-atoms models? Table 1 compares the performance of mW, SPC, SPCE, TIP3P, TIP4P, and TIP5P in representing key properties of water at room temperature and the melting point. mW outperforms the atomistic models in 6 out of the 10 properties listed in the table: the prediction of hexagonal ice as the stable crystal at room pressure and its melting point, the enthalpy of melting of ice, the density of the liquid at T_m and 298 K, and the maximum density of the liquid and the liquid−vapor surface tension. Of the other four, the enthalpy of vaporization is just 1.2% above the experimental value for mW. The enthalpy of sublimation of ice (not reported for most atomistic models) is only 1.7% higher than experiment. Let us address now the three properties for which mW is outperformed by at least one atomistic model. The predicted temperature of maximum density, 27 K below experiment, is in the middle of atomistic range (worst, TIP3P, 95 K below; best, TIP5P, 8 K above). The diffusion coefficient is the only property of Table 1 for which mW trails all atomistic models: mW predicts a value 2.8 times the experiment, while atomistic models predict from 1.04 (best, SPCE) to 2.3 (worst, TIP3P) of water's value. The second worst reproduced property is the density of ice, overestimated by all models, for which mW is better only to TIP5P (best: SPC).

Overall, mW outperforms the most popular atomistic models in the representation of the ten properties of Table 1. But there is a price paid for the lack of hydrogens: on the one hand, mW cannot "extend and bend" hydrogen bonds as water does, resulting in (i) a reduced density gap between liquid water and ice and (ii) a lower isothermal compressibility, $\kappa_T \approx 1.9\ 10^{-5}$ atm^{-1} at 300 K compared with the experimental value of $4.58\ 10^{-5}$ atm^{-1}.[46] While it may be possible to improve the flexibility of the model to better reproduce the compressibility and ice density without significant deterioration of other properties, it is not clear to us that this can be done while keeping a simple form of the intermolecular interactions. On the other hand, the lack of hydrogen atoms is responsible for the highest diffusivity of the monatomic model: coarse-grained models evolve on smoother potential energy surfaces better than fully atomistic ones,[12] and the hydrogen's effectively produce a friction on water's center of mass translation.

The true Achilles heel of coarse-grained models is the heat capacity: a model with less degrees of freedom necessarily underestimates C_p. Water's rotational contributions to the heat capacity -active in the liquid and vapor phases- are absent in the monatomic model. The underestimation of C_p will produce a degradation of the agreement in the energies and entropies as the temperature moves away from the one used in the parametrization (273 and 298 K, in this case).

mW displays the diffusional and thermodynamic anomalies of water. We note that the density of maximum diffusivity and the magnitude of the enhancement are in very good agreement

with the experiment, although the pressure is overestimated, due to a low compressibility. This supports a structural origin for the diffusivity maximum in water. It would be interesting to determine whether mW reproduces the hierarchy of anomalies[53] observed for atomistic models of water. The thermodynamic anomalies are produced by a sharp high- to low- density transformation of the liquid at T_{LL} that is fifty degrees below the TMD, as observed in experiments of nanoconfined water.[54] We computed the heat capacity of the liquid down to a few kelvins above T_{LL} and found a power law behavior (Figure 3) that predicts divergence at a temperature 17 K below the actual T_{LL} of the model. These results, and the observation of ice nucleation from supercooled water suggest that mW will be useful in understanding the puzzling behavior of water at low temperatures, close and inside "no man's land".[28]

The monatomic tetrahedral model faithfully reproduces the structure of ice, liquid water, and low-density amorphous ice using extremely short ranged interactions: all forces go smoothly to zero at 4.32 Å, a distance shorter than the second peak in the liquid's rdf. Compare this with the long ranged electrostatic forces used in atomistic simulations of water. We conclude that long-ranged interactions are not needed to model the structure of water. The introduction of a nonbond angle dependent term in the coarse-grained interaction potential is essential to capture the physics of water intermolecular interactions and results in a model of water in which the molecules are "hydrogen bonded" although there are no hydrogen atoms. The hydrogen atoms can be regarded as the "glue" that keeps the oxygens in hydrogen-bonded positions.

How well can the monatomic water model reproduce the structure and properties of aqueous solutions and water at interfaces? Electrostatic interactions are essential for the solvation of ions and hydrophilic molecules, but mW does not speak the language of electrostatics. It is necessary to mimic the effect of these interactions through short-ranged potentials to preserve the computational efficiency of the coarse-grained model. Even if the efficiency was not a concern, the use of electrostatics for the solute−solute interactions does not address the problem of how do water and solute interact without electrostatics. Preliminary results from our group show that it is possible to reproduce the main effect of hydrophilic and ionic solutes on the structure of water, the decrease in tetrahedrality evidenced in the experiments by the depression of the second peak in the OO rdf[55] with only short-ranged SW potentials.[56] It is still an open question whether this can be extended to model two challenging properties of ionic solutions: the stabilization of solvent-separated ion pairs in aqueous solutions and the layering of cations and anions at different depths from the water-vacuum interface.[57]

It has been reported that a good description of hydrophobic effects in simulations correlates with an accurate description of the liquid density over a broad temperature range.[58] The signatures of the hydrophobic effect have been traced to water's low compressibility and relatively low decrease of density on heating, compared to organic solvents.[59] Recently, Buldyrev et al.[23] found that the Jagla model (an isotropic ramp potential with two characteristic length-scales that displays the thermodynamic, structural, and diffusional anomalies as water but not water's characteristic liquid and crystal structures) produces waterlike solvation thermodynamics for hydrophobic solutes: a solubility minimum as a function of temperature and swelling of hydrophobic polymer chains at low temperature. Their study suggests that waterlike solvation of hydrophobic molecules may be given by the ability of the solvent to expand on cooling. The density of liquid mW is within 1% of experiment for 250 < T < 350 K, which is in better agreement than the atomistic models (Figure 3 and Table 1) despite the low TMD. The extent by which mW can predict hydrophobic hydration remains to be studied, but the good agreement in the density and its temperature dependence, energetics, structure, and surface tension suggests that mW will be a realistic water solvent for hydrophobic molecules in coarse-grained simulations.

An interesting question is whether the monatomic model, parametrized from bulk data, can reproduce interfacial properties of water. We have shown above that mW reproduces the liquid−vapor surface tension of water at ambient conditions. In work to be reported elsewhere,[60,61] we found that the monatomic model produces the phase behavior of interfacial atomistic models of water in hydrophobic confinement: mW confined between nanoscopic hydrophobic disks displays wetting-drying transitions[60] at surface separations in good agreement with those found in atomistic studies,[62,63] and at lower temperatures it forms bilayer ice and other ice structures related to bulk hexagonal ice,[61] also observed in atomistic simulations.[64,65]

V. Conclusions

Tetrahedrality, through the formation of hydrogen bonds, is arguably the defining characteristic of water interactions. Head-Gordon and Rick found that modified SPC/E and TIP4P-Ew models that form only two hydrogen bonds do not produce waterlike properties.[66] Debenedetti and co-workers reached the same conclusion for SPC/E potentials for which the H−O−H angle is modified to hinder the tetrahedral coordination of the molecules.[67] In this work, we strip water of atomistic detail and represent it as an atom with very short-ranged tetrahedral interactions. The success of the mW model in reproducing the liquid, crystal, and glass structures of water, their energetics, liquid anomalies, and the corresponding phase transitions strongly indicates that the nature of the intermolecular interactions, covalent/metallic or dipole/hydrogen bond, is less defining of the structural and thermodynamic behavior of these substances than the formation of tetrahedral configurations. More provocative, the monatomic water model mW is just a more tetrahedral silicon atom with the corresponding change in energy and density scale. Only one of the seven parameters of the reduced Stillinger−Weber potential for silicon is tuned to produce a model that is surprisingly accurate in the description of water. Water and silicon not only belong to the same family but they are close siblings.

Angell et al. have qualitative positioned water within the family of tetrahedral liquids and conclude that water behavior is intermediate between silicon and silica.[68] In developing mW we move a step further and quantify how different water, silicon carbon, and germanium are in terms of a single parameter: the strength of the tetrahedral interactions. This quantitative relationship provides a unified framework to understand the rise and death of anomalous behavior along the family of tetrahedral liquids. Results in this respect will be presented in a future communication.

mW is a model without hydrogens and electrostatics but, of course, there are properties of water that require the electrostatics and the hydrogen atoms for their description (e.g., dielectric properties, rotational dynamics, all its chemistry!). The mW coarse-grained model does not replace atomistic representations of water but provides insight on which intermolecular interactions are responsible for water behavior. We conclude that the lack of hydrogen's has more impact on water properties, that is, lower heat capacity, lower structural flexibility to accom-

modate compression, less hindered diffusivity, than the shortening of the intermolecular interactions to 4.32 Å. There is an increasing interest in developing theories[69] and models[70] to replace the long-ranged electrostatic interactions by effective short-range potentials in all atom simulations. Izvekov et al. recently coarse-grained the interactions of SPC and TIP3P models to produce fully atomistic models where the electrostatic interactions are replaced by a function that vanishes at 10 Å.[70] The atomistic short-ranged potentials reproduce the rdf, density, internal energy, compressibility, and diffusion coefficient of the original models. The success of this "coarse-graining in interaction space"[70] supports our conclusion that the topology of the interactions, and not the range of the potential, is the key to model water.

The most severe representability issue of isotropic monatomic water models, namely their inability to simultaneously reproduce the structure and energetics of water at any state point, is removed by the introduction of the tetrahedral interactions. The monatomic tetrahedral model predicts the studied water properties (with the notorious exception of the response functions) to have comparable or better accuracy than atomistic models. The use of anisotropic interactions does not degrade the efficiency of the model: mW is 2 orders of magnitude faster than the least expensive atomistic model.

Coarse-grained models of polymers, proteins, carbohydrates, biomembranes, and other molecules have been developed in recent years. We expect that mW will be combined with these or new models to produce a computationally efficient representation of water in coarse-grained simulations of biomolecules and materials. The accuracy of coarse-grained models in reproducing the properties of solutions and interfacial water, particularly for ion-containing systems, is a question that deserves further study.

Acknowledgment. This research was supported by NSF under Collaborative Research Grant CHE-0628257. We acknowledge the Center of High Performance Computing at the University of Utah for a generous allocation of computing time. We thank Alan Soper and Thierry Strassle for sharing their data on the radial and angular distribution functions of water, respectively, and Jack Simons and Austen Angell for their comments on an earlier version of the manuscript.

References and Notes

(1) Bernal, J. D.; Fowler, R. H. *J. Chem. Phys.* **1933**, *1*, 515.
(2) Berendsen, H. J. C.; Postma, J. P. M.; van Gunsteren, W. F.; Hermans, J. In *Intermolecular Forces*; Pullman, B., Ed.; Reidel: Dordretch, 1981; pp 331.
(3) Berendsen, H. J. C.; Grigera, J. R.; Straatsma, T. P. *J. Phys. Chem.* **1987**, *91*, 6269.
(4) Jorgensen, W. L.; Chandrasekhar, J.; Madura, J. D.; Impey, R. W.; Klein, M. L. *J. Chem. Phys.* **1983**, *79*, 926.
(5) Mahoney, M. W.; Jorgensen, W. L. *J. Chem. Phys.* **2000**, *112*, 8910.
(6) Rick, S. W.; Stuart, S. J.; Berne, B. J. *J. Chem. Phys.* **1994**, *101*, 6141.
(7) Wallqvist, A.; Berne, B. J. *J. Phys. Chem.* **1993**, *97*, 13841.
(8) Chen, B.; Xing, J. H.; Siepmann, J. I. *J. Phys. Chem. B* **2000**, *104*, 2391.
(9) Ren, P. Y.; Ponder, J. W. *J. Phys. Chem. B* **2003**, *107*, 5933.
(10) Debenedetti, P. G. *J. Phys.: Condens. Matter* **2003**, *15*, R1669.
(11) Headgordon, T.; Stillinger, F. H. *J. Chem. Phys.* **1993**, *98*, 3313.
(12) Molinero, V.; Goddard III, W. A. *J. Phys. Chem. B* **2004**, *108*, 1414.
(13) Izvekov, S.; Voth, G. A. *J. Chem. Phys.* **2005**, *123*, 4711.
(14) Johnson, M. E.; Head-Gordon, T.; Louis, A. A. *J. Chem. Phys.* **2007**, *126*, 144509.
(15) Ben-Naim, A. *J. Chem. Phys.* **1971**, *54*, 3682.
(16) Dill, K. A.; Truskett, T. M.; Vlachy, V.; Hribar-Lee, B. *Annu. Rev. Biophys. Biomol. Struct.* **2005**, *34*, 173.
(17) Bizjak, A.; Urbi, T.; Vlachy, V.; Dill, K. A. *Acta Chem. Slov.* **2007**, *54*, 532.
(18) Jagla, E. A. *J. Chem. Phys.* **1999**, *111*, 8980.
(19) Jagla, E. A. *Phys. Rev. E* **1998**, *58*, 1478.
(20) Franzese, G.; Malescio, G.; Skibinsky, A.; Buldyrev, S. V.; Stanley, H. E. *Nature* **2001**, *409*, 692.
(21) Xu, L. M.; Buldyrev, S. V.; Angell, C. A.; Stanley, H. E. *Phys. Rev. E* **2006**, *74*, 031108.
(22) Yan, Z. Y.; Buldyrev, S. V.; Giovambattista, N.; Stanley, H. E. *Phys. Rev. Lett.* **2005**, *95*, 130604.
(23) Buldyrev, S. V.; Kumar, P.; Debenedetti, P. G.; Rossky, P. J.; Stanley, H. E. *Proc. Natl. Acad. Sci. U.S.A.* **2007**, *104*, 20177.
(24) Poole, P. H.; Sciortino, F.; Grande, T.; Stanley, H. E.; Angell, C. A. *Phys. Rev. Lett.* **1994**, *73*, 1632.
(25) Truskett, T. M.; Debenedetti, P. G.; Sastry, S.; Torquato, S. *J. Chem. Phys.* **1999**, *111*, 2647.
(26) Bhat, M. H.; Molinero, V.; Soignard, E.; Solomon, V. C.; Sastry, S.; Yarger, J. L.; Angell, C. A. *Nature* **2007**, *448*, 787.
(27) Mcmillan, P. F.; Wilson, M.; Daisenberger, D.; Machon, D. *Nat. Mater.* **2005**, *4*, 680.
(28) Mishima, O.; Stanley, H. E. *Nature* **1998**, *396*, 329.
(29) Benmore, C. J.; Hart, R. T.; Mei, Q.; Price, D. L.; Yarger, J.; Tulk, C. A.; Klug, D. D. *Phys. Rev. B* **2005**, *72*, 132201.
(30) Watanabe, M.; Adachi, M.; Morishita, T.; Higuchi, K.; Kobatake, H.; Fukuyama, H. *Faraday Discuss.* **2007**, *136*, 279.
(31) Morishita, T. *Phys. Rev. E* **2005**, *72*, 021201.
(32) Stillinger, F. H.; Weber, T. A. *Phys. Rev. B* **1985**, *31*, 5262.
(33) Molinero, V.; Sastry, S.; Angell, C. A. *Phys. Rev. Lett.* **2006**, *97*, 075701.
(34) Plimpton, S. J. *J. Comp. Phys.* **1995**, *117*, 1.
(35) Garcia Fernandez, R. G.; Abascal, J. L. F.; Vega, C. *J. Chem. Phys.* **2006**, *124*, 144506.
(36) Tombari, E.; Ferrari, C.; Salvetti, G. *Chem. Phys. Lett.* **1999**, *300*, 749.
(37) Motakabbir, K. A.; Berkowitz, M. *J. Phys. Chem.* **1990**, *94*, 8359.
(38) Strassle, T.; Saitta, A. M.; Le Godec, Y.; Hamel, G.; Klotz, S.; Loveday, J. S.; Nelmes, R. J. *Phys. Rev. Lett.* **2006**, *96*, 067801.
(39) Vega, C.; de Miguel, E. *J. Chem. Phys.* **2007**, *126*, 154707.
(40) Barnard, A. S.; Russo, S. P. *Mol. Phys.* **2002**, *100*, 1517.
(41) Ghiringhelli, L. M.; Los, J. H.; Meijer, E. J.; Fasolino, A.; Frenkel, D. *Phys. Rev. Lett.* **2005**, *94*, 145701.
(42) Soper, A. K. *J. Phys.: Condens. Matter* **2007**, *19*, 335206.
(43) Higuchi, K.; Kimura, K.; Mizuno, A.; Watanabe, M.; Katayama, Y.; Kuribayashi, K. *Meas. Sci. Technol.* **2005**, *16*, 381.
(44) Petkov, V.; Takeda, S.; Waseda, Y.; Sugiyama, K. *J. Non-Cryst. Solids* **1994**, *168*, 97.
(45) Narten, A. H.; Levy, H. A. *J. Chem. Phys.* **1971**, *55*, 2263.
(46) *CRC-Handbook Handbook of Chemistry and Physics*, 81th ed.; CRC: Boca Raton, 2000−2001.
(47) Angell, C. A.; Shuppert, J.; Tucker, J. C. *J. Phys. Chem.* **1973**, *77*, 3092.
(48) Prielmeier, F. X.; Lang, E. W.; Speedy, R. J.; Ludemann, H. D. *Phys. Rev. Lett.* **1987**, *59*, 1128.
(49) Starr, F. W.; Sciortino, F.; Stanley, H. E. *Phys. Rev. E* **1999**, *60*, 6757.
(50) Prielmeier, F. X.; Lang, E. W.; Speedy, R. J.; Ludemann, H. D. *Phys. Rev. Lett.* **1998**, *59*, 1128.
(51) Sastry, S.; Angell, C. A. *Nat. Mater.* **2003**, *2*, 739.
(52) Moore, E. B.; Molinero, V., unpublished work.
(53) Errington, J. R.; Debenedetti, P. G. *Nature* **2001**, *409*, 318.
(54) Liu, D.; Zhang, Y.; Chen, C.; Mou, C.; Poole, P. H.; Chen, H. S. *Proc. Natl. Acad. Sci. U.S.A.* **2007**, *104*, 9570.
(55) Mancinelli, R.; Botti, A.; Bruni, F.; Ricci, M. A.; Soper, A. K. *Phys. Chem. Chem. Phys.* **2007**, *9*, 2959.
(56) Demille, R.; Molinero, V., unpublished work.
(57) Jungwirth, P.; Tobias, D. J. *J. Phys. Chem. B* **2002**, *106*, 6361.
(58) Paschek, D. *J. Chem. Phys.* **2004**, *120*, 6674.
(59) Pratt, L. R.; Pohorille, A. *Chem. Rev.* **2002**, *102*, 2671.
(60) Xu, L.; Molinero, V., unpublished work.
(61) Kastelowitz, N.; Molinero, V., unpublished work.
(62) Giovambattista, N.; Rossky, P. J.; Debenedetti, P. G. *Phys. Rev. E* **2006**, *73*, 041604.
(63) Zangi, R.; Hagen, M.; Berne, B. J. *J. Am. Chem. Soc.* **2007**, *129*, 4678.
(64) Koga, K.; Zeng, X. C.; Tanaka, H. *Phys. Rev. Lett.* **1997**, *79*, 5262.
(65) Koga, K.; Tanaka, H. *J. Chem. Phys.* **2005**, *122*, 104711.
(66) Head-Gordon, T.; Rick, S. W. *Phys. Chem. Chem. Phys.* **2007**, *9*, 83.
(67) Chatterjee, S.; Debenedetti, P. G.; Stillinger, F. H.; Lynden-Bell, R. M. *J. Chem. Phys.* **2008**, *128*, 124511.

(68) Angell, C. A.; Bressel, R. D.; Hemmati, M.; Sare, E. J.; Tucker, J. C. *Phys. Chem. Chem. Phys.* **2000**, *2*, 1559.
(69) Chen, Y. G.; Kaur, C.; Weeks, J. D. *J. Phys. Chem. B* **2004**, *108*, 19874.
(70) Izvekov, S.; Swanson, J.; Voth, G. *J. Phys. Chem.* **2008**, *112*, 4711.
(71) Vega, C.; Sanz, E.; Abascal, J. L. F. *J. Chem. Phys.* **2005**, *122*, 114507.
(72) Vega, C.; Abascal, J. L. F.; Sanz, E.; MacDowell, L. G.; McBride, C. *J. Phys.: Condens. Matter* **2005**, *17*, S3283.
(73) Wu, Y. J.; Tepper, H. L.; Voth, G. A. *J. Chem. Phys.* **2006**, *124*, 024503.
(74) Abascal, J. L. F.; Vega, C. *J. Chem. Phys.* **2005**, *123*, 234505.
(75) Chen, F.; Smith, P. E. *J. Chem. Phys.* **2007**, *126*, 221101.
(76) Vega, C.; Abascal, J. L. F. *J. Chem. Phys.* **2005**, *123*, 144504.
(77) Angell, C. A. *Annu. Rev. Phys. Chem.* **2004**, *55*, 559.

JP805227C

CHAPTER 3

GROWING CORRELATION LENGTH IN SUPERCOOLED WATER

THE JOURNAL OF CHEMICAL PHYSICS **130**, 244505 (2009)

Growing correlation length in supercooled water

Emily B. Moore and Valeria Molinero[a)]
Department of Chemistry, University of Utah, 315 South 1400 East, Salt Lake City, Utah 84112-0850, USA

(Received 12 March 2009; accepted 3 June 2009; published online 29 June 2009)

The evolution of the structure of water from the stable high temperature liquid to its glass, low-density amorphous ice (LDA), is studied through large-scale molecular dynamics simulations with the mW model [J. Phys. Chem. B **113**, 4008 (2009)]. We characterize the density, translational, and orientational ordering of liquid water from the high temperature stable liquid to the low-density glass LDA at the critical cooling rate for vitrification. A continuous transition to a tetrahedrally ordered low-density liquid is observed at 50 K below the temperature of maximum density and 25 K above a temperature of minimum density. The structures of the low-density liquid and glass are consistent with that of a continuous random tetrahedral network. The liquid-liquid transformation temperature T_{LL}, defined by the maximum isobaric expansivity, coincides with the maximum rate of change in the local structure of water. Long-range structural fluctuations of patches of four-coordinated molecules form in the liquid. The correlation length of the four-coordinated patches in the liquid increases according to a power law in the range 300 K to $T_{LL}+10$ K; a maximum is predicted at T_{LL}. To the best of our knowledge this is the first direct estimation of the Widom line of supercooled water through the analysis of structural correlations. © *2009 American Institute of Physics*. [DOI: 10.1063/1.3158470]

I. INTRODUCTION

Water is a ubiquitous liquid with many unusual properties. It has been known for centuries that there exists a temperature of maximum density (TMD) for water located just above the melting point. More recent experiments in the 1970s by Angell and co-workers[1,2] were able to measure the properties of supercooled water and find that the density of the liquid drops sharply on cooling, accompanied by an increase in the constant temperature heat capacity Cp and the isothermal compressibility κ_T. More intriguing, the increase in Cp and κ_T seemed to follow power laws that would diverge at a singular temperature $T_s=228$ K.[3] Equilibration of bulk liquid water is impossible at this temperature because T_s lies just below the temperature of homogeneous nucleation of ice, $T_H=231$ K.

Several theories have been proposed to explain the anomalous thermodynamic behavior of water.[4–7] All theories attribute the anomalies of water to the formation of hydrogen bonded tetrahedral structures that become more favorable at low temperatures.[7] The two that are currently under consideration are the liquid-liquid phase transition[5] and the singularity free[6] hypotheses. In both theories the anomalies are a result of anticorrelated volume and entropy fluctuations, that would result from the formation of patches of fully hydrogen bonded water molecules as the temperature decreases.[7] In the singularity-free hypothesis, the enhanced fluctuations result in maxima for the response functions but do not lead to a first order transition. The liquid-liquid transition hypothesis proposes that supercooled water separates into two phases, low-density liquid (LDL) and high-density liquid (HDL), for pressures higher than that of a liquid-liquid critical point (LLCP). Support for this hypothesis arises from simulations of various water models[5,8] and also from the existence of at least two different amorphous solid phases of water that interconvert through a reversible, sharp, first-order-like transition.[9] Careful decompression experiments by Mishima and Stanley[10] suggest that the LLCP of water could be located around $T_c^{LL}=220$ K and $p_c^{LL}=1000$ atm. A more recent estimation based on a scaled equation of state, yields a similar critical temperature, $T_c^{LL}=232$ K, and a considerably lower critical pressure, $p_c^{LL}=270$ atm.[11]

The liquid-liquid transition in water has some important differences with its close cousin, the vapor-liquid transition. First, the higher entropy phase (by definition the higher temperature one) is the denser one, leading to a negatively sloped coexistence line in the p-T plane. This characteristic is shared with the liquid-ice transition. Second, on approaching the LLCP the difference in entropy between the liquid phases ΔS is more significant than the difference in density, leading to an estimated slope of the coexistence line $(dp/dT)_{LL}=\Delta S/\Delta V$ that is ~30 times higher than for the liquid-vapor transition.[11,12] The preponderance of entropy over density as the relevant order parameter is also common to the liquid-crystal transition. A very important difference between liquid-liquid and liquid-ice transitions, however, is that the latter involves phases of different symmetries and does not end in a critical point.

At pressures lower than the liquid-liquid critical point, in the supercritical region, liquid water would consist of a fluctuating mixture of molecules with local ordering similar to those found in LDL and HDL. The structure fluctuations would be more pronounced at the supercritical continuation of the first order liquid-liquid transition line, called the

[a)]Author to whom correspondence should be addressed. Electronic mail: valeria.molinero@utah.edu.

Widom line $T_W(p)$,[13–16] at which the correlation length of the structure fluctuations ξ reaches its maximum value. Emanating from the critical point, there must also be loci of maximum values of the heat capacity, isothermal compressibility, and isobaric expansivity. These loci of maximal response converge as the system approaches the critical point.[17] Atomistic simulations of the ST2 model of water show that the loci of maximum response functions converge to a single line already at about a thousand atmospheres away from the LLCP.[18] Correlation lengths in deeply supercooled water have not been computed before from simulations. Correlation lengths have been derived from the experimental structure factor, $S(q)$, of supercooled water, although the results give a contradictory account. Bosio and co-workers[19] computed the structure factor using x-ray and small angle neutron scattering (SANS) and concluded that the correlation length increased with supercooling. Xie *et al.*[20] used small angle x-ray scattering (SAXS) to investigate the density fluctuations from 273 to 239 K. They found that in this range the correlation length increases slowly, less than would be expected if a liquid-liquid transformation were pending just below T_H. The study of long-range structure fluctuations is a challenge for simulations due to the large system sizes required to access the low q region of the structure factor. Based on the experimental results, the increase in $S(q)$ is expected at $q<1$ Å^{-1}, and an appropriate characterization of the correlation length would require access to $q\sim0.1$ Å^{-1}. This requires simulation cells of at least $\sim$15 nm side, involving more than 100 000 water molecules. Simulation studies of ordering in supercooled water have been limited to systems with less than 1000 molecules, making it possible to extract qualitative information about the intermediate-range ordering of four-coordinated (LDL-like) molecules.[21] Here we study the structure fluctuations in water from the hot liquid to the deeply supercooled liquid regime, through large-scale molecular dynamics (MD) simulations involving more than a quarter million molecules using a novel coarse-grained water model. From these simulations we extract correlation lengths that show a power-law increase in supercooled water.

In addressing the evolution of structure in stable and supercooled water by MD simulations, one main limitation is the computational expense. In simulations, it is difficult to equilibrate the liquid in the deeply supercooled region or simulate systems that are large enough to allow the study of long-range correlations in density and structure fluctuations. To address these issues, we developed a monatomic model of water, mW, that represents each water molecule as a single particle with tetrahedral interactions that mimic the effect of hydrogen bonds.[22] The monatomic water mW model belongs to a family of tetrahedral potentials[23] that also model the group IV elements of the periodic table C,[24] Si,[25] and Ge.[26] The mW model does not have hydrogen atoms or electrostatics yet it reproduces the structure of water, ice, and LDA glass, the phase transitions between them (melting, freezing, and liquid-liquid transformation) and the thermodynamic and dynamic anomalies of liquid water. The accuracy of mW in describing the structure, anomalies, and phase behavior of water is comparable to or better than that of the most popular atomistic water models (SPC, SPCE, TIP3P, TIP4P, and TIP5P) while the mW simulations are about a hundred times less expensive.[22] For an exhaustive assessment of the properties and limitations of the mW model we refer the reader to Ref. 22. The use of the mW model allows for simulations of large systems for long times, providing the opportunity to compute and analyze the temperature dependence of the long-range correlation of structure fluctuations for temperatures down to T_H, from which we determine the location of the Widom line.

A second question that we address in this study is how the structure of liquid water evolves as it is cooled from high temperature, into the metastable supercooled region, and finally transforming into a glass. Equilibrium properties of bulk liquid water have been studied in experiments down to $T\approx235$ K.[27,28] Below this temperature the rate of ice nucleation increases precipitously and the liquid cannot be equilibrated at $T<T_H=231$ K. Between T_H and the glass transition of water, $Tg\approx136$ K,[2] liquid water is in "no-man's land".[29] In this region the rate of ice nucleation becomes comparable to the time required for equilibration of the liquid and its properties cannot be probed with current experimental techniques. Crystallization, however, can be avoided by hyperquenching liquid water at a rate of $\sim10^6$ K s^{-1}.[2] The resulting system is a glass, low-density amorphous ice (LDA). LDA is vitrified LDL and its structure is quite different from that of room temperature water. This high quenching rate makes it impossible to study the evolution of the structure of water as it approaches T_H and crosses into "no-man's land".

The low computational cost and fast equilibration of mW water, due to the lack of hydrogen atoms, permit the study of the evolution of the structure of water over a broad temperature range as it converts to LDA. In addition, this analysis can be done under conditions that best mimic experiment, at the critical cooling rate for vitrification, which is 10^{10} K s^{-1} for the mW model. This leads to a better equilibration of the low-density phase that attains a structure consistent to that of a random tetrahedral network. It should be noted that the critical cooling rate in the simulations is $\sim10^4$ times higher than in the experiment. This is because the crystallization rate (as well as the diffusivity) is higher in the absence of hydrogen atoms; the dynamics of the monatomic water evolves in a smoother potential energy surface than fully atomistic water.

This paper is organized as follows: Sec. II details the water model and simulation methods, Secs. III–VI present the analysis of the change in structure for the water as it is quenched from a temperature close to the boiling point to the LDA glass, and a discussion of the validity of mixture models to describe the density of water. To the best of our knowledge, this paper presents the first determination of a power-law increase in the correlation length of structure fluctuations in supercooled water and a direct determination of the Widom line as the locus of maximum correlation length. Section VII contains a discussion of these results.

II. WATER MODEL AND SIMULATION METHODS

Water was modeled by the mW force field.[22] The mW interaction potential is given by a sum over pairs and triplets of water sites

$$E = \sum_i \sum_{j>i} \phi_2(r_{ij}) + \sum_i \sum_{j\neq i} \sum_{k>j} \phi_3(r_{ij}, r_{ik}, \theta_{ijk}), \quad (1)$$

$$\phi_2(r) = A\varepsilon\left[B\left(\frac{\sigma}{r}\right)^p - \left(\frac{\sigma}{r}\right)^q\right]\exp\left(\frac{\sigma}{r - a\sigma}\right), \quad (2)$$

$$\phi_3(r_{ij}, r_{ik}, \theta_{ijk}) = \lambda\varepsilon[\cos\,\theta_{ijk} - \cos\,\theta_{0ijk}]^2 \times \exp\left(\frac{\gamma\sigma}{r_{ij} - a\sigma}\right)\exp\left(\frac{\gamma\sigma}{r_{ik} - a\sigma}\right), \quad (3)$$

where $A=7.049\,556\,277$, $B=0.602\,224\,558\,4$, $p=4$ $q=0$, and $\gamma=1.2$ give the form of the potential, $\theta_o=109.47°$ and $\lambda=23.15$ encourages tetrahedral configurations. The energy scale $\varepsilon=6.189$ kcal/mol and characteristic size $\sigma=2.3925$ Å determine the strength of the interactions and the excluded size of the water molecule and $a=1.8$ defines the cutoff for all interactions at $a\sigma=4.3$ Å.[22] The parameters of the mW potential are identical to those of Stillinger–Weber silicon,[25] except for ε, σ, and λ that were adjusted to reproduce the experimental values of the melting temperature of hexagonal ice, and the density and enthalpy of vaporization of liquid water at that temperature.[22] It is known that isotropic coarse-grained models of water perform poorly in terms of transferability across a temperature range and in their ability to simultaneously reproduce thermodynamic and structural properties of the liquid.[30] This is mainly due to the fact that isotropic, purely radial, interactions do not suffice to represent the physics of water interactions. We found that the introduction of anisotropic interactions that mimic the effect of hydrogen bonds allow for a good description of the thermodynamic anomalies of water, its phase change enthalpy and the formation of phases that were not considered in the parametrization, such as LDA (Ref. 22) and water clathrates.[31]

MD simulations were performed using LAMMPS.[32] The systems consisted of cubic simulation cells with periodic boundary conditions. The equations of motion were integrated using the velocity Verlet algorithm with a time step of 5 fs. All simulations were done at room pressure. The temperature and pressure in the simulations were controlled using the Nose–Hoover thermostat and barostat with relaxation times 0.5 and 2.5 ps, respectively, for the smaller system and both 10 ps for the larger system.

The properties of ice were computed from a *NPT* simulation of a periodic cell of hexagonal ice containing 36 864 mW particles. The structure factors and correlation lengths in liquid water where computed from *NPT* simulations of an $N=262\,144$ water system (~20 nm cell length) at constant temperature. All other properties of liquid and glassy water were computed from *NPT* simulations of the 32 768 molecule system (~10 nm cell length) for which T was varied linearly between 350 and 100 K at a rate of 10 K ns^{-1}, the critical cooling rate to avoid ice crystallization with mW water.

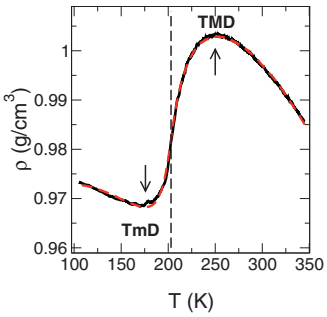

FIG. 1. (Color online) Density of mW water, as the temperature is cooled at the critical rate for vitrification (full line). The arrows indicate the density maximum at TMD=250±1 K and density minimum at TmD=175±3 K. The vertical dashed line indicates the temperature of maximum rate of change in the density, the liquid-liquid transition temperature $T_{LL}=202\pm2$ K. The fit to Eq. (7) with quadratic expressions for V_L and V_H (dashed line) accurately reproduces the density of water from hot stable liquid to low temperature glass.

III. DENSITY EXTREMA AND LIQUID-LIQUID TRANSFORMATION.

The best and oldest known example of water's anomalies is the density maximum ρ_{max}.[28] The temperature of maximum density for bulk water is TMD=277 K. Recently it has been shown that, under conditions of confinement in silica nanopores that prevent crystallization, water displays a maximum at TMD≈275 K and also displays a minimum density ρ_{min} at TmD≈203 K.[33] A density minimum in supercooled water was formerly predicted by atomistic simulations[18,34] and recently reported for the water-like Jagla model.[35] Between the TMD and TmD confined liquid water undergoes a continuous structural transition that has been monitored through Raman scattering[36] and proton chemical shift in NMR.[37] The liquid-liquid transformation temperature of water in silica nanopores, defined as the temperature of maximum structural change, was found to be $T_{LL}\approx235$ K.[36,37]

The temperatures of density minimum and liquid-liquid transformation lie below the temperature of homogeneous nucleation of bulk water and cannot be resolved at the $\sim10^6$ K/s hyperquenching rate needed to vitrify water droplets in experiments. We characterize the density and water structure as it is cooled from the hot liquid at 350 K to the LDA glass at 100 K at the critical cooling rate for vitrification in these simulations, 10^{10} K/s. Cooling at the subcritical cooling rate of 2×10^9 K/s produces results identical to those shown below down to ~202 K, but lead to ice formation instead of vitrification in the low temperature region.

Figure 1 shows the evolution of the density in the cooling run from 350 to 100 K. The density increases in the stable region, reaches a maximum at TMD=250±1 K, followed by a sharp drop, with a maximum isobaric expansivity α_p at 202±2 K and a minimum at TmD=175±3 K. On warming up the hyperquenched system from 100 K at the same rate, we observe a slight density relaxation at $T>145$ K. This suggests that mW water vitrifies at $T_g\sim145$ K for this cooling rate. The location of the TmD ob-

tained upon warming is slightly displaced to higher temperatures, TmD=182±3 K. The magnitude of density relaxation between cooling and warming cycles is just 0.25% at 182 K.

The locus of maximum α_p is the liquid-liquid transformation temperature, $T_{LL}=202\pm2$ K for mW water. In the first order transition region, $p>p_c$, the density would present a discontinuity as HDL converts to LDL. In the supercritical region, $p<p_c$, α_p should display a finite maximum that—as indicated in Sec. I—must coincide with the loci of maximum in all response functions and correlation length as the system approaches the critical point. We use the acronym T_{LL} indistinctly for the continuous transformation seen at pressures below the critical pressure and the discontinuous, truly first order, transition at higher pressures between HDL and LDL.

Note that the density extrema and liquid-liquid transformation in mW are displaced ~30 K down with respect to water in the nanopore, leading to the same gap TMD-T_{LL} ≈50 K and TMD-TmD≈75 K as in the experiment. It is not clear whether or how the results for nanoconfined water can be translated to bulk water, as the thermodynamics of a nanoconfined liquid is strongly influenced by the interactions with the confining interface. We expect however, a displacement of the liquid properties of mW to lower temperatures with respect to experimental water in bulk, as the mW model was parametrized to reproduce the experimental melting temperature of ice, while T_m should be higher for a monatomic model because the loss of rotational contributions to the liquid entropy would destabilize the monatomic liquid phase, as discussed in Ref. 22.

The density maximum predicted by the mW model, 1.003 g/cm^3 is in excellent agreement with 0.999 97 g/cm^3 of experiments. The predicted density minimum is 0.967 g/cm^3, higher than the 0.925 g/cm^3 reported for water confined in silica nanopores.[36] The model predicts that the density of the low-density liquid is 2.3% lower than that of ice, as also reported in Ref. 38 based on the experimental densities from Refs. 39. The absolute densities of ice and LDA predicted by the mW model are, however, higher than in experiment. We attribute this to the inability of the coarse-grained model to reproduce the extension of the O–H–O hydrogen bonds, due to the lack of hydrogen atoms.

The transformation from high- to low-density liquid is continuous. A small hysteresis, less than 8 K, is observed on warming up. Ice formation occurred in the warming up cycle as the low-density liquid approached T_{LL}. A continuous liquid-liquid transformation is consistent with the most probable scenario for water that involves the existence of a first order high-density to low-density liquid-liquid phase transition (LLPT) in the supercooled region that would end at a positive pressure liquid-liquid critical point (LLCP).[10] It is also consistent with the singularity free scenario.[6] A preliminary determination indicates that the mW model presents a LLCP around 190 K and 1200 atm,[40] thus T_{LL} at $p=1$ atm belongs to the Widom line, the supercritical extension of the first order liquid-liquid transition line.[13,14] The Widom line is the locus of maximum correlation length. In Sec. VI we determine the temperature of maximum correlation length and show that it coincides with T_{LL} computed from the maximum isobaric expansivity. Prior to that, in Secs. IV and V we discuss the changes in local ordering that occur in liquid water in its path to LDA and the validity of mixture models for the density.

IV. INCREASE IN LOCAL ORDERING FROM HIGH TEMPERATURE LIQUID WATER TO LDA GLASS.

A. Pair distribution function

The tetrahedral topology of water's hydrogen bonded configurations imparts to the liquid structure characteristics that are very different from those of simple liquids: (i) the average coordination number of water is low, 5.2±0.1 neighbors up to 3.5 Å at room temperature[41] and 3.9±0.1 in LDA at 80 K,[42] (ii) the ratio of the positions of the first and second peak in the oxygen-oxygen radial distribution function (rdf) corresponds to those of a tetrahedron, and (iii) the angular distribution function (adf) presents a prominent peak around tetrahedral angles. The mW model quantitatively reproduces these features and provides an adf and rdf in excellent agreement with experiment for the room temperature liquid and LDA glass.[22]

The rdf between two water sites was computed from the simulation trajectories as

$$g(r)=\frac{V}{N^2}\left\langle \sum_{i=1}\sum_{j\neq 1}\delta(r-r_{ij})\right\rangle, \tag{4}$$

where V is the volume, r_{ij} is the distance between i, j molecules, and $\langle\cdots\rangle$ denotes an ensemble average. From the rdf we computed the average number of neighbors n_c in the liquid up to a distance r_c,

$$n_c=4\pi\frac{N}{V}\int_0^{r_c} r^2 g(r)dr. \tag{5}$$

Figure 2 displays the rdf of mW water as it is cooled from 350 to 100 K at the critical cooling rate for vitrification, 10 K/ns. The glass has the rdf of LDA (see Ref. 22 for a comparison with experiment). The liquid rdf changes sharply around the liquid-liquid transformation temperature $T_{LL}=202\pm2$ K. Vitrification around 145 K has no distinct effect on the structure. The main changes on cooling are (i) an increase in intensity of the "tetrahedral peaks," centered at 2.75 and 4.45 Å and (ii) a decrease in density in the broad region around 3.3 Å that corresponds to "interstitial" water molecules loosely coordinated to the central one. In agreement with atomistic simulations the number of neighbors up to $r_c\sim3.25$ Å is constant, 4.03, for all temperatures.[43]

Cooling at the subcritical rate of 2×10^9 K/s leads to the formation of ice, evidenced by the splitting of the second peak of the rdf. The structural transformation of stable liquid water to LDA at room pressure produces a set of invariant points in the rdf. The three lowest in the model are at 2.9, 4.0, and 5.1 Å, in excellent agreement with those at 2.95, 3.9, and 5.1 Å reported from x-ray diffraction of water between 313 and 262 K.[44] The existence of isosbestic points in the rdf and other spectra of liquid water has been considered as evidence for the existence of two structural motifs.[45] Section V addresses this issue.

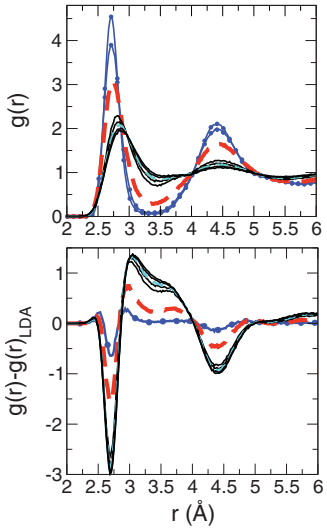

FIG. 2. (Color online) Upper panel: Radial distribution function (rdf) of liquid mW water hyperquenched at the critical cooling rate for vitrification. The full lines correspond to the structure of the high temperature high-density liquid from 350 K to TMD=250 K, with the rdf for T=300 K shown with a thin dashed line. The structure at the liquid-liquid transformation temperature T_{LL}=202 K is shown with a thick dashed line and the rdf of low-density liquid and glass at 160 and 120 K with dotted lines. Lower panel: Differential rdf of the liquid with respect to the LDA glass at 120 K; same symbols as in upper panel. Notice that the interstitial region centered at 3.3 Å arises from the merging of two distinct interstitial bands, one centered at 3.6 Å and another at 3.1 Å. The liquid-liquid transformation involves the loss of interstitial waters between the first and second shell and a strengthening of the tetrahedral peak centered at 4.5 Å.

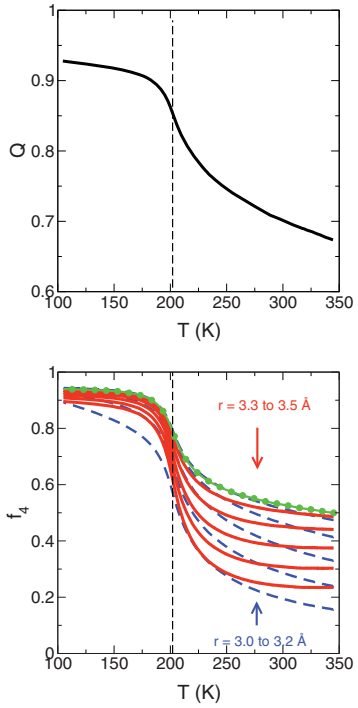

FIG. 3. (Color online) Upper panel: Evolution of the orientational order parameter, Q, on hyperquenching of liquid water at the critical cooling rate for vitrification. The dashed vertical line indicates the temperature for which the rate of change of tetrahedrality, dQ/dT, is maximal. This temperature coincides with the temperature of the liquid-liquid transformation determined from the density (Fig. 1) and the fraction of four-coordinated molecules (lower panel of this figure). Lower panel: Fraction of four-coordinated molecules f_4 increases on cooling of liquid water. The different curves represent f_4 values computed using various first coordination shell radial cutoffs, r_c, that include the minimum in the rdf of room temperature water, 3.5 Å, to the end of the first peak in LDA, 3.0 Å. The fraction of four-coordinated molecules increases for 3.0 Å$<r_c<$3.2 Å from 18% to 50% (thick dashed lines), reaches a maximum at 3.25 Å (line with circles), r_c for which the average number of neighbors is independent of temperature) and decreases from 50%–23% for 3.3 Å$<r_c<$3.5 Å (full lines). The vertical dashed line indicates the location of the liquid transformation temperature, T_{LL}, determined as the temperature where the maximum rate of structural change df_4/dT occurs. T_{LL} is independent of the radial cutoff used, and coincides with the one determined from the change in tetrahedrality (upper panel) and density (Fig. 1). The low-density glass has the structure of a random tetrahedral network.

B. Orientational order

We measured the average tetrahedral ordering of the four-closest neighbors around the water molecules through the order parameter Q,[46] computed for each configuration of the N=32 768 water system as

$$Q = 1 - \frac{3}{8N}\sum_{k=1}^{N}\sum_{i=1}^{3}\sum_{j=i+1}^{4}\left(\cos\,\theta_{ikj} + \frac{1}{3}\right)^2, \qquad (6)$$

where θ_{ikj} is the angle subtended between the central water molecule k and two of its four-closest neighbors. Q is one for a perfect tetrahedral crystal where all θ_{ikj}=109.47° and zero for a system in which the distribution of these angles is random. This quantity cannot be measured in experiments, but it has been used to characterize the structure of liquid and amorphous solid water in simulations.[47–49] The structure of the liquid water becomes more tetrahedral on cooling, as seen in Fig. 3. At T=300 K and p=1 atm, the orientational order predicted by the mW model, Q=0.70, agrees with the one predicted by the atomistic TIP5P model, Q=0.69.[50] A steep increase in tetrahedral ordering is observed for T below the TMD of the model, TMD=250 K.[22] The maximum rate of change in tetrahedrality, dQ/dT, of liquid water occurs at T_{LL}^{Q}=202±1 K, which is the same liquid-liquid transformation temperature T_{LL} determined from the maximum $d\rho/dT$. Atomistic simulations also show that there is a maximum rate of change in tetrahedrality for water in the supercooled region, at the liquid transformation temperature defined by a maximum in heat capacity.[49] A coincidence of the maximum dQ/dT and Cp is also observed for the mW model.[51]

At the liquid-liquid transformation temperature T_{LL} the average tetrahedrality of water is Q=0.85. It continues to grow on cooling, slowly below the TmD, until it reaches $Tg \approx 145$ K. Below Tg the changes in tetrahedral ordering are minimal. It attains a maximum Q=0.93 for the hyperquenched LDA glass at 100 K. Q of LDA in this work is higher than the 0.84 reported for hyperquenched SPCE water, a potential known to underestimate the tetrahedrality of water.[48] The faster dynamics of the coarse-grained model also facilitates the relaxation to the tetrahedral low-density structures.

What is the maximum tetrahedral ordering of LDA that is still compatible with a truly amorphous state? Hexagonal ice at 100 K has $Q=0.99$. LDA glass may be modeled as a random tetrahedral network (RTN).[52] This is the model used to represent *a*-Si and *a*-Ge, known to be isomorphic with amorphous solid water.[52,53] The RTN model assumes that all molecules have exactly four neighbors and first neighbor distances deviate little (e.g., ~1%–2%) from those of the tetrahedral crystal; the angles in the RTN, however, are not perfectly tetrahedral, resulting in loss of long-range order in the solid. Assuming that coordination defects decrease the tetrahedral ordering, the upper limit of Q will be determined by the minimum angular standard deviation that is consistent with a RTN. These are 9.1° to 11.4° for RTN constructed to represent the amorphous phases of C, Si, and Ge.[54] The angular distribution functions for the four-closest neighbors of LDA and hexagonal ice at 100 K are Gaussian with mean values of 108.9° and 109.5°, respectively. What distinguishes glass from ice is the magnitude of the angular dispersion: 11° for the LDA and 4° for the crystal at 100 K. A better measure of the actual standard deviation of the intermolecular angles is obtained if the structures are quenched to the local minimum to remove the vibrational contribution. We find that this intrinsic angular dispersion of ice is negligible, while that of hyperquenched LDA is 9.5°, in agreement with what is expected for continuous random tetrahedral networks. Nevertheless, liquid water does not reach a state of perfect RTN in our hyperquenching simulations: only ~90% to 95% of the molecules are four-coordinated in the glass, as discussed in Sec. IV C. The average Q for the water molecules in LDA that have four neighbors up to $r_c=3.5$ Å is 0.96. This is likely close to the upper limit for an amorphous tetrahedral solid. It is clear that while Q is an appropriate order parameter to describe the liquid-liquid transformation in water, it is not a good one to distinguish LDA from ice.

C. Population of *N*-coordinated molecules

To further characterize the structure of liquid water we computed the fraction f_N of molecules with $N=0,1,\ldots,8$ neighbors within the first coordination shell up to a cutoff distance r_c. A natural cutoff distance to define the first coordination shell is the location of the first minimum of the rdf, at 3.5 Å for $T=300$ K. As the first peak becomes more pronounced at low temperatures, an alternative definition for the first shell could include waters that are found within the distances encompassed by the first peak in LDA, 3.0 Å. It is useful at this point to address the question: how does the choice of r_c affect the analysis of water structure? This question is relevant to interpret the results arising from experimental techniques that differ in their spatial reach.

The lower panel of Fig. 3 presents the temperature evolution of f_4, the fraction of four-coordinated molecules, for a series of shell cutoff distances $3.0 \leq r_c \leq 3.5$ Å. The f_4 curves have a sigmoidlike shape for all r_c with an increase in the fraction of four-coordinated molecules observed in the supercooled region. The maximum rate of change for the structural transformation occurs at $T_{\mathrm{LL}}^{f4}=201\pm2$ K, irrespective of the choice of r_c. This is the same liquid-liquid temperature as determined from the density and the tetrahedral order parameter. The fraction of four-coordinated liquid, f_4, increases around T_{LL}^{f4} while all other f_N experience a concomitant sharp decrease (not shown). f_4 levels off to a maximum $f_4=0.92\pm0.03$ (depending on the choice of r_c) for the hyperquenched glass at 100 K. This glass has 4.06 neighbors in the first shell.

While the different $f_4(T)$ curves converge in the low temperature limit, the f_4 predicted at high temperatures is strongly dependent on the radius used to define the first neighbor shell (Fig. 3). The average number of neighbors for a radial cutoff of ~3.25 Å is ~4.05 for $350\ \mathrm{K}<T<100$ K, yet f_4 is a strongly varying function of T. The liquid transformation monitored at $r_c=3.25$ Å occurs with constant average coordination, mainly through a compensation of the fraction of undercoordinated (f_3) and overcoordinated (f_5) water molecules. The maximum dynamic range for f_4 is found at the extremes, $r_c=3.5$ Å and 3.0 Å (Fig. 3). For $r_c=3.5$ Å, a shell that encompasses all the neighbors up to the first minimum of the rdf at 300 K, the fraction of molecules with less than four neighbors is always insignificant and we find that at $T=300$ K f_4 is 0.24, f_5 is ~0.44, f_6 is ~0.25, and f_7 is ~0.06.

While the similarity of $Q(T)$ and $f_4(T)$ curves may give the impression that the four-coordinated molecules in the liquid have Q values close to those of LDA, this is not the case. The four-coordinated molecules in high temperature water are less orientationally ordered than in the low temperature liquid. At $T=350$ K, for example, the average tetrahedrality of the four-coordinated molecules is $0.72<Q_4<0.77$ (depending on the choice of r_c). These values are closer to the $Q=0.67$ obtained when all molecules at $T=350$ K are considered than to the $Q=0.93$ of LDA.

By all measures, the liquid transformation on cooling corresponds to an increase in tetrahedrality. Based on this we classify the water molecules into two structural components: those with four neighbors up to r_c (which we refer to as low, *L*, for the low temperature structure) and all others (high, *H*). It should be kept in mind that the *H* and *L* type of water molecules of are not two distinct species but only structural motifs selected from the continuum structure of the liquid. At room temperature, the exchange rate of molecules between *L* and *H* states is on the order of 1 ps.

V. TWO-COMPONENT ANALYSIS OF THE ANOMALOUS DENSITY OF WATER

We now address the validity of describing the density of water as a combination of the density of the *L* and *H* structural components introduced in Sec. IV. As early as 1892, Röngten[55] proposed that water was a mixture of isolated "icebergs" in a sea of denser liquid. Much debate ensued on whether liquid water consists of a few well-defined structural motifs or a continuum of structures. Vedamuthu *et al.*[56] analyzed the experimental density of water from 243 to 313 K, finding that the molar volume can be decomposed as a sum of contributions from two components,

$$V = f_L V_L + f_H V_H, \tag{7}$$

where f_L and f_H=(1-f_L) are the fraction of molecules of the low and high-density components, with molar volume V_L and V_H that differ in ~25%. These authors considered that most of the temperature dependence was implicit in $f_L(T)$, for which they assumed a sigmoidal shape. Their results indicated that the density maximum could be explained by an increase in the fraction of low-density component in the liquid. The same mixture model with pressure and temperature dependent coefficients was used to explain water's isothermal compressibility minimum at ~323 K (Ref. 56) and the change of the radial distribution functions with pressure and temperature.[57] Robinson *et al.* interpreted V_L and V_H as the molar volumes of the pure *L* and *H* components (which they associated with the structures of hexagonal ice *Ih* and the high-pressure polymorph ice *II*, respectively). In Eq. (7), V_L and V_H are the volumes of the pure *L* and *H* liquids only if *L* and *H* form an ideal mixture. The sigmoidlike form of $f_4(T)$ (Fig. 3) points to strong cooperativity in liquid water that would contradict the idea of an ideal mixture. In a more general case, V_L and V_H in Eq. (7) are partial molar volumes,

$$V_i = \left(\frac{\partial V}{\partial n_i}\right)_{n_j,p,T}, \tag{8}$$

where n_i is the number of moles of component *i* and the derivative is taken at constant *T*, *p*, and number of moles of *j*. It should be noted, however, that the composition f_4 [f_L in Eq. (7)] is not a true external variable: the proportion of *L* and *H* structures in liquid water cannot be modified independently of *T*.

The molar volume of liquid water in our simulations is accurately reproduced by Eq. (7) if V_L and V_H are represented by quadratic functions of *T*. Figure 1 shows the fit of the density to Eq. (7) with f_4 defined from r_c=3.5 Å. The selection of any other cutoff, $3.0 \leq r_c \leq 3.5$ Å, produces a fit of the same quality, but the actual volumes associated with *L* and *H* are cutoff dependent as are the identities of *L* and *H*. At the melting temperature, V_H is 10 to 20% smaller than V_L, with the lowest difference corresponding to the maximum cutoff, r_c=3.5 Å. We find that for some values of r_c Eq. (7) yield a nonmonotonous $V_H(T)$: it decreases down to 200 K followed by an increase in the low temperature region. These results may be biased by the insensitivity of Eq. (7) to the values of V_H in the temperature range where (1-f_4) is small. On the other hand, V_L is a monotonously increasing function of *T* for all choices of r_c. A Voronoi analysis of the volume of four-coordinated clusters in SPCE water indicated that the clusters of four-coordinated molecules do not attain a volume higher than the rest of the liquid until they reach a certain size (about 10–20 molecules) that depends also on the value of the tetrahedral order parameter *Q*.[46] The clustering of four-coordinated molecules is discussed in Sec. VI; for the purpose of Eq. (7), this cooperative effect in the volume of *L* is convoluted with the temperature dependence in the partial molar volume V_L.

Our results indicate that, in the analysis of experimental data using Eq. (7), caution should be taken in the interpretation of the meaning of V_H and V_L as their values depend on the choice of f_L and their interpretation as volume of two components on the assumption of ideal solution of *L* and *H*.

The temperatures of density extrema can also be analyzed in terms of Eq. (7). TMD and TmD are given by the two zeros of α_p and the liquid-liquid transformation temperature T_{LL} by its maximum,

$$\alpha_p V = \left(\frac{dV}{dT}\right)_p = (V_L - V_H)\frac{df_4}{dT} + f_4\frac{dV_L}{dT} + (1-f_4)\frac{dV_H}{dT}. \tag{9}$$

The thermal expansivity of V_L and V_H are responsible for the existence of density extrema. If V_L and V_H were constants, the density would decrease monotonously. The sharpness of the density change, however, is exclusively due to the change in structure of the liquid on cooling, given by df_4/dT. T_{LL} and $T_{LL}^{f^4}$ are identical because the first term of Eq. (9) dominates between TMD and TmD, and V_L and V_H are slowly varying functions of *T*.

VI. GROWING CORRELATION LENGTH IN SUPERCOOLED WATER

We now address what is the organization of the *L* molecules in water, and whether the increase in four coordination on cooling is accompanied by structure fluctuations with growing correlation length. We present first an analysis of the clustering of the *L* molecules and then the calculation of the correlation length from the analysis of the structure fluctuations.

To investigate the medium range order and development of *L* domains in water structure we computed the average radius of gyration $R_{g,N}$ of *N*-coordinated molecules,

$$R_G^2 = \frac{1}{M^2}\sum_{i>j}^{M}(r_i - r_j)^2, \tag{10}$$

where *M* is the number of water molecules in the cluster, *r* are the molecular coordinates and the sum is over all the pairs of molecules in the cluster. A distance r_c=3.5 Å, corresponding to the first minimum in the radial distribution function of mW liquid at room temperature, was used as a cutoff for the clustering of *N*-coordinated molecules. The largest cluster is defined as the one containing the most molecules for each configuration.

Figure 4 displays the average $R_{g,4}$ over all the *L* clusters and the average radius of gyration of the largest clusters above their percolation temperature $T_p \approx 225$ K. They both show two regimes: a constant $R_{g,4}$ for $T > 300$ K followed by an increasing cluster size and radius of gyration in the supercooled region. These two regimes are mirrored by the change in the fraction of four-coordinated molecules (Fig. 2). In agreement with our findings, a recent report on the relation of the dynamics and structure of liquid water[58] indicates that the ratio of molecules with high and low *Q* in bulk TIP5P water and the ratio of spectral intensities attributed to HDL and LDL in the IR spectra of water confined in silica nanopores follow the same trend observed for the monatomic liquid water: the "structural composition" of water is tem-

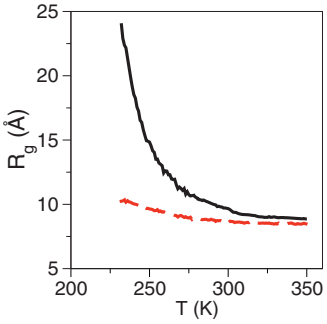

FIG. 4. (Color online) The average radius of gyration of the largest cluster of four-coordinated molecules, $\langle R_g^{\text{largest}} \rangle$, (smooth line) shows a steep increase between room temperature and the percolation threshold of the four-coordinated molecules around 225 K. The average over all clusters of four-coordinated molecules, multiplied by a factor of 4, $4^*\langle R_g^{\text{ALL}} \rangle$, is shown by the dashed line. A cutoff distance corresponding to the first minimum in the rdf of room temperature water was selected for clustering.

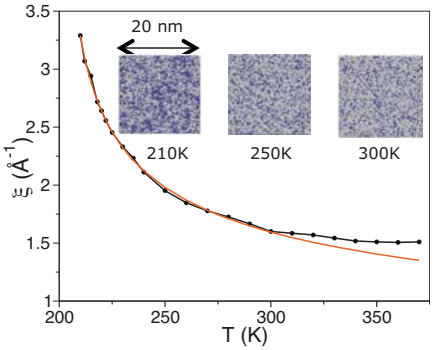

FIG. 5. (Color online) Correlation length of the structure fluctuations, ξ (line with circles, where circles represent the data points) computed from equilibrium simulations of systems with 262 144 water molecules (linear cell dimensions ~20 nm), vary little from the boiling point to room temperature while showing a pronounced increase at low temperatures. At $T \leq 300$ K, the correlation length increases with a power-law (full smooth line). The maximum correlation length defines the Widom temperature for the mW water model at room pressure, $T_W = 200$ K, that coincides with the liquid-liquid transformation temperature deduced from the change in density and local structure (Figs. 1 and 2). Insets: Snapshots of the 262 144 molecule system are shown at room temperature, the TMD and 10 K above the liquid-liquid transition. The darker spots signal four-coordinated molecules, the others are shown in a lighter tone. Long-range correlations of four-coordinated molecules are evident at low temperature.

perature insensitive at temperatures higher than about 300 K, below which it starts to change toward the low-density form.

In the "normal liquid" regime, at $T > 300$ K when the concentration of L is almost constant, the largest four-coordinated clusters contain ~60 molecules with an average radius of gyration of 9 ± 1 Å. The nonsphericity NS of the clusters, defined as the ratio between the actual R_g and the R_g of a sphere containing the same number of molecules with first neighbors distance of 3.5 Å, is ~1.5 over this temperature range. The four-coordinated clusters are immersed in a network of percolated H clusters. A comparison of the size and NS of the largest four-coordinated clusters with the largest six-coordinated ones at room temperature shows that the four-coordinated ones are more compact (1.5 versus 2.2) and with less particles (60 versus 300), in spite of the two fractions, f_4 and f_6, being equal.

Between room temperature and the temperature of maximum density, TMD=250 K, the number of molecules in the largest cluster triples, accompanied by an increase in radius of gyration from 9 to 14 Å, and the clusters become less spherical, NS increases from 1.5 to 1.8. Below TMD, the largest cluster grows dramatically, spanning the whole system at ~225 K. A snapshot of a liquid configuration at 210 K (Fig. 5) shows well separated L and H domains in the percolated structure.

A direct measurement of the radius of gyration and shape of low-density liquid clusters is not possible in experiments. The correlation length of the density fluctuations, however, can be extracted from the analysis of the structure factor $S(q)$ obtained in SANS or SAXS experiments. In terms of the Ornstein–Zernicke equation the growth in the structure factor at low q (long distance) takes the form

$$S(q) = S_n + \frac{Ck_bT}{q^2 + \xi^{-2}}, \tag{11}$$

where ξ is the correlation length, S_n is a background component, and Ck_b is a constant. The structure factor of supercooled water has been obtained from x ray, SANS and SAXS experiments.[19,20] The correlation lengths derived from these measurements do not agree with each other, and indicate different trends with supercooling: The x-ray and SANS results from Refs. 19 suggest a significant increase in the correlation length with supercooling, while a study of the density fluctuations from 273 to 239 K through SANS in Ref. 20 indicates that the correlation length increases slowly. This increase is from $\xi \approx 3.6$ to 3.8 Å when the correction in Eq. (11) involves a constant nonzero background and from 2.0 Å $< \xi <$ 2.8 Å when the background is assumed to be zero.

We computed the structure factor of water from 370 to 210 K for simulation cells with linear dimensions ~20 nm, containing more than $\frac{1}{4}$ million molecules. To our knowledge, this is the largest water system for which structural correlations have been analyzed through simulations. The structure factor $S(q)$ was calculated from the Fourier Transform of the corresponding rdf,

$$S(q) = 1 + 4\pi\rho \int_0^\infty \frac{\sin(qr)}{qr} r^2 g(r) dr, \tag{12}$$

where the density ρ and rdf $g(r)$ were computed over 4 ns NPT equilibrium trajectories of the $N = 266\,144$ molecule system at each T, after an equilibration period of at least 6 ns. Hyperquenching simulations, such as those presented in Secs. III and IV for the analysis of the density and local structure, do not suffice to gather the statistics needed to compute the structure factor. We investigated the long-range correlations in water density down to $q = 0.1$ Å^{-1}. The difference in density between the L and H components for the mW model was not enough to produce a discernible increase in $S(q)$ at low q (Fig. 6). Visual inspection of the system, however, shows well-defined clusters and a growing charac-

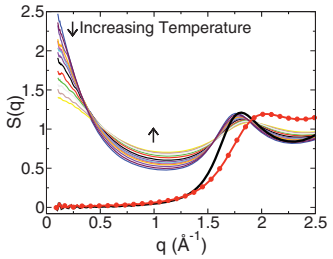

FIG. 6. (Color online) Structure factors for four-coordinated molecules, $S_4(q)$ (bold lines), are shown in order of increasing temperature from the top down; 210, 212, 215, 218, 220, 222, 225, 230, 240, 250, 260, 280, and 300 K. The arrows indicate the direction of increasing temperature. A significant increase in the low q region, associated with the development of larger patches of four-coordinated molecules, is observed for all the temperatures. The thick curves correspond to the total structure factor $S(q)$ at 300 K (full line) and 210 K (line with small circles), for which no increase at low q is observed in the simulations.

teristic size of the four-coordinated domains when the liquid is cooled toward T_{LL} (see snapshots in Fig. 5). Not only the proportion of L particles increases on cooling but they also agglomerate into larger, better-defined, domains as the system approaches T_{LL}. This is characteristic of water's liquid-liquid transition, where there is more of a change in ordering rather than a change in density.

To quantify this increase in structural correlation length, we computed the structure factor $S_4(q)$ from the density correlations of the four-coordinated liquid L alone, using Eq. (12), where ρ is replaced by ρ_4 and $g(r)$ by $g_4(r)$, with L defined as molecules that are four-coordinated up to a radial cutoff distance r_c. $S_4(q)$ measures structure fluctuations rather than density fluctuations. The resulting $S_4(q)$ for $r_c=3.3$ Å and $r_c=3.2$ Å showed no apparent increase in the low q region. For all the other r_c values of our study (3.0, 3.1, 3.4, and 3.5 Å) $S_4(q)$ showed a pronounced increase at low q, in the range below 1 Å^{-1} (Fig. 6 shows the structure factors for $r_c=3.5$ Å), consistent with an increase in the compressibility of the liquid as it approaches the Widom line.

The largest increase in $S_4(q)$ at low q occurs for $r_c=3.5$ Å. In what follows we restrict the analysis of structural correlations to this cutoff value. The correlation lengths ξ were obtained by fitting $S_4(q)$ to the Ornstein–Zernicke Eq. (11) with a q-independent background in the range $q=0.1-1.0$ Å^{-1}. We find that ξ increase with supercooling from 1.5 Å at room temperature to 3.3 Å at 210 K (Fig. 5). In agreement with the results of Ref. 20, we find the assumption of zero background leads to the prediction of smaller values of ξ. We distinguish two regimes for the correlation length ξ, same as we found for the radius of gyration and the fraction of four-coordinated molecules:

(i) From the boiling point to room temperature, water behaves as a "normal liquid" with almost constant structural composition in terms of L and H and little change in ξ, from 1.5 Å at 370 K to 1.6 Å at 300 K.

(ii) Between 300 and 210 K, the correlation length increases according to a power law,

$$\xi = \xi_o \left(\frac{T}{T_W} - 1 \right)^{-\gamma}, \tag{13}$$

with $\xi_o=1.28\pm0.03$ Å, $\gamma=0.30\pm0.02$, and $T_W=200\pm2$ K (Fig. 5). The temperature of maximum correlation length, T_W is the locus of the Widom line[14] at room pressure. The locus of maximum correlation length, maximum isobaric expansivity, and maximum rate of change in local structure coincide: $T_W=T_{LL}=T_{LL}^{f4}=T_{LL}^{Q}$. This is what is expected if the liquid-liquid transformation has a critical point at positive pressure, which is the case for the mW water model and the most probable scenario for real water.

Equation 13 suggests that the correlation length diverges at $T_W=200\pm2$ K. If the liquid-liquid transition is continuous at room pressure, however, the increase in ξ should round when the system approaches T_W (that is the same as T_{LL}) leading to a finite maximum. We have been unable to determine this maximum correlation length and, in general, ξ at $T<210$ K because of the spontaneous ice formation in the system as it is equilibrated close to T_{LL} and enters no-man's land.

Our simulations support the analysis of the x-ray and SANS experiments[19] in which a growing correlation length was found for the density fluctuations in supercooled water. The long-range structure fluctuations would lead to significant density fluctuations if the experimental difference between the density of LDL and HDL were reproduced by the model. The simulations presented here are, to the best of our knowledge, the first to yield correlation lengths for the long-range structure fluctuations of supercooled water.

Using statistical mechanical arguments, Berthier *et al.*[59] demonstrated that the length scale of dynamical fluctuations in a liquid (the characteristic size of the domains that have correlated dynamics) is related to the cross correlations between local fluctuations of the dynamical variable (e.g., density) and the local enthalpy. As the local enthalpy[51] as well as local dynamics[60] of liquid water depend on the local structure of the liquid, a corollary of this relation would be the prediction of a growing dynamical correlation length ξ_d in liquid water accompanying the power-law increase in structural correlation length ξ as the liquid approaches the Widom line. It should be noted that the relation derived in Ref. 59 holds even in the absence of any large-scale static correlations. In water and other liquids that present a liquid-liquid critical point, however, dynamical correlations may be driven by structural correlations.

A relationship between the Widom line and the breakdown of the Stokes–Einstein (SE) relationship in water has been proposed in the literature, and interpreted in terms of dynamical heterogeneities and an increase in the fraction of tetrahedrally coordinated molecules in the liquid.[15,58,61] The onset temperature $T_x\approx290$ K at which the SE relation changes to a fractional SE relation for water confined in MCM-41-S silica nanopores correlates with the onset of increase in the population of LDA-like water molecules in the confined liquid, determined from the decomposition of the IR spectra.[58] In the present work we show that the onset of

increase in L population coincides with the onset temperature of power-law increase in the correlation length ξ, that for the mW model occurs at 300 K. The increase in dynamic correlation length associated with the growth of the static correlations as water approaches the Widom line may be associated with the breaking of the SE relation reported in Ref. 58.

VII. CONCLUSIONS

In this work we presented an analysis of the structural transformation of water from the stable high temperature liquid phase to the low temperature glass using large-scale molecular dynamics simulations. The evolution of the structure of water on hyperquenching has been studied before through simulations.[34,48] Two characteristics, however, make the simulations of the present work unique: First, liquid water was hyperquenched at the critical cooling rate for vitrification, the slowest cooling rate that does not produce ice crystallization. This condition mimics that of experiments and leads to more relaxed structures for low-density amorphous water compared to those formed at higher rates. Second, we perform equilibrium simulations of systems containing more than $\frac{1}{4}$ million water molecules to analyze the existence of large-scale structure fluctuations as the system approaches a continuous liquid-liquid transformation in the supercooled region. The simulation of long times and large-scale systems were made possible by the use of the mW water model, which is more than a hundred times faster than atomistic simulations with Ewald sums.[22]

The evolution from high temperature liquid water to LDA glass was analyzed through the following order parameters: (i) a thermodynamic property, the liquid density, (ii) two measures of local structure, the tetrahedral order parameter Q, and the fraction of four-coordinated molecules f_4 using a variety of first shell distance cutoffs and (iii) a measure of the long-range structure fluctuations in the system, the correlation length ξ. The tetrahedrality of the liquid, measured by Q and f_4, increases monotonously on cooling. The density displays two extrema, a density maximum and density minimum, which bracket a sharp continuous liquid-liquid (LL) transition. All these thermodynamic and structural properties change maximally (ρ, Q, f_4) or are maximal (ξ) at the same temperature, the liquid-liquid transformation temperature, $T_{LL}=202\pm2$ K.

The final product of the hyperquenching of liquid water is glass or ice depending on the cooling rate. At the critical cooling rate for vitrification the simulations produce low-density amorphous ice. We have shown here and in Ref. 22 that the monatomic model faithfully reproduces the angular and radial distribution function of water at room temperature and in the LDA glass. The latter has the structure of a random tetrahedral network: the fraction of four-coordinated molecules is close to one, the orientational order parameter is close to that of ice, a Gaussian distribution of water-water-water angles is tetrahedral with 9.5° angular dispersion and the density is lower than that of the crystal.

The anomalous temperature dependence of the density of water from high temperature liquid to LDA glass can be written as a simple combination of contributions from two structural components, L and H, where L denotes the four-coordinated molecules and H all the others. The coefficients of Eq. (7), however, should not be interpreted as the molar volumes of two different structural components L and H but rather as their partial molar volumes subject to a constraint, as the "composition" of the liquid cannot be modified independent of temperature. This implies that caution should be taken when interpreting the density of water in terms of a mixture model, as methods or approximations that provide distinct $f_4(T)$ curves would lead to different sets of V_L and V_H in Eq. (7). The same applies to the interpretation of other extensive thermodynamic properties (e.g., enthalpy, entropy, and free energy) in terms of mixture models. The thermodynamics of liquid water, in bulk, and in confinement is discussed in a separate communication.[51]

This leaves the question: are there two structural components in liquid water? The existence of isosbestic points in the rdf and spectra of water has been considered an indication of the existence of two components, or structural motifs, in liquid water.[45,62] In our simulations, we find isosbestic points in the rdf, at the same positions as in the experiments. Isosbestic points, however, do not need to arise from the existence of distinct species;[63] Smith *et al.*[64] showed that isosbestic points in the IR spectra of water arise from a single peaked distribution of hydrogen bonded configurations. The L and H structural components defined in this work do not correspond to well-defined structures separated by an energy barrier but rather they arise from the projection of the continuous structure of the liquid according to a two state basis set, each state associated with different number of neighbors in the first coordination shell. The arbitrariness of the selection becomes evident in the choices of the cutoff that define the first shell: any value from 3.0 to 3.5 Å yields valid "mixtures" in which the identity of the L and H components themselves change, as well as the properties associated with them. The same arbitrariness may be associated with the classification of water into two components through the analysis of experimental data arising from different techniques. Widely different fractions of the low-density/fully hydrogen bonded/tetrahedral component at room temperature have been suggested in the literature from the analysis of the density,[56] x-ray emission and absorption spectroscopy,[62,65] and Raman spectroscopy.[36,64]

Our results point to three distinct temperature regions in terms of water structure: from the boiling point to room temperature the structural composition of the liquid and the correlation length changes little and the liquid behaves like a normal liquid. From room temperature to the temperature of minimum density the tetrahedrality of the liquid increases dramatically, with a corresponding drop in density. The liquid-liquid transformation is responsible for the anomalies of water in this second region. The correlation length of structure fluctuations increases in a power-law fashion with a maximum predicted at the liquid-liquid transformation temperature T_{LL}. In the third region, at temperatures lower than the temperature of minimum density, liquid water, and its glass LDA have the structure of a random tetrahedral network.

As expected from previous estimations of $\Delta S/\Delta V$ for the

LL transition in the vicinity of its critical point,[11] the signature of the liquid-liquid transition is ordering, the liquid approaching a structure close to that of ice albeit without translational symmetry, more than a volumetric change. We clearly observe a pronounced increase in the structure factor $S_4(q)$ of four-coordinated molecules at low q values. The growing correlation length of the structure fluctuations below room temperature, due to the formation of extended patches of four-coordinated liquid, follows a power-law from which we determine the Widom temperature. This temperature coincides with that of T_{LL} computed from the density and fraction of molecules with four neighbors or highly tetrahedral local environment. The existence of long-range structure fluctuations is not a trivial corollary of an increase in ρ, f_4, and Q, but it implies a high degree of cooperativity that is, for the water model of this study, associated with the existence of a close first order phase transition. The good agreement between the water properties predicted with the mW model and experiment suggests, but does not prove, that this may also be the case for real water.

ACKNOWLEDGMENTS

We thank Pablo Debenedetti for his insightful comments on the thermodynamics of mixtures. This work has been partially supported by a Seed Grant by the University of Utah. We acknowledge the Center of High Performance Computing at the University of Utah for allocation of computing time.

[1] C. A. Angell, J. Shuppert, and J. C. Tucker, J. Phys. Chem. **77**, 3092 (1973).
[2] C. A. Angell, Annu. Rev. Phys. Chem. **55**, 559 (2004).
[3] R. J. Speedy and C. A. Angell, J. Chem. Phys. **65**, 851 (1976).
[4] R. J. Speedy, J. Phys. Chem. **86**, 982 (1982); C. A. Angell, Science **319**, 582 (2008).
[5] P. H. Poole, F. Sciortino, U. Essmann, and E. H. Stanley, Nature (London) **360**, 324 (1992).
[6] S. Sastry, P. G. Debenedetti, F. Sciortino, and H. E. Stanley, Phys. Rev. E **53**, 6144 (1996).
[7] H. E. Stanley and J. Teixeira, J. Chem. Phys. **73**, 3404 (1980).
[8] I. Brovchenko, A. Geiger, and A. Oleinikova, J. Chem. Phys. **123**, 044515 (2005).
[9] O. Mishima, L. D. Calvert, and E. Whalley, Nature (London) **314**, 76 (1985).
[10] O. Mishima and H. E. Stanley, Nature (London) **392**, 164 (1998).
[11] D. Fuentevilla and M. Anisimov, Phys. Rev. Lett. **97**, 195702 (2006).
[12] O. Mishima, J. Chem. Phys. **123**, 154506 (2005).
[13] J. M. H. Levelt, Ph.D. thesis, University of Amsterdam, 1958.
[14] L. M. Xu, P. Kumar, S. V. Buldyrev, S. H. Chen, P. H. Poole, F. Sciortino, and H. E. Stanley, Proc. Natl. Acad. Sci. U.S.A. **102**, 16558 (2005).
[15] P. Kumar, S. Buldyrev, S. R. Becker, P. H. Poole, F. Starr, and H. Stanley, Proc. Natl. Acad. Sci. U.S.A. **104**, 9575 (2007).
[16] L. M. Xu, S. V. Buldyrev, C. A. Angell, and H. E. Stanley, Phys. Rev. E **74**, 031108 (2006); G. Franzese and H. Stanley, J Phys.: Condens. Matter **19**, 205126 (2007).
[17] H. E. Stanley, *Introduction to Phase Transitions and Critical Phenomena* (Clarendon, Oxford, 1972).
[18] P. H. Poole, I. Saika-Voivod, and F. Sciortino, J. Phys.: Condens. Matter **17**, L431 (2005).
[19] L. Bosio and H. Stanley, Phys. Rev. Lett. **46**, 597 (1981); L. Bosio, J. Teixeira, and M. C. Belllissent-Funel, Phys. Rev. A **39**, 6612 (1989).
[20] Y. Xie, K. F. Ludwig, Jr., G. Morales, D. E. Hare, and C. M. Sorensen, Phys. Rev. Lett. **71**, 2050 (1993).
[21] I. Okabe, H. Tanaka, and K. Nakanishi, Phys. Rev. E **53**, 2638 (1996).
[22] V. Molinero and E. B. Moore, J. Phys. Chem. B **113**, 4008 (2009).
[23] V. Molinero, S. Sastry, and C. A. Angell, Phys. Rev. Lett. **97**, 075701 (2006).
[24] A. S. Barnard and S. P. Russo, Mol. Phys. **100**, 1517 (2002).
[25] F. H. Stillinger and T. A. Weber, Phys. Rev. B **31**, 5262 (1985).
[26] M. H. Bhat, V. Molinero, E. Soignard, V. C. Solomon, S. Sastry, J. L. Yarger, and C. A. Angell, Nature (London) **448**, 787 (2007).
[27] E. Tombari, C. Ferrari, and G. Salvetti, Chem. Phys. Lett. **300**, 749 (1999).
[28] P. G. Debenedetti and H. E. Stanley, Phys. Today **56** (6), 40 (2003).
[29] O. Mishima and H. E. Stanley, Nature (London) **396**, 329 (1998).
[30] M. E. Johnson, T. Head-Gordon, and A. A. Louis, J. Chem. Phys. **126**, 144509 (2007).
[31] L. C. Jacobson, W. Hujo, and V. Molinero, "Thermodynamic Stability and Growth of Guest-Free Clathrate Hydrates: A Low-Density Crystal Phase of Water," J. Phys. Chem. B (in press).
[32] S. J. Plimpton, J. Comput. Phys. **117**, 1 (1995).
[33] D. Z. Liu, Y. Zhang, C. C. Chen, C. Y. Mou, P. H. Poole, and S. H. Chen, Proc. Natl. Acad. Sci. U.S.A. **104**, 9570 (2007).
[34] B. Guillot and Y. Guissani, J. Chem. Phys. **119**, 11740 (2003).
[35] L. Xu, S. Buldyrev, N. Giovambattista, C. Angell, and H. Stanley, J. Chem. Phys. **130**, 054505 (2009).
[36] F. Mallamace, C. Branca, M. Broccio, C. Corsaro, C. Y. Mou, and S. H. Chen, Proc. Natl. Acad. Sci. U.S.A. **104**, 18387 (2007).
[37] F. Mallamace, C. Corsaro, M. Broccio, C. Branca, N. Gonzalez-Segredo, J. Spooren, S. H. Chen, and H. E. Stanley, Proc. Natl. Acad. Sci. U.S.A. **105**, 12725 (2008).
[38] R. C. Dougherty, Chem. Phys. **298**, 307 (2004).
[39] S. LaPlaca, Acta Crystallogr. **13**, 503 (1960); O. Mishima, J. Chem. Phys. **100**, 5910 (1994).
[40] L. Xu and V. Molinero, "Liquid-liquid transformation of water in bulk and in nanopores" (unpublished).
[41] A. K. Soper, J. Phys.: Condens. Matter **19**, 335206 (2007).
[42] J. L. Finney, A. Hallbrucker, I. Kohl, A. K. Soper, and D. T. Bowron, Phys. Rev. Lett. **88**, 225503 (2002).
[43] H. Tanaka, Phys. Rev. Lett. **80**, 113 (1998).
[44] L. Bosio, S. H. Chen, and J. Teixeira, J. Appl. Crystallogr. **27**, 1468 (1976).
[45] G. W. Robinson, C. H. Cho, and J. Urquidi, J. Chem. Phys. **111**, 698 (1999).
[46] J. R. Errington, P. G. Debenedetti, and S. Torquato, Phys. Rev. Lett. **89**, 215503 (2002).
[47] J. R. Errington and P. G. Debenedetti, Nature (London) **409**, 318 (2001); P. Kumar, S. V. Buldyrev, and H. E. Stanley, "A tetrahedral entropy for water," Proc. Natl. Acad. Sci. U.S.A. (submitted).
[48] N. Giovambattista, F. W. Starr, F. Sciortino, S. V. Buldyrev, and H. E. Stanley, Phys. Rev. E **65**, 041502 (2002).
[49] P. Kumar, Z. Yan, L. Xu, M. Mazza, S. Buldyrev, S. Chen, S. Sastry, and H. Stanley, Phys. Rev. Lett. **97**, 177802 (2006).
[50] C. Nieto-Draghi, J. B. Avalos, and B. Rousseau, J. Chem. Phys. **118**, 7954 (2003).
[51] K. Welke, E. B. Moore, and V. Molinero, "Two-component analysis of the anomalous thermodynamics of water" (unpublished).
[52] S. Rice and M. Sceats, J. Phys. Chem. **85**, 1108 (1981).
[53] C. J. Benmore, R. T. Hart, Q. Mei, D. L. Price, J. Yarger, C. A. Tulk, and D. D. Klug, Phys. Rev. B **72**, 132201 (2005).
[54] D. Polk and D. Boudreau, Phys. Rev. Lett. **31**, 92 (1973); F. Wooten, K. Winer, and D. Weaire, *ibid.* **54**, 1392 (1985); B. R. Djordjevic, M. F. Thorpe, and F. Wooten, Phys. Rev. B **52**, 5685 (1995).
[55] W. C. Rongten, Ann. Phys. Chem. **45**, 91 (1892).
[56] M. Vedamuthu, S. Singh, and G. W. Robinson, J. Phys. Chem. **99**, 9263 (1995).
[57] J. Urquidi, S. Singh, C. H. Cho, and G. W. Robinson, Phys. Rev. Lett. **83**, 2348 (1999).
[58] L. Xu, F. Mallamace, Z. Yan, F. Starr, S. Buldyrev, and E. H. Stanley, "Appearance of a fractional Stokes-Einstein relation in water and a structural interpretation of its onset," Nat. Phys. (in press).
[59] L. Berthier, G. Biroli, J. P. Bouchaud, L. Cipelletti, D. El Masri, D. L'Hote, F. Ladieu, and M. Pierno, Science **310**, 1797 (2005).
[60] F. Sciortino, A. Geiger, and H. E. Stanley, Nature (London) **354**, 218 (1991).

[61] P. Kumar, Proc. Natl. Acad. Sci. U.S.A. **103**, 12955 (2006).
[62] T. Tokushima, Y. Harada, O. Takahashi, Y. Senba, H. Ohashi, L. G. M. Pettersson, A. Nilsson, and S. Shin, Chem. Phys. Lett. **460**, 387 (2008).
[63] P. L. Geissler, J. Am. Chem. Soc. **127**, 14930 (2005).
[64] J. D. Smith, C. D. Cappa, K. R. Wilson, R. C. Cohen, P. L. Geissler, and R. J. Saykally, Proc. Natl. Acad. Sci. U.S.A. **102**, 14171 (2005).
[65] J. D. Smith, C. D. Cappa, K. R. Wilson, B. M. Messer, R. C. Cohen, and R. J. Saykally, Science **306**, 851 (2004).

CHAPTER 4

FREEZING, MELTING AND STRUCTURE OF ICE IN A HYDROPHILIC NANOPORE

PAPER www.rsc.org/pccp | Physical Chemistry Chemical Physics

Freezing, melting and structure of ice in a hydrophilic nanopore

Emily B. Moore,[a] Ezequiel de la Llave,[b] Kai Welke,[a] Damian A. Scherlis[b] and Valeria Molinero*[a]

Received 22nd September 2009, Accepted 28th January 2010
First published as an Advance Article on the web 26th February 2010
DOI: 10.1039/b919724a

The nucleation, growth, structure and melting of ice in 3 nm diameter hydrophilic nanopores are studied through molecular dynamics simulations with the mW water model. The melting temperature of water in the pore was T_m^{pore} = 223 K, 51 K lower than the melting point of bulk water in the model and in excellent agreement with experimental determinations for 3 nm silica pores. Liquid and ice coexist in equilibrium at the melting point and down to temperatures as low as 180 K. Liquid water is located at the interface of the pore wall, increasing from one monolayer at the freezing temperature, T_f^{pore} = 195 K, to two monolayers a few degrees below T_m^{pore}. Crystallization of ice in the pore occurs through homogeneous nucleation. At the freezing temperature, the critical nucleus contains ~75 to 100 molecules, with a radius of gyration similar to the radius of the pore. The critical nuclei contain features of both cubic and hexagonal ice, although stacking of hexagonal and cubic layers is not defined until the nuclei reach ~150 molecules. The structure of the confined ice is rich in stacking faults, in agreement with the interpretation of X-ray and neutron diffraction experiments. Though the presence of cubic layers is twice as prevalent as hexagonal ones, the crystals should not be considered defective *Ic* as sequences with more than three adjacent cubic (or hexagonal) layers are extremely rare in the confined ice.

1. Introduction

Confinement is known to affect the phase behavior of liquids.[1] Water is arguably the most studied liquid in bulk and in confinement due to its relevance in technology and the natural sciences, from biology to geology. Understanding how the anomalous thermodynamics and phase diagram of water depend on the characteristic dimensions of confinement is an active research area of fundamental and practical interest.[2] MCM-41 and SBA-15 nanoporous silica are widely used in studies of water confined in cylindrical geometries, as these materials provide well defined arrays of monodisperse cylindrical nanopores with a tunable diameter from 2 to 10 nm. NMR analysis indicates that MCM-41 pores (2–4.4 nm diameter) have an atomically smooth interior surface, while SBA-15 presents a more corrugated interface.[3,4] The melting and freezing behavior of water in silica pores has been characterized through NMR, differential scanning calorimetry (DSC), and neutron and X-ray diffraction.[5–10] These studies show that the melting temperature of ice in the pores is depressed with respect to the bulk. The depression in the melting point can be represented by a modified Gibbs–Thomson equation taking into account that the effective radius of the confined ice cylinder is smaller than the radius R of the pore, due to the existence of a water layer of width d that is not crystallized at T_m,[6] $\Delta T_m = K_{GT}/(R - d)$. The Gibbs–Thomson constant, K_{GT}, can be derived from classical thermodynamics by adding an interfacial term to the free energy of each phase. Under the assumption that the liquid phase completely wets the pore, the decrease in the melting point depends only on properties of bulk water. For a cylindrical nanopore[6] $K_{GT} = 2T_m^{bulk}\gamma_{ice-liquid}V_{liquid}/\Delta H_m$, where V_{liquid} is the molar volume of the liquid phase, $\gamma_{ice-liquid}$ is the interfacial tension between ice and liquid, and ΔH_m is the enthalpy of melting of ice. The value of the constant, evaluated from the experimental bulk quantities at T_m^{bulk} is K_{GT} = 52.4 K nm.[9] From the analysis of ice melting in MCM-41 and SBA-15 silica pores with radii ranging from 2 to 12 nm, the constants were fitted to K_{GT} = 49.5 ± 2 K nm and d = 0.35 ± 0.4 nm,[5] K_{GT} = 52 ± 2 K nm and d = 0.38 ± 0.06 nm,[7] and K_{GT} = 52.4 ± 0.6 K nm and d = 0.6 ± 0.01 nm.[6] A recent study of the melting point depression in acid-functionalized SBA-15 silica pores (for which the walls were decorated with carboxylic, phosphonic and sulfonic acid) revealed that the change in water–pore interactions has an extremely weak effect on ΔT_m.[11] The freezing temperature T_f of water in the nanopores also decreases with the radius of the pore. Although freezing—contrary to melting—is a non-equilibrium process, a modified Gibbs–Thomson equation was also found to fit the depression in T_f.[11] More intriguing, the temperature gap between freezing and melting, as well as the enthalpy of melting, vanish for pores of a diameter ~2.7 nm.[6,11] This effect has been attributed to the end of the first-order character of the crystallization transition under conditions of extreme confinement.[6]

[a] *Department of Chemistry, University of Utah, 315 South 1400 East, Salt Lake City, UT 84112-0850, USA. E-mail: Valeria.Molinero@utah.edu*
[b] *Departamento de Química Inorgánica, Analítica y Química Física, Facultad de Ciencias Exactas y Naturales, Universidad de Buenos Aires, Ciudad Universitaria, Buenos Aires, Pab II, C1428EHA, Argentina*

The T_f, T_m and ΔH_m of water in the nanopores have been determined accurately from NMR and DSC analysis. The structure of water in the crystallized nanopores, however, remains elusive. The modified Gibbs–Thomson relation suggests the presence of a non-freezable water layer, but it provides no insight into its structure nor is it accurate in describing its width (partly because the radii of the pores are subject to uncertainties and reported values depend on the measurement techniques). NMR results show evidence of the presence of mobile components in the nanopores that have been interpreted as viscous liquid and a plastic form of ice.[12] NMR cannot indicate, however, the localization of the liquid inside the pore, *e.g.* whether all the liquid is at the interface. Neutron diffraction studies of filled and partly filled SBA-15 pores show the existence of defective cubic ice and an amorphous component in the crystallized pore.[13–15] It should be noted that cubic ice formed in bulk samples does not have a pure cubic structure but contains hexagonal stacking faults (evident in the form of the 100 peak of *Ih* in the diffraction patterns), in amounts that depend on the method and experimental conditions under which the ice is formed.[16–19] Liu *et al.* conjectured that there is an interfacial region between the ice at the center of the $R = 4.3$ nm pore and its surface that contains a disordered form of water/ice, which reversibly converts to ice at lower temperatures.[13] X-ray diffraction studies of MCM-41 and SBA-15 pores of diameter 4.4–72 nm also provide evidence of the presence of a hexagonal and cubic ice hybrid, although no features characteristic of hexagonal ice were found for pores of diameter 4.4 nm.[20] Morishige and Uematsu modeled the experimental diffraction pattern as arising from hexagonal ice with a certain probability of stacking faults; they found that the density of faults decreased as the pores become wider and proposed that the stacking sequences of the confined ice are nearly random.[20]

Molecular simulations have a spatial resolution that makes them optimum for the study of ice structure in the nanopores, the existence and distribution of a liquid phase and of the melting, nucleation and growth processes. The study of water crystallization through atomistic simulations, however, is challenging, as crystallization requires spontaneous nucleation of small crystallites and their growth. Ice nucleation is a stochastic rare event, and its modeling through simulations requires either extensive sampling involving very long simulations or the use of simulation techniques to sample rare events. The first strategy, also known as the ''brute force'' approach, was pursued in the studies of the nucleation of ice from bulk water,[21] from a system with a water–vacuum interface,[22] from water confined between planar surfaces[23–30] and in narrow carbon nanotubes.[31] Spontaneous crystallization of water in simulations of hydrophilic cylindrical nanopores has not been reported to date. The second strategy has been applied to study the nucleation of bulk ice through Monte Carlo (MC) simulations with umbrella sampling along a predefined reaction coordinate that accounts for the global change in symmetry as liquid water transforms into ice,[32,33] and through metadynamics simulations,[34] which favored the crossing of nucleation barriers along the same reaction coordinate as in ref. 32. The umbrella sampling[25] and the metadynamics[27] simulations led to different results, predicting, respectively, hexagonal (*Ih*) and cubic (*Ic*) ice to be the product of crystallization, in spite of using the same TIP4P model under equal temperature and pressure conditions, and applying biased sampling along the same reaction coordinates. *Ih* is the stable crystal of TIP4P water at room pressure.[35,36] Brukhno *et al.* introduced a maximum projection method that distinguishes cubic and hexagonal ice, which they used to bias the formation of ice in parallel tempering umbrella sampling MC simulations.[33] Their method as is cannot be used to recognize *Ih* and *Ic* arbitrarily oriented in the simulation cell (because it is not rotationally invariant), although it is adequate to grow ice with hexagonal and cubic stacking in a predetermined fixed orientation. The orientation of the stacking faults in confined ice, however, is not known beforehand and the axis of the stacking (the *c*-axis) may change directions as the crystal grows along the pore.

In this work, we use molecular dynamics simulations to address the following questions: how do the temperatures of melting and freezing of water in the nanopore compare with bulk water, how does water nucleate and grow ice in a hydrophilic nanopore, and what is the structure of the crystallized water in the pore. The most critical challenges faced by molecular simulations of nucleation and growth of ice, and the recognition of its structure, are:

(i) The accuracy of the water models. Of the most popular atomistic models of water, only TIP4P predicts that ice *Ih* is the most stable phase, while TIP3P, SPC, SPC/E and TIP5P predict that ice *II* is the stable crystal at room pressure.[37,38] The melting point of *Ih* with TIP4P is 232 K;[37] an improved version of the model, TIP4P/ice predicts 272.2 K.[39] The melting point of *Ic* for the TIP4P/ice model has not been reported to date.

(ii) The computational cost of atomistic simulations limits the studies to small systems (to date, less than 800 molecules simulated with classical methods using rigid water potentials). In the case of ''brute force'' simulations, this cost hinders the production of enough unconstrained simulations to extract information on the size of the critical nuclei and mechanisms of crystallization.

(iii) Methods to sample rare events relying on the mapping of the free energy along a reaction coordinate for the nucleation and growth seem to give either inconsistent structures or be limited to growing ice in predetermined directions, making them inadequate to elucidate the stacking structure of ice in the nanopores.

(iv) The lack of simple to implement rotationally invariant methods to identify the growth of hexagonal and cubic ice, as pure crystals or in randomly oriented stacked configurations.

In this work we address (i) and (ii) by using the mW coarse-grained model of water whose computational implementation is 180 times more efficient than that of atomistic models with Ewald sums,[40] yet accurately describes the thermodynamics and structures of liquid water, *Ih* and *Ic*. The monatomic water model mW represents each water molecule by a single particle with three-body nonbonding interactions that mimic hydrogen bonds.[40] mW reproduces the structure of water phases (ice, clathrates, liquid, low density amorphous ice),[40–42] the thermodynamic anomalies of water and the enthalpy of the phase transitions between liquid, vapor and

ice with comparable or better accuracy than the most popular atomistic water models, including TIP4P/ice.[40] Important for this study, mW predicts that the most stable crystal is hexagonal ice, with melting temperature $T_m^{Ih} = 274$ K. mW predicts that cubic ice is slightly less stable, $T_m^{Ic} = 271$ K, in excellent agreement with the 271.7 K estimated from thermodynamic cycles.[43] While the thermodynamics and structure of water are well represented by the mW model,[40–42] water mobility is not. Although mW correctly describes the well-known diffusion anomaly of water (the existence of a diffusivity maximum on compression), it does not reproduce the characteristic times of diffusion of the liquid.[40] The diffusivity of liquid mW water is about twice the experimental value at room temperature, with the difference increasing upon cooling. The diffusion coefficient of mW is less sensitive to temperature than found in experiments because the energy of the coarse-grained model only depends on the oxygen positions, and thus it does not account for the full barrier of breaking hydrogen bonds as water diffuses. We note, however, that the energy of the hydrogen bonds is well accounted for in mW, which reproduces the enthalpies of vaporization and melting within just 0.17 kcal mol^{-1} of the experimental values;[40] it is the *barrier* for breaking the bonds that is smaller, not the energy difference between stable states. The faster dynamics of mW is an asset for the study of crystallization, as both nucleation and growth rates are enhanced in the coarse-grained model. Thus, in addition to the 180 times increase in efficiency of the mW model (measured in terms of the computing time required to simulate a fixed amount of time, *e.g.* 10 ns, for a given number of molecules), the rate of nucleation and growth of ice in the mW model is enhanced due to the faster intrinsic dynamics of the coarse-grained water. This makes it possible to produce an ensemble of crystallizing trajectories through unconstrained (“brute force”) MD simulations of supercooled water, the approach we take in this work.

The last challenge, the recognition of hexagonal and cubic ice, is addressed with a novel, simple method that makes use of the correlation of bond order parameters[44,45] to compute the number of staggered and eclipsed intermolecular O$\cdots$O bonds that distinguish the two polymorphs. The method we introduce in this work is easy to implement and recognizes *Ic*, *Ih* and any hybrids of the two, irrespective of the orientation of the crystallites in space. This feature makes it particularly suitable to characterize the structure of ice as it grows in the anisotropic environment of the nanopore, without assuming that the stacking faults have a preferred alignment with the axis of the pore.

We present a study of the nucleation, growth, structure and melting of ice in a cylindrical hydrophilic nanopore with an internal diameter of 3 nm. For this work, we select a simple—idealized—pore: the pore wall itself is made of water. The configuration of the molecules of the wall corresponds to that of liquid water at 298 K. The molecules of the pore wall are allowed to vibrate, but they are restrained from diffusing away through soft harmonic intermolecular bonds with their closest neighbors in the wall. The intermolecular interactions of water with the wall are the same as for water with itself. The rationale for studying the melting and freezing of water in a water–wall pore is that under the assumption of complete wetting of the pore wall by water, the Gibbs–Thomson constant depends only on bulk water properties. The implication is that for a fully wetting surface the equilibrium melting temperature of water in the pore depends on the radius of the pore, but not on the chemical details of its surface. This corollary agrees with the results of recent experiments, in which it was found that decoration of the surface of SBA-15 silica with acid groups did not affect the melting and freezing temperatures of water.[11] Experimental studies on MCM-41 and SBS-15 silicas suggest that even in the crystallized pore there may be a layer of liquid water wetting the pore wall.[5–7,12–15] Based on these arguments, we expect that the thermodynamics of melting and freezing of water reported for water confined in SBS-15 and MCM-41 silica are common to other hydrophilic nanopores for which water wets completely the surface, such as the one selected for this study.

The paper is organized as follows: section 2 describes the simulation methods and models. Section 3 presents a new method for the identification of ice polymorphs and shows the equivalence to crystallographic methods for the classification of stacking faults in ice. Section 4 presents the results for the nanopores and section 5 the most important conclusions of this work.

2. Simulation model and methods

Water potential

The monatomic water model mW consists of a sum of pairwise, ϕ_2, and three-body, ϕ_3, contributions:[40]

$$E = \sum_i \sum_{j>i} \phi_2(r_{ij}) + \sum_i \sum_{j\neq i} \sum_{k>j} \phi_3(r_{ij}, r_{ik}, \theta_{ijk})$$

$$\phi_2(r_{ij}) = A\varepsilon\left[B\left(\frac{\sigma}{r_{ij}}\right)^{p_{ij}} - \left(\frac{\sigma}{r_{ij}}\right)^{q_{ij}}\right] \exp\left(\frac{\sigma}{r_{ij} - a\sigma}\right)$$

$$\phi_3(r_{ij}, r_{ik}, \theta_{ijk}) = \lambda\varepsilon[\cos\theta_{ijk} - \cos\theta_0]^2 \times \exp\left(\frac{\gamma\sigma}{r_{ij} - a\sigma}\right) \exp\left(\frac{\gamma\sigma}{r_{ik} - a\sigma}\right) \quad (1)$$

where r_{ij} is the distance between particles i and j, θ_{ijk} is the angle formed by the vectors $\dot{r}_{ij}$ and $\dot{r}_{ik}$, $A = 7.049556277$, $B = 0.6022245584$, $p = 4$, $q = 0$, $\gamma = 1.2$, $a = 1.8$, $\theta_0 = 109.47^\circ$, $\sigma = 2.3925$ Å, $\varepsilon = 6.189$ kcal mol^{-1}, and $\lambda = 23.15$. The three-body term adds an energy penalty to configurations with angles that depart from θ_0, encouraging “hydrogen bonded” tetrahedral configurations. The mW model does not have electrostatics or hydrogen atoms. The short-range of the potential (less than 4.32 Å) and the lack of hydrogen atoms, allowing for longer integration steps, makes mW 180 times faster than atomistic simulations of rigid models with Ewald sums. We refer the interested reader to ref. 40 for the details on the parameterization, validation, benchmarking and evaluation of the mW model.

Pore systems

The pore-wall and the liquid contained in the pore were made of water. An open cylindrical nanopore was built from an

instantaneous configuration of liquid water containing 12 288 coarse-grained molecules equilibrated at 298 K and 1 atm (density 0.997 g cm^{-3}) in a simulation cell 5 nm wide in the x and y directions and about 15 nm long in the z direction. The molecules in this configuration were assigned to two groups, according to their position: *pore wall* and *water*. The *pore wall* was made of the particles found (a) outside a cylinder of radius 1.5 nm from the center of the block in (x,y) and (b) their z positions were not in the first 1 nm slab of the block:

$$(x_i - x_{\text{center}})^2 + (y_i - y_{\text{center}})^2 \geq (1.5\,\text{nm})^2 \cap z_i > 1\,\text{nm} \quad (2)$$

This defines a pore wall made of 7859 particles forming an open cylindrical pore of radius 1.5 nm and length 14 nm. The remaining 4429 particles form the *water* phase. The water phase was T-shaped, with a flexible 1 nm length head block that allows for expansion of the liquid on cooling and crystallization. The nonbonding interactions between *all* particles were described with the mW model. The particles in the pore wall vibrate like in a solid: the wall molecules were restrained around their original intermolecular distances through harmonic bond potentials, $K(r_{ij} - r_{ij}^{o})^2$, with their first neighbors within the wall ($r_{ij}^{o} < 3.5$ Å). We used a soft bond constant, $K = 30$ kcal $Å^{-2}$, compatible with the large time step of the mW model (10 fs, see below) but sufficient to ensure that the intermolecular structure of the wall remains the one of the equilibrium configuration of liquid water at 298 K from which the pore wall was made. The pore wall vibrates like a solid but it has the structure (in terms of intermolecular distances and angles) of liquid water at 298 K. From the point of view of the water inside the pore, the wall presents the structure and interactions of liquid water. To quantify the roughness of the pore wall, we computed the width over which the radial density of the wall, measured from the center of the pore, decays from 90 to 10% of its bulk matrix value. The $t_{10\text{–}90}$ computed over a 100 ns trajectory of the pore filled with water at 200 K was 1.45 Å.

Simulation methods

We carried out molecular dynamics simulations in the *NPT* ensemble using LAMMPS.[46] The equations of motion were integrated with the Velocity Verlet algorithm with a time step of 10 fs. The systems were simulated with periodic boundary conditions. The temperature was controlled with a Nose–Hoover thermostat with relaxation time 0.5 ps. The pressure was controlled at $p = 1$ atm through a Nose–Hoover barostat with time constant 2.5 ps. The z dimension of the cell was allowed to dilate and contract independently of the x and y dimensions, to account for the anisotropy introduced by the pore.

Tetrahedral order and alignment in bulk reference systems

Periodic cells of *Ih* and *Ic*, containing 576 and 512 water particles, respectively, were built using crystallographic data. The simulation cells for low-density amorphous ice (LDA, the glass of water) and liquid water contained 512 water molecules each, simulated at 150 and 298 K, respectively. The LDA was produced by cooling of the bulk liquid at the critical vitrification rate, following the protocols of ref. 41. The tetrahedral order parameter q_t and orientational alignment a (eqn (3) and (5), see section 3) were computed from 200 configurations extracted from 0.5 ns simulations.

Freezing temperature

To compute the fastest cooling rate that produces ice crystallization and the freezing temperature T_f^{pore}, liquid water in the pore was first equilibrated at 220 K for 20 ns and subsequently cooled from 220 to 180 K at linear rates 10, 1, 0.5, 0.2 and 0.1 K ns^{-1}. Each temperature ramp was simulated by setting the target temperature of the thermostat as a linear function of time. Crystallization was quantified through the analysis of the total number of molecules in the ice phase, N_{ice}, and the number of molecules in the largest ice nuclei, $N_{\text{largest ice cluster}}$, as a function of temperature. T_f^{pore} was considered to be that for the onset of ice growth in the system.

Isothermal freezing of water in the nanopore

To garner statistics on the process of crystallization and the structure of ice in the nanopore, we performed ten independent simulations at T_f^{pore}. These simulations started from uncorrelated configurations from a simulation of liquid water in the pore at 220 K, quenched instantaneously to T_f^{pore} and evolved for 80 to 170 ns, until the crystallization of water in the pore was complete. Completion of the crystallization was monitored through the time evolution of the energy and the number of molecules in the ice phase.

Melting temperature of ice in the nanopore

We determined the melting temperature T_m^{pore} for ice in the pore from constant temperature simulation of fully crystallized systems (the result of the crystallization simulations described above) at $p = 1$ atm and $T = 220$, 225, 230 and 235 K for 10 ns. The enthalpy of melting was computed from the difference of the enthalpy of water in the pore at the lowest temperature for which all water in the pore is liquid and the highest temperature for which there is ice in the pore, divided by the total number of molecules in the water phase.

3. Identification of ice

Here we introduce a simple method to identify hexagonal and cubic ice as crystallization proceeds from liquid water. Two challenges must be addressed: the first is to distinguish liquid from crystal, and the second is to differentiate *Ic* and *Ih* polymorphs.

The *CHILL* algorithm

To distinguish liquid from crystal we adopt the local bond order parameter method developed by ten Wolde *et al*. for the identification of crystal nuclei in Lennard-Jones systems,[45] based on the order parameters introduced by Steinhardt *et al*.[44] In this method, molecules are classified as belonging to the crystal or liquid based on the coherence of their orientational order with that of their neighbors. The analysis of the coherence of local ordering rather than the local ordering itself is particularly critical for the identification of ice from deeply supercooled liquid water, as the structure of the latter becomes increasingly tetrahedral on cooling,

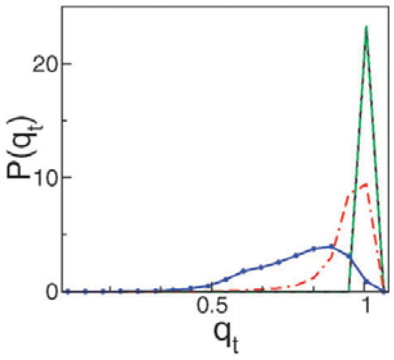

Fig. 1 Probability density of the tetrahedral order parameter q_t shown for *Ih* (solid black), *Ic* (dashed green), low-density amorphous ice LDA (dash-dotted red) and room temperature liquid water (dotted blue). Note that the distributions for *Ih* and *Ic* overlap completely, because they both have perfectly tetrahedral environments. The overlap in $P(q_t)$ for *Ih*, *Ic* and LDA does not allow these structures to be distinguished using q_t.

acquiring the structure of a random tetrahedral network in the glass state.[41] The local tetrahedral order q_t around each molecule k is defined by[47]

$$q_t(k) = 1 - \frac{3}{8}\sum_{i=1}^{3}\sum_{j=i+1}^{4}\left(\cos\theta_{ikj} + \frac{1}{3}\right)^2 \qquad (3)$$

where θ_{ikj} is the angle subtended between the central water molecule k and two of its 4-closest neighbors. $q_t(k)$ is 1 for a tetrahedral configuration. Fig. 1 displays the distribution of local tetrahedral ordering around the water molecules in *Ih*, *Ic* and low-density amorphous ice (LDA) at 150 K, and liquid water at room temperature. $P(q_t)$ cannot distinguish the ice phases from the LDA glass. Patches of tetrahedrally coordinated molecules with LDA-like structure develop and increase in size as liquid water is cooled, rendering the distribution of tetrahedral order of the liquid increasingly overlapped with that of the crystals.[41]

The increasing tetrahedrality of liquid water on cooling hinders the possibility of using a measure of local tetrahedrality around each water molecule as classification of belonging to ice or liquid.[41] The tetrahedra centered on neighbor molecules, however, are aligned in a well-defined way in ice and randomly aligned in the liquid and glass. This difference is the basis of the identification of crystal particles of the bond order parameter method that we adopt in this work. The local order around each water i is defined by a local orientational bond order parameter vector $\dot{q}_l(i)$ with $2l + 1$ complex components

$$q_{lm}(i) = \frac{1}{4}\sum_{j=1}^{4} Y_{l,m}(\hat{r}_{ij}). \qquad (4)$$

The $q_{lm}(i)$ project the orientational structure of the four closest neighbors of a molecule on a basis of spherical harmonics $Y_{l,m}(\theta_{ij},\phi_{ij}) = Y_{l,m}(\hat{r}_{ij})$, where $\hat{r}_{ij}$ is the unit vector that connects i with one of its four closest neighbors j. The alignment of the orientation of the local structures is measured by the normalized dot product of $\dot{q}_l$ between each pair of neighbor molecules,

$$a(i,j) = \frac{\hat{q}_l(i)\cdot\hat{q}_l(j)}{|\hat{q}_l(i)||\hat{q}_l(j)|} = \frac{\sum_{m=-l}^{l} q_{lm}(i)q^*_{lm}(j)}{\left(\sum_{m=-l}^{l} q_{lm}(i)q^*_{lm}(j)\right)^{1/2}\left(\sum_{m=-l}^{l} q_{lm}(j)q^*_{lm}(i)\right)^{1/2}}, \qquad (5)$$

where q^*_{lm} is the complex conjugate of q_{lm}. To determine the optimum l that distinguishes between structures *Ih*, *Ic* and the liquid, we computed the distribution of alignments, $P_l(a)$, for $l = 1, 2, \ldots 10$ for *Ih*, *Ic* and LDA at $T = 150$ K, and liquid water at 300 K. We found that $l = 3$ and 4 provide the best resolution of these structures. In what follows we adopt $l = 3$, as it involves the least number of calculations. It should be noted that while the global orientational order parameter Q_l of the crystals is zero for $l = 3$, it is not for $l = 4$,[44] thus, classification based on the latter should be used in cases where the total order needs to be biased (*e.g.* in an umbrella sampling or metadynamics calculation) towards the formation of the crystal phase. The global order is always zero for the amorphous systems.

Fig. 2 shows the distributions of alignment between local structures for $l = 3$. Contrary to the local tetrahedrality q_t, the alignment a presents sharply distinct distributions for ice and LDA glass. Moreover, the distribution of tetrahedral alignments allows for a distinction between cubic and hexagonal ice. All water molecules in *Ih* and *Ic* are tetrahedrally coordinated. The main difference between these polymorphs is that in cubic ice all water molecules have a staggered arrangement of intermolecular bonds with respect to its four neighbors, while in hexagonal ice three of the intermolecular bonds are staggered and one, parallel to the *Ih* *c*-axis, is eclipsed. With

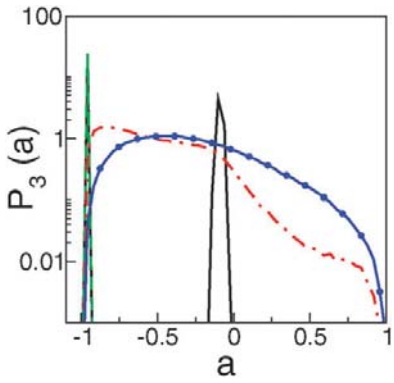

Fig. 2 Probability density of the alignment of orientational order, $P_3(a)$. Same symbols as in Fig. 1. The distribution of alignments is sharp for *Ih* and *Ic*, with a peak around $a = -1$ for both *Ih* and *Ic* that signal a staggered arrangement of intermolecular bonds (with all four neighbors in *Ic*, with three of the four neighbors in *Ih*), and a peak around $a = -0.11$ for *Ih* that corresponds to the neighbor with eclipsed configuration. We use the number of staggered and eclipsed neighbors to distinguish between molecules that belong to different ice polymorphs and the liquid.

$l = 3$, perfect staggered water–water bonds yield $a = -1$ and perfect eclipsed bonds $a = -0.11$. This provides the basis for the classification of the structures of ice and liquid as the crystallization of water proceeds in the nanopore.

We classify the molecules according to the alignment of their orientation with respect to that of its four closest neighbors into four groups:

• ***C***: A molecule that belongs to the cubic ice phase has all bonds with its four closest neighbors staggered. To allow for thermal fluctuations, we define a staggered bond as one with $a < -0.8$.

• ***H***: A molecule that belongs to the hexagonal ice phase. It has three staggered bonds ($a < -0.8$) and one eclipsed bond ($-0.2 < a < -0.05$) with its four closest neighbors.

• ***I***: A molecule that belongs to the ice phase but does not satisfy the strict requisites for being ***H*** or ***C***. This is the case for molecules in the surface of crystallites. We define ***I*** as those having (i) only two staggered bonds and at least one neighbor with more than two staggered bonds, or (ii) three staggered bonds, no eclipsed bond, and at least one neighbor with two staggered bonds. The latter allows for the identification of ice in non-compact crystallites.

• ***L***: A molecule that belongs to the liquid or amorphous phase. These are molecules that do not satisfy the requisites indicated above. ***L*** indicates that the structure is amorphous as in the liquid. The mobility of the ***L*** molecules is used to distinguish whether they form a liquid or a glass (*e.g.* LDA).

Using this algorithm, that we name *CHILL*, we find that 100% of the molecules in *Ih* are classified as *H*, 100% of the molecules in *Ic* as *C*, 0.1% of the molecules in room temperature water are classified as crystalline, and 12% of the LDA glass is classified as crystal, of which 91% is *I*. The largest ice cluster in LDA was found to contain 19 ± 8 water molecules. The finding of small ice nuclei in LDA is a consequence of the metastable nature of this phase, and not an artifact of the identification method.

Identification of stacking sequences in ice

Our classification of the ice polymorphs with the *CHILL* algorithm is based on the identification of the number of staggered and eclipsed bonds for each water molecule. The usual classification of hexagonal and cubic crystal is based on the repetition of sequences of layers: ABABAB... for hexagonal and ABDABDABD... for cubic. A fault is a break in the ordering of the sequences of the cubic or hexagonal crystal.[18] A growth fault is the incorporation of a single hexagonal (cubic) sequence in a cubic (hexagonal) lattice. An example of a cubic sequence with a growth fault is ABDA**B**A̲DBADB, where the introduction of A̲ layer, leaves **B** flanked by two identical layers, producing a hexagonal layer (*h* layer).[18] A deformation fault incorporates two adjacent hexagonal (cubic) layers in a cubic (hexagonal) sequence. An example of a deformation fault in a cubic sequence is ABDA**B**A̲B̲DABD that arises from the addition of A̲B̲ to a cubic sequence and yields two layers (**BA**) with hexagonal order. Instead of using the letters A, B and D to indicate the absolute position of the layers, it is more convenient to indicate whether the layers are hexagonal (flanked by identical ones), or cubic (flanked by distinct ones). We use lowercase *h* and *c* to denote a hexagonal and cubic layer, respectively.[17,18] In terms of our classification of the *molecules* based on the number of staggered and eclipsed bonds with their four closest neighbors, an *h* layer corresponds to the plane between two adjacent layers of *H* molecules; and a *c* layer to the plane between two layers of *C* molecules. Note that an isolated layer of *H* (or *C*) molecules is not possible, as the definition of staggered or eclipsed bonds involves always a pair. Fig. 3 illustrates the correspondence of the layer-based and molecule-based assignments for the repeated *hhc* sequence, also known as 9R.[48]

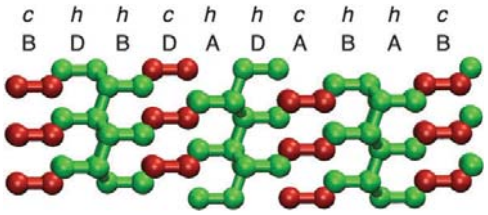

Fig. 3 Assignment of hexagonal and cubic layers for the 9R structure, a repetition of the *hhc* stacking sequence. The water molecules (hydrogen not shown) are colored according to the classification as hexagonal *H* (green) or cubic *C* (red). The lower row of labels indicate the absolute positions of the layers (here named A, B and D), and the upper label indicates whether it is a hexagonal layer *h*, or a cubic layer *c*. An easy way to visualize a *h* (or *c*) layer is to look for the plane between pairs of adjacent *H* (or *C*) molecules along the *c*-axis of the stacked crystal.

4. Results and discussion

A Freezing temperature of water in the nanopore

Although water is not a good glass former, micron-sized droplets of water can be vitrified when cooled at rates of about 10^6 K s^{-1}.[49] Due to the lack of hydrogen atoms, crystal nucleation and growth are faster in the mW model than in real water.[40] The maximum cooling rate that produces crystallization of bulk mW is $q_x = 2$ K ns^{-1} for a system of 32 768 molecules and $q_x = 1$ K ns^{-1} for 512 molecules.[40,41] The temperature of crystallization of water at q_x is $T_f^{bulk} \approx 200$ K for these systems. This temperature is about 30 K lower than for bulk experimental water, for which the temperature of homogeneous nucleation is 231 K.[50]

We quantified the degree of crystallization of water in the pore for quenching rates ranging from 10 to 0.1 K ns^{-1}. Fig. 4 shows the number of particles in the largest ice nucleus (including cubic, hexagonal and interfacial ice) along these quenching trajectories. The fastest cooling rate that leads to crystallization—albeit converting only 25% of the water into ice—is 1 K ns^{-1}. This is comparable to q_x for the bulk system, although in the bulk simulations essentially all the water was crystallized at 1 K ns^{-1}. We found that not even the slowest quenching rates lead to crystallization of all the water at 180 K. The maximum conversion to ice was 66%. The other 34% of water consists of a liquid layer of water that wets the surface of the pore (more details in 4.C and 4.D). Our results

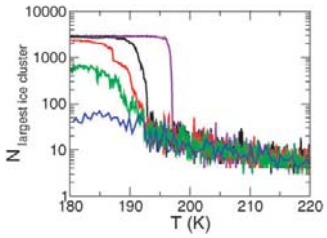

Fig. 4 Number of particles in the largest ice nucleus *versus* temperature, along the quenching trajectories with constant cooling rate 0.1 K ns^{-1} (violet), 0.2 K ns^{-1} (black), 0.5 K ns^{-1} (red), 1 K ns^{-1} (green) and 10 K ns^{-1} (blue). Crystallization is observed for $q_x \leq 1$ K ns^{-1}. The onset temperature of crystallization ranges from 196 K for the slowest ramp to 193 K for 1 K ns^{-1}. At the end of the cooling ramp, the percentage of ice was 25% of the total water in the pore for 1 K ns^{-1}, 54% for 0.5 K ns^{-1}, 62% for 0.2 K ns^{-1} and 66% for 0.1 K ns^{-1}.

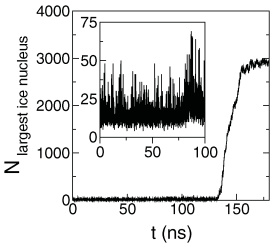

Fig. 5 Number of particles in the largest ice nucleus *versus* time for a representative crystallizing trajectory. A latent period, $0 < t < t_n = 130$ ns, is followed by ice growth. The inset shows a detail of the largest nucleus size during the latent period. From the largest size attained before nucleation, we estimate the critical nucleus size to contain about 75–100 water molecules at 195 K.

confirm the existence of mobile liquid water in the crystallized pores previously deduced from NMR and DSC measurements.

The freezing temperature of water in the pore, T_f^{pore}, ranged from 197 to 193 K for rates 0.1 K ns^{-1} to 1 K ns^{-1} (Fig. 4). The crystallization of ice in the quenching simulations started in the head of the pore for the 0.1 K ns^{-1} simulation, inside the volume confined by the pore for the 0.2 and 0.5 K ns^{-1} ones, and from different nucleation sites, inside the pore and in the head, for the 1 K ns^{-1}. We selected $T_f^{pore} = 195$ K for the studies of isothermal freezing described in the next section. The freezing point depression, measured with respect to bulk mW water is $\Delta T_f \approx 7$ K. The experimental freezing temperature of water in the 3 nm diameter pores of MCM-41 is ~213–223 K,[6,7] this is 8–18 K lower than the temperature of homogeneous nucleation of water, T_H. In separate work,[51] we show that the freezing temperature of water tracks closely the temperature of the high- to low-density transformation in the supercooled liquid.[41]

B Nucleation and growth of ice in the nanopore

Crystallization involves the nucleation and growth of ice crystallites. Fig. 5 shows the number of molecules in the largest ice nucleus as a function of time for a representative freezing trajectory at $T_f^{pore} = 195$ K. There are two well defined time regimes: an induction period during which ice nuclei containing less than 70 water particles form and dissolve, and a growth period in which the nuclei develop into larger crystals. The induction time is stochastic, for this set of ten simulations it was found to last between 52 and 134 ns. After the growth started at the nucleation time t_n, all samples crystallized within 17 ± 4 ns. From the size of the unsuccessful nuclei formed during the induction period in the isothermal and quenching trajectories, we estimate that the critical ice nucleus contains about 75–100 water molecules. The radius of gyration of the ice nuclei of critical size, 0.8–1.2 nm, is similar to the radius of the pore, 1.5 nm. The nucleation of ice is homogeneous: the formation of the nuclei is not assisted by the pore wall surface.

In all the isothermal simulations, the full pore crystallized from a single nucleus that grows to form a crystal that spans the entire pore. This is not surprising, as formation of the critical nucleus is a rare event and the volume of water in the pore is small (~100 nm^3). We found that in 8 out of 10 simulations the successful nuclei originated in the head of the pore, the ~1 nm slab at the extreme of the periodic system. It should be noted that in our simulations, the volume ratio between the water contained in the pore and its head is approximately 3 : 1. When the relative frequency of successful nucleation events is weighted by such a ratio, it turns out that the specific probability (per unit of volume) of an event leading to crystallization inside the pore is only 6% at 195 K. This result is reflecting that the growth of ice is hindered under confinement because the radius of the pore is comparable to the critical nucleation size. In experiments where the pores are usually much longer than in the simulations, we expect a larger fraction of successful nucleation events inside the pore.

Fig. 6 shows snapshots of the growth of ice in the pore. Only the water molecules that belong to the cubic (*C*) or hexagonal (*H*) polymorphs are shown. These are surrounded by interfacial ice (*I*) and embedded in the liquid (*L*). The crystallization starts with the formation of a small nucleus in which cubic and hexagonal features are present, although stacking of *h* and *c* layers are not yet evident until the nuclei reach ~150 molecules. These grow into a single crystallite comprised of well-defined stacking planes. The orientation of the stacking with respect to the axis of the pore is random, and is determined by the initial growth of the critical nucleus.

C Structure of ice in the nanopores

Fig. 7 shows representative snapshots of the confined ice after crystallization is complete. All the samples present profuse stacking of *h* and *c* layers in a continuous crystallite, with a *c*-axis that changes direction every 5.5 ± 2 nm. Table 1 summarizes the average percentages of liquid and ice (cubic, hexagonal and interfacial) in the crystallized nanopores. We verified that the molecules classified as part of the liquid phase are mobile within the time scale of the simulations. As observed in the quenching simulations, not all the water in the pore can be crystallized at $T_f^{pore} = 195$ K, although this temperature is ~30 K below the corresponding melting point (see 4.D below). Liquid water accounts for 37.4 ± 4.4% of the equilibrium contents of the pore at 195 K. Most of the liquid, 88 ± 6%, is in the first monolayer that wets the pore

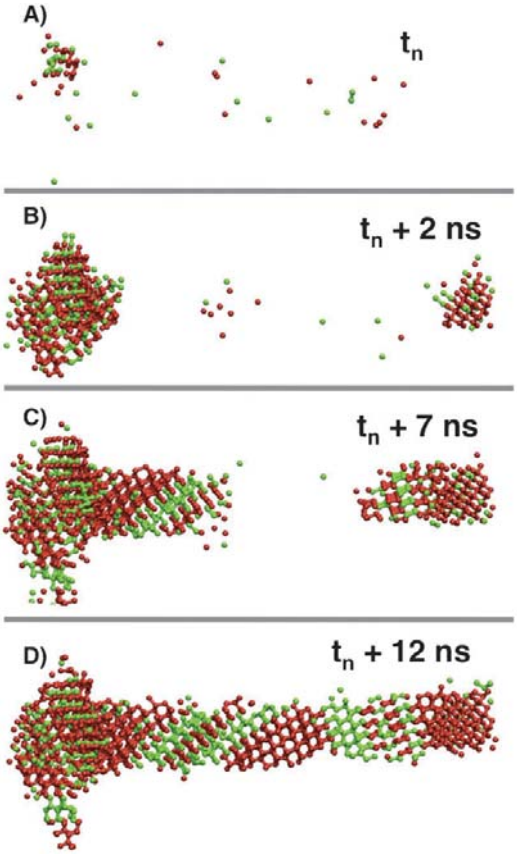

Fig. 6 Progression of crystallization from the nucleation time, t_n, for a representative crystallizing trajectory. Only the hexagonal *H* (green) and cubic *C* (red) water particles are shown. The largest ice nucleus (including hexagonal, cubic and interfacial ice) along this progression contains 127, 1021, 2109 and 2844 molecules. Note that the system crystallizes from a single ice nucleus, which appears to grow from the left and right side of the figure due to the periodic boundary conditions of the simulations. The stacking directions are not well defined for the critical nucleus, but develop soon afterwards and are already well defined 2 ns after nucleation.

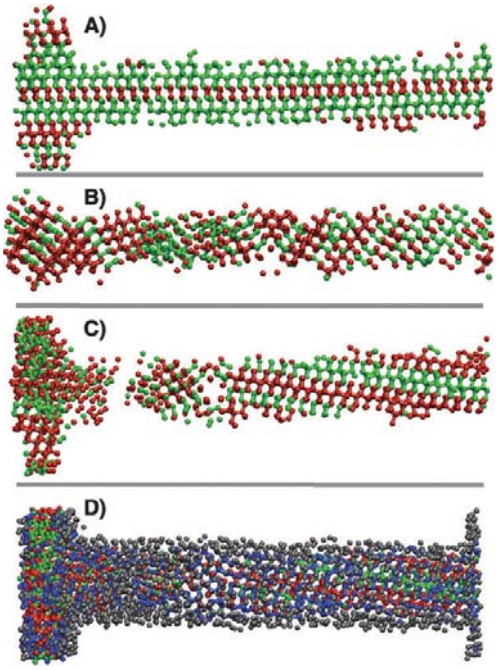

Fig. 7 Configurations of the confined ice at the freezing temperature. Panels A, B and C show the cubic (red) and hexagonal (green) components of the ice formed in three different simulations. The lower panel displays also the interfacial ice (blue) and liquid (grey) of the configuration of panel C.

wall. Of this wetting layer, $\frac{3}{4}$ of its molecules are liquid and the other $\frac{1}{4}$ belong to interfacial ice (Table 1).

The ratio of cubic to hexagonal ice in the pore is about 2 : 1 (Table 1). The energy of bulk *Ih* and *Ic* are similiar: at 195 K the mW model predicts $H_{Ic} - H_{Ih} = 0 \pm 30$ J mol^{-1}, in good agreement with the 35 J mol^{-1} measured with adiabatic calorimetry.[52] In spite of the variety of stacking arrangements found in the ten crystallized pores, their energies per mole of water were identical within 80 J. This suggests that stacking does not affect significantly the energy of the crystals, and is consistent with the almost random arrangement of *h* and *c* layers observed in these pores. From the analysis of the stacking sequences of the ten pores, we computed the probabilities for pairs of layers of type *hh*, *hc*, *ch* and *cc* to be followed by a *c* layer.[17,19] These are, respectively, $\alpha = 0.72$, $\beta = 0.71$, $\gamma = 0.70$ and $\delta = 0.61$. Note that the probability that two hexagonal layers are followed by a third *h*, $1 - \alpha = 0.28$, is much lower than the probability of *c* following a *cc* sequence, $\delta = 0.61$. Hansen *et al.* obtained the same qualitative result from their analysis of the diffraction patterns of bulk ice I formed by decompression of ice V and IX.[17] Morishige and Uematsu estimated the growth fault probabilityα from the analysis of the diffraction patterns of ice in silica nanopores: they reported values of α which increase from 0.1 to 0.53 as the pore diameter narrows from 72 to 9.8 nm.[20] The value we find for the 3 nm pore, $\alpha = 0.72$, is consistent with an extrapolation of the trend towards higher growth fault probability deduced from their X-ray diffraction experiments.

The diffraction patterns on ref. 17 indicate that the hexagonal sequences in ice I obtained from decompression of ice V and IX appear mainly in pairs (deformation faults) and rarely as singles (growth faults). This is not the case in the narrow $R = 1.5$ nm nanopores: we find four times as many hexagonal growth faults (a *chc* sequence) than hexagonal deformation faults (*chhc* sequence). The ratio is almost 1 : 1 for the cubic faults (*hch vs. hcch* sequences). Cubic and hexagonal deformation faults (*hcch vs. chhc*) occur in a 3 : 2 proportion. It should be noted, however, that these faults are not embedded in long cubic or hexagonal sequences: pure cubic or hexagonal sequences with more than three layers are rare in the nanoconfined ice.

Table 1 Percentages of liquid and cubic, hexagonal and interstitial ice in the crystallized nanopores. 1st and 1st + 2nd shells denote the layers of water within 0.35 and 0.55 nm of the pore surface, respectively

	%Hexagonal (H)	%Cubic (C)	%Interfacial (I)	%Liquid (L)
All water, 195 K	11.2 ± 3.3	23.2 ± 3.6	28.2 ± 1.0	37.4 ± 4.4
1st shell, 195 K	2.2 ± 1.1	4.0 ± 1.9	22.5 ± 3.4	71.3 ± 3.1
All water, 220 K	7.9 ± 2.5	19.2 ± 2.2	22.3 ± 1.9	50.6 ± 2.1
1st shell, 220 K	0.8 ± 0.4	2.5 ± 0.8	12.8 ± 1.7	83.9 ± 3.8
1st + 2nd shell, 220 K	1.7 ± 0.5	4.4 ± 0.9	17.1 ± 1.8	76.8 ± 4.1

D Melting point of ice in the nanopore

In the simulations, we observed melting of ice in the nanopore at 225 K but not at 220 K. We assign the melting point of ice in the pore to $T_m^{pore} = 222.5 \pm 2.5$ K. This is in excellent agreement with the $215 \leq T_m^{pore} \leq 231$ K predicted for $R = 1.5$ nm by the Gibbs–Thomson equation with the K_{GT} and d fitted from experiments in MCM-41 and SBA-15 pores.[5–7] The agreement with the experiments confirms that the depression in the melting point is determined by the properties of pure water and ice (well reproduced by the mW model), and not the details of the water–pore interaction.[11] It is not possible to determine K_{GT} and d from a single pore radius. Nevertheless, we note that the amount of water in the pore, about one monolayer ($d \sim 0.35$ nm) at $T_f^{pore} = 195$ K, increased to about two monolayers at 220 K. Table 1 shows that the total fraction of liquid in the pore increased from 37% at 195 K to 51% at 220 K, and that the fraction of liquid in the water layer that contacts the pore wall increased from 71.3% at 195 K to 83.9% at 220 K. Moreover, at 220 K the liquid makes up $\frac{3}{4}$ of the total water in the first plus second layer combined, $d < 0.55$ nm from the surface of the pore. The width of the liquid layer observed in the simulation just below T_m^{pore} is $\sim$0.5 nm, in good agreement with the 0.35–0.6 nm obtained from the fit of the experimental T_m^{pore} to the modified Gibbs–Thomson equation.[5–7] The observed increase in the amount of liquid in equilibrium with the pore as the temperature approaches the melting point confirms the conjecture of Liu *et al.*[13] of an interfacial region where water reversibly converts to a disordered form of ice (that we call interfacial ice) at lower temperatures. Premelting has been observed for other liquids confined by cylindrical nanopores and simple models predict a continuous increase of the liquid layer on heating followed by a sharp transition at T_m^{pore}.[53]

The enthalpy of melting of water in the nanopore was 42% of the bulk value. A comparable reduction in the value of the enthalpy of fusion has been reported in experimental studies.[6,8] The ratio $\Delta H_m^{pore}/\Delta H_m^{bulk}$ observed in this work agrees quantitatively with that of ref. 8 for a 3 nm diameter MCM-41 pore, but it is larger than that reported in ref. 6 for the same diameter pore. It should be noted that these two works differ in the assignment of the size of the pore: while $R = 1.5$ nm could correspond to MCM-41 C12 according to ref. 6, that diameter would be intermediate between those of MCM-41 C14 and MCM-41 C16 according to ref. 8. The reduction in the enthalpy of melting we observe is consistent with the lower fraction of ice in the pore, about 50% of the total amount of confined water.

5. Conclusions

In this work, molecular simulations were used to determine the existence and location of liquid water in crystallized nanopores, the structure of the nanoconfined ice, and the microscopic mechanism of nucleation and growth of ice in the pores. To the best of our knowledge, this is the first simulation study that reports the nucleation and structure of ice in hydrophilic nanopores. The main challenges to this endeavor have been the difficulty in nucleating ice in simulations and a lack of a simple rotationally invariant methods to identify ice and its polymorphs. In this work, we surmounted the first through the use of an accurate and efficient coarse-grained model of water and the second through the development of a simple method to classify each molecule as belonging to liquid, hexagonal, cubic or interfacial ice based on the number of staggered and eclipsed water–water intermolecular bonds with its four closest neighbors.

The equilibrium melting temperature of the confined ice in the 3 nm pore with water walls is in excellent agreement with the experimental melting point in MCM-41 silica with the same pore diameter. This may either indicate that the interactions of water with a water wall and with a silica wall are similar, or that the ice–liquid equilibrium temperature is not very sensitive to the details of the water–pore interaction. The latter possibility is supported by the results of Findenegg and coworkers on surface modified SBA-15.[11] Determination of the melting temperature for other water–pore potentials is necessary to clarify the weights of the two arguments.

The simulations confirm conjectures on the existence of a liquid layer at the surface of the pore and its widening as the temperature approaches the melting point.[13] At 220 K, about 3 K below the melting point, the liquid encompasses two water layers, while at 195 K, the freezing temperature, the liquid extends over one monolayer. The water–water and water–wall interactions are identical in this study, thus the formation of a premelted layer does not arise from a difference in interactions but from the fact that the liquid can accommodate better to the structure of the wall than the crystal. For surfaces that present strong water absorption, known to be the case in titania nanopores,[54] the wall will be paved with an additional adsorbed water layer—thus essentially making it a narrower pore with a water surface, as the one considered in this study. The situation may be different for partially wetting and non-wetting interfaces, for which the formation of a liquid layer at the pore surface may not offer a free energy advantage.

The nucleation of ice in the pore is homogeneous: the pore wall surface does not assist in the formation of the ice

crystallites; it does not even wet the nuclei. From the analysis of the largest ice nucleus *vs.* time in the isothermal crystallization trajectories and the quenching runs, we estimate that the critical nucleus contains $\sim$75 to 100 molecules and its radius of gyration is $\sim$1.0 nm, close to the 1.5 nm radius of the pore, thus hindering nucleation. The effect should be more pronounced for narrower pores, for which crystallization is not observed in the experiments.[6,11] Stacking layers become apparent in nuclei of $\sim$150 molecules, and their orientation is maintained when these crystallites grow, giving rise to varied assortments of crystal orientations with respect to the axis of the pore. The nanoconfined ice is rich in stacking faults, in agreement with the interpretation of X-ray diffraction of Morishige and Uematsu,[20] and neutron diffraction of Dore and coworkers.[13–15] We find a 2 : 1 ratio of cubic to hexagonal layers in the confined ice. This is the same ratio derived from the neutron diffraction spectra of ice I recovered by decompression of ice V.[17] A difference, however, is the abundance of both growth and deformation faults in the confined ice, while the former are absent in the bulk ice. In spite of the relative abundance of cubic layers, the confined ice should not be considered a cubic ice with defects: *Ic* (and *Ih*) domains with more than three layers are rare in this narrow pore.

The results and insights from NMR, DSC, neutron and X-ray diffraction experiments and simulations are complementary and yield a more complete picture of the state of water in nanoporous materials. This work shows the suitability of coarse-grained simulations with the mW model in describing the phase behavior and structure of water in crystallized nanopores. The very good agreement between the simulations of water confined in a pore with water walls and the experiments reported for water in nanoporous silica suggests that either the details of the wall–water interaction potential have small effect on the ice-structure and liquid–ice equilibrium in nanopores or that the interactions of water with a silica wall and a water wall are similar. These are both interesting possibilities that we will investigate in the future.

Acknowledgements

This work was supported by the Beckman Young Investigator Program (V.M.) and a collaborative research grant of the Agencia Nacional de Promoción Científica y Tecnológica de Argentina (V.M. and D.S.) K.W. acknowledges a student fellowship from DAAD and the exchange program at TU-Braunschweig for supporting his stay at the University of Utah. We thank the Center of High Performance Computing of the University of Utah for allocation of computing time.

References

1 C. Alba-Simionesco, B. Coasne, G. Dosseh, G. Dudziak, K. E. Gubbins, R. Radhakrishnan and M. Sliwinska-Bartkowiak, *J. Phys.: Condens. Matter*, 2006, **18**, R15.
2 I. Brovchenko and A. Oleinikova, *Interfacial and Confined Water*, Elsevier, Amsterdam, 2008.
3 I. Shenderovich, G. Buntkowsky, A. Schreiber, E. Gedat, S. Sharif, J. Albrecht, N. Golubev, G. Findenegg and H. Limbach, *J. Phys. Chem. B*, 2003, **107**, 11924.
4 I. G. Shenderovich, D. Mauder, D. Akcakayiran, G. Buntkowsky, H.-H. Limbach and G. H. Findenegg, *J. Phys. Chem. B*, 2007, **111**, 12088.
5 R. Schmidt, E. Hansen, M. Stöcker, D. Akporiaye and O. Ellestad, *J. Am. Chem. Soc.*, 1995, **117**, 4049.
6 S. Jahnert, F. V. Chavez, G. E. Schaumann, A. Schreiber, M. Schonhoff and G. H. Findenegg, *Phys. Chem. Chem. Phys.*, 2008, **10**, 6039.
7 A. Schreiber, I. Ketelsen and G. H. Findenegg, *Phys. Chem. Chem. Phys.*, 2001, **3**, 1185.
8 S. Kittaka, S. Ishimaru, M. Kuranishi, T. Matsuda and T. Yamaguchi, *Phys. Chem. Chem. Phys.*, 2006, **8**, 3223.
9 K. Morishige and K. Kawano, *J. Chem. Phys.*, 1999, **110**, 4867.
10 K. Morishige, H. Uematsu and N. Tateishi, *J. Phys. Chem. B*, 2004, **108**, 7241.
11 G. H. Findenegg, S. Jaehnert, D. Akcakayiran and A. Schreiber, *ChemPhysChem*, 2008, **9**, 2651.
12 J. B. W. Webber, J. C. Dore, J. H. Strange, R. Anderson and B. Tohidi, *J. Phys.: Condens. Matter*, 2007, **19**, 415117.
13 E. Liu, J. C. Dore, J. B. W. Webber, D. Khushalani, S. Jähnert, G. H. Findenegg and T. Hansen, *J. Phys.: Condens. Matter*, 2006, **18**, 10009.
14 J. Seyed-Yazdi, H. Farman, J. C. Dore, J. B. W. Webber and G. H. Findenegg, *J. Phys.: Condens. Matter*, 2008, **20**, 205108.
15 J. Seyed-Yazdi, H. Farman, J. C. Dore, J. B. W. Webber, G. H. Findenegg and T. Hansen, *J. Phys.: Condens. Matter*, 2008, **20**, 205107.
16 W. F. Kuhs, D. V. Bliss and J. L. Finney, *J. Phys. Colloques*, 1987, **48**, 631.
17 T. C. Hansen, M. M. Koza and W. F. Kuhs, *J. Phys.: Condens. Matter*, 2008, **20**, 285104.
18 T. C. Hansen, A. Falenty and W. F. Kuhs, "Modelling ice *Ic* of different origin and stacking faulted hexagonal ice using neutron powder diffraction data", in *Physics and Chemistry of Ice*, ed. W. F. Kuhs, RSC Publishing, Royal Society of Chemistry, Cambridge, 2006, p. 201.
19 T. C. Hansen, M. M. Koza, P. Lindner and W. F. Kuhs, *J. Phys.: Condens. Matter*, 2008, **20**, 285105.
20 K. Morishige and H. Uematsu, *J. Chem. Phys.*, 2005, **122**, 044711.
21 M. Matsumoto, S. Saito and I. Ohmine, *Nature*, 2002, **416**, 409.
22 L. Vrbka and P. Jungwirth, *J. Phys. Chem. B*, 2006, **110**, 18126.
23 K. Koga and H. Tanaka, *J. Chem. Phys.*, 2005, **122**, 104711.
24 K. Koga, H. Tanaka and X. C. Zeng, *Nature*, 2000, **408**, 564.
25 K. Koga, X. C. Zeng and H. Tanaka, *Phys. Rev. Lett.*, 1997, **79**, 5262.
26 P. Kumar, F. W. Starr, S. V. Buldyrev and H. E. Stanley, *Phys. Rev. E: Stat., Nonlinear, Soft Matter Phys.*, 2007, **75**, 011202.
27 N. Giovambattista, P. J. Rossky and P. G. Debenedetti, *Phys. Rev. Lett.*, 2009, **102**, 050603.
28 N. Giovambattista, P. J. Rossky and P. G. Debenedetti, *Phys. Rev. E: Stat., Nonlinear, Soft Matter Phys.*, 2006, **73**, 041604.
29 R. Zangi and A. E. Mark, *J. Chem. Phys.*, 2003, **119**, 1694.
30 R. Zangi, *J. Phys.: Condens. Matter*, 2004, **16**, S5371.
31 K. Koga, G. T. Gao, H. Tanaka and X. C. Zeng, *Nature*, 2001, **412**, 802.
32 R. Radhakrishnan and B. L. Trout, *J. Am. Chem. Soc.*, 2003, **125**, 7743.
33 A. V. Brukhno, J. Anwar, R. Davidchack and R. Handel, *J. Phys.: Condens. Matter*, 2008, **20**, 494243.
34 D. Quigley and P. M. Rodger, *J. Chem. Phys.*, 2008, **128**, 154518.
35 H. Tanaka and I. Okabe, *Chem. Phys. Lett.*, 1996, **259**, 593.
36 R. G. Fernandez, J. L. F. Abascal and C. Vega, *J. Chem. Phys.*, 2006, **124**, 144506.
37 C. Vega, E. Sanz and J. L. F. Abascal, *J. Chem. Phys.*, 2005, **122**, 114507.
38 C. Vega, J. L. F. Abascal, E. Sanz, L. G. MacDowell and C. McBride, *J. Phys.: Condens. Matter*, 2005, **17**, S3283.
39 J. L. F. Abascal, E. Sanz, R. G. Fernandez and C. Vega, *J. Chem. Phys.*, 2005, **122**, 234511.
40 V. Molinero and E. B. Moore, *J. Phys. Chem. B*, 2009, **113**, 4008.
41 E. B. Moore and V. Molinero, *J. Chem. Phys.*, 2009, **130**, 244505.
42 L. C. Jacobson, W. Hujo and V. Molinero, *J. Phys. Chem. B*, 2009, **113**, 10298.
43 W. Zhang, C. He, J. Lian and Q. Jiang, *Chem. Phys. Lett.*, 2006, **421**, 251.

44 P. J. Steinhardt, D. R. Nelson and M. Ronchetti, *Phys. Rev. Lett.*, 1981, **47**, 1297.
45 P. R. Ten Wolde, M. J. Ruiz-Montero and D. Frenkel, *J. Chem. Phys.*, 1996, **104**, 9933–9947.
46 S. J. Plimpton, *J. Comput. Phys.*, 1995, **117**, 1.
47 J. R. Errington and P. G. Debenedetti, *Nature*, 2001, **409**, 318.
48 L. S. Ramsdell, *Am. Mineral.*, 1947, **32**, 64.
49 C. A. Angell, *Annu. Rev. Phys. Chem.*, 2004, **55**, 559.
50 P. G. Debenedetti, *J. Phys.: Condens. Matter*, 2003, **15**, R1669.
51 E. B. Moore and V. Molinero, Liquid–liquid transformation in water controls the temperature of homogeneous nucleation of ice, manuscript in preparation.
52 O. Yamamuro, M. Oguni, T. Matsuo and H. Suga, *J. Phys. Chem. Solids*, 1987, **48**, 935–942.
53 D. Wallacher and K. Knorr, *Phys. Rev. B: Condens. Matter Mater. Phys.*, 2001, **63**, 104202.
54 E. Mamontov, D. J. Wesolowski, L. Vlcek, P. T. Cummings, J. Rosenqvist, W. Wang and D. R. Cole, *J. Phys. Chem. C*, 2008, **112**, 12334.

Chapter 5

LIQUID-ICE COEXISTENCE BELOW THE MELTING TEMPERATURE IN HYDROPHILIC AND HYDROPHOBIC NANOPORES

Abstract

Nanoconfined water exhibits freezing and melting temperatures typically lower that that of bulk water. The melting point depression for confinement within cylindrical nanopores is often described in terms of an inverse relationship with the pore radius, where smaller pore radii are found to have larger melting temperature depressions. However, the effect of the interaction strength between the pore wall and the confined water on phase changes is unclear. In the case of melting, it is unclear how the nature of the pore wall affects the liquid-ice coexistence below the melting temperature in confinement. In this chapter, we study the effect of the interaction strength between the pore wall and the confined fluid on the melting temperature for the case of water confined within nanopores of varying hydrophilicity/hydrophobicity. Using molecular dynamics simulations with the mW water model, we examine the liquid-ice coexistence and melting temperature of water confined within strongly hydrophobic to strongly hydrophilic 4 nm diameter cylindrical pores. We find that the water-pore interaction strength affects the width of the liquid layer and that the radius of the confined ice corresponds to the melting temperature, rather than the radius of the pore.

Introduction

Understanding the behavior of substances in confinement has practical relevance in biological systems and in the design of nanomaterials,[1,2] as well as fundamental importance in clarifying finite size and surface force effects on phase transitions.[1] In comparison to bulk systems, confinement typically leads to decreases in the freezing and melting temperatures,[3-6] though in some cases the opposite is possible.[7] Differences in the temperature of phase transitions from the bulk result from the high surface to volume ratio present within confined systems.[2,8] Of particular interest is the effect of the nature of the confining material on the phase transitions of the confined substance.

In this chapter, we study the effect of changing the water-pore interactions of cylindrical nanopores, from strongly hydrophobic to hydrophilic, on the melting temperature of ice. Experimental studies of cylindrical nanopores typically utilize hydrophilic nanoporous silica, SBA-15 and MCM-41, which allow for pore radius selection from 1 nm to 4 nm (MCM-41) and from 2.5 up to 5 nm (SBA-15).[6] Ice melting and freezing temperatures are lower than in bulk water, decreasing as the pore radius is decreased.[9,10] The melting point depression can be described by a modified Gibbs-Thomson equation, $\Delta T_m = -K_{GT}/(R-d)$, where K_{GT} is the Gibbs-Thomson constant, R is the radius of the pore and d is the width of a liquid layer that wets the pore wall.[2,6] $K_{GT} = 2T_m^{bulk}\gamma_{ice\text{-}liq}V_{liq}/\Delta H_m$, where T_m^{bulk} is the bulk melting temperature, $\gamma_{ice\text{-}liq}$ is the liquid-ice surface tension, V_{liq} is the molar volume of the liquid phase and ΔH_m is the enthalpy of melting of the ice phase.[11] This constant was found to be 52.4 K nm when using values for bulk water.[5] Similar values, ranging from 49.5 ± 2 K nm[4] to 52.4 ± 0.6 K nm[6] have been determined from fits to the modified Gibbs-Thomson equation using data from silica nanopores. For the case of water, radii above 5 nm have the same melting temperature as water in bulk,[6] while pores less than ~1.5 nm in diameter, extreme confinement, do not exhibit a first order melting transition.[6,11] For water confined within pores having a

radius intermediate between extreme confinement and bulk-like behavior, experimentally determined melting temperatures from silica pores have been fit to the modified Gibbs-Thomson equation with d ranging from 0.35 ± 0.04 nm[12] up to 0.60 ± 0.01 nm.[6]

It is currently unclear what effect the chemical nature of the pore wall has on the melting temperature depression and the state of water in the pore.[6] Findenegg and coworkers used calorimetry to study the melting of ice in SBA-15 pores functionalized with carboxylic acid, sulfonic acid or phosphonic acid.[6] They found that the melting temperature was minimally affected by changes in the surface-modifier, suggesting a weak dependence of the melting point on the water-pore interactions. Analysis of the melting temperature depression of MCM-41 nanopores with hydrophobic groups of the type R-N^+-$(CH_3)_3$ where the R groups range from C_8H_{17} to $C_{18}H_{37}$,[13] suggest no difference in melting temperature above a pore radius of 3 nm. From a radius of 3 nm down to 2.5 nm, the melting temperature of the hydrophobic pores is as much as 12 K lower than the undecorated MCM-41 pores with the same radius, though melting within individual pores was spread out over a temperature of more than 10 K.[13]

Below the melting temperature, there exists a premelted layer of liquid water at the surface of ice, in bulk as well as in confinement.[14] Within nanopores, the width of the liquid layer cannot be determined directly, with reported values being obtained from fits of the melting temperature to the modified Gibbs-Thomson equation.[15] Unfortunately, this only provides the width of the liquid layer at the melting temperature, assuming the K_{GT} constant and the determination of the pore radius is accurate, and provides no insight into the temperature dependence of the liquid layer width in confinement.

In this chapter, we will investigate the effect of the water-pore interaction on the melting temperature, and the coexistence of liquid and ice in the nanopores using molecular dynamics simulations using the mW water model.

Methods

Nanopore Models

Nanopores were built as described in chapter 4, with the same T-shape and 1 nm head block, with the cylindrical opening within the pores having a radius of 2 nm. This resulted in systems containing 12,288 molecules, with 5,439 molecules forming the pore wall and 6,849 water molecules found within the pore and the head block. The length of the nanopore is 11.5 nm, not including the head block.

Force Fields

Water was modeled using the coarse-grained mW water potential, as described in chapter 2. The particles that form the pore walls were modeled using the same form and constants of the mW water potential, with pore-pore interactions the same as water-water interactions. For the water-pore interactions σ, λ and ε were changed, while all other constants remained the same as in the mW potential. Changing the characteristic size σ_{wp} to 3.2 Å minimized diffusion of water molecules into the pore wall while changing λ_{wp} to 0.0 maintained that no particular orientational preference was encouraged, no hydrogen bonding, between the water molecules and molecules that formed the pore wall. To vary the strength of the water-pore interactions, ε_{wp} was set to 0.1 kcal mol^{-1}, 0.2 kcal mol^{-1}, 0.3 kcal mol^{-1}, 0.5 kcal mol^{-1} or 1.0 kcal mol^{-1}. In a sixth case, the water-pore interactions were set to water-water, with ε_{wp} of 6.189 kcal mol^{-1}, σ_{wp} = 2.3925 and λ = 23.15, the same as in chapter 4.

Simulation Protocol

Using LAMMPS,[16] molecular dynamics simulations were carried out in the isothermal-isobaric ensemble, with equations of motion integrated with the Velocity

Verlet algorithm with a timestep of 10 fs. The temperature was controlled with the Nose-Hoover thermostat, with a relaxation time of 0.5 ps. The Nose-Hoover barostat was used to control the pressure, 1 atm for all simulations, with a time constant of 2.5 ps. The expansion/contraction of the simulation cell in the x and y dimensions were coupled. Due to the anisotropy of the system, the z dimension was allowed to dilate and contract independently. The systems were simulated with periodic boundary conditions. The isothermal simulations were performed at temperatures ranging from 190 K to 260 K, long enough for equilibration of the water within the pore, requiring up to 200 ns at each state point. The CHILL algorithm, described in the previous chapter, was used to distinguish between core ice, interfacial ice and liquid water.

The pore with ε_{wp} = 0.1 kcal mol^{-1} is strongly hydrophobic, resulting in expulsion of the liquid from the pore rapidly upon melting. Because of this, we were able to study this particular pore up to the melting temperature, but not at higher temperatures.

Starting Configuration

Each simulation was started with the same structure, consisting of annealed ice within the pore, shown in Figure 5.2. To make the starting structure, a nanopore with water-pore interactions set to water-water containing liquid water was allowed to freeze at 190 K. The system was then annealed for 100 ns at 220 K until the only liquid water remaining was a monolayer wetting the pore wall.

Hydrophilicity/Hydrophobicity of Nanopores

Contact Angle. To assess the hydrophilicity/hydrophobicity for each water-wall interaction strength, ε_{wp}, we performed simulations of water nanodroplets on a stationary plate with the water-wall interactions the same as the water-pore interactions used in the nanopore simulations, Figure 5.1. The droplets consisted of water molecules

modeled with the mW model. The plate consisted of 3785 stationary mW water molecules in a structure corresponding to an instantaneous configuration of liquid water at 298 K. The simulations were done at constant volume (with enough room to prevent interactions between replicas of the droplet due to periodic boundary conditions) at 298 K. Each NVT simulation was run for 20 ns.

Adsorption Energy. The adsorption energy for the hydrophilic pores was determined as in Ref. [17], computing the average interaction energy between water and pore over 25 ns simulations of nanopores 10% filled with water, for which the water-water interaction was turned off to efficiently sample the energy of adsorption at the limit of very low water content.

Radial Density Profiles

We computed histograms of the number of water molecules classified as core ice (cubic and hexagonal ice), interfacial ice, liquid or pore wall, binned every 0.2 Å from the center of the pore along the pore and averaged over the length of the simulation. The histograms were normalized by the volume of the cylindrical bins.

Results

Using molecule dynamics simulations of nanopores 11.5 nm in length with a cylindrical cavity 4 nm in diameter filled with water, we vary the strength of the water-pore interactions to determine the effect of hydrophobic and hydrophilic interactions on the melting temperature, amount of liquid in coexistence with ice and the mechanism of melting.

We determine whether each pore is hydrophilic or hydrophobic from the contact angle of a nanodroplet of water on a planar surface with the same water-surface interactions as the water-pore interactions. To compare the strength of the

hydrophilicity for pores with hydrophilic water-pore interactions, we calculated the surface adsorption energy for each pore wall. Figure 5.1 shows the adsorption energies and the contact angles for the various nanopores used in this study. The transition from hydrophobic to hydrophilic is identified by a change in contact angle to less than 90° between droplet and plate. The hydrophilicity increases with water-pore attraction: $\varepsilon_{wp} \leq$ 0.3 kcal mol^{-1} corresponds to hydrophobic pores and $\varepsilon_{wp} >$ 0.3 kcal mol^{-1} to hydrophilic pores. Throughout this chapter, comparisons will be made to that of a pore with water-pore interactions equal to that of water-water interactions, which has an adsorption energy of 6.83 ± 0.08 kcal mol^{-1}, in comparison to the adsorption energy of 5.63 ± 0.08 kcal mol^{-1} and 1.68 ± 0.09 for ε_{wp} = 1.0 and ε_{wp} = 0.5 kcal mol^{-1}, respectively.

Melting Temperature

We conducted isothermal simulations with water-pore interactions from i) ε_{wp} = 0.1 kcal mol^{-1} (strongly hydrophobic, sufficient to cause expulsion of the liquid from the pore immediately upon melting) to ε_{wp} = 1.0 kcal mol^{-1} (strongly hydrophilic), and ii) a pore with ε_{wp} and other parameters equal to that of water. Each filled pore was simulated between 190 K and 260 K, for up to 200 ns at each temperature. The simulations of all nanopores started from the same annealed ice structure, shown in Figure 5.2, with velocities randomized at the onset of each simulation. Data for the melting temperatures, obtained from the molecular dynamics simulations are shown in Figure 5.3. The melting temperatures were determined from the simulations by the appearance of a sharp increase in the fraction of liquid in the pore, from predominately ice to all liquid.

The simulations predict a melting temperature of 241 ± 1 K for the hydrophobic pore walls and for the hydrophilic pore with water-like wall-water interactions (shown in Figure 5.3). For the hydrophilic pore walls with ε_{wp} = 0.5 and 1.0 kcal mol^{-1}, the melting temperature decreases with increasing hydrophilicity to 236 ± 1 K and 227 ± 2 K,

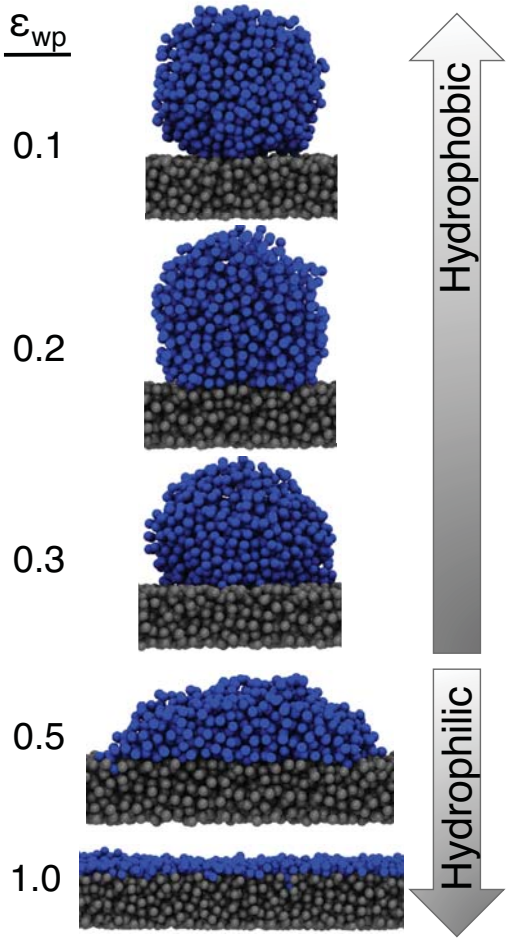

Figure 5.1 Hydrophilicity/Hydrophobicity of Water-Pore Interactions
The interaction strengths, ε_{wp} of the various nanopores used in this study are shown in units of kcal/mol. The results of simulations of a nanodroplet of water on a plate, with the plate consisting of stationary molecules in the configuration of an instantaneous snapshot of liquid water 298 K liquid, is shown. The change from hydrophilic to hydrophobic water-pore interaction occurs at ε_{wp} above 0.3 kcal mol^{-1}, when the contact angle, the angle from the surface of the plate to the surface of the droplet, becomes less than 90°.

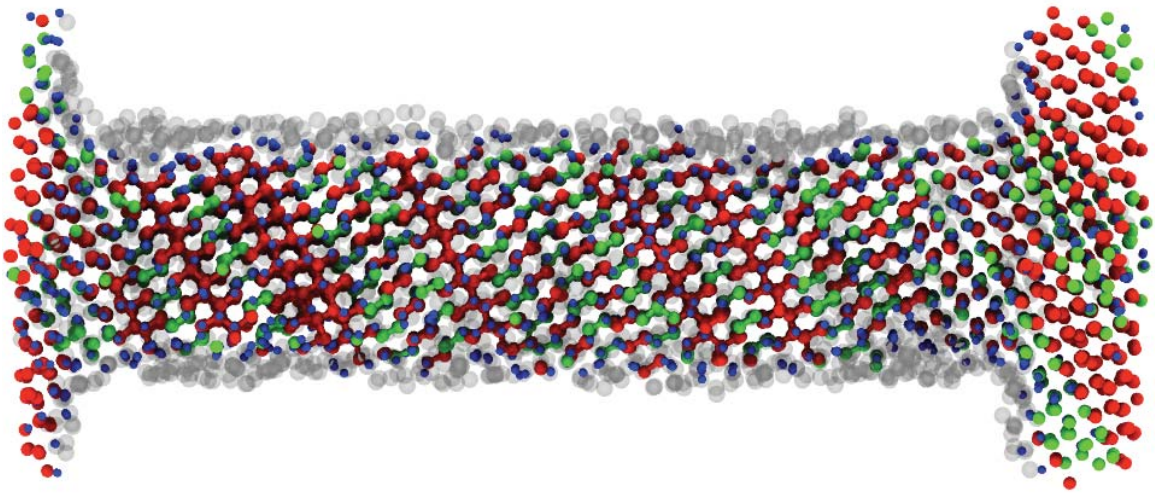

Figure 5.2 Annealed Ice
Each simulation started from the same annealed ice configuration. The contents of the pore and the head block are shown. Within the pore, excluding the end reservoir, the configuration consists of cubic ice (red) with hexagonal (green) stacking faults, surrounded by interfacial ice (blue) with a liquid monolayer (transparent grey) wetting the pore wall (not shown), for a total of 70% ice and 30% liquid. 'Bonds' are shown between molecules of the same type, cubic or hexagonal, that are within 3.5 Å distance.

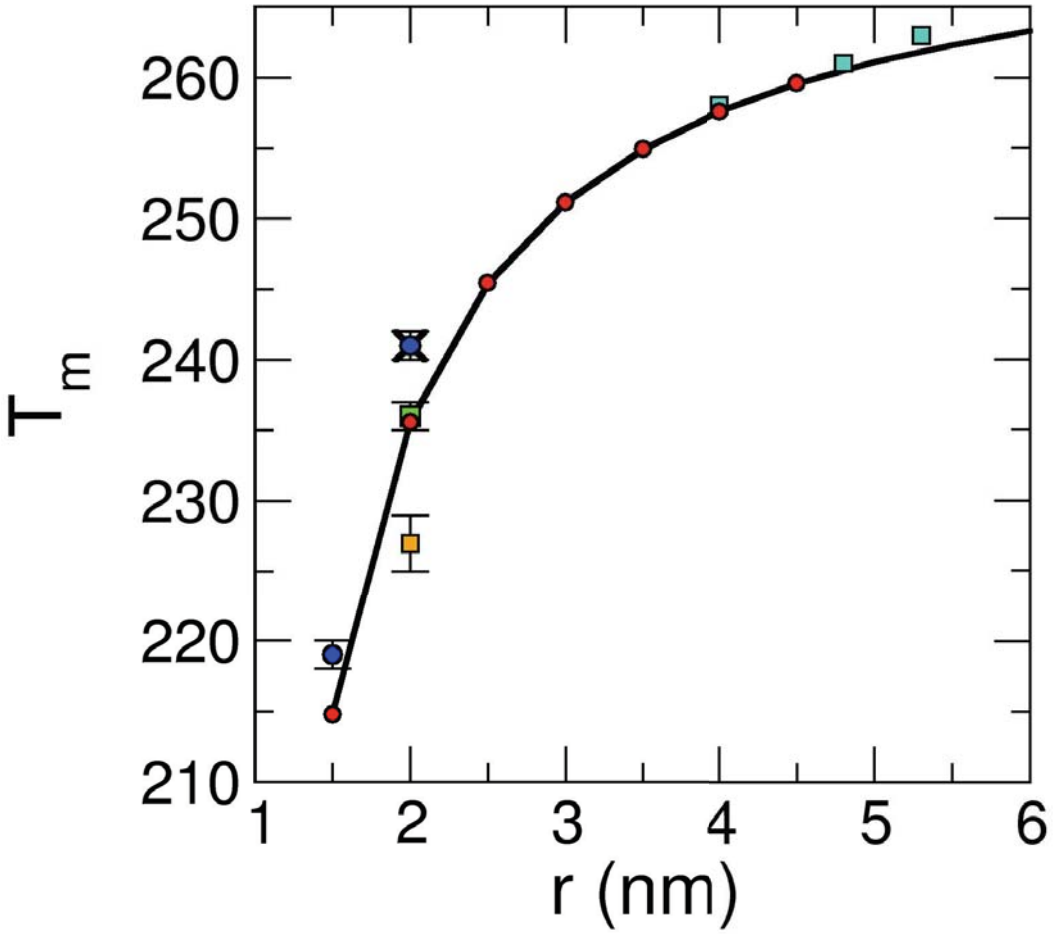

Figure 5.3 Melting Temperatures
The melting temperature versus pore radius is shown for the simulations (blue circles, green and orange squares and black X), the Gibbs-Thomson equation with d = 0.6 nm (solid line) and Ref. [6] experiments, water in silica nanopores (red circles) and water in acid functionalized silica nanopores (turquoise squares). From the simulations, the orange square corresponds to the melting temperature of the nanopore with ε_{wp} = 1.0 kcal mol^{-1}, green square corresponds to ε_{wp} = 0.5 kcal mol^{-1}, blue circles correspond to the pore made out of water and the black X corresponds to the pores with ε_{wp} = 0.1, 0.2 and 0.3 kcal mol^{-1} (melting temperatures overlap).

respectively. Melting temperatures of ice in silica pores determined by Findenegg et al.,[6] consistent with the modified Gibbs-Thomson fit using the same K_{GT} and with d = 0.60 ± 01 nm, are also shown in Figure 5.3. The hydrophobic and water-like pores have a melting temperature slightly above that found by Findenegg et al. for the 2 nm diameter silica pore, the pore with ε_{wp} = 1.0 kcal mol^{-1} has a lower melting temperature and the melting temperature for the pore with ε_{wp} = 0.5 kcal mol^{-1} is in excellent agreement.

As an initial approximation, we assume that the K_{GT} constant from the Gibbs-Thomson equation is independent of temperature and water-pore interaction strength. In this case, the results suggest that the hydrophobic nanopores and the water-like pore have a larger ice radius, R - d, corresponding to a thinner liquid layer wetting the pore wall than the pores with ε_{wp} = 0.5 and 1.0 kcal mol^{-1}. The pore with ε_{wp} = 0.5 kcal mol^{-1} would then have a liquid layer thickness of 0.6 nm at the melting temperature, while ε_{wp} = 1.0 kcal mol^{-1} has a thicker liquid layer. In the following section, we compare the liquid-ice coexistence across a range of temperatures, allowing for direct observation of the width of the liquid layer and ice core.

Liquid-Ice Coexistence

The modified Gibbs-Thomson equation provides an indirect measure of the thickness of liquid layer wetting the pore wall at the melting temperature. The width, d of the water layer obtained from fitting the experimental melting temperature in silica pores to the modified Gibbs-Thomson equation, as shown in Figure 5.3, predicts 44% of the water in the pore is liquid at the melting temperature, in excellent agreement with the 45 ± 2 % obtained from the simulations of the water-like pore at 240 K, just prior to melting. While accurate at the melting temperature for water-like pores, the modified Gibbs-Thomson equation does not provide any insight into how the liquid layer changes with temperature, or with water-pore interactions strength, which could effect the value

of K_{GT}. Studies of ice at a flat silica interface[14,18] as well as phenomenological models of premelting within cylindrical nanopores[10,19] show a strong temperature dependence on the width of the liquid. Using the results of the molecular dynamics simulations, we present here an analysis of the liquid layer at the water-pore interface across temperatures from 190 K up to the melting temperature.

Fraction of Liquid in Coexistence with Ice. Figure 5.4 shows the fraction of liquid inside the pore as a function of temperature for all the pores of this study. Each pore shows a similar trend. At 190 K, all pores have the lowest fraction of liquid water present through the temperature range 190-260 K. The slope of the curve around 190 K suggests that the fraction of liquid will not go to zero before vitrification occurs, likely around 150 K,[20] even for the most hydrophobic case. As the temperature increases up to 10 K from the melting point, the fraction of liquid increases modestly. Near the melting temperature, the increase in the fraction of liquid within the pore becomes more pronounced, increasing about 5 % in 10 K. Once the melting temperature is reached, the liquid fraction increases abruptly to one.

The coexistence of liquid and ice has been described using a phenomenological model,[10,19] in which the free energy for the melting and freezing of pure water within an infinite cylindrical pore with radius R_o, containing a cylindrical core of ice of radius R ($R_o - R$ is the thickness of the liquid layer) is given by,

$$F = \pi\rho_s R^2 \mu_s + \pi\rho_l \left(R_0^2 - R^2\right)\mu_l + 2\pi R\gamma_{sl} + 2\pi R\gamma_{lw} + 2\pi R_0\left(\gamma_{sw} - \gamma_{sl} - \gamma_{lw}\right)\exp\left(\frac{R - R_0}{\xi}\right) \quad (5.1)$$

where ρ_s and ρ_l are the number densities of the solid and the liquid, μ_s and μ_l are the chemical potential of the solid and the liquid, γ_{sw}, γ_{sl} and γ_{lw} are the interfacial tensions associated with the solid/liquid, solid/wall and liquid/wall interfaces. The first two terms correspond to the volume free energy of the liquid and ice, while the third and fourth term correspond to the solid/liquid and liquid/wall interfacial energies. The final term

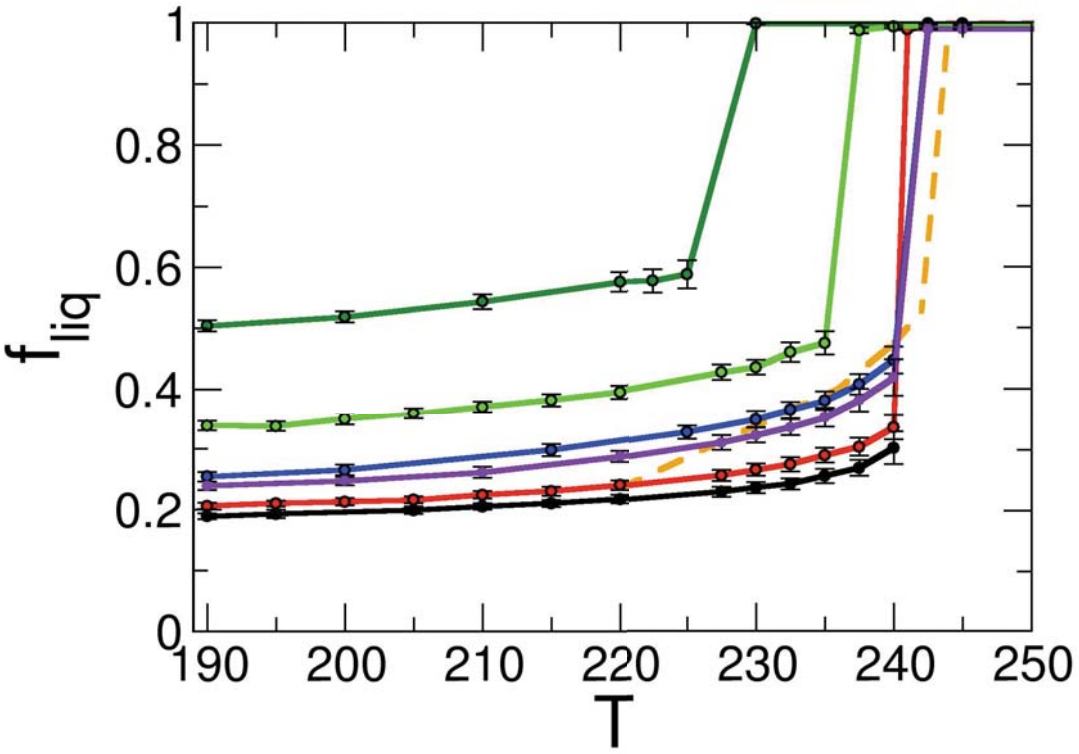

Figure 5.4 Fraction of Liquid
The fraction of liquid in the nanopores is shown as a function of temperature for all water-pore interaction strengths, ε_{wp} = 0.1 (black), 0.2 (red), 0.3 (purple), water (blue), 0.5 (light green), and 1.0 kcal mol^{-1} (dark green). Each point was obtained as an average of the fraction of liquid over the course of the simulations, from 50-200 ns in length. The error bars correspond to the standard deviation from the average. Dashed orange line corresponds to the predicted liquid fraction using the phenomenological model and water and water-pore interaction parameters of Ref. [19] for a pore of 2 nm radius.

corresponds to a short-range, exponential relationship, between the solid/liquid and the liquid/wall interfaces, with a correlation length, ξ.[10,19] Factoring out all terms that depend only on the constant, R_0 and substituting for the chemical potential a term dependent upon the mean enthalpy of fusion from T to the bulk melting temperature T^0,

$$\mu_s - \mu_l = \Delta_{fus} h \left(\frac{T - T^0}{T^0} \right) \tag{5.2}$$

results in the following equation for the free energy in terms of the radius of the cylindrical ice core,

$$F(R) = \pi \rho_s R^2 \Delta_{fus} h \left(\frac{T - T^0}{T^0} \right) + 2\pi R \gamma_{sl} + 2\pi R_0 \left(\gamma_{sw} - \gamma_{sl} - \gamma_{lw} \right) \exp\left(\frac{R - R_0}{\xi} \right). \tag{5.3}$$

From the global minima of the free energy as a function of R over a range of temperatures, the radius of the ice core and the radius of the liquid layer can be found, allowing for the determination of the total fraction of liquid. In general, this model predicts a continuous increase in the liquid layer upon heating, and a sharp transition upon reaching the melting temperature.

A direct comparison with predictions from this model to those found from our simulations is shown in Figure 5.4. Linear extrapolations of the enthalpy of fusion and the interfacial tensions were obtained from Ref.[21] as used in Ref. [19], assuming a hydrophilic pore like silica, where the value of γ_{sw} - γ_{sl} - γ_{lw} is positive as in the case where the liquid completely wets the pore wall. The correlation length obtained from the references is short, 0.17 nm. The model predicts an onset temperature of premelting near 198 K with a steep increase of the fraction of liquid up to the melting temperature at 242 K. While this is qualitatively similar to the simulation results, with a melting

temperature, T_m = 243 K, near that of the water-like pore and the hydrophobic pores, the model predictions show a stronger temperature dependence of the liquid fraction as evidenced by the higher slope of the liquid fraction curve below the melting temperature, with no liquid present at low temperatures. Increasing the hydrophilicity, i.e. increasing the value of $\gamma_{sw} - \gamma_{sl} - \gamma_{lw}$, increases the fraction of liquid within the pore leading to a lower melting temperature, while a negative value of $\gamma_{sw} - \gamma_{sl} - \gamma_{lw}$, as in the case of a hydrophobic pore, decreases the fraction of liquid present and increases the melting temperature. In the following section, we look more closely at the width of the liquid layer and core ice as a function of temperature and water-pore interaction strength.

Experimental analysis of the temperature dependence of the width of the liquid layer for an ice/silica flat surface shows temperature dependent logarithmic growth, with large increases within 10 K of the melting temperature.[6,14] This is precisely what we observe, though with one notable difference being a continuous presence of liquid layer for all temperatures in the simulations, rather than onset of a premelted layer at a specific temperature. The simulations used in this study were equilibrated for up to 200 ns and the fraction of liquid remained consistent, though it is possible that longer simulations could result in the eventual freezing of the liquid layer in the lower range of temperatures analyzed.

Width of the Liquid Layer. We now describe the width of the liquid layer as a function of temperature over various water-pore interaction strengths. In Figure 5.5 we show snapshots, side and top view, of all pores except ε_{wp} = 0.2 kcal mol^{-1} showing the liquid layer, interfacial ice and core ice (cubic ice with hexagonal stacking faults) at 190 K and 240 K. All pores show a central region consisting of core ice with an outer layer of interfacial ice (having structure intermediate between that of cubic and hexagonal ice)

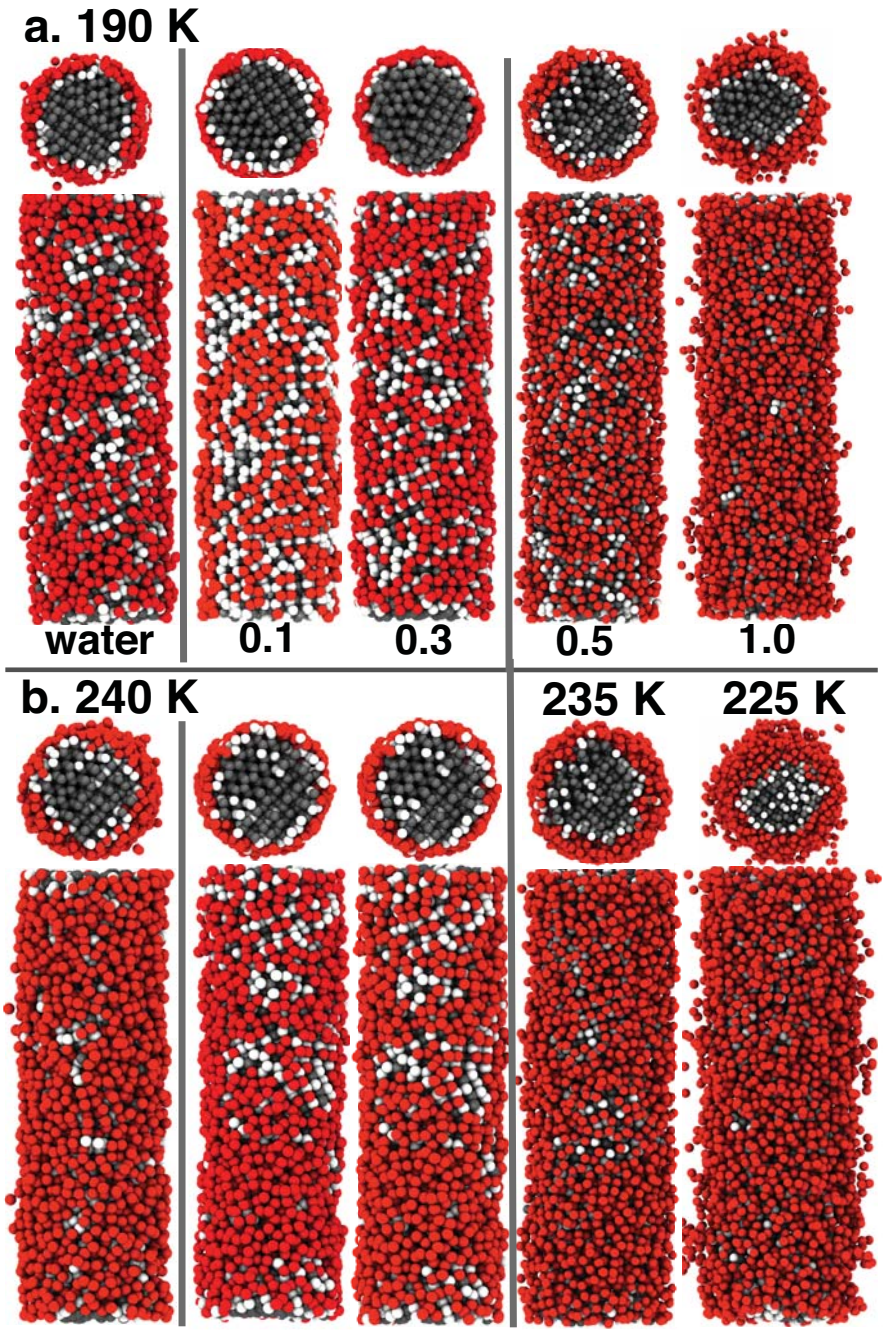

Figure 5.5 Liquid Layer Thicknesses
Snapshots showing the state of water inside nanopores with ε_{wp} = 0.1, 0.3, 0.5, 1.0 kcal mol^{-1} at a) 190 K and b) just below the melting temperature. For comparison, the pore made out of water is also shown. Core ice (hexagonal and cubic) is shown in grey, interfacial ice in white and the liquid layer in red. The pore walls are not shown.

and a final outer layer consisting of liquid. Notice the decreasing patchiness of the liquid found at each temperature upon decreasing the hydrophobicity. Nearly 20% of the water within the pore with ε_{wp} = 0.1 kcal mol^{-1} is liquid at 190 K, though there are a significant number of patches of water in contact with the pore wall without a liquid layer present. For the most hydrophilic case, with ε_{wp} = 1.0 kcal mol^{-1} there is significant layering of the liquid at the surface, from two layers at 190 K to more than three layers just below the melting temperature.

To provide a better cross-sectional view of the location of the core ice, interfacial ice and liquid layers, Figure 5.6 shows a plot of the radial density of the core ice, interfacial ice, liquid layer and the pore wall for the strongly hydrophobic pore, the pore made out of water and the hydrophilic pores. In each case, the core ice fills the innermost region of the pore, with a slight amount of interfacial ice, up to 1.25-1.5 nm from the center of the pore. Between the core ice and the pore wall, there is a small amount of interfacial ice and varying amounts of liquid. At a temperature just below the melting temperature, the outer layer of ice decreases, with corresponding growth in the amount of liquid. The amount of interfacial ice found between the core ice and the pore wall remains the same or slightly decreases at the higher temperature.

For the water-pore interactions without hydrogen bonding (all simulations except for the water-water pore), increasing the strength of the interaction decreases the melting temperature. Comparing Figure 5.6 panels a, c and d, the radius of the ice core for the hydrophobic pore just below the melting temperature, panel a, is about 1.4 nm as judged from the width at half of the maximum of density, 0.4 g cm^{-3}. The hydrophilic pores with water-pore interactions having no preference for tetrahedral structure (the result of no hydrogen bonding), panels c and d, have ice core radii of about 1.2 and 1 nm. Comparing the pore with water-water interactions, in which the potential has a preference for tetrahedral interactions, Figure 5.6 panel b, the melting temperature is the

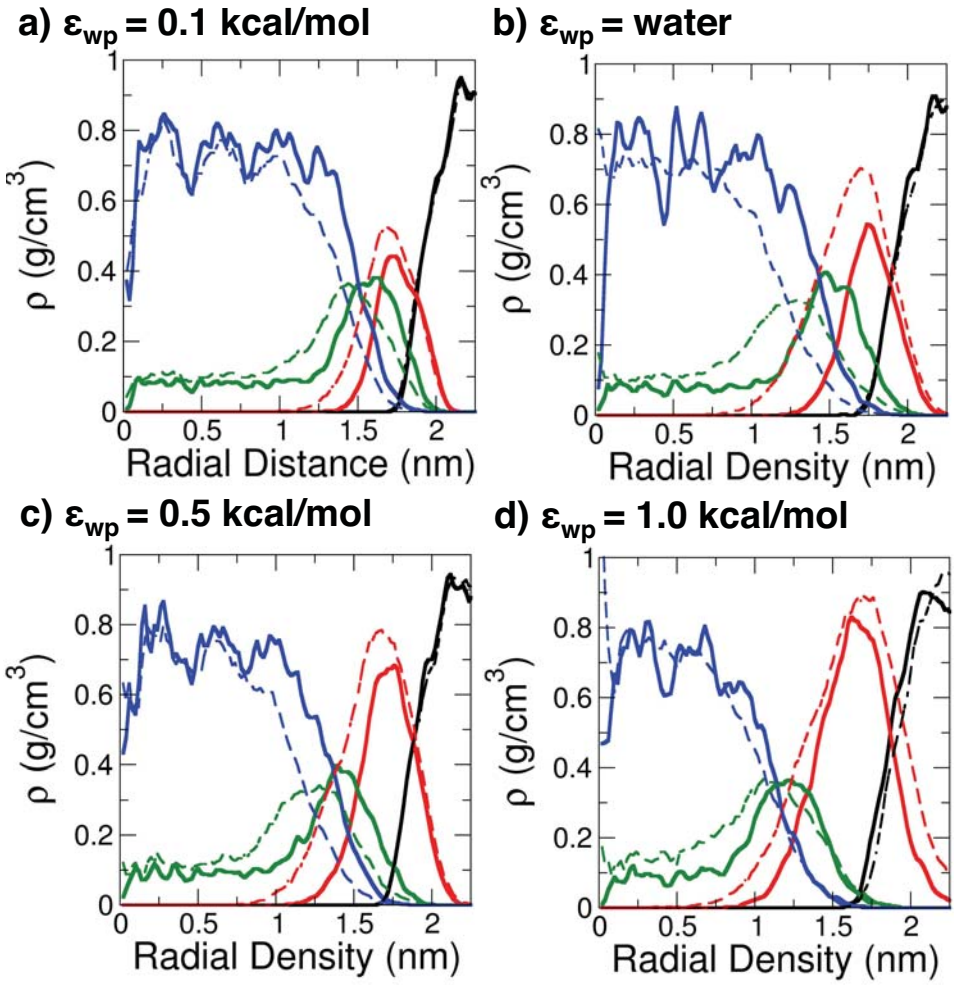

Figure 5.6 Radial Density Distributions of Liquid and Ice
The radial density for molecules that form the pore wall (black), liquid water (red), interfacial ice (green) and core ice (blue) is shown. For comparison, distributions are shown at 190 K (solid lines) and just below the melting temperature (dashed lines).

same as the case of the hydrophobic pore, while the radius of the core ice, 1.2 nm, is less than that of the hydrophobic pore, suggesting that the presence of hydrogen bonding between the water within the pore and the pore wall decreases the interfacial tension and acts to stabilize the core ice.

Mechanism of Ice Melting

Melting of the core ice occurs through continued growth of the liquid layer, at the expense of the ice. Figure 5.7 shows snapshots of the melting of core ice for the case of the pore made out of water at 242 K, the lowest temperature for which melting is observed for this water-pore interaction strength. Starting from the initial configuration, Figure 5.5 panel a, there is only a single monolayer of liquid wetting the pore wall. As the temperature increases, the thickness of the liquid layer increases from a patchy monolayer to a monolayer with patches of bilayer, see Figure 5.2. At and above the melting temperature, the bilayer regions increase, resulting in the eventual dissolution of the core ice region completely.

Conclusions

Using molecular dynamics simulations of nanopores with a radius of 2 nm and varying the strength of the water-pore interactions from strongly hydrophobic to strongly hydrophilic, we study the liquid-ice coexistence from 190 K up to the melting temperature and the effect of water-pore interaction strength on the melting temperature.

We find that even at the lowest temperature studied there exists a premelted layer. The width of the premelted layer is the least for the hydrophobic pores, while increasing the water-pore interaction strength increases the liquid layer width. Upon warming the nanopore, the width of the liquid layer increases, with the largest increases

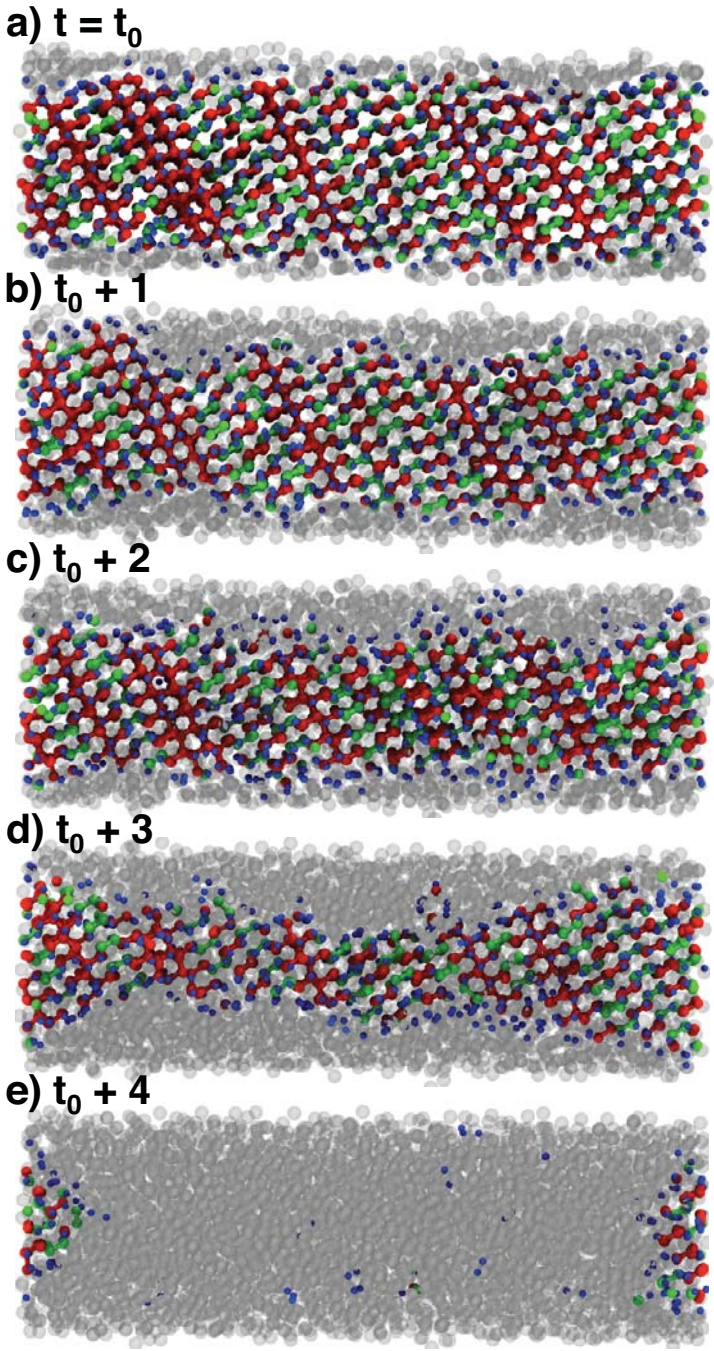

Figure 5.7 Melting
The nanopore made out of water as it melts at 242 K. The core ice, shown with cubic ice (red) and hexagonal ice (green) begins as stacking faulted region filling the majority of the pore. The interfacial ice (blue) surrounds the core ice and the liquid (transparent grey) wets the pore wall (not shown). At this temperature, the melting occurs rapidly, within 4 ns of the start of the isothermal simulation. The starting configuration is shown in panel a, followed by the next 4 ns at 1 ns intervals. Melting within the pore is complete by panel e, though the water within the head block (not shown), which has a melting temperature of bulk water, remains crystalline, leading to some remaining crystal in contact with the head pore at either end of the pore.

occurring within 10 K of the melting temperature, consistent with experimental analysis of water on a flat surface.[6,14]

The melting temperature was the same for all hydrophobic pores, 241 ± 1 K, consistent with the similarity in ice core radius observed for these pores. Analysis of the effect of water-pore strength on melting temperature in partially filled 1.5 nm radius pores, using analogous molecular dynamics simulations with the mW water model,[22] shows no difference between melting temperatures of hydrophobic pores and water-water pores, same as shown here for the completely filled pores, suggesting that the minimal effect of the hydrophobic pores on the melting temperature, in comparison to the pores made out of water, persists at smaller pore radii. The hydrophilic pores without hydrogen bonding water-pore interactions had melting temperatures that decreased with increasing water-pore interaction strength, 236 ± 1 K and 227 ± 2 K, consistent with a decreasing ice core radius. The nanopore with water-pore interactions the same as water-water interactions, with hydrogen bonding, had a melting temperature the same as the hydrophobic pores, though with slightly larger ice core radius. For all nanopores, melting followed the same trend, with the liquid layer increasing, leaving regions of the core ice only 3-4 layers thick just prior to complete melting of the core ice.

While it is the radius of the core ice that determines the melting temperature, hydrophilic and hydrophobic water-pore interactions and the presence of hydrogen bonding effect differently the width of the liquid layer, and ultimately the radius of the ice core. Further analysis into the effect of hydrophilic and hydrophobic pores, with and without hydrogen bonding, is necessary to more fully understand the effect of water-pore interaction on the premelted layer of confined water.

References

[1] C. Alba-Simionesco, B. Coasne, G. Dosseh, G. Dudziak, K. E. Gubbins, R. Radhakrishnan, and M. Sliwinska-Bartkowiak, J. Phys. Condens. Matter **18**, R15 (2006).

[2] I. Brovchenko and A. Oleinikova, *Interfacial and Confined Water*. (Elsevier, Amsterdam, 2008).

[3] G. Rennie and J. Clifford, J. Chem. Soc. Faraday Trans. I **73** (1977); C. Jackson and G. McKenna, J. Chem. Phys. **93**, 9002 (1990); Y. Hirama, T. Takahashi, M. Hino, and T. Sato, J. Colloid Interface Sci. **183**, 1185 (1996).

[4] R. Schmidt, E. Hansen, D. Stocker, D. Akporiaye, and O. Ellestad, J. Am. Chem. Soc. **117** (1995).

[5] K. Morishige and K. Kawano, J. Chem. Phys. **110**, 4867 (1999).

[6] G. Findenegg, S. Jähnert, D. Akcakayiran, and A. Schreiber, ChemPhysChem **9**, 2651 (2008).

[7] A. Watanabe, T. Iiyama, and K. Kaneko, Chem. Phys. Lett. **305**, 71 (1999); M. Sliwinska-Bartkowiak, G. Dudzial, R. Sikorski, R. Gras, K. Gubbins, and R. Radhakrishnan, Phys, Chem. Chem. Phys. **3**, 1179 (2001); N. Kastelowitz, J. C. Johnston, and V. Molinero, J. Chem. Phys. **132**, 124511 (2010).

[8] O. Petrov and I. Furó, Phys. Rev. E **73**, 11608 (2006).

[9] J. Jelassi, H. Castricum, M. Bellissent-Funel, J. Dore, J. Webber, and R. Sridi-Dorbez, Phys. Chem. Chem. Phys. **12**, 2838 (2010).

[10] D. Wallacher and K. Knorr, Phys. Rev. B **63**, 104202 (2001).

[11] S. Jahnert, F. Chavez, G. Schaumann, A. Schreiber, M. Schonhoff, and G. Findenegg, Phys, Chem. Chem. Phys. **10**, 6039 (2008).

[12] R. Schmidt, M. Stöcker, E. Hansen, D. Akporiaye, and O. Ellestad, Microporous Materials **3**, 443 (1995).

[13] J. Deschamps, F. Audonnet, N. Brodie-Linder, M. Schoeffel, and C. Alba-Simionesco, Phys, Chem. Chem. Phys. **12**, 1440 (2010).

[14] Y. Li and G. Somorjai, J. Phys. Chem. C **111**, 9631 (2007).

[15] A. Endo, T. Yamamoto, Y. Inagi, K. Iwakabe, and T. Ohmori, J. Phys. Chem. C **112**, 9034 (2008).

[16] S. Plimpton, J. Comp. Phys. **117**, 1 (1995).

[17] E. de La Llave, V. Molinero, and D. Scherlis, J. Chem. Phys. **133**, 034513 (2010).

[18] H. Lowen, Phys. Rep. **237**, 249 (1994).

[19] R. Denoyel and R. Pellenq, Langmuir **18**, 2710 (2002).

[20] E. B. Moore and V. Molinero, J. Chem. Phys. **130**, 244505 (2009).

[21] M. Brun, A. Lallemand, J. Quinson, and C. Eyraud, Thermochim. Acta **21**, 59 (1977).

[22] E. Gonzalez Solveryra, E. de La Llave, D. A. Scherlis, and V. Molinero, In preparation (2011).

CHAPTER 6

ICE CRYSTALLIZATION IN WATER'S "NO-MAN'S LAND"

THE JOURNAL OF CHEMICAL PHYSICS **132**, 244504 (2010)

Ice crystallization in water's "no-man's land"

Emily B. Moore and Valeria Molinero[a)]
Department of Chemistry, University of Utah, 315 South 1400 East, Salt Lake City, Utah 84112-0850, USA

(Received 8 April 2010; accepted 19 May 2010; published online 23 June 2010)

The crystallization of water at 180 K is studied through large-scale molecular dynamics simulations with the monatomic water model mW. This temperature is in the middle of water's "no-man's land," where rapid ice crystallization prevents the elucidation of the structure of liquid water and its transformation into ice with state of the art experimental methods. We find that critical ice nuclei (that contain less than ten water molecules) form in a time scale shorter than the time required for the relaxation of the liquid, suggesting that supercooled liquid water cannot be properly equilibrated in this region. We distinguish three stages in the crystallization of water at 180 K: concurrent nucleation and growth of ice, followed by consolidation that decreases the number density of ice nuclei, and finally, slow growth of the crystallites without change in their number density. The kinetics of the transformation along the three stages is well described by a single compacted exponential Avrami equation with $n \approx 1.7$. This work confirms the coexistence of ice and liquid after water is crystallized in "no-man's land": the formation of ice plateaus when there is still 15%–20% of liquid water in the systems, thinly dispersed between ice I crystals with linear dimensions ranging from 3 to 10 nm. We speculate that the nanoscopic size of the crystallites decreases their melting point and slows their evolution toward the thermodynamically most stable fully crystalline state.
 [doi:10.1063/1.3451112]

I. INTRODUCTION

Little is known about the state of liquid water and the mechanism of crystallization of ice in the heart of what is known as water's "no-man's land."[1] This is the region of water's phase diagram where crystallization of supercooled water is too fast to be studied with the state of the art experimental techniques. Its upper boundary corresponds to the temperature of homogeneous nucleation of ice, $T_H \approx 235$ K.[2,3] Its lower boundary is the highest temperature at which amorphous water can be detected in experiments, $T_x \approx 155$ K.[4,5] Understanding the mechanisms, extent, and product of water crystallization in "no-man's land" is of central importance for the prediction of cloud formation in the atmosphere[6–8] and the state of water in interstellar space.[9,10]

The structure and thermodynamics of liquid water at the melting point are very different from those of the low-density amorphous ice (LDA) glass: the coordination in the first shell decreases from 5.1 in the liquid to 4 in the glass,[11] the excess enthalpy with respect to ice is from 6.00 to 1.35 kJ/mol,[12] and the excess entropy is from 22.0 to 1.7 J/K mol.[13] Several hypotheses[14–18] have been proposed to explain these stark differences and the thermodynamic anomalies of liquid water, such as the density maximum at 4 °C and the increase in heat capacity and compressibility upon cooling.[1,2,19] There is now general consensus that the structural transformation in liquid water at room pressure is continuous.[12,13] This is consistent with both the liquid-liquid critical point (LLCP) (Ref. 14) and singularity free (SF) (Ref. 15) hypotheses. The LLCP theory proposes that two distinct phases of liquid water, low-density liquid and high-density liquid, exist at pressures higher than a critical pressure p_c in the supercooled region of water's phase diagram. The two liquid phases would convert through a first order transition that ends at a critical point; the latter tentatively located at $p_c \approx 1000$ atm and at $T_c \approx 220$ K.[20] In the SF theory the structural transition is continuous at all pressures.[15,21] The existence of two distinct glass phases (LDA and high-density amorphous ice) that interconvert through a sharp and reversible transition at high pressure supports the LLCP scenario.[22–24]

Knowledge of the structure and thermodynamics of liquid water in "no-man's land" is the key for a comprehensive understanding of water and an assessment of existing theories. A direct experimental study, however, has not yet been possible due to the rapid crystallization of ice in this region. The result of the crystallization of water in "no-man's land" is also disputed.[4,7,10,25–31] Diffraction patterns of water crystallized at temperatures lower than about 200 K display all the diffraction peaks characteristic of cubic ice but only one (the 100 peak) of hexagonal ice.[7,10,25,26,30,32] Studies of cubic ice produced from decompression of high-pressure ice phases show that the 100 signal arises from the presence of hexagonal layers intercalated as stacking faults into a cubic structure.[33–35] The detailed structure (fraction of cubic and hexagonal ice I polymorphs and distribution and type of stacking faults) of the ice formed by crystallization of liquid water in "no-man's land" is not known. Similarly, there is not

[a)]Author to whom correspondence should be addressed. Electronic mail: Valeria.Molinero@utah.edu.

yet a clear consensus on the fraction of water that remains in the liquid state after crystallization: the final percentage of noncrystalline water—either amorphous solid or liquid—has been reported to be within 5% and 50%, depending on the sample preparation and the method of analysis.[10,25–27,36] Through a combination of x-ray diffraction and calorimetry, Kohl *et al.*[26] concluded that at most 20% of the water that crystallized at 183 K remains in a liquid or amorphous form, while Jenniskens and Blake[25] employed a combination of transmission electron microscopy, temperature programed desorption, and infrared spectroscopy to study water crystallized under the same conditions and concluded that 50% of the water remains in amorphous or liquid state.

Molecular simulations have an optimum spatial resolution for the study of the structure of liquid water and ice nuclei and the microscopic mechanisms of ice formation. The computational cost of atomistic simulations, however, has limited the study of ice crystallization to small systems (less than 800 rigid water molecules modeled with classical potentials).[37,38] A study of the formation of ice crystallites requires simulation cells with dimensions of at least 10 nm (~33 000 water molecules) to allow for the development of crystal domains of a size comparable to the ~5 nm deduced from the width of the ice diffraction peaks in experiments.[9,25] The formation of ice proceeds through nucleation and growth of the crystallites.[3] The spontaneous creation of ice nuclei is stochastic and controls the crystallization at temperatures above T_H; advanced sampling methods can be used to reduce its computational cost.[39–41] Water crystallization in "no-man's land", on the other hand, may be dominated by the slow growth of the ice crystals in the viscous environment of the deeply supercooled liquid, requiring long simulations for the completion of the crystallization. Considering the challenges associated with the atomistic modeling of ice crystallization, it is not surprising that very few atomistic simulations of ice nucleation and growth have been reported to date,[37–41] none of them in water's "no-man's land".

In this work, we overcome the computational limitations of atomistic simulations through the use of a very efficient coarse-grained model of water, the monatomic water (mW) model.[42] Molecular simulations with the mW model are more than two orders of magnitude computationally more efficient than with atomistic water models using Ewald sums.[42] The mW model represents each water molecule as a single particle that interacts through very short-ranged interactions, which encourage "hydrogen-bonded" structures between the water molecules, without the explicit inclusion of hydrogen atoms. The coarse grained model reproduces the structure of liquid water, the LDA glass, ice and clathrate hydrates, and the thermodynamics of the phase transformations between them.[42–47] In previous work we used large-scale molecular dynamics (MD) simulations with the mW model to characterize the evolution of the structure of liquid water from stable liquid at 350 K to the LDA glass at 100 K, when the liquid is cooled at the slowest rate that avoids ice crystallization.[43] In agreement with the inferences from experiments, we found that the structural transformation is continuous at room pressure. A liquid-liquid transformation temperature, defined as the temperature for which there is a maximum change in the density and structure of liquid water, occurs at T_{LL}=201 K. We have also determined that domains of four-coordinated water molecules develop in liquid water already at room temperature and their characteristic length grows as water is supercooled, reaching a maximum correlation length at T_{LL}.[43] A growing correlation length is consistent with the existence of a LLCP at high pressures, which for the mW model seems to be located around 1200 atm and 190 K.[48]

The melting temperature of hexagonal ice is 274 K in the mW model.[42,44] Crystallization of mW water occurs at around 200 K if the liquid is quenched at a rate slower than the critical rate for vitrification (10 K/ns).[42,43] This sets the upper limit for "no-man's land" in the mW model; the lower is set by the glass transition temperature, $T_g \approx 150$ K.[43] In this study we investigate the crystallization of water in the heart of "no-man's land", at $T=180$ K, conditions at which the structure of the liquid is already close to that of the random tetrahedral network of the LDA glass[43] while the mobility of water is large enough to allow for complete crystallization within coarse-grained simulations lasting less than 1 μs.

We have recently used the mW water model to study the freezing, melting and structure of ice in hydrophilic nanopores at 195 K, the T_H of water in the pore.[46] Under these conditions, we found that the rate of crystallization was controlled by the rate of formation of the critical ice nuclei. We estimated the critical ice nuclei to contain a core of about 75–100 water molecules at T_H. The crystallization of water in the pore resulted in single crystals of ice I that contained cubic and hexagonal layers in a ratio of about 2:1, surrounded by a sheath of liquid water. In agreement with the results of NMR experiments, we found liquid water in equilibrium with ice in the pore down to 180 K, 50 K below the melting point (the simulations predicted T_m=230 K for water in the 3 nm diameter pore,[46] same as determined through differential scanning calorimetry in Ref. 49). In the present work, we use the models and methodology of Ref. 46 to identify ice and analyze the nucleation and growth of ice I in bulk water at 180 K. We address two fundamental questions: first, whether liquid water can be equilibrated in "no-man's land". This region has been defined in terms of the impossibility of characterizing the liquid with the state of the art methods; our question is whether the liquid can be equilibrated at all before it crystallizes to ice. Second, what is the mechanism by which ice nucleates and grows in "no-man's land", how does the structure of water evolve through the crystallization process, and what is the fraction and distribution of liquid water in coexistence with ice in the crystallized system.

II. MODEL AND METHODS

A. Water potential

Water was modeled using the mW model.[42] The mW potential consists of a sum of pairwise $\phi_2(r)$ and three-body $\phi_3(r,\theta)$ contributions,

$$E = \sum_i \sum_{j>1} \phi_2(r_{ij}) + \sum_i \sum_{j\neq 1} \sum_{k>j} \phi_3(r_{ij}, r_{ik}, \theta_{ijk}),$$

$$\phi_2(r_{ij}) = A\varepsilon\left[B\left(\frac{\sigma}{r_{ij}}\right)^p - \left(\frac{\sigma}{r_{ij}}\right)^q\right]\exp\left(\frac{\sigma}{r_{ij}-a\sigma}\right), \quad (1)$$

$$\phi_3(r_{ij}, r_{ik}, \theta_{ijk}) = \lambda\varepsilon(\cos\,\theta_{ijk} - \cos\,\theta_0)^2 \times\exp\left(\frac{\gamma\sigma}{r_{ij}-a\sigma}\right)\exp\left(\frac{\gamma\sigma}{r_{ik}-a\sigma}\right),$$

where $A=7.049\,556\,277$, $B=0.602\,224\,558\,4$, $p=4$ $q=0$, $\gamma=1.2$, $a=1.8$, $\theta_0=109.47°$, $\sigma=2.3925$ Å, $\varepsilon=6.189$ kcal mol^{-1}, and $\lambda=23.15$. The three-body term adds an energy penalty to configurations with angles different from θ_0, which in this parametrization encourage hydrogen-bonded tetrahedral configurations. The mass of a mW particle corresponds to that of a water molecule. The mW model was parametrized to reproduce the melting temperature, vaporization enthalpy, and density of liquid water at 298 K and 1 atm. The mW model does not have electrostatics or hydrogen atoms, allowing for longer integration steps, up to 10 fs. This, coupled with the short range of the potential (less than 4.32 Å), and the decrease in the number of particles, make the mW model about 180 times computationally more efficient than atomistic simulations of rigid water models using Ewald sums.[42,50]

B. Simulation methods

MD simulations were performed using LAMMPS.[51] Systems consisted of 32 768 mW particles in a cubic simulation cell with periodic boundary conditions (cell dimensions ~10 nm). The velocity Verlet algorithm was used to integrate the equations of motion with a time step of 10 fs. All simulations were evolved at a pressure of 1 atm in the isothermal isobaric ensemble (NpT). Temperature and pressure were controlled using the Nosé–Hoover thermostat and barostat with relaxation times of 1.0 and 5.0 ps, respectively.

C. Isothermal crystallization of instantaneously quenched liquid water

We selected five uncorrelated configurations from a single MD trajectory of water at $T=300$ K. The configurations were instantaneously quenched to $T=110$ K and evolved under NpT conditions at that temperature for 0.3 ns. The end points of the short simulations at 110 K are the starting configurations for the five *QL* (for instantaneously *quenched liquid*) 590 ns simulations at 180 K.

D. Isothermal crystallization of warmed-up LDA glass

It is not possible to instantaneously quench liquid water in experiments. The initial configuration for the study of crystallization above T_g involves the heating of LDA glass to the target temperature. We vitrified liquid water to LDA by cooling of the liquid from 350 to 100 K at the critical cooling rate for vitrification of mW water, 10 K ns^{-1}.[43] Then, the glass was heated at 10 K ns^{-1} from 100 up to 180 K. Upon reaching 180 K, the temperature was held constant and the system was allowed to evolve for 590 ns. This trajectory and system is termed *WG* (for *warmed glass*).

E. Identification of ice

As a measure of water's crystallinity during nucleation and growth, we utilize the CHILL algorithm that we previously developed for the identification of ice.[46] The algorithm makes use of the local coordination of the water molecules and the correlation of orientations between the first coordination shells of neighboring waters to determine the amount of *liquid*, ice I (which we refer to as *core* ice) and *interfacial* ice (an intermediate between ice I and liquid) present in each configuration of the system. We denote the sum of core ice and interfacial ice as *total* ice.

F. Identification of ice nuclei

Individual ice nuclei are characterized using a clustering algorithm with a distance cutoff of 3.5 Å, the first minimum of the water-water radial distribution function (rdf). Starting from a molecule classified by the CHILL algorithm to have the local symmetry of core ice, the clustering algorithm finds all similarly classified neighboring molecules within the distance cutoff, searching around all new positively identified molecules until no more are found. The second hydration shell in ice I includes 12 molecules. To be considered as an ice nucleus, more than two neighboring tetrahedra must be involved in the ice cluster. While counting the number of ice nuclei, we consider only those formed by more than ten water molecules.

G. Diffusion

The mean square displacement, $\langle r^2(t)\rangle$, was determined as the average over all particles of the squared displacement from their original positions at $t=0$, the beginning of the simulations at 180 K. Statistics was collected for each of the QL and WG systems over the 590 ns simulations.

H. Radial distribution function

The rdf between water molecules was computed for the selected configurations of the simulation trajectories as

$$g(r) = \frac{V}{N^2}\sum_{i=1}^{N}\sum_{j\neq 1}^{N}\delta(r - r_{ij}), \quad (2)$$

where δ is Dirac's delta function, V is the volume, and r_{ij} is the distance between i and j molecules.

I. Radius of gyration and nonsphericity

The radius of gyration R_G of each ice nucleus is a measure of its size,

$$R_G^2 = \frac{1}{N^2}\sum_{i>j}^{N}(r_i - r_j)^2, \quad (3)$$

where N is the number of water molecules in the nucleus, r are the molecular coordinates, and the sum is over all pairs of molecules in the nucleus. The nonsphericity (NS) is the ratio

between the actual R_G of the nucleus and the R_G of a sphere containing the same number of molecules.[43] A NS of 1 corresponds to a perfectly spherical nucleus. The less spherically shaped nuclei have higher NS values.

III. RESULTS AND DISCUSSION

We investigate the kinetics and microscopic mechanism of crystallization of ice from liquid water during isothermal simulations at 180 K. This temperature is right in the middle of "no-man's land", where ice crystallization is too fast to be characterized with the current experimental methods. We perform a series of 590 ns long MD simulations on systems containing 32 768 water molecules ($\sim$1000 nm^3 volume per simulation cell). Two different sets of starting liquid configurations were considered in this study: five initial configurations obtained from instantaneous quenching of liquid water from 300 to 110 K, with 0.3 ns at 110 K during which the number in neighbors of the first coordination shell decreases from 5.1 to 4.2, followed by an instantaneous warm-up from 110 to 180 K. We denote these as the QL systems. The advantage of using these initial conditions is the complete absence of viable ice nuclei at the beginning of the simulation trajectory. It is, however, impossible to instantaneously quench a liquid in experiments. We obtain a more realistic initial configuration by quickly warming a previously formed LDA glass to 180 K. We denote this system as WG.

Figure 1 presents snapshots for one of the QL systems along the crystallization trajectory. For clarity, panels (a)–(h) show only water molecules that are parts of core ice clusters, while the last panel shows all core ice, interfacial ice, and liquid water in different colors, at the end of the 590 ns simulation. The snapshots provide valuable insight into the process of ice formation in "no-man's land": first, the induction period is negligible; viable ice nuclei are formed within the first nanosecond. An analysis of the individual nuclei indicates that the critical nuclei, which have equal probability of growth and dissolution, contain no more than ten water molecules. Second, the ice nuclei form randomly within the 1000 nm^3 volume of the periodic cell. Third, ice nucleation and growth occur concurrently for about a hundred nanoseconds. Nucleation cannot be separated from growth. Fourth, by the end of the simulation, most of the water crystallized in the form of a few ice crystallites with linear dimensions on the order of 5 nm; the ice crystallites are separated by thin regions of amorphous water.

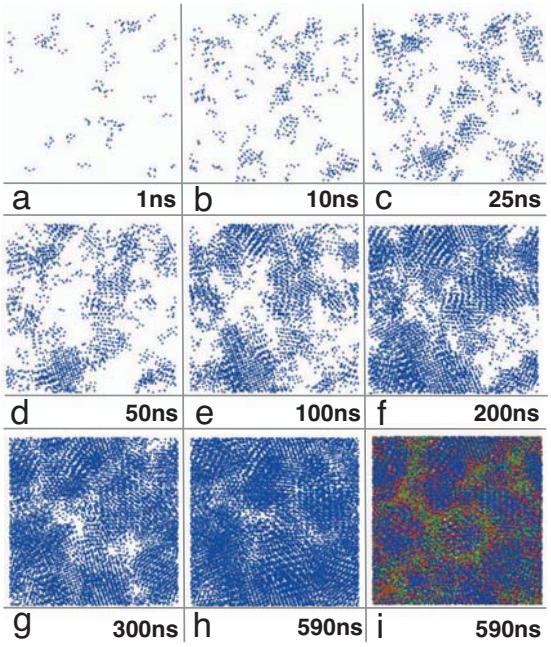

FIG. 1. Snapshots of the crystallization of water at 180 K, starting from instantaneously quenched liquid (QL). The simulation cell has $\sim$10 nm side. Through panels (a)–(h), the water molecules that belong to the ice cores are shown in blue and all other molecules are hidden. During stage I [panels (a)–(e)], there is an increase in the number and size of the ice nuclei. Stage II starts when the number of ice nuclei peaks at 100 ns [panel (e)] and continues until only a few nuclei result from the process of growth and consolidation. Stage III starts at 300 ns [panel (g)] and involves slow growth and consolidation of the crystallites. At t=590 ns [panel (i)], 80% of the water has crystallized: 50% forms the core of the crystallites (blue), 30% is interfacial ice surrounding them (orange), and 20% remains in the amorphous state between crystallites (green). By t=590 ns, the crystallites had reached sizes of several nanometers and further consolidation is no longer possible through rearrangement in the time scales accessible to the simulations.

A. Kinetics of ice crystallization

To quantify the nucleation and growth of ice from supercooled water, we computed the time evolution of the fraction f_{ice} of interfacial and core ice, and their sum, total ice. These are shown in Fig. 2(a). In the case of the QL systems, the curve represents an average over five trajectories and the error bars measure the variability between simulations. The curves of Fig. 2(a) confirm the assessment about the lack of induction period for the nucleation: the ice starts to form immediately after the temperature of the systems is set at 180 K. Notice the small dispersion for the set of QL trajectories. This indicates that the overall advance of the crystallization is not very sensitive to the initial liquid structure, consistent with a negligible stochastic induction period.

We start with the analysis of the fraction of interfacial ice. The trajectories exhibit a significant initial (t=0) fraction of the water molecules as interfacial ice: 20% for the WG and 8% for the QL systems (this fraction is less than 0.2% in water at 300 K). The high fraction of interfacial ice at t=0 may seem surprising as there is very little core ice present. The molecules classified as interfacial ice have a local structure intermediate between a tetrahedrally coordinated liquid and ice as if they were at the interface of ice crystals. Nevertheless, we observe that until the ice crystallites become relatively large [e.g., panel (d) of Fig. 1] most of the molecules classified as interfacial ice form small clusters and sparse threads and are actually unrelated to crystal cores. While the initial amount of interfacial ice in QL doubles to 16% during the first 2 ns, only 2% of core ice forms in the QL systems during that period. This suggests that the increase in interfacial ice is due primarily to the structural relaxation of supercooled liquid water and is not driven by the formation of ice crystallites. Even relatively large clusters of

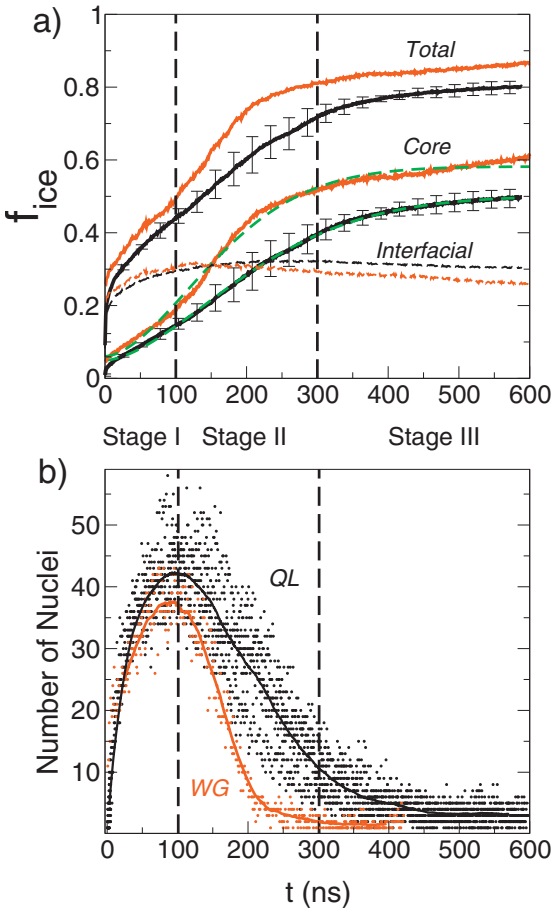

FIG. 2. (a) Fraction of total, core, and interfacial ice over the course of the 590 ns simulations at 180 K. Orange lines: crystallization of warmed-up LDA glass, WG. Black lines: average for the crystallization of the five instantaneously quenched liquid, QLs. The dashed green lines are the fractions of core ice described by Eq. (4) with the coefficients of Table I. (b) Time evolution of the number of ice nuclei containing ten or more molecules of core ice. The volume of the simulation cell is ~1000 nm^3. Black and orange dots represent the data for the QL and WG simulations, respectively. The lines are running averages to assist the visualization. The dashed vertical lines distinguish three stages in ice crystallization: development of nuclei in stage I, consolidation of neighboring nuclei in stage II, and growth and aging of crystallites in stage III.

interfacial water are unable to nucleate the formation of ice crystals; thus, we conclude that these threads and clusters of water molecules with structure intermediate between ice and liquid are a constitutive part of the structure of water at 180 K. As the ice crystallites grow, genuine interfacial ice forms at their surface. By the end of the simulation, the molecules classified as interfacial ice are actually on the surface of ice crystallites, as seen in panel (i) of Fig. 1. The result is that except for a moderate increase during the first ~50 ns, the fraction of interfacial ice remains essentially constant and is not a good indicator of the advance of the crystallization.

The water molecules in core ice have the same local ordering of bulk ice I. As illustrated in Fig. 1, the increase in

TABLE I. Kinetic coefficients that best represent the evolution of core ice in the simulations, according to Eq. (4).

	QL	WG
$f_{\text{core}}^{\text{final}}$	0.50	0.59
$f_{\text{core}}^{\text{initial}}$	0.05	0.06
k (ns^{-n})	0.000 11	0.000 12
n	1.66	1.72
$t=k^{-1/n}$ (ns)	240	200

core ice reflects the advance of the crystallization. Figure 2(a) shows that, as expected, there is no core ice in the QL systems at the beginning of the simulation at 180 K. The WG system (which had a history as LDA) starts with 5% of core ice already present in the glass. This is in agreement with the 5% ice determined in LDA through calorimetry and x-ray diffraction experiments.[26,52] The evolution of core ice is qualitatively the same for the initial configurations obtained from the liquid or the glass: both lack a noticeable induction time and increase in a sigmoidlike manner, resulting in the conversion of 50%–60% of the water into core ice.

It is customary to analyze the kinetics of crystallization using Avrami's equation,[53]

$$f_{\text{ice\_core}}(t) = f_{\text{core}}^{\text{initial}} + (f_{\text{core}}^{\text{final}} - f_{\text{core}}^{\text{initial}})[1 - \exp(-kt^n)], \qquad (4)$$

where $f_{\text{ice\_core}}$ is the fraction of core ice, $f_{\text{core}}^{\text{initial}}$ is the initial amount of core ice, and $f_{\text{core}}^{\text{final}}$ accounts for the predicted amount of core ice at the end of the crystallization. The Avrami exponent n reflects the steepness of the crystallization process. Along with the rate coefficient k, n determines the characteristic time scale of the crystallization, $\tau_x = k^{-1/n}$. Table I lists the parameters that best represent the growth of core ice. The best fits to Eq. (4) are shown in Fig. 2(a). The time scales, $\tau_x = k^{-1/n}$, for the formation of core ice in the simulations are 240 ns for QL and 200 ns for WG. The Avrami exponents obtained from simulations are $n=1.66$ for QL and 1.72 for WG. The optimized parameters would suggest that there is already 5% of core ice at the beginning of the QL simulations, essentially the same as for WG, although that fraction of core ice is actually not achieved in the QL simulations until $t=20$ ns. Forcing of $f_{\text{core}}^{\text{initial}}$ in QL to zero results in a slightly poorer fit with $n=1.3$ and $\tau_x=200$ ns.

Hage *et al.*[54] used fourier transform infrared spectroscopy (FTIR) to analyze the kinetics of crystallization of hyperquenched glassy water heated to temperatures in the range of 140–146 K. Their analysis resulted in Avrami exponents of $n=1.5\pm0.2$, very well reproduced by our simulations. A comparison of the time scales of crystallization in the simulation and experiment is not as straightforward for two reasons: first, there have been no experimental determinations of crystallization rates at 180 K. The closest temperature at which the kinetics was studied is 155 K.[55] We extrapolated the experimental data from measurements in the range of 125–155 K in Refs. 10 and 54–56, assuming an Arrhenius temperature dependence with constant activation energy and pre-exponent. This results in predicted rates of crystallization on the order of 10^{-2} s at 180 K. These extrapolated time scales are 10^5 times longer than predicted by the mW simu-

lations. This leads us to the second, and fundamental, reason that prevents a direct comparison: the dynamics, including the diffusion and crystallization, of the mW model are intrinsically faster than that of a fully atomistic system.

Faster crystallization in the coarse-grained simulations is expected because coarse-grained models evolve in a smoother potential energy landscape than atomistic systems. At room temperature, the diffusion coefficient of mW water is about twice the experimental value, and this ratio increases upon cooling.[42] Since the energy of the coarse-grained model depends only on the oxygen positions, mW simulations underestimate the barrier for breaking hydrogen bonds that is part of the mechanism of mobility and of crystallization of water. We note that the mW model correctly accounts for the energy of breaking hydrogen bonds: the enthalpy of vaporization and melting determined using the mW model are within just 0.17 kcal mol^{-1} of the experimental values.[42] Thus, the energy difference between stable states is well accounted for, leaving only the *barrier* for breaking bonds underestimated. This barrier controls the mobility of water, and since the time scales of growth depend on the ability of molecules to diffuse to and incorporate into the developing ice interface, the barrier also modulates the rate of crystallization. If the mobility and crystallization rates are affected to the same extent by the decrease in the barriers due to the removal of the explicit hydrogen atoms, then the ratio of the diffusion coefficients in the coarse-grained simulations and experiment could be used to scale the rate of crystallization in the simulations to compare it with the experiments at the same temperature, $\tau_x^{\text{expt}} = \tau_x^{\text{mW}}(D^{\text{mW}}/D^{\text{expt}})$. We cannot test the validity of this conjecture because there is no experimental data on water's diffusivity at 180 K (determination is prevented by the fast crystallization rates). The diffusion coefficient of water in the simulations at 180 K can be estimated from the evolution of the mean square displacement $\langle r^2(t)\rangle$ (see Fig. 3),

$$\log\langle r^2(t)\rangle = \log(6D) + \upsilon \log(t). \tag{5}$$

In the case of Fickian diffusion, $\upsilon = 1$ and D is the diffusion coefficient. The $\langle r^2(t)\rangle$ in the simulations does not increase linearly with time. As crystallization progresses, the mobility of water becomes increasingly hindered by the crystallites, leading to the observed subdiffusive behavior: $\upsilon = 0.4$ for QL and 0.5 for WG. The D obtained from the fits to Eq. (5) are 6×10^{-8} $cm^2\ s^{-1}$ for QL and 4×10^{-8} $cm^2\ s^{-1}$ for WG. These are only approximations to the actual diffusion coefficient because $\upsilon < 1$ and the liquid is out of equilibrium, transforming into ice in a time scale comparable to its mobility. For example, the average displacement of the water molecules after 200 ns, the characteristic time scale for the crystallization, is just 10 Å. This is less than three times the diameter of a water molecule. From this and the structural relaxation of the QL, we infer that at 180 K, and probably throughout most of "no-man's land", the time scale for the relaxation of the liquid is comparable to the time scale for its crystallization to ice. We conclude that *liquid water cannot be equilibrated in "no-man's land"*.

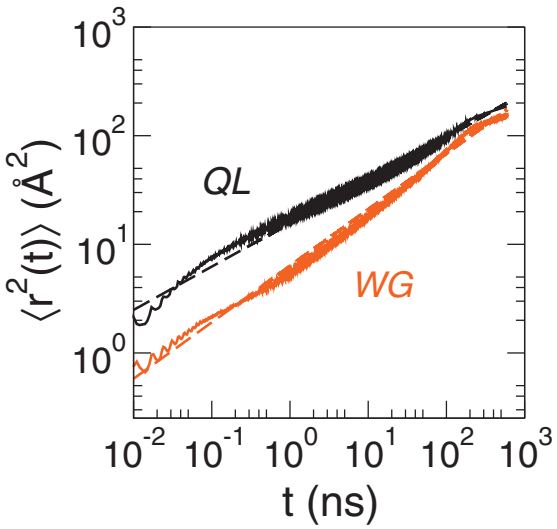

FIG. 3. Mean square displacement of water at 180 K. The initial mobility is higher for the instantaneously quenched liquid (QL) (black line) than for the warmed glass WG (orange line). The dashed lines show the best fit to Eq. (5). Water mobility in the QL and WG systems is strongly subdiffusive due to the formation of ice crystallites along the simulations. The exponent ν in Eq. (5) is 0.4 for QL and 0.52 for WG.

B. Mechanism of crystallization of ice

In the absence of enough microscopic data on the evolution of ice structure during the crystallization, the value of the Avrami exponent n has been used to infer the mechanism of formation of ice just above the glass transition temperature. The exponents n found in this study are identical, within the error bars, to the 1.5 ± 0.2 found by Hage *et al.*[54,55] in their experimental study of ice crystallization from warmed-up LDA in the range of 140–155 K. These authors found that when isothermal crystallization was preceded by annealing at lower temperatures, allowing for the formation of crystalline seeds, the Avrami exponent rose to $n \approx 2.4$.[54] Jenniskens and Blake[10] studied ice crystallization starting with LDA warmed at 125–143 K. They monitored the growth through the 220 peak of cubic ice, which they measured by x-ray diffraction. In that temperature range, they observed a regime of fast increase of intensity of the 220 peak, followed by a regime of more gradual increase. They optimized the Avrami exponent for each regime, finding $n = 2.0 \pm 0.3$ for the rapid growth and 0.8 ± 0.3 for the gradual growth.[10] Jenniskens and Blake contended that the intermediate values of Hage *et al.* are related to the blending of the two regimes due to the lack of ice seeds in the glass (usually formed by previous annealing). From this broad range of n values, several hypotheses have been put forth for the mechanism of crystallization of ice: diffusionally controlled growth of spherical crystallites with constant nucleation rate for $n \approx 2.5$ (Refs. 10 and 54) and with rapidly decreasing nucleation rate for $n \approx 1.5$,[10] and that the value of n is not related to the shape of the crystallites but indicates that the crystallization barrier decreases as crystallization proceeds.[55] Different from the previously described results, Kay and co-

workers found $n \approx 4$ for the crystallization of thin LDA films deposited on metallic substrates at temperatures between 140 and 146 K, which they interpreted in terms of random bulk nucleation with a constant rate and isotropic growth of the crystalline nuclei.[36,57] A value of $n=3$ is expected for isotropic growth of spherical crystals, while $n=1$ is a limiting case for random appearance of icelike molecules in the system. The high value of n in Refs. 36 and 57 suggests that a few relatively large ice seeds may exist under the conditions of these experiments and dominate the growth of ice, while smaller nuclei form and compete to grow ice in the present simulations and the experiments of Refs. 10, 54, and 55. In what follows, we characterize the nucleation and growth of the ice crystallites that give rise to $n \approx 1.7$ in the simulations.

A complete elucidation of the microscopic mechanism of crystallization of ice in "no-man's land" requires an analysis of the size, distribution, and structure of individual ice nuclei and their evolution in time. The temporal and spatial resolution needed to address the nucleation and growth of individual ice nuclei is inaccessible to current experimental methods, while it is available in the simulation trajectories of this work. Figure 2(b) shows the number of core ice nuclei as a function of time. Only ice nuclei with more than ten molecules of core ice were considered. The WG system starts with ten of these nuclei, while there is none at the beginning of the QL trajectories. Nevertheless, all the systems exhibit similar evolutions of the number of ice nuclei with time: a sharp rise in the number of nuclei during the first ~40 ns [Figs. 1(a)–1(c)], followed by a slower increase that leads to a maximum density of nuclei around 100 ns [Figs. 1(d) and 1(e)], after which the density of ice nuclei decreases due to consolidation of nuclei into larger clusters, leaving a handful of ice crystallites [Figs. 1(f) and 1(g)]. The number of crystallites remains constant during the last stage of growth ($t>250$ ns for WG and $t>350$ for QL). Based on these regimes, we distinguish three stages in the crystallization of ice: *stage I*, during which there is an increase in the number of ice nuclei, *stage II* characterized by a decrease in the number of nuclei due to consolidation, and *stage III* during which there is ice formation without change in the number of crystallites.

Stage I is characterized by the random formation of ice nuclei throughout the system and their growth until crowding occurs and nuclei cannot grow without impinging on each other. The nucleation time usually involves a latent stage during which small subcritical nuclei form and dissolve until a critically sized nucleus develops and grows. Based on the size of nuclei that grow without dissolution, we estimate that the critical ice nuclei at 180 K contain less than ten molecules, smaller than the size of two adjoined tetrahedral units.[58] There is essentially no latent period at 180 K: there are no nuclei at the beginning of the QL trajectories, and 2 ns later these have an average of four nuclei, each consisting of about ~20 molecules. These nuclei are already larger than a critical nucleus and continue to grow. Thus, the latent stage before the appearance of viable nuclei is shorter than 2 ns. This is less than the time required for the system to relax to the structure of metastable liquid mW water at 180 K [between 2 and 12 ns, based on the initial relaxation of interfacial ice (Fig. 2(a)) and the average time it takes for a molecule to displace a molecular diameter, 3.5 Å (Fig. 3)].

The density of ice nuclei in the QL trajectories increases until $t=100$ ns when it reaches ~0.05 nuclei/nm^3 (45 ± 15 nuclei in ~1000 nm^3 volume). About 80% of these nuclei have formed by $t=40$ ns, at which time the fraction of core ice is just 8% because the nuclei are relatively small. The ice nuclei have a broad range of compactness. The nonsphericity coefficient NS of nuclei with less than 1000 molecules ranges from NS=1.7 (very nonspherical) to NS=1.1 (nearly spherical). The corresponding radii of gyration R_G are below 2 nm.

At $t \approx 40$ ns, the rate of nucleation (formation of nuclei with more than ten molecules) starts to decrease noticeably as the nuclei grow large enough to touch and coalesce [e.g., panels (d) and (e) of Fig. 1]. By $t=100$ ns, the fraction of core ice reached 16%, the value that corresponds to the percolation threshold in a randomly growing system[59] and the nuclei are already crowding one another. We also find that at $t=100$ ns, one or two nuclei have outsized the other ~40 nuclei and grown to contain over 1500 water molecules (about one-third of the core ice in the system at that time). The radii of gyration of these large nuclei range from six to nine molecular diameters. Their sphericity is relatively low, NS=1.5 ± 0.2. We note that the NS of the nuclei is not associated with an evident preferential growth parallel or perpendicular to the axis of the ice crystals but to their formation through a combination of growth of small ice clusters and their consolidation with neighboring nuclei. Figure 4 shows the rdf of water as a function of the fraction of core ice for the same QL trajectory displayed in Fig. 1. Even when the ice clusters are quite extended, the signature peak characteristics of ice structure are barely noticeable in the rdf. The presence of ice is not evident in the rdf until the end of stage I when there is already 16% of core ice in the system.

The evolution of WG is similar to QL, with the difference that in WG there were already 11 nuclei at $t=0$, the largest containing 145 molecules and the remaining 10 with an average size of 21 ± 11 molecules. Consistent with our estimation of a critical nucleus with less than ten molecules, all these nuclei survived and continued to grow, leading to a lack of latent stage in WG. As observed for the QL systems, a maximum density of nuclei was reached at ~100 ns, but, due to the initial seeding, there are less and larger ice nuclei at that time. Two nuclei out of the 40 total contain about 1500 molecules, while the remaining nuclei consist of 500 molecules or less.

Stage II is characterized by the growth and consolidation of ice nuclei to yield a few crystallites in the 1000 nm^3 volume. In the simulations at 180 K, this period extends from 100 to ~350 ns in the QL systems and ~250 ns for the WG system. The maximum rates of ice crystallization, measured as $df_{\text{ice\_core}}/dt$, occur during this stage.

The density of ice nuclei decreases by an order of magnitude during stage II as the nuclei consolidate into larger crystallites. This decrease in the number of nuclei continues until they form one or two large nuclei (containing more than 30% of the water in the ~1000 nm^3 volume) along with smaller ones separated by interfacial ice and liquid water.

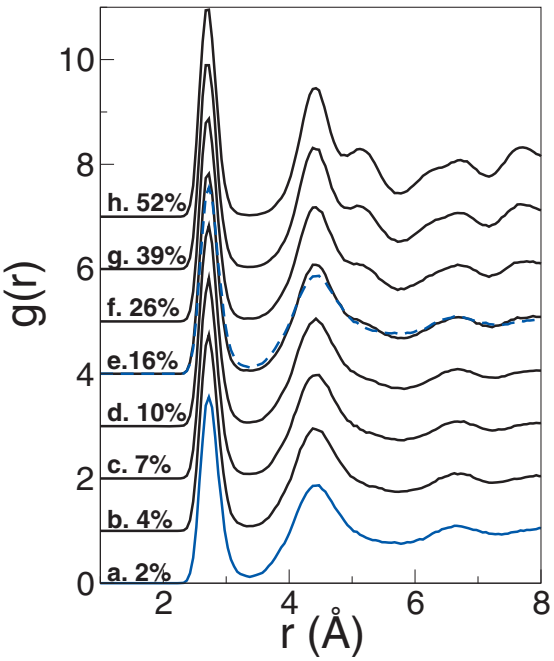

FIG. 4. Water-water rdf as ice crystallizes from supercooled water at 180 K. The labels indicate the fraction of core ice and the corresponding snapshot in Fig. 1. The curves are displaced vertically to facilitate the visualization. The rdf for 2% ice is duplicated (solid and dashed blue lines) to show how insensitive the rdf is to the changes that occur due to crystallization during stage I. The ice signatures become evident when the system enters stage II and the ice crystallites thicken.

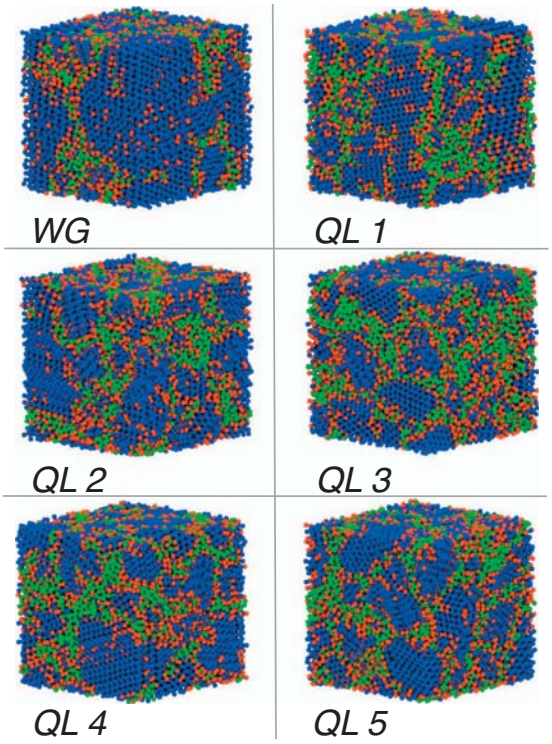

FIG. 5. Final structures of water in the six simulation cells after 590 ns at 180 K. The core of the ice crystallites is shown in blue, the interfacial ice in orange, and the liquid between crystallites in green. The WG system has the largest crystallites. The simulation cells are 10 nm per side and periodic in the three dimensions.

Through this process of consolidation, the larger nuclei of core ice percolate the simulation cell and R_G can no longer be used to measure the size or shape of the crystallites.

The consolidation in the QL systems results in one or two large ice clusters surrounded by a handful of smaller ones. For the WG system, consolidation results in a single ice crystallite that encompasses half of the simulation cell (~16 000 molecules). We find that this crystallite in the WG system originates in the pre-existing largest ice core nucleus inherited from the LDA glass. Without competition between multiple equivalently sized nuclei, the crystallization process in WG is dominated by the consolidation of smaller nuclei to a single large crystallite rather than multiple nuclei growing to large size before consolidating.

Stage III is reached at the end of the consolidation process (~250 ns for WG and ~350 ns for QL) when the ice crystallites are already too large to reorganize and fuse within the time scale of the simulation. This stage is characterized by a slow growth in the size of crystallites without change in the number of ice clusters (compare, for example, the structure of ice at 300 and 590 ns in Fig. 1). We define a crystallite in terms of connectivity, and a crystallite can contain several regions in which ice grew with different orientations, as is clear in the structure of the six systems at the end of the simulations (Fig. 5). By the end of the isothermal crystallization simulations, the QL systems contain $50 \pm 3\%$ core ice, $30 \pm 1\%$ interfacial ice, and $20 \pm 2\%$ liquid. The fraction of ice is higher for WG: 60% is core ice, 25% is interfacial ice, and 15% is liquid. The interfacial ice is at the surface of the cores and not as isolated threads as in the beginning of the simulation. The liquid water remaining at 590 ns is located in the narrow regions between the ice domains. A similar fraction of ice, 65%, has been estimated after water crystallization in thin film experiments.[36] Jenniskens and Blake[10,25] monitored the fraction of ice through the 220 diffraction peak of Ic and found ~30% conversion of LDA into cubic ice when applying a heating ramp up to 172 K. The results we report here for core ice include both cubic and hexagonal polymorphs. A detailed study of the structure of the ice formed at 180 K, including the formation of cubic and hexagonal patterns and stacking faults, is presented in a separate communication.[60] Here, we note that in agreement with Refs. 25 and 10, the fraction of cubic ice at the end of the crystallization simulations of this study is 30%–40%, with the higher amount corresponding to the WG system. We found that ice I formed by crystallization of supercooled liquid water (either hyperquenched from the liquid or warmed up from the LDA glass) consists of intercalated layers of cubic and hexagonal ice in a ratio of about 2:1.[60] This is the same ratio deduced for the structure of ice I obtained by decompression of high pressure ice polymorphs[33–35] and by freezing of liquid water in nanopores.[46,61]

IV. CONCLUSIONS

We investigated the kinetics and mechanism of ice crystallization from liquid water at 180 K through large-scale MD simulations with the mW model. At this temperature, the crystallization rate is too fast for a study of its kinetics with the state of the art experimental methods and too slow for atomistic simulations. To the best of our knowledge, this is the first simulation study that reports on crystallization of ice in water's "no-man's land" and the first microscopic study of the formation and growth of ice nuclei in this region. We note that atomistic simulations of water crystallization at 180 K would probably take about 10^7 times more computing time: the mW model is not only 180 times more efficient that atomistic models (i.e., it takes less than 1/100th of CPU time to simulate the same number of nanoseconds) but it also has an intrinsically faster dynamics due to the absence of hydrogen atoms. An Arrhenius extrapolation to 180 K of the experimental crystallization rates around 140–150 K predicts crystallization times that are 10^5 times slower than observed in the coarse-grained simulations. We conjecture that the ratio between the crystallization times may be associated with the ratio between the characteristic times of diffusion of water in the experiment and the model. Further simulation studies at temperatures for which experimental crystallization and diffusion data for water is available are necessary to assess the validity of this hypothesis.

The characteristic time for crystallization of water at 180 K is mainly determined by the growth of ice. The formation of viable nuclei (larger than the critical size, which we estimate to consist of less than ten molecules) occurs in less than 2 ns, a time that is *shorter* than the time needed for the equilibration of the liquid. This implies that at 180 K, and probably throughout all "no-man's land", liquid water is in what Kiselev labeled the "nonthermodyamic habitat,"[62–64] where a liquid cannot be equilibrated because the characteristic time for the formation of a critical nucleus is comparable to or shorter than the relaxation time to local equilibrium. This scenario was already anticipated by Kauzmann in 1948 as the resolution of his now famous paradox on the entropy of liquids becoming negative when extrapolated into the deeply supercooled regime: "The following resolution of the paradox is proposed: there is reason to believe that as the temperature is lowered, the 'ambiguous' regions of phase space intermediate between the definitely crystalline and definitely liquid regions begin to be able to contribute significantly to the partition function of the liquid. This means that the free energy barriers between the liquid and the crystal tend to become relatively small at low temperatures. In particular, the barrier to crystal nucleus formation, which tends to be very large just below the melting point, may, at low temperatures, be reduced to approximately the same height as the free energy barriers which impede molecular reorientations in the liquid and which have been shown to be responsible for glass formation. Under these circumstances, crystal nuclei will form and grow at about the same rate as the liquid changes its structure following a change in temperature or pressure. In other words, the time required for the liquid to crystallize becomes of the same order as the time required for it to change its structure following some change in its surroundings. If, then, measurements are to be made on such a liquid before it has had a chance to crystallize, these measurements must also be made before the liquid can bring its structure into equilibrium with its surroundings."[65] This is the case for liquid water at 180 K: the local structure of liquid water, after undergoing a structural transition at higher temperature involving a decrease in density, has nearly attained the rdf, fraction of four-coordinated molecules and tetrahedrality of LDA, which is itself very close in local structure to crystalline ice I.[43] As the liquid approaches the local structure of ice, the barriers that separate the liquid and ice states decrease, making nucleation unavoidable before liquid water relaxes to a local thermodynamic equilibrium. The mobility of water decreases with time and it is strongly subdiffusive due to the concurrent crystallization. Although we find that water presents considerable mobility at 180 K [in disagreement with a recent conjecture that water is a solid glass below 228 K (Ref. 66)], our results indicate that the equilibrium diffusion coefficient of water cannot be determined in "no-man's land" because by the characteristic time of the crystallization of ice, the molecules have displaced over just three molecular diameters.

The simulations predict that the kinetics of ice crystallization at 180 K follows Avrami's equation with $n \approx 1.7$, in excellent agreement with the $n=1.5\pm0.2$ determined from experiments of crystallization of warmed-up LDA around 150 K.[54,55] We find that crystallization occurs through random nucleation and growth of the crystallites. We distinguish three stages in the crystallization of ice: a first stage during which the density of ice nuclei increases at the same time as the nuclei grow in size, a second stage in which the density of nuclei decreases due to the consolidation of neighboring ice nuclei into larger crystallites, and a third stage during which the crystallites grow slowly without any change in the number of ice clusters. At the end of the crystallization, 80%–85% of the liquid has crystallized (50%–60% forming the core of the crystallites, the rest paving their surfaces). The remaining ~20% of the water molecules remained in the amorphous phase in the interstices between ice domains. Our results are consistent with the analysis of Jenniskens and co-workers, who investigated the changes in the structure and morphology of the crystallized water films from 140 to 210 K and concluded that liquid ice was present in coexistence with the ice crystallites,[25] and the analysis of Dohnalek *et al.*, who estimated that about 65% of the water is in the crystal state after LDA is crystallized around 140 K.[36] The latter is comparable to the percentage of core ice obtained at the end of the crystallization trajectories. The characteristic sizes of the crystalline ice domains at the end of the crystallization (see Fig. 4) range from about 3 to 10 nm, in good agreement with the ~7 nm deduced from the broadening of the diffraction peaks in Ref. 10. The nanoscopic size of the ice crystallites, which decreases their melting point according to the Gibbs–Thomson effect,[67] may be responsible for the lack of significant driving force for further growth during stage III. The nanocrystalline state, however, should be metastable with respect to the consolidation into macroscopic crystals; thus, we expect a very slow evolution toward larger

ice crystals and higher fraction of ice as the system evolves toward equilibrium. The time scale of that aging process should be controlled by the kinetic barriers for the consolidation of crystallites into seamless larger ice crystals.

It may be surprising that a model without hydrogen atoms is able to describe the structure of water and its mechanism of crystallization. We note, however, that although the hydrogen atoms are not present in the mW model, their effect on the organization of the water molecules is taken into account through the three-body term of the mW potential that encourages tetrahedral configurations. Thus, effectively, mW produces hydrogen-bonded structures without the explicit inclusion of hydrogen atoms. In this respect, we previously demonstrated that the mW model reproduces the structure of ice, clathrates, liquid, and LDA, and the phase transformations between them.[42–47] The results of this work, along with our previous study of the melting, nucleation, and structure of ice in hydrophilic nanopores[46] and ice confined between parallel surfaces,[47] indicate that the mW model is appropriate to gain insight into the microscopic mechanism of nucleation and growth of ice.

ACKNOWLEDGMENTS

This work was supported by the Beckman Foundation through a Young Investigator Award to V.M. . We acknowledge the Center of High Performance Computing of the University of Utah for allocation of computing time and Bruce Kay for his comments on the time dependence of ice growth.

[1] O. Mishima and H. E. Stanley, Nature (London) **396**, 329 (1998).
[2] P. G. Debenedetti, J. Phys.: Condens. Matter **15**, R1669 (2003).
[3] D. J. Safarik and C. B. Mullins, J. Chem. Phys. **121**, 6003 (2004).
[4] R. S. Smith and B. D. Kay, Nature (London) **398**, 302 (1999).
[5] S. M. McClure, E. T. Barlow, M. A. Akin, D. J. Safarik, T. M. Truskett, and C. B. Mullins, J. Phys. Chem. B **110**, 17987 (2006).
[6] E. Whalley, Science **211**, 389 (1981).
[7] B. J. Murray, D. A. Knopf, and A. K. Bertram, Nature (London) **434**, 202 (2005).
[8] D. A. Hegg and M. B. Baker, Rep. Prog. Phys. **72**, 056801 (2009).
[9] P. Jenniskens and D. F. Blake, Science **265**, 753 (1994).
[10] P. Jenniskens and D. F. Blake, Astrophys. J. **473**, 1104 (1996).
[11] J. L. Finney, A. Hallbrucker, I. Kohl, A. K. Soper, and D. T. Bowron, Phys. Rev. Lett. **88**, 225503 (2002).
[12] G. P. Johari, G. Fleissner, A. Hallburcker, and E. Mayer, J. Phys. Chem. **98**, 4719 (1994).
[13] R. J. Speedy, P. G. Debenedetti, R. S. Smith, C. Huang, and B. D. Kay, J. Chem. Phys. **105**, 240 (1996).
[14] P. H. Poole, F. Sciortino, U. Essmann, and H. E. Stanley, Nature (London) **360**, 324 (1992).
[15] S. Sastry, P. G. Debenedetti, and F. Sciortino, Phys. Rev. E **53**, 6144 (1996).
[16] R. J. Speedy, J. Phys. Chem. **86**, 982 (1982).
[17] C. A. Angell, Science **319**, 582 (2008).
[18] H. Tanaka, J. Chem. Phys. **112**, 799 (2000).
[19] C. A. Angell, Annu. Rev. Phys. Chem. **55**, 559 (2004).
[20] O. Mishima and H. E. Stanley, Nature (London) **392**, 164 (1998).
[21] L. P. N. Rebelo, P. G. Debenedetti, and S. Sastry, J. Chem. Phys. **109**, 626 (1998).
[22] O. Mishima, L. D. Calvert, and E. Whalley, Nature (London) **314**, 76 (1985).
[23] M. M. Koza, H. Schober, H. E. Fischer, T. Hansen, and F. Fujara, J. Phys.: Condens. Matter **15**, 321 (2003).
[24] R. J. Nelmes, J. S. Loveday, T. Strässle, C. L. Bull, M. Guthrie, G. Hamel, and S. Klotz, Nat. Phys. **2**, 414 (2006).
[25] P. Jenniskens, S. F. Banham, and D. F. Blake, J. Chem. Phys. **107**, 1232 (1997).
[26] I. Kohl, E. Mayer, and A. Hallbrucker, Phys. Chem. Chem. Phys. **2**, 1579 (2000).
[27] R. Souda, J. Phys. Chem. B **112**, 11976 (2008).
[28] R. Souda, Phys. Rev. Lett. **93**, 235502 (2004).
[29] G. P. Johari, J. Chem. Phys. **122**, 194504 (2005).
[30] B. J. Murray and A. K. Bertram, Phys. Chem. Chem. Phys. **8**, 186 (2006).
[31] S. N. Bhat, A. Sharma, and S. V. Bhat, Phys. Rev. Lett. **95**, 235702 (2005).
[32] E. Mayer and A. Hallbrucker, Nature (London) **325**, 601 (1987).
[33] T. C. Hansen, M. M. Koza, P. Lindner, and W. F. Kuhs, J. Phys.: Condens. Matter **20**, 285105 (2008).
[34] T. C. Hansen, M. M. Koza, and W. F. Kuhs, J. Phys.: Condens. Matter **20**, 285104 (2008).
[35] W. F. Kuhs, D. V. Bliss, and J. L. Finney, J. Phys. (Paris) **48**, 631 (1987).
[36] Z. Dohnálek, G. A. Kimmel, R. L. Ciolli, K. P. Stevenson, R. S. Smith, and B. D. Kay, J. Chem. Phys. **112**, 5932 (2000).
[37] M. Matsumoto, S. Saito, and I. Ohmine, Nature (London) **416**, 409 (2002).
[38] L. Vrbka and P. Jungwirth, J. Phys. Chem. B **110**, 18126 (2006).
[39] R. Radhakrishnan and B. L. Trout, J. Am. Chem. Soc. **125**, 7743 (2003).
[40] D. Quigley and P. M. Rodger, J. Chem. Phys. **128**, 154518 (2008).
[41] A. V. Brukhno, J. Anwar, R. Davidchack, and R. Handel, J. Phys.: Condens. Matter **20**, 494243 (2008).
[42] V. Molinero and E. B. Moore, J. Phys. Chem. B **113**, 4008 (2009).
[43] E. B. Moore and V. Molinero, J. Chem. Phys. **130**, 244505 (2009).
[44] L. C. Jacobson, W. Hujo, and V. Molinero, J. Phys. Chem. B **113**, 10298 (2009).
[45] L. C. Jacobson and V. Molinero, J. Phys. Chem. B **114**, 7302 (2010).
[46] E. B. Moore, E. de la Llave, K. Welke, D. A. Scherlis, and V. Molinero, Phys. Chem. Chem. Phys. **12**, 4124 (2010).
[47] N. Kastelowitz, J. C. Johnston, and V. Molinero, J. Chem. Phys. **132**, 124511 (2010).
[48] L. Xu and V. Molinero, J. Phys. Chem. B **114**, 7320 (2010).
[49] S. Jähnert, F. Vaca Chavez, G. E. Schaumann, A. Schreiber, M. Schoenhoff, and G. H. Findenegg, Phys. Chem. Chem. Phys. **10**, 6039 (2008).
[50] R. C. DeMille and V. Molinero, J. Chem. Phys. **131**, 034107 (2009).
[51] S. J. Plimpton, J. Comput. Phys. **117**, 1 (1995).
[52] E. Mayer, J. Phys. Chem. **90**, 4455 (1986).
[53] J. W. Christian, *The Theory of Transformations in Metals and Alloys. Part I: Equilibrium and General Kinetic Theory*, 2nd ed. (Pergamon, Oxford, 1975).
[54] W. Hage, A. Hallbrucker, E. Mayer, and G. Johari, J. Chem. Phys. **100**, 2743 (1994).
[55] W. Hage, A. Hallbrucker, E. Mayer, and G. Johari, J. Chem. Phys. **103**, 545 (1995).
[56] B. Schmitt, S. Espinasse, R. J. A. Grim, J. M. Greenberg, and J. Klinger, in *Laboratory Studies of Cometary Ice Analogues*, Physics and Mechanics of Cometary Materials, ESA SP-302, edited by J. Hunt and T. D. Guyenne (European Space Agency (ESA) Publication Division, Noordwijk, Netherlands, 1989), pp. 65–69.
[57] R. S. Smith, C. Huang, E. K. L. Wong, and B. D. Kay, Surf. Sci. **367**, L13 (1996).
[58] G. Malenkov, J. Phys.: Condens. Matter **21**, 283101 (2009).
[59] H. Scher and R. Zallen, J. Chem. Phys. **53**, 3759 (1970).
[60] E. B. Moore and V. Molinero, "Is it cubic? Ice crystallization from deeply supercooled water," J. Chem. Phys. (to be submitted).
[61] K. Morishige and H. Uematsu, J. Chem. Phys. **122**, 044711 (2005).
[62] S. B. Kiselev and J. F. Ely, J. Chem. Phys. **118**, 680 (2003).
[63] S. B. Kiselev, Int. J. Thermophys. **22**, 1421 (2001).
[64] S. B. Kiselev, Physica A **269**, 252 (1999).
[65] W. Kauzmann, Chem. Rev. (Washington, D.C.) **43**, 219 (1948).
[66] J. Swenson and J. Teixeira, J. Chem. Phys. **132**, 014508 (2010).
[67] B. Wu, S. W. McCue, P. Tillman, and J. M. Hill, Appl. Math. Model. **33**, 2349 (2009).

Chapter 7

IS IT CUBIC? ICE CRYSTALLIZATION FROM DEEPLY SUPERCOOLED WATER

Abstract

Water crystallization at 180 K is studied using large-scale molecular dynamics simulations of the mW water model. At this temperature, crystallization results in cubic ice with hexagonal stacking faults, though it is unclear how the cubic ice structure develops and how the hexagonal stacking faults form. In this work, we find that the relative amounts of cubic and hexagonal ice are kinetically controlled. Preferential development of cubic ice over hexagonal ice begins prior to the development of regular stacking patterns, starting with ice clusters as small as five molecules and continuing through clusters larger than 20,000 molecules. The size of the smallest cluster for which cubic ice is preferred precludes arguments for the cubic ice preference based upon growth of ice from the cubic or hexagonal unit cells. The stacking patterns that develop occur nearly randomly throughout the ice structures, with growth and deformation faults found. We also find that large ice crystallites are formed through a process of consolidation. In this process, multiple small clusters join, through direct attachment or rearrangement mechanisms. For all systems, the resulting structures contain a single large ice crystallite consisting of 15 ± 1% hexagonal ice, 35 ± 3% cubic ice and 30 ± 1% interfacial ice, though the static structure factor fails to show any characteristic

hexagonal ice peaks. In fact, characteristic cubic ice peaks cannot be distinguished until 10% of the system is cubic and hexagonal ice (25% interfacial).

Introduction

Recent experiments have shown that homogeneous freezing of water results in cubic ice at temperatures up to ~235 K, much higher than previously thought possible. Earth's atmosphere, from the upper troposphere to the lower mesosphere, has temperatures ranging from 200 K to less than 120 K.[1] An important mechanism for cloud development within these regions is the homogeneous nucleation of ice from aqueous aerosols, previously thought to freeze predominately to the hexagonal ice structure. Freezing to the cubic ice structure would result in cloud microphysics different from those predicted, altering our understanding of the processes typical within these clouds and requiring changes in current cloud modeling efforts.

Observations of the rare Schiener's halo, first described in 1629,[2] was proposed to be the result of refracted light from cubic ice in the atmosphere by Whalley in 1981.[3] For this to be true, cubic ice would have to develop from the liquid under atmospheric conditions. Experimental difficulty in observing formation of cubic ice from liquid water lead, in part, to the proposal that Schiener's halo may be due to development of polycrystalline hexagonal ice and may not provide evidence of atmospheric cubic ice at all.[4] While laboratory formation of cubic ice was first observed, through recovery of high pressure ice, as a new crystalline structure by Dewar in 1905[5] and first characterized as cubic ice from samples obtained through vapor deposition by Konig in 1942,[6] formation of cubic ice from the liquid was not observed until 1987, when hyperquenched aerosol droplets were found to crystallize to the cubic structure.[7] Since then, cubic ice has been found from direct measurements of characteristic cubic diffraction patterns in ice particles from the atmosphere, constituting 25% of the ice particles in one study of

Antarctic polar stratospheric clouds.[8] More recent studies show that homogeneous nucleation of pure water and aqueous solution aerosols result in cubic ice at temperatures as high as ~235 K and are metastable up to 243 K.[9,10] Studies prior to this reported homogeneous nucleation of pure water droplets to predominately cubic ice only when hyperquenched to temperatures of 190 K or lower.[7] Based on the new, higher temperatures at which cubic ice has been observed, reanalysis of the homogeneous nucleation data obtained to date,[11] along with studies to expand our current understanding of cubic ice are underway by atmospheric scientists, with the goal of better understanding the role of cubic ice in cold cloud processes.

Of particular interest is the nanoscopic structure of cubic ice within cirrus clouds found in the upper troposphere and in polar stratospheric and mesospheric clouds, which play important roles in determining Earth's climate. Cirrus clouds, covering 20-30% of Earth, exert radiative warming by scattering incoming sunlight and absorbing radiation from the Earth's surface.[12] Polar stratospheric and mesospheric clouds provide sites for chemical reactions that contribute to ozone depletion. The structure of the ice particles, determined by the particle formation conditions, affects the optical and chemical properties of the clouds.

Transformations between phases in atmospheric water droplets depend strongly on temperature. Atmospheric water can exist in multiple crystalline and amorphous phases with a complex series of size, time and temperature dependent phase transitions possible. The crystalline phases include hexagonal and cubic ice, while water's amorphous phases include the liquid, supercooled liquid (liquid water below the melting temperature, T_m) and the highly viscous amorphous solid water found at temperatures below 150 K.[13] Supercooled liquid water can exist down to a temperature of ~235 K before crystallization becomes unavoidable.[14] While hexagonal ice is the stable phase below T_m, nucleation to the metastable cubic ice has been observed from 160 - 240 K

before transforming to hexagonal ice over time. Cubic and hexagonal ice have different radiative properties and the transition from cubic to hexagonal ice can result in dehydration of the cold clouds, altering the water vapor concentration.[15] In comparison to a cloud containing atmospheric water particles that freezes predominately to hexagonal ice, crystallization to cubic ice would result in significantly different microphysical properties. [16,17] It is currently unclear what crystal structures predominate from the freezing of water under typical conditions in the upper atmosphere.[10]

The differences between cubic and hexagonal ice are subtle but significant.[16] Hexagonal and cubic ice have similar densities, though cubic ice has a higher vapor pressure[16] and lower melting temperature. From calculations of the free energies of cubic and hexagonal ice over temperatures from 53-273 K the free energy of hexagonal ice was found to be about 100 J mol^{-1} lower than cubic.[18] Cubic ice consists of connected six-membered rings, all in chair conformation with each water molecule forming a tetrahedron with its four nearest neighbors. Hexagonal ice consists of six-membered rings also, but two-thirds of the rings form the chair conformation perpendicular to the hexagonal axis, while the remaining third form the boat conformation. During crystal growth, conversion from a cubic to a hexagonal layer can occur through a 60° or 180° rotation about the 111 plane of cubic ice.[19] Rotations occurring during the growth of cubic ice result in hexagonal ice stacking faults within the cubic ice structure.

The observance of cubic ice nucleating from supercooled water is consistent with the empirically determined Ostwald step rule,[20] in which crystallization from solution occurs first to the structure that is easiest to form, rather than the most stable, with a transition to the most stable ice structure occurring in a subsequent step. The preferential formation of the metastable cubic ice over the hexagonal structure has long been attributed to a lower surface tension in the cubic ice nucleus when compared to hexagonal ice.[19,21-23] Theoretically, it has been determined that the 111 plane of cubic ice

has a lower interfacial energy than the basal or prism planes of hexagonal ice below a critical temperature.[21] This argument depends on the critical nucleus in both ices having the faceted structure of pure cubic or hexagonal ice. In chapter 6, we showed that the critical nucleus at 180 K consists of around 10 core molecules, too small to show specific faceted character. In order to answer fully the question of why cubic ice forms instead of hexagonal, the structure of the critical nuclei that lead to the growth of cubic ice is needed.

The relative amount of cubic ice and the structure of any constituent hexagonal stacking faults at conditions found in the atmosphere have yet to be determined. Recent studies of cubic ice formed in the laboratory include vapor deposition,[24] relaxation of high pressure ices by warming at ambient pressure[25] and cooling emulsions of microdroplets.[9] Analysis of the resulting cubic structures show evidence of the 100 hexagonal plane, suggesting that hexagonal stacking faults are intrinsic to the naturally forming cubic ice structure.[26,27] Indeed, stacking faults, along with the presence of amorphous water, make exact determinations of the structure of cubic ice under various conditions difficult.[25] From fits to neutron powder diffraction analysis of the decompression of ice V and IX, Hansen et al.[25] found that the amount of cubic ice present remained in the 90 - 95% range from 165 - 190 K, where hexagonal ice was found predominately within two-layer deformation faults within the cubic structure. The amount of cubic ice decreased significantly to about 40% at 200 K and continued to decrease until pure hexagonal ice was found at 240 K. During the transition to hexagonal ice, the amount of cubic and hexagonal interfaces, where a rotation had led to a switch from cubic (hexagonal) to hexagonal (cubic), did not increase, suggesting that the transition into hexagonal ice occurs through growth of the hexagonal deformation faults to include more layers at the expense of the cubic ice. Murray and Bertram[9] found that water droplets less than 10 microns in diameter cooled from room temperature to 173 K

contain from 50-80% cubic ice, with smaller droplets corresponding to the higher percentages of cubic ice. This size dependence is an effect of the more efficient transfer of evolved heat from crystallization in smaller droplets, while larger droplets heat up towards the cubic to hexagonal recrystallization temperature.[11]

In addition to the issue of which ice phase is present, amorphous water can also coexist with the ice.[28,29] Liquid water in bulk cannot be equilibrated at temperatures below ~235 K, though Jenniskens et al. found significant percentages of amorphous water, up to 50%, coexisting with cubic ice in vapor deposited water. In that study, cubic ice developed at 160 K through rapid growth of small ice domains, within an amorphous water matrix.[24] The resulting cubic ice was thought to have layers of liquid or amorphous water covering the crystallites, as evidenced by significant peak broadening found in structure factor analysis.

In this chapter, we focus on the evolution of cubic and hexagonal ice features throughout crystallization from the liquid at 180 K, a temperature under which upper tropospheric cirrus and polar stratospheric clouds form. We utilize the mW model in large-scale molecular dynamics simulations allowing analysis of the evolution of cubic ice with stacking faults at length scales large enough to permit spontaneous appearance of many nuclei, development of stacking faults and the consolidation of growing nuclei into larger crystallites. We first describe the final ice structures obtained from the simulations and compare these with experiments. We then describe the development of hexagonal and cubic local symmetry within the nuclei, including the appearance of stacking patterns. Finally, we show two mechanisms through which consolidation of neighboring nuclei into larger crystallites occurs. Implications of these findings within the context of cold cloud formation are then discussed.

Methods

Simulations

The mW water model, introduced in chapter 2, is used in all simulations. Molecular dynamics (MD) simulations of water in bulk were performed using LAMMPS.[30] The systems consisted of 32,768 mW particles in cubic simulation cells (~10 nm edge length), simulated with periodic boundary conditions. The equations of motion were integrated using the velocity Verlet algorithm with time step 10 fs. The Nose-Hoover thermostat and barostat were used to control the temperature and pressure (NPT ensemble), with relaxation times of 1.0 and 5.0 ps, respectively.

Isothermal Crystallization of Water. Two different sets of liquid configurations were used as starting points for the isothermal simulations considered in this study: five initial configurations were obtained from instantaneous quenching of liquid water from 300 to 110 K, with 0.3 ns at 110 K, followed by an instantaneous warm-up from 110 to 180 K. We refer to these as the *QL* systems. We obtained a sixth initial configuration by fast warming to 180 K of a previously formed LDA glass. We refer to this system as *WG*. Upon reaching 180 K, for all systems, the temperature was held constant and the system was allowed to evolve for 590 ns (*QL* systems) and 600 ns (*WG* system).

Ice Identification

As a measure of water's crystallinity during nucleation and growth, we utilize the CHILL algorithm described previously in chapter 4 for the identification of cubic and hexagonal ice in confined water.

Identification of Nuclei and Crystallites. To characterize individual ice nuclei, we use the same clustering method as described in chapter 6. In this case, we distinguish between C and H molecules, while in chapter 6 we considered these 'core' molecules without differentiating between the two structures.

Static Structure Factor. The static structure factor S(q), was computed from the radial distribution function, g(r) as in chapter 3. The results for S(q) determinations are shown for three different types of systems in this chapter. In the case of the hyperquenched water, the focus of this chapter, S(q) was determined for individual configurations at intervals during the crystallization of hyperquenched water. For comparison with purely hexagonal and purely cubic systems, the S(q) was determined for pure hexagonal and pure cubic ice structures in NPT simulations at 195 K using simulation cells with linear dimensions ~50 nm. Also for comparison, the S(q) for low-density amorphous water (LDA) was obtained from a single configuration taken at 150 K after quenching liquid water from 300 K at a rate of 10 Ks^{-1} for a system with linear dimensions of 10 nm.

Results

A series of instantaneous quenches from liquid water at 300 K to the supercooled liquid at 180 K were produced, resulting in trajectories in which crystallization occurs. These were generated from a single trajectory at 300 K, where five configurations were selected at 3 ns intervals from which new simulations were initiated and evolved at 180 K and 1 atm for 590 ns. We refer to these systems as the *quenched liquid* systems (QL). We obtained a sixth initial configuration by fast warming to 180 K of a previously formed LDA glass. We refer to this system as the *warmed glass* (*WG)*. Using the CHILL algorithm, we differentiate between cubic, hexagonal and interfacial ice and the liquid throughout crystallization, allowing for a microscopic analysis of the evolution of ice formation. Throughout this chapter, C is used to represent molecules with cubic local symmetry and H for molecules with hexagonal local symmetry. C+H refers to the total amount of C and H molecules in the system at the point in the crystallization process being described.

In chapter 6 we distinguished three stages in the crystallization process of water at 180 K, based upon the development, consolidation and growth of the ice nuclei. We consider ice nuclei as clusters of more than ten C and H molecules.

Stage I. This stage consists of the development and growth of multiple ice nuclei, distributed throughout the simulation cell. Development of the initial nuclei is quick, with all five QL systems containing viable nuclei by t = 3 ns. We estimate that the critical ice nuclei at 180 K contain less than ten molecules, based upon the size of nuclei that grow without dissolution. In both QL and WG, these initial nuclei continue to grow as new nuclei develop, until crowding of neighboring nuclei within the simulation cell occurs. Once this begins, the total number of individual nuclei reaches a maximum of ~0.05 nuclei/nm^3 (45±15 nuclei in 1000 nm^3 volume), signaling the beginning of Stage II.

Stage II. Growth of the nuclei continues with crowding leading to consolidation of neighboring nuclei, decreasing the total amount of individual nuclei until only a few (1-4) remain. Of the remaining nuclei, one consists of more than 10,000 molecules, while the remaining few nuclei consist of less than 200 molecules. The nuclei, and regions within the same nuclei, are separated by interfacial ice and amorphous water.

Stage III. The final stage is reached at the end of the consolidation process (~250 ns for WG and ~350 ns for QL) when the ice crystallites become too large to consolidate further within the time scale of the simulation. This stage is characterized by a slow growth in the size of crystallites without any change in the number of ice nuclei.

At the end of the crystallization, 80% of the liquid has crystallized (~50% C+H, cubic ice with hexagonal stacking faults, the rest being interfacial ice covering the crystallite surface). The leftover 20% of the water molecules remain as amorphous water in the interstices between ice domains.

From the kinetics of ice formation, we now turn attention to the cubic and hexagonal structure of the resulting ice. First, the final crystal structures obtained from the simulations will be compared to experimental cubic ice. The process of crystallization will then be described, starting with the development of the initial nuclei, development of stacking patterns, onset of cubic structure preference and then the mechanisms for consolidation into the larger crystallites.

Final Ice Structure: Composite of Cubic and Hexagonal Ice

Pure cubic and pure hexagonal ices have give different diffraction patterns, resulting in different characteristic peaks in their structure factors.[31] Analysis of the structure factor of an ice sample can indicate the presence (or absence) of cubic and hexagonal ice structures. Figure 7.1 (panels a and b) show the structure factors for pure hexagonal ice and pure cubic ice from q = 1 - 5 $Å^{-1}$ (1.3 - 6.3 Å) obtained from simulations of the pure structures as outlined in the methods section. Peaks are labeled with the Miller indices of the crystal planes. The main characteristic peaks found in the structure factor of hexagonal ice include a triplet of peaks corresponding to the 100, 002 and 101 hexagonal ice planes centered at 1.7 $Å^{-1}$, a singlet at 2.3 $Å^{-1}$ (102) and a second triplet of peaks (110, 103 and 112) with the two outer edges found at 2.8 (110) and 3.3 $Å^{-1}$ (112). The main characteristic peaks in the structure factor of cubic ice include three single peaks at 1.7, 2.8 and 3.3 $Å^{-1}$, corresponding to the 111, 220 and 311 cubic ice planes, respectively.[7,9,25] Peaks found in experiment and those found in simulations are compared in the following sections.

Experimental determinations of the structure factor of cubic ice show the peaks characteristic of the cubic ice structure and at least the 100 peak of hexagonal ice, indicative of stacking faults. Increasing presence of hexagonal peaks is typical, with heating above 240 K resulting in a transition to hexagonal ice. X-ray analysis of

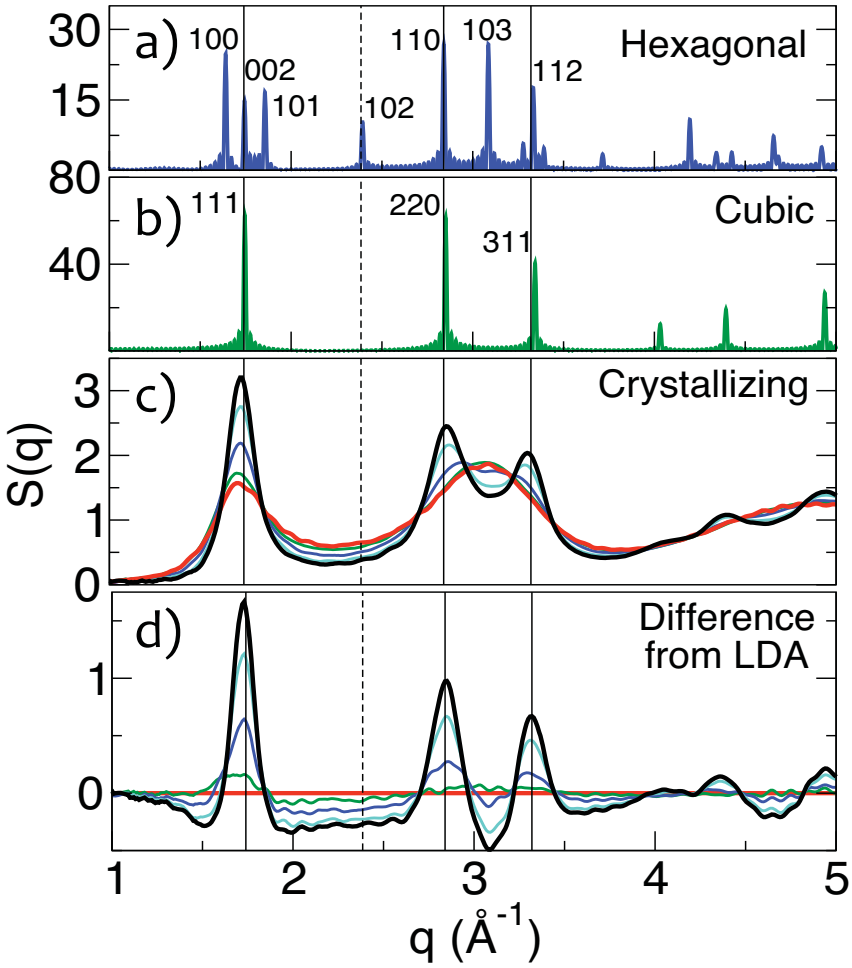

Figure 7.1. Evolution of Ice Development in Static Structure Factor
The S(q) is shown first for pure hexagonal ice and cubic ice. Relevant peaks have been labeled with their Miller indices. The S(q) for a single QL simulation at various percentages of C+H content is shown, along with the S(q) for LDA. (LDA in red, 5% C+H in green, 10% C+H in blue, 20% C+H in turquoise and 50% C+H in black) To highlight the evolution of peaks as the amount of ice within the system increases, the bottom panel shows the difference from LDA (colors same as in 'crystallizing' S(q) panel. Vertical lines at 1.74, 2.34 (dashed), 2.84 and 3.32 provide a guide to the eyes for comparison of the presence (solid) or absence (dashed) for four relevant peaks.

micron-sized water droplets hyperquenched at rates of 10^6 - 10^7 Ks^{-1} to temperatures ranging from 130 - 190 K by Kohl et al.[26] resulted in X-ray diffractograms with the 100 hexagonal peak and increasing cubic number and intensity of cubic peaks as the temperature of droplet deposition increased. At a temperature of 130 K, only the hexagonal 100 and cubic 111 peaks were discernable, while at 190 K all characteristic cubic peaks were clearly present with the additional hexagonal 100 peak. Above 230 K, a phase transition from cubic to hexagonal ice was observed.

From the neutron powder diffraction data of the ice V recovered to room pressure at temperatures from 145 – 240 K, Hansen et al.,[25] found similar results in the temperature range of 147 – 185 K. From temperatures of 190 K and up, they found a mixture of characteristic peaks in the structure factor, with the hexagonal 101 and 102 peaks appearing. By 240 K the system converted to hexagonal ice, with a structure factor matching that of pure hexagonal ice with no cubic peaks present.

From selected area x-ray diffraction studies of a 10 μm diameter area of vapor-deposited water, Jenniskens and Blake[32] monitored the growth of cubic ice from the increase in intensity of the 220 cubic ice peak. Around 150 K, the cubic 220 and 311 peaks become distinguishable from the amorphous water background, and continue to become more defined until development of the 220 peak slowed at about 165 K. Further heating resulted in sublimation at 180 K.

Final crystal structures from *QL* and *WG* systems are shown in Figure 7.2. Crystallization of mW hyperquenched in a periodic, 1000 nm^3 sized simulation cell, results in a single large crystallite consisting of stacking-faulted cubic and hexagonal ice, with 1-2 small nuclei (<200 molecules) remaining. Each crystallite is bordered by interfacial ice and amorphous water.

Figure 7.1(c) shows the evolution of the structure factor during the development of ice in the simulations. The structure factor results from one trajectory is shown, but all

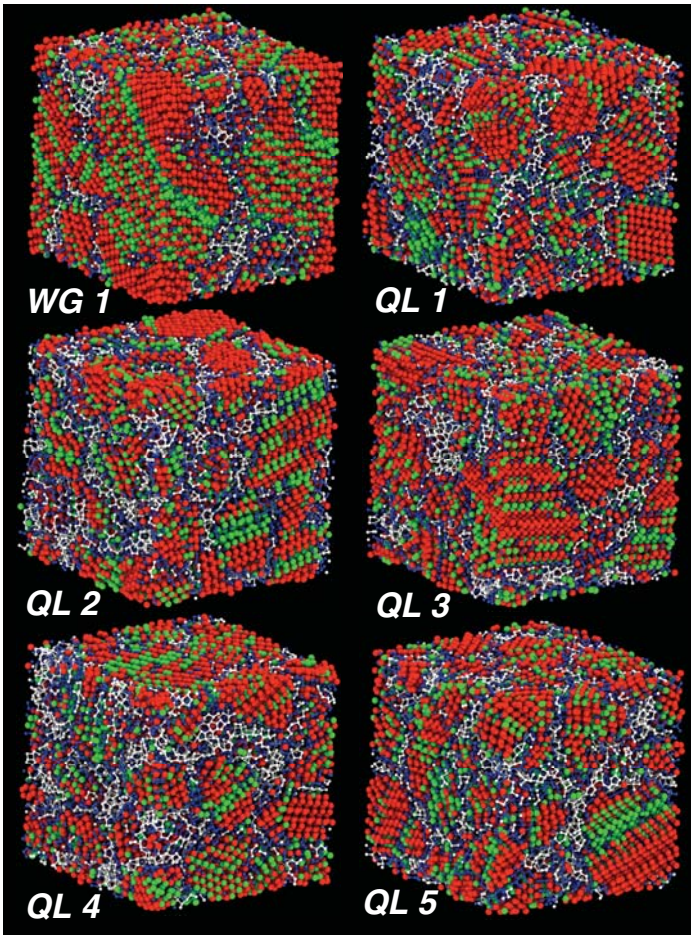

Figure 7.2. Final Ice Structures
Final structures of water in the six simulation cells (one WG system and five QL systems) are shown after 590 ns at 180 K. The C molecules are shown in red, H in green, the interfacial ice in blue and the liquid in grey. The simulation cells are 10 nm per side and periodic in the three dimensions.

trajectories, QL and WG, follow similar changes in structure factor during crystallization. To further highlight the development of structure, we show the S(q) results with 100% of the LDA S(q) subtracted in Figure 6(c). Initially, liquid water at 180 K has a structure similar to that of LDA, with broadened peaks at 1.7 $Å^{-1}$ and 3.2 $Å^{-1}$. At 5% *C+H* (the total amount of C molecules plus the total amount of H molecules), there is a slight sharpening of the 1.7 $Å^{-1}$ peak, but no other discernable differences from the LDA structure factor curve. At 10% *C+H*, other characteristically cubic peaks begin to appear, including the beginnings of the 2.8 and 3.3 $Å^{-1}$ peaks, in addition to further sharpening of the 1.7 $Å^{-1}$ peak. Increased sharpening of the three characteristic cubic peaks continues, resulting in broadened peaks at 1.7, 2.8 and 3.3 $Å^{-1}$ for the final crystal structure (50% C+H).

Overall, the changes in structure factor throughout crystallization in the simulations are in good agreement with the results found from the determination of the crystal structure of hyperquenched water droplets, vapor deposited water and recovered ice V. The lack of a distinguishable 100 peak can be attributed to the significant broadening of the peaks, which is due to the presence of amorphous water, crystallite size and random orientation of regions of the crystallites.[29]

In the following section, we compare the results obtained from the crystallization simulations to those of the experimental results based on the amount of amorphous ice and the presence of stacking faults.

Presence of Amorphous Water. The coexistence of cubic ice and liquid or amorphous water is thought to occur in the temperature range of 140-210 K based on changes found in the structure and morphology of crystallizing water films.[29] The amount of amorphous ice that persists up to the transition to hexagonal ice is unclear. In the work of Jenniskens, et al.,[29] crystallization from the low density amorphous ice was found to occur within regions of restrained amorphous water. The restrained amorphous

water has a structure that is slightly more ordered than the low density amorphous ice. They propose that the restrained amorphous water they observe coexisting metastably with the cubic ice contains short-range hexagonal stacking order, which prevents its incorporation into the developing cubic ice. They observe 30% crystallization to cubic ice, leaving up to 70% of the water as amorphous. Kohl, et al., however, find through x-ray diffraction and differential scanning calorimetry evidence of only a 20% amorphous component.

From the simulations, the amount of amorphous water decreases from 85% at the beginning of the simulations, right before the onset of crystallization, to ~ 20% of the total system at the end of the simulations. This latter amount is similar to the maximum amount of amorphous water attributed to the droplets deposited at 190 K of Kohl et al., (with droplets deposited at lower temperatures containing more amorphous liquid, up to 95% amorphous at 130 K).

Stacking Faults. From analysis of neutron powder diffraction data, Hansen et al. [25] found that upon decompressing and warming ice V to 145-185 K and 1 atm, it yields crystallites of cubic ice with hexagonal stacking faults. The authors deduced that cubic ice constituted up to about 95% of the recovered crystallites. From a fit of the powdered diffraction data to a structural model,[33] the hexagonal stacking present was estimated to occur predominately as growth (single) and deformation (double) faults. They concluded that cubic ice recovered from ice V at 170 K contained 37% growth faults, 40% deformation faults, 23% in three, four or five layers and 1% with six or more layers. The crystallites increased in size over time and temperature, from 25 nm at 147 K to 70 nm at 190 K. On warming further, the cubic ice transformed to hexagonal ice.

Cubic and hexagonal stacking fractions were not quantitatively determined from the X-ray analysis of hyperquenched water droplets,[26] though characteristics of the diffraction results were attributed to the presence of stacking. Similarly, no quantitative

determinations of the amounts of stacking fractions was done in the study of vapor deposited water, though twinning planes (deformation faults) were observed from bright-field imaging of the samples. To the best of our knowledge, the cubic and hexagonal stacking patterns formed from warming of the LDA ice have not yet been reported.

Ice from the simulations consisted of 50 ± 3% cubic ice with hexagonal stacking. We find examples of various stacking sequences in the final WG and QL systems, Figure 7.2, with ratios of cubic to hexagonal layers from 1:1 up to 8:1, with no greater than 8 sequential cubic layers or 5 sequential hexagonal layers. As reported in the analysis of recovered ice V[25], we find that hexagonal stacking faults occur predominately in growth and deformation faults. Three or more consecutive hexagonal layers are rare, constituting less than 5% of total occurrences of hexagonal layering. We consider the resulting ice to be a composite of cubic and hexagonal ice rather than cubic ice with hexagonal impurities.

Chapter 4 includes detailed analysis of ice formed within a 3 nm diameter hydrophilic pore. Here we briefly compare relevant results from the nanoconfined crystallization to the bulk. As in the bulk system, the resulting nanoconfined ice is also rich in stacking faults. In the nanoconfined case, there were four times the amount of hexagonal growth faults as deformation faults, with the bulk containing about half as many growth faults as deformation faults. Stacking of more than three identical layers, cubic or hexagonal, were rare in the nanoconfined ice, while in the bulk up to eight layers of cubic ice is common. Similar to the nanoconfined ice, hexagonal stacking in greater than three layers is rare. Only single cases of four and five layer hexagonal stacking exist in the bulk ice structures. Confinement increases the likelihood of a mismatched layer, leading to more growth faults and a decrease in the average number of continuous cubic structure layers. The free growth possible in the bulk systems continues much farther

into the development of the nuclei, until multiple nuclei are large enough to hinder growth of their neighbors.

The hexagonal stacking faults obtained from the simulations are consistent with the results of those found previously from fits to experimental data, while in comparison to nanoconfined ice, the bulk cubic ice with stacking faults contains less stacking faults overall, and a lower prevalence of growth faults.

Development of Ice Nuclei

From small crystalline domains within the surrounding liquid, cubic ice develops, though experiments currently lack the necessary temporal and spatial resolution necessary to provide detailed descriptions of the nucleation and growth mechanism. Mechanisms inferred from the Avrami exponent, obtained from fits to the Avrami equation described in chapter 6, give unclear results that differ depending on the preparation and history of the cubic ice sample. Proposed mechanisms include a constant[24] or rapidly decreasing nucleation rate with diffusion controlled growth of spherical nuclei[34] and a constant nucleation rate with isotropic nuclei growth.[35] Development of stacking within cubic ice is also unclear from experimental studies, though the resulting ratio of cubic to hexagonal ice is typically 2:1, determined from recovered ice V[25,27,33] and nanoconfined water[36] prior to onset of the transition to hexagonal ice.

We now present a general overview of the development of cubic and hexagonal ice structures. Figure 7.3 shows snapshots of the evolution of cubic and hexagonal ice for a representative system. Nucleation occurs rapidly, with clusters containing C and H molecules found throughout the simulation cell (Figure 7.3 panel a). These initial nuclei continue to grow while new nuclei develop. Notice the beginning of stacking patterns, alternating layers of C and H, found at 10% C+H (Figure 7.3 panel b). By 25% C+H

(Figure 7.3 panel c), a process of consolidating the growing nuclei has begun, resulting in the final crystal structure (Figure 7.3 panel d), with a section of the final crystallite containing aligned layers that span the height of the simulation cell.

Figure 7.4 shows the development of cubic ice preference, the amount of C per H molecule, as a function of the total fraction of C+H, f_{C+H} in the system for the five QL and single WG crystallization trajectories. Initially, there is a slight preference for hexagonal ice, with 1 C for every 2 H molecules present, indicative of the substantial difference between the initial liquid structure and the final ice structure. Quickly the amount of C that develops overtakes the amount of H, reaching 1.5 C molecules for every H by 5% C+H and about 2 C for every H by 15% C+H. At 15% C+H content, consolidation of the nuclei begins. The development of cubic preference is similar for each crystallizing trajectory up to the onset of nuclei consolidation, where further growth of the nuclei requires cooperative rearrangements resulting in variations in the final amount of cubic preference, from 1.8 to 2.5 more C than H.

We now focus on the growth of individual nuclei from their initial appearance to the point where consolidation of neighboring nuclei into larger crystallites begins, where the total amount of cubic and hexagonal ice in the QL systems reaches 15%. This includes analysis of the initial development of nuclei, size and general morphology, and the evolution of hexagonal and cubic stacking.

At t = 0, the fraction of cubic and hexagonal ice in the QL systems is 1%, half of which consist of molecules with cubic local symmetry and half with hexagonal local symmetry. C and H molecules appear throughout the simulation cell, and are not in clusters consisting of more than four or five molecules, though most are isolated and have no C or H nearest neighbors. Once the system consists of 3% C and H, all QL trajectories have developed nuclei, with each system containing an average of five nuclei

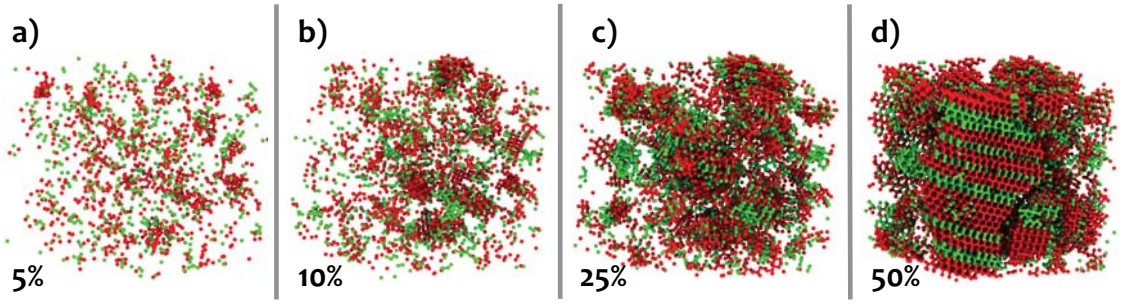

Figure 7.3. Evolution of Cubic and Hexagonal Stacking
Snapshots of a single QL trajectory at 5, 10, 25 and 50% C+H molecules is shown. The C molecules are red while H molecules are green. Notice that at 5% C+H content, small clusters of predominately C molecules are distributed throughout the simulation cell. By 10% C+H content, 5-10 clusters have begun to dominate in size. At 25% C+H consolidation has occurred such that many clusters are have grown into one another, making it difficult to distinguish between clusters visually. By 50% C+H, the end of the simulation, regions of ice span the height of the simulation cell.

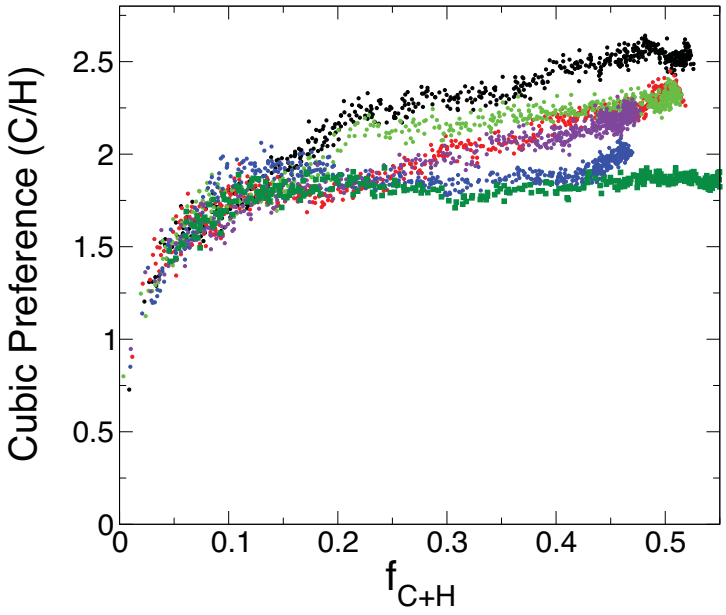

Figure 7.4. Development of Cubic Preference During Crystallization
Cubic preference, the amount of C molecules for each H molecule, increases as crystallization proceeds. Initially hexagonal is preferred, but quickly the amount of cubic ice overtakes the hexagonal ice, eventually reaching 1.8-2.5 times more cubic than hexagonal.

with 11-35 molecules. The nuclei appear as chains or clusters of complete or partially developed six-membered rings, as shown in Figure 7.5 panel a. Most of the nuclei do not consist of a single C or H type, but consist of C intermixed with H. As the majority of these initial clusters survive, growing into larger nuclei, the critical nucleus size is 10 or less at 180 K.

Typically, the process from the initial appearance of a small cluster of C and H molecules to the formation of a stable, persistent core (Figure 7.5) involves an initial stage of structural change, where the constituent molecules that make up an ice nucleus do not change significantly, but their positions, and thus each molecule's local environment, shifts. Figure 7.5 panel a shows an example of this, where a persistent core has not yet developed, though fluctuations between partial and complete six-membered rings occur. The appearance of six-membered rings stabilizes this shifting; increasing the lifetime of an individual clusters arrangement of molecules, Figure 7.5 panel b. Once multiple connected six-membered rings develop, forming a stable core typically consisting of C molecules as shown in Figure 7.5 panel c, growth continues from this core region, through addition of molecules to the outer edges, Figure 7.5 panel d.

The persistence of hexagonal structures appears dependent upon the presence of adjacent cubic structures. Pairs of H molecules often appear along the outer edges of a more developed stacking of C molecules. Once a pair of H molecules 'connects' two more developed cubic structures, growth perpendicular to the hexagonal c-axis continues with the hexagonal layer fixed in-between, representing one way that a hexagonal deformation fault forms within a predominately cubic structure, Figure 7.5 e. The presence of persistent stacking patterns appear in nuclei containing about 200 or more water molecules and is first observed when the system contains about 10% cubic and hexagonal ice.

Preference for Cubic Ice

Prior investigations of the polycrystalline nature of deeply supercooled water involved determinations of a smaller specific interfacial energy for the cubic 111 planes than the hexagonal prism or basal planes, based on a model of broken hydrogen bonds along these planes,[19] and from approximations of the interfacial energy and the enthalpy difference between the cubic and hexagonal ices[22]. For each of these determinations, it was found that below a critical temperature, the activation energy is less for a cubic embryo than a hexagonal one, thus cubic nuclei develop and grow. Our results suggest alternatively, that the cubic and hexagonal stacking patterns found upon crystallization of deeply supercooled water originate from ice clusters too small to have cubic or hexagonal planes, thus previous thermodynamic arguments for the cubic preference may not be relevant to growth of stacking faulted cubic ice.

To determine the onset of *C* preference in the ice clusters, we investigate the relative fractions of the two ice types in clusters containing 2 to 15 *C* and *H* molecules. Figure 7.6 shows the distributions for clusters of size two, five, ten and sixteen from the simulations up to 15% C+H molecules. Analysis of clusters containing two, three and four *C* and/or *H* molecules are found to follow a binomial distribution, indicating random clustering. For example, 25% of clusters containing only two molecules consist of zero C molecules (all H molecules) and 28% consist of all C molecules, the remaining 47% of clusters consist of one C molecule and one H molecule, similar to what would be expected for a random distribution of two types into pairs (25% of clusters consisting of 2 C, 25% consisting of 2 H and 50% consisting of 1 C and 1 H). For clusters consisting of five molecules or more, the distribution shifts, favoring more cubic molecules, with larger shifts occurring for larger cluster sizes. Very few clusters are found containing only C or only H molecules, particularly for clusters containing more than five molecules. Since stacking within a nucleus does not occur until much larger sizes (200 molecules or

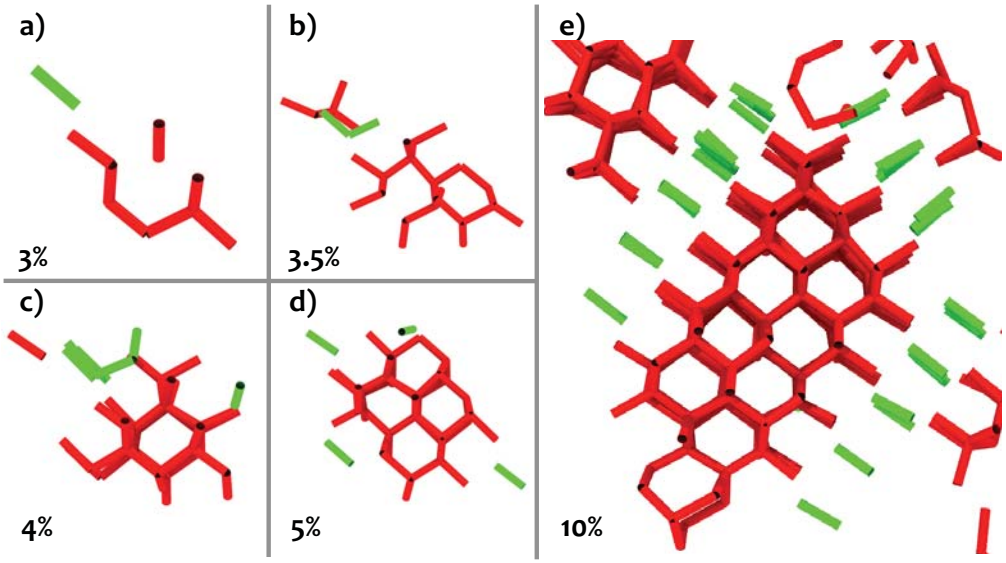

Figure 7.5 Development of Stacking within Individual Nuclei
Growth of a single nucleus from initial fluctuating cluster (panel), development of a persistent cubic core (panels b-d) up to appearance of hexagonal stacking faults. Each line corresponds to the 'bond' between neighboring C (red) and H (green) molecules.

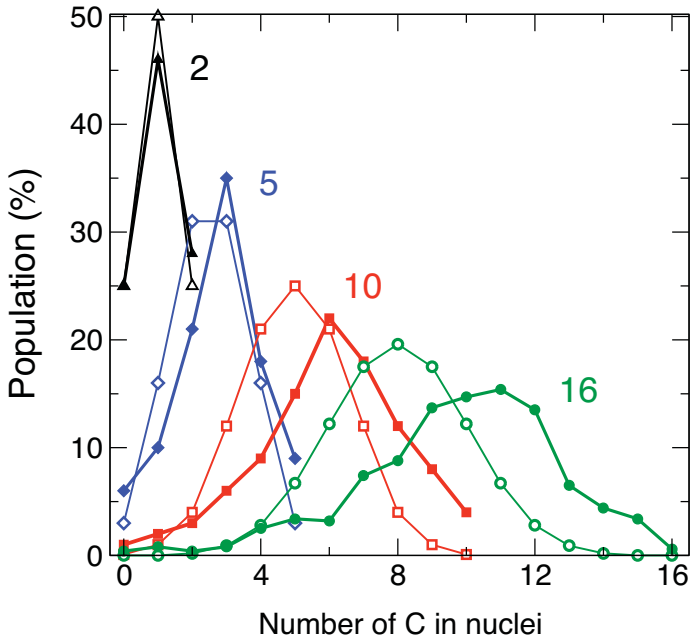

Figure 7.6. Development of Cubic Preference within Nuclei
The population distribution is shown for clusters of size two (triangles), five (diamonds), ten (squares) and sixteen (circles) water molecules. Lines with open symbols are the expected population for a random distribution, while filled symbols show actual distribution from QL simulations. The average ratio of C:H is 1 for clusters with 2 core ice molecules, 1 for size 3, 1.3 for size 5 , 1.7 for size 16.

more), the onset of cubic ice preference significantly precedes stacking development and does not occur in the presence of clusters consisting of solely cubic ice or solely hexagonal ice. Thus, we do not observe in the simulations the development of cubic or hexagonal ice from a pure cubic or pure hexagonal origin.

The mW water model accurately reproduces the experimental determinations of the melting temperature and the relative stability of the ice structures. Cubic ice has a melting temperature 3 K below hexagonal ice in the simulations, making hexagonal ice slightly more stable than cubic, as in experiments.[18] The entropy difference between the two structures is negligable, so the thermodynamic stability is represented by the enthalpy of crystallization. For a 2:1 preferences for cubic ice, there would need to be ~1 kJ mol^{-1} difference favoring cubic over hexagonal ice development at 180 K, which is not found in the simulations.

A comparison of the average potential energy of the molecules in the clusters of various sizes shows that the distribution of energies for clusters of sizes 2-16 overlap. For clusters of size 16, the average potential energy of a molecule in a cluster containing 8 or less C molecules was -48.36 ± 0.42 kJ/mol, for clusters containing 9 or more C molecules the average potential energy is -48.36 ± 0.46 kJ/mol. For molecules in clusters containing 0-5 C molecules, the average potential energy is -48.40 ± 0.50 kJ/mol while those containing 11-16 C molecules had an average energy of -48.32 ± 0.42 kJ/mol showing no significant differences regardless of constituent amount of C molecules.

With the occurrence of cubic preference appearing at very small cluster sizes (5 and up) and the lack of a significant energy difference between clusters of varying amounts of constituent C and H molecules, cubic preference due to thermodynamic arguments can be ruled out, leaving kinetics as the determining factor. This could be the result of degeneracy related to the anisotropy of the ice structures, perhaps there are

more ways to form the cubic ice than the hexagonal ice during growth from the initial nuclei or the kinetic barriers could be different, favoring the cubic ice. This remains an open question for future studies.

Mechanisms of Consolidation of Ice Crystallites

Once the amount of *C*+*H* molecules reaches 15% of the system, the total number of nuclei decreases through growth and consolidation of neighboring nuclei into larger crystallites. We use the term crystallites here to differentiate between smaller nuclei that have grown predominately through incorporation of neighboring individual molecules at the periphery of the nucleus from larger structures that have developed predominately through consolidation of two or more neighboring nuclei.

We distinguish two different mechanisms of consolidation during crystallization of ice from hyperquenched water. Representative examples are shown in Figure 7.7. The first mechanism involves *direct attachment* of one nucleus to a neighboring nucleus. The second mechanism involves *rearrangement* of a nucleus along with attachment. In a third case, two nuclei grow close but neither rearrangement nor direct attachment occurs in the timescales of the simulations. Instead, a barrier of *interfacial* ice and amorphous water develops between the two misaligned crystallites. It is within this stage, with the growth of the nuclei into large crystallites, that the *interfacial* ice is found solely as an interface between the structured ice crystallite and the surrounding liquid. We now describe each mechanisms in detail.

Mechanism 1: Direct attachment. This mechanism of consolidation occurs when two neighboring nuclei have parallel stacking axes (see the arrows in Figure 7.7 a). Figure 7.7 a shows an example of the direct attachment mechanism of consolidation. As two nuclei grow towards one another, (left and center panels) the nuclei merge into a single crystallite (right panel).

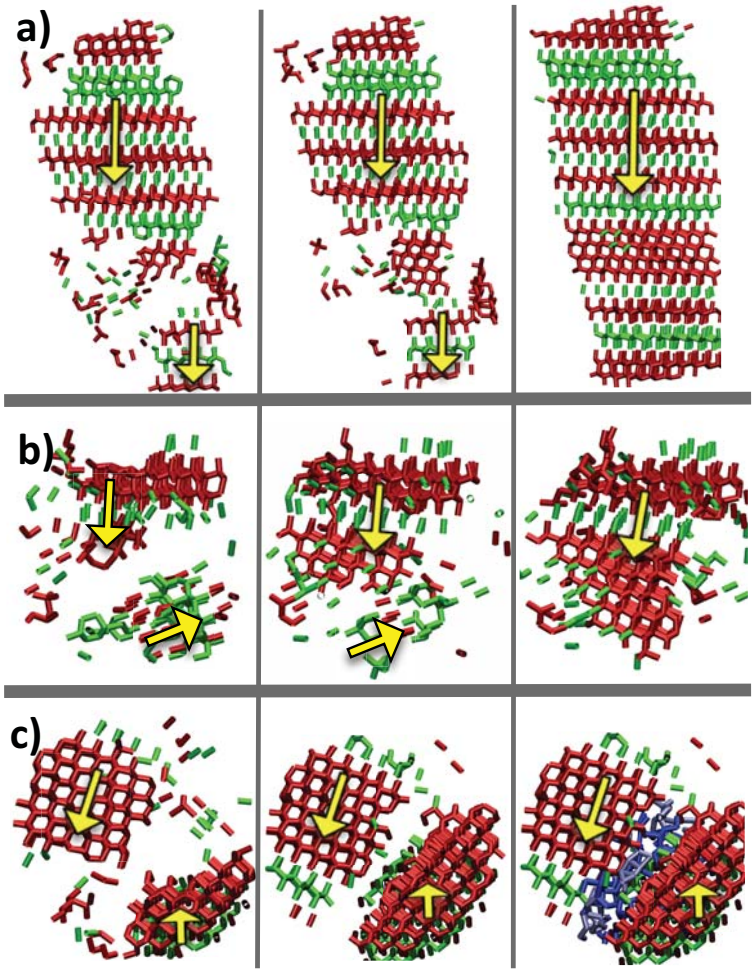

Figure 7.7. Consolidation Mechanisms and Non-consolidation
Examples of the two types of consolidation mechanisms and one of non-consolidation are shown as a series of snapshots from QL systems. "Bonds" are shown between neighboring C molecules (red) and between neighboring H molecules (green). In a) two nuclei grow near one another (left), with their stacking planes aligned. They are able to consolidate (center), maintaining both of their original stacking planes (right). For the case of b) two nuclei have grown near one another with their stacking planes misaligned (left). A process of rearrangement occurs, allowing the smaller nucleus to be incorporated into the larger nucleus (center), while sacrificing the stacking plane of the smaller nucleus (right). In c) two nuclei grow close with stacking planes misaligned (left). Rearrangement would require much longer timescales than those achieved by our simulations, so the two nuclei remain separated by a layer of liquid water and interfacial ice (center). The layer of interfacial ice (grey) and liquid water (blue) is shown (right).

Mechanism 2: Rearrangement. This mechanism of consolidation occurs when two neighboring nuclei meet with their stacking planes misaligned, Figure 7.7 b. One nucleus, typically the smaller of the two, rearranges over a time ranging from 10 - 100 ns (left and center panels), so that the stacking axis orients parallel to the larger nucleus as the two join (right panel). Diffusion is very slow at the low temperatures of the simulations, so that becoming part of the developing nuclei requires only small local rearrangements to occur.

Non-consolidation. When two neighboring crystallites approach one another with their stacking axes misaligned, but each has a size too large to be easily rearranged, consolidation of the two does not occur, Figure 7.7 c (left and center panels). The near edges of the two nuclei then remain bordered by *interfacial* ice and/or amorphous water, as shown in Figure 7.7 c (right panel). Compared to the time for rearrangement observed in smaller nuclei, which consist of generally less than 1000 molecules, the time required for rearrangement of the large crystallites (containing >2000 molecules) reach beyond the timescales of the simulations presented here. When raised to a higher temperature, 260 K, above the region of no-man's land but still below the melting temperature of water, further consolidation is observed in timescales of less than 100 ns. The resulting structure upon annealing is a single, completely aligned crystallite with 2:1 cubic to hexagonal ratio with nearly all hexagonal stacking faults as deformation faults. Consolidation continues through the direct and rearrangement mechanisms until only one crystallite remains. After 590 ns, the five simulations of liquid water instantaneously quenched to 180 K consist of 15 ± 1% *H*, 35 ± 3% *C*, 30 ± 1% interfacial and 20 ± 2% amorphous water.

Conclusions

Using the mW water model in molecular dynamics simulations, we studied the process of crystallization from the liquid to cubic ice with hexagonal stacking faults at 180 K. Previous experimental studies have shown evidence of the stacking faulted cubic ice and in this work, the onset of stacking, development of cubic ice preference and consolidation of the nuclei into larger crystallites is analyzed in detail.

From the structure factor obtained from simulations, the peaks characteristic to cubic ice are observed consistent with experimental results. Using the CHILL algorithm to distinguish molecules with cubic, hexagonal, interfacial and amorphous local symmetry provides molecular level detail into the structure development. After nearly 600 ns of simulations of the 1000 nm^3 volume systems, the liquid water crystallized to a complex consolidation of 30% cubic ice with 15% of the system consisting of hexagonal stacking faults, 30% interfacial ice surrounding the stacking faulted cubic ice crystallites and 20% amorphous ice filling the spaces between the crystallites. The 100 hexagonal peak in the structure factor could not be distinguished from the 111 peak of cubic ice, likely due to peak broadening from the small size of the crystallites and amorphous water present. The majority of hexagonal stacking was found as deformation faults, precluding the development of peaks in the structure factor that result from more than two layers of hexagonal ice.

Only a subtle sharpening of a single peak was observed with 5% cubic and hexagonal ice in the system. More significant peak structure had developed by 10% cubic and hexagonal ice content. This is consistent with the development of persistent stacking fractions occurring in nuclei consisting of ~200 molecules, which first occurs around 10% C+H. Prior to this, C and H molecules are arranged in a nearly random distribution of clusters. Without many multiple stacked layers of a particular ice type, the planes that give rise to peaks of higher order than the 111 of cubic and likely, the 100 of hexagonal

ice, do not form. Experimental determinations of the amount of ice present typically follow the growth of a single peak through crystallization, with the relative growth of the peak compared to its maximum used to determine the relative amount of ice present. With the significant development of ice remaining essentially indistinguishable up until 10% crystallized, the possibility of 'hidden' amounts of ice in experimental samples should be considered.

The resulting crystallites consisted of 20% amorphous liquid. While the results from simulations are consistent with those of experiment, differences in the way in which amorphous water is characterized in the various experimental methods and within the simulations presented here make comparisons of the precise amount of amorphous component subject to some uncertainty. It is clear from both experiment and simulation that the amorphous component in the crystallization of cubic ice is considerable, at least during initial formation of the crystallites. The combination of cubic, amorphous water and hexagonal ice present in the 180 K isothermal simulations suggests that in estimations of the structure of water found in cold clouds, the use of thermodynamic values from the assumption of a single predominate ice structure, hexagonal or cubic, may not be sufficiently accurate.

Similar to results found from the decompression of high pressure polymorphs[25,33] and freezing of water in nanopores,[36] we find a preference for cubic ice that develops quickly upon onset of crystallization, resulting in final crystal ratios (C:H) of 1.8:1 to 2.5:1. The preference for cubic ice is observed in clusters as small as size 5, and this coupled with a lack of sufficient difference in potential energy between clusters of different C and H constituents, we conclude that the preference for cubic ice precedes the development of cubic and hexagonal stacking patterns, which occurs in the absence of a purely hexagonal or purely cubic origin.

References

[1] A. Gettelman and P. Forster, J. Meteor. Soc. Japan **80**, 911 (2002); U. Von Zahn and U. Berger, Journal of Geophysical Research **108**, 8451 (2003); F. Lübken, J. Lautenbach, J. Höffner, M. Rapp, and M. Zecha, Journal of Atmospheric and Solar-Terrestrial Physics **71**, 453 (2009).

[2] A. Bravais, J. Ec. Polytech. **18**, 1 (1847).

[3] E. Whalley, Science **211**, 389 (1981).

[4] A. Weinheimer and C. Knight, Journal of the Atmospheric Sciences **44**, 3304 (1987).

[5] J. Dewar, Chem. News **91**, 216 (1905).

[6] H. Konig, Z. Kristallogr. **105**, 279 (1943).

[7] E. Mayer and A. Hallbrucker, Nature **325**, 601 (1987).

[8] J. Goodman, O. Toon, R. Pueschel, K. Snetsinger, and S. Verma, Journal of Geophysical Research **94**, 16449 (1989).

[9] B. J. Murray and A. K. Bertram, Phys. Chem. Chem. Phys. **8**, 186 (2006).

[10] B. J. Murray, D. A. Knopf, and A. K. Bertram, Nature **434**, 202 (2005).

[11] B. J. Murray, S. L. Broadley, T. W. Wilson, S. J. Bull, R. H. Wills, H. K. Christenson, and E. J. Murray, Phys. Chem. Chem. Phys. **12**, 10380 (2010).

[12] M. Baker, Science **276**, 1072 (1997).

[13] B. J. Murray and E. J. Jensen, J. Atmos. Sol.-Terr. Phy. **72**, 51 (2009).

[14] S. Mossop, Proc. Phys. Soc. London, Sect. B **68**, 193 (1955); O. Mishima, Nature **384**, 546 (1996).

[15] D. Murphy, Geophys. Res. Lett **30**, 2230 (2003).

[16] J. Shilling, M. Tolbert, O. Toon, E. Jensen, B. Murray, and A. Bertram, Geophysical Research Letters **33**, L17801 (2006).

[17] M. Krämer, C. Schiller, A. Afchine, R. Bauer, I. Gensch, A. Mangold, S. Schlicht, N. Spelten, N. Sitnikov, and S. Borrmann, Atmos. Chem. Phys **9**, 3505 (2009); E. Jensen, L. Pfister, T. Bui, P. Lawson, and D. Baumgardner, Atmos. Chem. Phys **10**, 1369 (2010).

[18] H. Tanaka and I. Okabe, Chem. Phys. Lett. **259**, 593 (1996).

[19] T. Takahashi and T. Kobayashi, J Cryst Growth **64**, 593 (1983).

[20] P. Wolde and D. Frenkel, Phys. Chem. Chem. Phys. **1**, 2191 (1999).

[21] T. Takahashi, J Cryst Growth **59**, 441 (1982).

[22] G. P. Johari, J. Chem. Phys. **122**, 194504 (2005).

[23] G. P. Johari, Philosophical Magazine B **78**, 375 (1998).

[24] P. Jenniskens and D. Blake, Astrophys. J. **473**, 1104 (1996).

[25] T. Hansen, M. Koza, P. Lindner, and W. Kuhs, J. Phys. Condens. Matter **20**, 285105 (2008).

[26] I. Kohl, E. Mayer, and A. Hallbrucker, Phys. Chem. Chem. Phys. **2**, 1579 (2000).

[27] W. Kuhs, D. Bliss, and J. Finney, J. Physique C1 **48**, 631 (1987).

[28] G. P. Johari, J. Chem. Phys. **109**, 1070 (1998).

[29] P. Jenniskens, S. F. Banham, and D. F. Blake, J. Chem. Phys. **107**, 1232 (1997).

[30] S. Plimpton, J. Comp. Phys. **117**, 1 (1995).

[31] E. F. Burton and W. F. Oliver, PNAS **153**, 166 (1936).

[32] P. Jenniskens and D. Blake, Science **265**, 753 (1994).

[33] T. C. Hansen, M. M. Koza, and W. F. Kuhs, J. Phys. Condens. Matter **20**, 285104 (2008).

[34] W. Hage, A. Hallbrucker, E. Mayer, and G. Johari, J. Chem. Phys. **103**, 545 (1996).

[35] Z. Dohnalek, G. Kimmel, R. Ciolli, K. Stevenson, R. Smith, and B. Kay, J. Chem. Phys. **112**, 5932 (2000).

[36] K. Morishige and H. Uematsu, J. Chem. Phys. **122**, 044711 (2005).

Chapter 8

RELATIONSHIP BETWEEN STRUCTURE AND CRYSTALLIZATION KINETICS IN SUPERCOOLED WATER

Abstract

Homogeneous nucleation of ice is studied through molecular dynamics simulations using the mW water model. The liquid-liquid transformation temperature T_{LL}, the temperature at which the maximum rate of change in the local structure of water occurs, is found to be the locus of the maximum crystallization rate. This is the first direct evidence obtained from simulation of a structural connection to the kinetic limit of stability of the liquid phase. Above T_{LL}, crystallization shows timescales dominated by the nucleation process with well-defined timescales for nucleation and growth. The critical ice nuclei are found to contain 70-130 water molecules and are preferentially wetted by four-coordinated molecules in the liquid phase. Below T_{LL}, crystallization timescales are dominated by the growth of ice nuclei, with nucleation and growth occurring simultaneously.

Introduction

Liquid water can be supercooled below water's melting temperature, while remaining a liquid, to the homogeneous nucleation temperature, T_H ~ 235 K[1]. For temperatures below T_H, homogeneous nucleation of the bulk liquid cannot be avoided and water rapidly crystallizes.[2] Evidence of the presence of liquid water in coexistence

with ice[3] and the glass[4] suggest that liquid water can persist at temperatures below T_H, but it is unknown what determines the lowest temperature at which the bulk liquid can be equilibrated.

It is well known that water undergoes significant changes in structure[5,6] and thermodynamics[7] when cooled to temperatures approaching T_H. The heat capacity and thermal expansivity increase dramatically.[8] Extrapolations of these response functions to temperatures below T_H result in divergence at an experimentally unreachable temperature, $T_S \sim 228$ K.[9] Diffusion[10] and density[11] of liquid water decreases as the average number of nearest neighbors for each molecule transitions upon cooling from 5.2 ± 0.1 at 298 K[12] to an average local liquid structure approaching, but not quite reaching, the four coordinated structures found in hexagonal and cubic ice[13] and the low-density amorphous ice (3.9 ± 0.1 at 80 K[14]). Increasing fractions of locally favored structures,[15] local tetrahedral structure for water[16] and local icosahedral structure for simple liquids,[15] can result in frustration of the liquid leading to glass or gel formation when the locally favored structure is not similar to the structure of the lowest energy crystalline phase.[15] In this chapter, we show evidence that it is the change in liquid structure that leads to the diminished lifetime of the bulk liquid phase at T_H.

It is difficult to experimentally probe this low temperature range, due to rapid crystallization facilitated by impurities that lead to heterogeneous nucleation and the shock sensitivity of this highly metastable liquid.[17] While the average local coordination becomes more tetrahedral, density fluctuations present in the liquid, which facilitate the formation of crystalline nuclei, increase. Using small-angle x-ray scattering (SAXS)[18] and small-angle neutron scattering (SANS),[19] increased density fluctuations upon cooling are observed, though accounts differ on the magnitude of the correlation lengths of these fluctuations. In chapter 3, the liquid phase in equilibrium was studied over the temperature range from 300 K – 210 K. Correlation lengths were determined for this

temperature range, showing power law behavior. Recent experiments[20] confirmed our prior results; the exact power law fit we predicted was observed.

We also found that from the boiling point to T = 300 K, water maintains a near constant structural composition, with no significant change in the amount of four-coordinated molecules present. No anomalous behavior is observed, consistent with experimental structural[6] and thermodynamic analysis.[21] In the temperature range from 300 K to 210 K, there is an increase in structural correlation length coinciding with an increase in the fraction of four coordinated molecules. The liquid develops regions of four coordinated molecules that form an interconnected network at the percolation temperature of ~225 K.

Efforts to develop a unified description of water's behavior, metastable and stable, have resulted in a number of theories, notably the liquid-liquid phase transition[22] and the singularity free[23] hypotheses. Each hypothesis attributes water's anomalies to the development of increasingly tetrahedral structure at low temperatures. The former invokes two phases of liquid, a low-density liquid (LDL) and high-density liquid (HDL), while the latter posits that no singularity is required as a maximum in response functions is a thermodynamic necessity upon cooling of liquids with a density anomaly.[23]

Simulations seem ideally suited for the study of supercooled water, providing the ability to probe with atomistic detail regions of water's phase diagram inaccessible to experiment. While experiments are hindered by the rapid rate of crystallization of water near T_H, occurring on the order of a second or less,[2] the timescales of crystallization are long by atomistic simulation standards, where microsecond simulations are a challenge.[24,25] The only successful case of spontaneous crystallization of the bulk liquid using molecular dynamics prior to the work presented here was the result of six, multiple microsecond, simulations of 512 TIP4P water molecules, from which only one crystallization event occurred.[25] Special sampling techniques have been used to reduce

the computational cost of studying crystallization, including Monte Carlo simulations utilizing umbrella sampling with the global change in symmetry during crystallization as the predefined reaction coordinate[26] and simulations utilizing metadynamics,[24] a method to accelerate achievement of rare events. The latter study concluded that simulation cells containing at least 2,000-4,000 water molecules are needed to avoid finite size effects. Atomistic simulations of this size resulting in crystallization are not currently possible.

The mW model, a coarse-grained model of water introduced in chapter 2, is able to overcome these barriers of time and size, resulting in simulations capable of providing insight into regions of water's phase diagram which atomistic simulations and experiments cannot yet provide. The mW model is able to reproduce water's anomalies, phase transitions (see chapter 2) and thermodynamics (see chapter 3) at less than $1/100^{th}$ the computational cost of atomistic models. Each water molecule is represented as a single particle, resulting in increased diffusivity in comparison to experiment and a smoother energy potential sampled by the coarse-grained model, while maintaining water's connectivity through tetrahedral interactions that mimic hydrogen-bonding.

Attempts to equilibrate liquid water at temperatures below 210 K result in the onset of crystallization within 4 ns for a system with ~260,000 molecules. Extrapolating the correlation length of structural fluctuations to temperatures below 210 K show a maximum at $T_W = 200 \pm 2$ K. Hyperquenching of the liquid at a rate of 10^{10} Kns^{-1} allows structural analysis of the liquid through the range of temperatures in which crystallization inhibits isothermal analysis of the liquid, $150 K < T < 210 K$. The maximum rate of change from the predominately high-density liquid (local coordination >4) to that of the low-density, locally tetrahedral, structure occurs at $T_{LL} = 202 \pm 2$ K (see chapter 2).

In this work, we present results of nearly a thousand simulations in the temperature range of $T_{LL} \pm 10$ K. Analysis of the crystallization process over this range of

temperatures shows two distinctly different regions of crystallization kinetics. The change in kinetics occurs at T_{LL}, evidence that the homogeneous nucleation temperature of water is induced by the structural change, increased tetrahedrality, of the liquid phase. Characteristics of the growing nuclei are determined, including the size of the critical nucleus, the radius of gyration and the local liquid environment.

Methods

Molecular Dynamics

All simulations were performed with the molecular dynamics code LAMMPS.[27] The systems consisted of 4,096 mW[28] water molecules in a cubic cell with periodic boundary conditions. Preliminary simulations were completed with 4,096 and 13,768 molecule systems where the 4,096-molecule (5 nm box edge length) system gave results consistent with the larger system size. The results presented below were obtained from the 4,096-molecule system size. The equations of motion were integrated using the Velocity Verlet algorithm with a timestep of 10 fs. In the simulations presented, constant pressure, temperature and number of molecules were maintained, with the pressure being 1 atm unless otherwise noted. The temperature and pressure in the simulations were controlled with the Nose-Hoover thermostat and barostat, with time constants of 1 ps and 5 ps, respectively.

Temperature Quench

A series of simulations were run with the goal of collecting the many hundreds of crystallizing trajectories necessary for statistical analysis of the crystallization mechanism and timescales. To produce independent trajectories, starting configurations were taken at 500 ps intervals from a single simulation at 300 K. From the starting configuration, the temperature was dropped to the temperature of interest, T_{quench}. The

quench temperatures ranged from 192 to 210 K, all at a pressure of 1 atm. From the time at which T_{quench} is reached, the simulation was run until 70% of system was crystallized, as determined by the order parameters described below. The time required to convert 70% of the water into ice is considered the crystallization time, τ_X. For each T_{quench}, 60 - 110 crystallized trajectories were collected, resulting in nearly a thousand simulations up to 350 ns in length.

Identification of the Ice Nuclei

The CHILL algorithm (see methods section in chapter 7) was used to distinguish between molecules with local environments of the liquid, cubic ice (C), hexagonal ice (H) and an intermediate structure, interfacial ice. We consider an ice nucleus to consist of clusters of molecules with any ice-like local environment (C, H and interfacial). The size of the crystalline nuclei is determined by counting how many molecules having ice-like local environments can be found along a continuous path using 3.5 Å as the neighbor distance cutoff.

Mean First Passage Time (MFPT) Method

The mean first passage time (MFPT)[29] method provides a way to determine the characteristic timescale of the barrier crossing event for an activated process, in this case when nucleation has occurred, and the magnitude of the chosen order parameter that corresponds to a 50% chance of crystallization. The ice nucleus size, n, and its radius of gyration Rg, were chosen as order parameters for the advance of the crystallization. Analysis using the nuclei size is described in detail below.

With the size of the ice nuclei as the order parameter, the nucleation time τ_{nuc} and the critical nuclei size, n^* can be determined. No *a priori* knowledge of the critical nucleus size is required, though many crystallizing trajectories are necessary for

sufficient statistics.[30] For a series of trajectories at a given temperature, the mean time of first appearance is recorded for the largest nucleus in each configuration. A plot of the mean first passage time, the time it takes for a given nucleus size, n, to grow rather than dissolve for the first time, versus nuclei size results in a sigmoidal curve that can be described by the following equation:[29]

$$\tau(N_N) = \frac{\tau_N}{2}\left\{1 + erf\left[\left(N_N - N_N^*\right)c\right]\right\} \tag{8.1}$$

where τ(n) is the mean first passage time as a function of cluster size, n. τ_{nuc} is the nucleation time and n^* is the critical cluster size. c is a measure of the local curvature at the top of the barrier and the error function is

$$erf(x) = \frac{2}{\sqrt{\pi}}\int_0^x e^{-t^2}\,dt \tag{8.2}$$

The time corresponding to the plateau at the top of the sigmoidal curve is the nucleation time, and the inflection point corresponds to the critical nucleus size. For cases where the barrier to nucleation is low compared to the thermal energy (<kT), the plot of the MFPT vs nuclei size lacks a plateau or a well-defined inflection point.

Radius of Gyration and Nonsphericity of Nuclei

Determinations of the radius of gyration, Rg and nonsphericity, NS of the nuclei are detailed in the methods section of chapter 3.

Iso-configurational Ensemble

A series of simulations were run to compare the growth probabilities of selected critically sized nuclei based on radius of gyration. Configurations containing a critically sized nucleus, with size n*, were chosen and the radius of gyration and nonsphericity of the nucleus was recorded. A series of 200 simulations were run from 50 starting configurations at 205 K, each initiated with newly randomized velocities, resulting in 200 unique simulations from each starting configuration. The probability of growth from the initial nucleus was calculated as the number of trajectories (out of the two hundred total) that resulted in nuclei growth after 5 ns.

Local Liquid Environment of the Nuclei

To characterize the solvation shell of the crystalline clusters, analysis of trajectories at 1 atm of pressure and temperatures of 200 K and 205 K were used. For configurations at 5 ps intervals, the total number of four-coordinated, N_4 and higher-coordinated molecules (5-, 6- and 7-coordinated molecules), N_H in the liquid phase were determined. The ratio of four-coordinated to higher-coordinated, N_4/N_H represents the ratio expected to surround each nucleus if no preference is shown for either type. For the same configurations, the nuclei were located and the total number of four-coordinated, n_4 and higher-coordinated molecules, n_H in the liquid phase, located within a 3.5 Å distance from the nucleus were found. The ratio of four-coordinated to higher-coordinated molecules found within this first neighbor shell of each nucleus, n_4/n_H represents the local liquid environment of the nucleus.

Results

Hundreds of crystallizing trajectories were obtained in order to compare the trend in crystallization timescales and mechanism to the structural changes found in

water across the temperature range of T_{LL} ± 10 K. We present here the results of this analysis, starting with examples of representative crystallization events at various temperatures along with the average crystallization times. We then compare the crystallization times to the changes in liquid structure over the same temperature range and show that the crystallization rate reaches a maximum at the temperature where the greatest structural change within the liquid is found, at T_{LL}.

Maximum Crystallization Rate Occurs at T_{LL}

Crystallization is the result of nucleation, the development of a critically sized nucleus that has a 50% chance of growing or dissolving, and growth, the addition of molecules to the growing nucleus. To determine the onset and progress of crystallization, we look at three indicators; the average potential energy per molecule, the largest ice cluster size and the total amount of ice. A substantial decrease in the potential energy, a global property of the system, signals when crystallization has occurred. While useful for providing a general timeline of a crystallization event, it lacks the molecular level detail necessary for precise determinations of the onset and progress of crystallization and differentiation between nucleation and growth. To obtain molecular level detail of crystallization, we use the CHILL algorithm (see Appendix A) to distinguish between molecules having the local symmetry of ice and liquid based upon the arrangement of nearest neighbors. Molecules with local symmetry of cubic, hexagonal or interfacial ice structures are considered ice and the remaining molecules are considered liquid. This allows for characterization of the pre-critical nuclei, nucleation and the onset of growth.

In Figure 8.1, the potential energy per molecule (panels a and b), the fraction of total molecules contained in the largest nucleus, f_{LN} and the fraction of total ice, f_{ICE} (panels c and d) as a function of time are shown for representative crystallizing

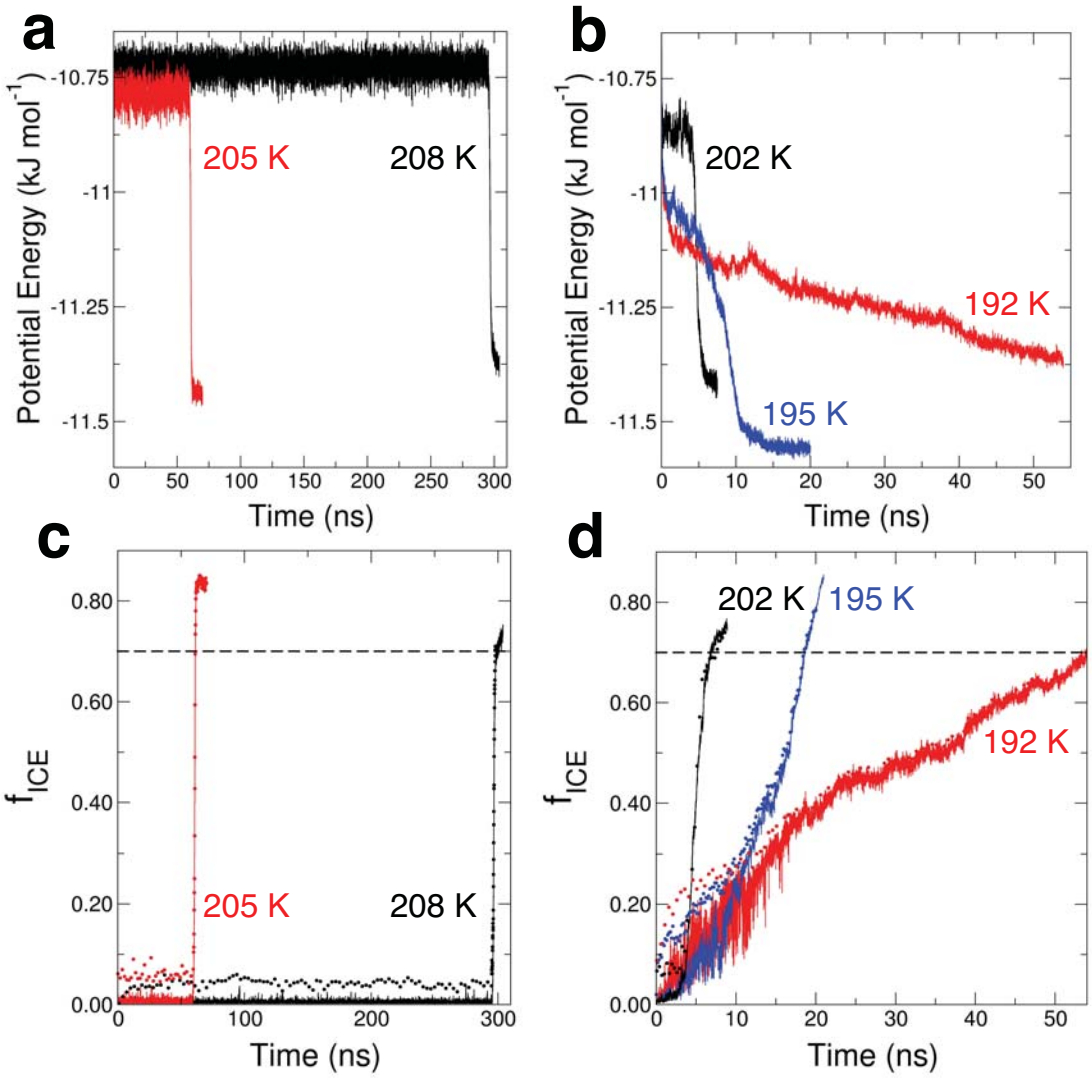

Figure 8.1. Advance of the crystallization
The potential energy of individual crystallizing trajectories as a function of time at a) 208 K (black) and 205 K (red) and b) T_{LL} = 202 K (black), 195 K (blue) and 192 K (red). The fraction of the total system made up of the largest ice nucleus (solid) and the total amount of ice in the system (circles) for c) 208 K (black) and 205 K (red) and d) 202 K (black), 195 K (blue) and 192 K (red). Horizontal dashed line shows where 70% of the system is ice.

trajectories at temperatures above T_{LL} (panels a and c) and temperatures at or below T_{LL} (panels b and d). For the determination of crystallization times, we consider a system as crystallized at the point where 70% ice is reached. Once the largest nucleus reaches more than ~50% of the total system, growth of the nucleus includes essentially all ice within the system as any other nuclei have either dissolved or been incorporated into the growing nucleus, shown by the overlap found in f_{LN} and f_{ICE} above $f_{ICE} = 0.20$ (Figure 8.1 panel c) and $f_{ICE} = 0.40$ (Figure 8.1 panel d). An energy cutoff could have been used to determine the crystallization times, though particularly at low temperatures, the average potential energy per molecule does not give a consistent measure of the amount of ice that has formed.

For temperatures above T_{LL} (Figure 8.1 panel a), the energy fluctuates around its average value for the liquid state until crystallization occurs. A quick decrease in energy signals crystallization, with the lower energy crystalline state being reached within a few nanoseconds. The values of f_{LN} shows a similar fluctuation at an average size prior to crystallization (Figure 8.1 panel b), the development and dissolving of pre-critical nuclei, with a quick increase over the course of a few nanoseconds at the onset of growth, resulting in more than 70% of the system crystallizing. For temperatures at or below T_{LL} a different trend occurs. Instead of an abrupt drop in energy at the onset of growth (Figure 8.1 panel b), there is a slow decline in energy during crystallization, requiring many nanoseconds to reach the lower energy crystalline state. The corresponding increase in f_{LN} shows a similar lack of abrupt change, with large fluctuations occurring in the nucleus size below $f_{LN} \sim 0.30$, and many nanoseconds passing from the onset of growth and the point of 70% crystalline.

The average crystallization time for each temperature is given in Table 4.1, along with nucleation and growth times and the critical nucleus sizes, to be described in the following section. The average crystallization time decreases upon cooling, finding a

minimum just below T_{LL} and then increases again. This trend is illustrated in Figure 8.2 panel a. The spread in crystallization times is larger at higher temperatures. This is due to the stochastic process of nucleation during the crystallization time, which will be discussed in the following section. The crystallization rate J, is the number of crystallization events that occur per unit of time, given by $J = \tau_X^{-1}$. Due to the inverse relationship between crystallization time and rate, upon cooling to T_{LL} the rate of crystallization increases, finding a maximum around T_{LL} before decreasing again. The decrease in crystallization rate, a result of a change in mechanism, will also be described in the next section.

We now compare the trend found in crystallization times with the structural changes that occur upon cooling the liquid. In Figure 8.2 panel b, we show the fraction of four-coordinated molecules, the amount of molecules with four neighbors within a 3.5 Å radial cutoff, over the temperature range 150 – 245 K. As detailed in chapter 3, from the

Table 8.1

Crystallization Times and Critical Nucleus Sizes

Temperature (K)	τ_N (ns)	τ_G (ns)	τ_X (ns)	n*
180[a]	<1	285 ± 20	285 ± 20	< 10
192	<1	25 ± 3	25 ± 3	-
195	<1	10 ± 3	12 ± 3	-
200	3 ± 2	5± 2	6 ± 2	103
202	5 ± 3	3 ± 1	8 ± 3	96
205	30 ± 28	2 ± 1	36 ± 28	96
208	240 ± 88	2 ± 1	183 ± 88	91

[a] Results for 180 K are determined in chapter 7.

boiling temperature to 300 K, no increase in the number of four-coordinated molecules occurs. The amount of four-coordinated molecules increases slowly in the range from 300 K (23% four-coordinated) to 240 K (30% four-coordinated). The rate of structural change increases quickly from 240 K to 180 K, with a maximum change in structure found at $T_{LL} = 202 \pm 2$ K.

A plot of the temperature versus crystallization time results in a nose-shaped curve, shown in Figure 8.2 panel a, with the point centered just below T_{LL}. Above T_{LL}, the liquid consists of molecules with high-coordination local environments, with an average coordination number larger than four. Below T_{LL}, the liquid consists of predominately lower-density, four coordinated, local environments (> 60% of molecules). T_{LL} is not the percolation temperature, which is ~ 225 K, but the point of greatest growth of the already existing network of four-coordinated regions. At the temperature of maximum structural change, the crystallization time is minimal, corresponding to a maximum crystallization rate. We propose that the location of the maximum crystallization rate sets the homogeneous nucleation temperature and is a consequence of the increase in tetrahedral structure.

Direct comparison of the simulation and experimental crystallization rates is not possible, because coarse-grained models evolve on a smoother potential energy landscape, thus requiring less configurational space sampling prior to achievement of crystallization. This results in intrinsically faster timescales for crystallization events. For the mW model, in which the energy for hydrogen bond breaking is correct, as evidenced by the very good agreement in the enthalpy of vaporization and melting to that of experiment, (see chapter 2) it is only the barrier for bond breaking that is underestimated by the monatomic model. Estimates of the nucleation rate at 200 K, from recent extrapolations of experimental results to temperatures below T_H, range from 10^{21}-10^{24} cm^{-3} s^{-1}. Simulations using the mW model at 200 K have a nucleation rate of

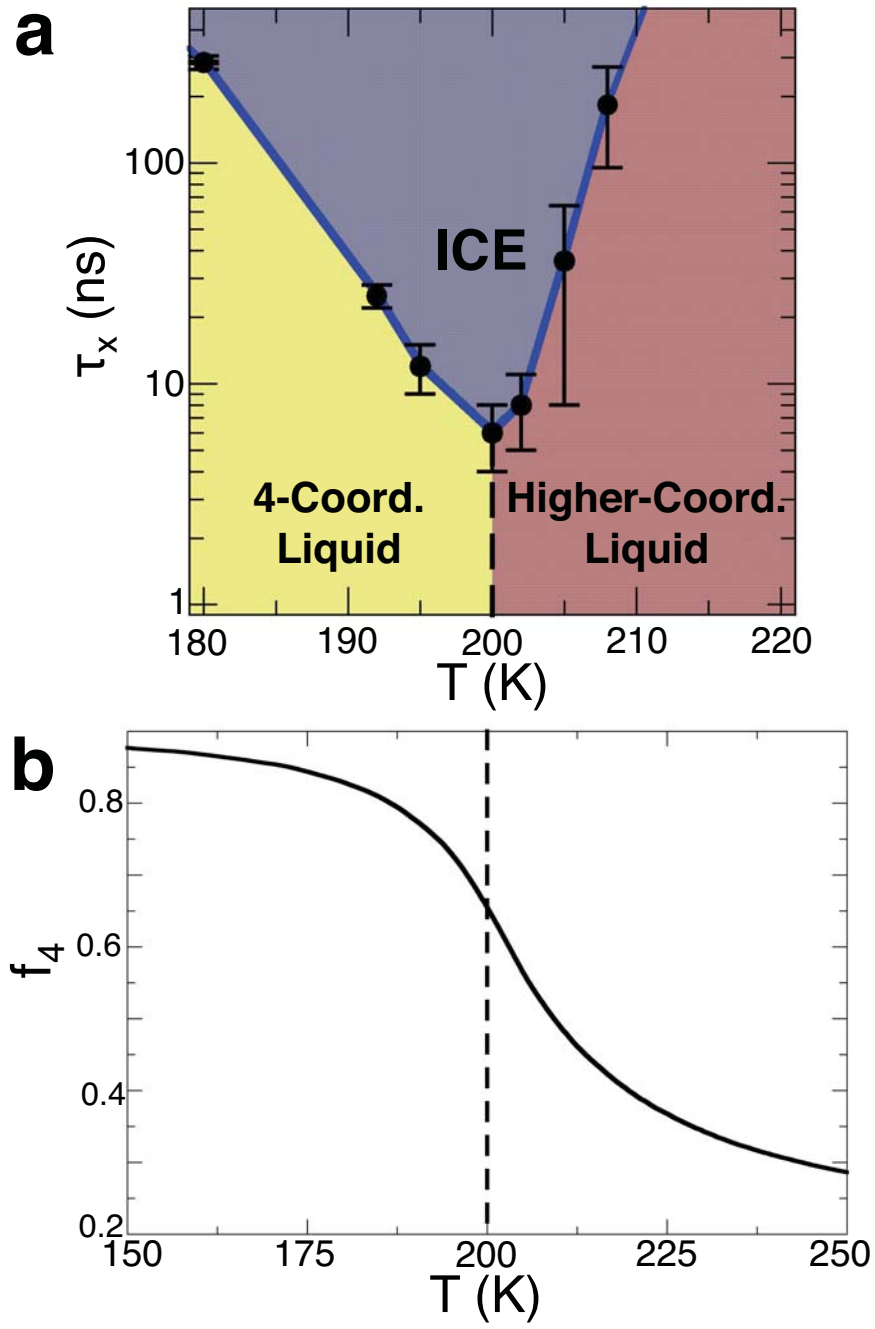

Figure 8.2. Maximum Structural Change and Maximum Crystallization Rate Average crystallization times are shown in panel a. Note y-axis is in log scale. Maximum crystallization rate is found at T – 200 K, just below T_{LL}. The change in fraction of four coordinated molecules is shown in panel b. Maximum change in fraction of four coordinated molecules occurs at T_{LL} = 202 K. Horizontal dashed line in panel b corresponds to temperature of maximum crystallization rate in panel a.

3 x 10^{29} cm^{-3} s^{-1}, five to eight orders of magnitude faster. While the absolute crystallization times may not be comparable to experiments, a scaling factor may exist allowing for conversion of simulation timescales to experimental timescales. This possibility is discussed in more detail in chapter 6. For this chapter, we are interested in the general trend in crystallization times.

Experiments cannot determine the crystallization rate below T_H ~235 K, as the timescales of crystallization becomes too short to measure with state of the art instruments.[2] Though mW is the only water model developed to-date capable of spontaneous crystallization within observable timescales in simulation cells large enough to avoid finite size effects, above T ~ 210 K crystallization requires timescales longer than multiple microseconds, too long to observe even with the mW model. Using techniques developed for rare event sampling, such as forward flux sampling, higher temperature crystallization events can be achieved. While application of forward flux sampling using the mW water model will be completed in the future, this chapter focuses on only the temperature range surrounding T_{LL}, where experimental crystallization rates are not available, and may not even be possible to obtain (see chapter 6).

In experiment, T_H is the temperature below which the equilibration of the liquid phase becomes too short, a second or less, to be measured with current instruments. It is at this point in which rapid crystallization precludes study of the liquid phase (and the crystallization process, for that matter) in experiments. In the mW simulations, we are able to simulate crystallization in a range of temperatures, from the stochastic nucleation above T_{LL} to temperatures where rapid nucleation occurs prior to the equilibration of the liquid, below T_{LL}. When onset of crystallization begins before the liquid can be equilibrated, a kinetic spinodal has been reached. The kinetic spinodal is a limit of stability, the location of which is dependant upon the ease at which the ice forms from the liquid. With the ability to observe with microscopic detail the crystallization process,

the determination that the maximum crystallization rate is found at the temperature of greatest structural change provides evidence that the kinetic limit of stability for the liquid is reached due to the structural changes found in water upon cooling.

Crystallization Kinetics Change at T_{LL}

We now describe the observed change in crystallization mechanism, from nucleation-dominated above T_{LL} to growth-dominated below T_{LL}. First, the crystallization timescales will be separated into their component nucleation and growth times, with the aid of the MFPT method to determine the nucleation time and the critical cluster size. To illustrate the differences between the two crystallization regimes, we describe each region in detail.

The mean first passage time (MFPT) method of Wedekind et al.[29] is used to extract the nucleation times t_N and critical nucleus size n^* from the analysis of about a hundred crystallizing trajectories for each quench temperature. Accurate values of n^* and τ_N can be extracted through the MFPT analysis when the characteristic time of nucleation is much larger than the characteristic time of crystal growth. During crystallization, nuclei develop and dissolve until a nucleus of critical size, n^*, forms. A critically sized nucleus has a 50% chance of either growing or dissolving into the surrounding liquid. Once a critically sized nucleus develops and grows, rather than dissolving, nucleation has occurred and growth of this nucleus continues until the system is crystallized. When distinct nucleation and growth times exist, the result is a MFPT curve that is sigmoidal with a plateau at large nucleus sizes. This is the situation for $T > T_{LL}$, where Figure 8.3 panel a shows a plateau above nuclei sizes of ~175 molecules for $T = 208$ K.

In the case of a low barrier to nucleation, growth times are no longer distinct from nucleation times, as the two are occurring simultaneously. The resulting MFPT

curves contain, instead of a plateau, a continuous increase at large nuclei sizes for 202 K and 200 K, Figure 8.3 panel b. This demonstrates a change in the mechanism of crystallization, from nucleation-dominated crystallization with distinct nucleation and growth times, above T_{LL}, to growth-dominated crystallization where nucleation and slow growth occur simultaneously, below T_{LL}. The nucleation time, τ_N obtained from the fit of the MFPT curves to equation 4.1 and the growth time, τ_G the average time from development of the critical cluster size to τ_X, are presented in Table 4.1.

Temperatures above T_{LL}

For temperatures above T_{LL}, the time of nucleation is much larger than the time of

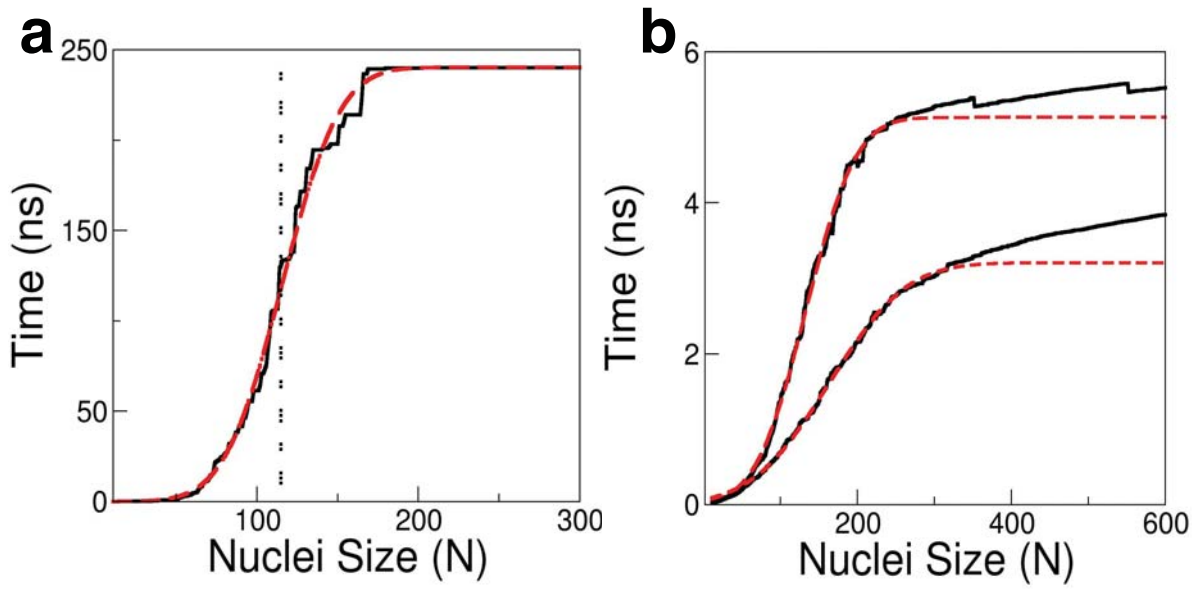

Figure 8.3. Mean First Passage Time Data and Fits
Panel a) Smooth line is the mean first passage times for 208 K. Dashed line is the fit to equation 4.1. Vertical dashed line is the inflection point of the curve, which corresponds to the critical nucleus size. Uncertainty in the critical nucleus size is determined from the standard deviation of the mean first passage times. The plateau at large (greater than 200) nucleus size corresponds to the nucleation time. Panel b) Smooth line is the mean first passage times for 202 K (upper set of curves) and 200 K (lower set of curves). Dashed line shows fit to equation 4.1. A plateau is not found at large cluster sizes for temperatures below T_{LL} = 202 K.

growth. Three stages of crystallization are found for temperatures above T_{LL}.

Induction Stage. During this stage, structure and density fluctuations in the supercooled liquid water give rise to ice nuclei that are too small to survive and so they dissolve. Due to the stochastic nature of crystallization, where the time to each nucleation event cannot be predicted precisely, each trajectory begins with an induction stage of varying length. In Figure 8.1 panel a, the induction times range from 50 ns for 205 K to nearly 300 ns for the 208 K trajectory. The size of the largest ice nucleus fluctuates from 10 - 150 molecules, with the average size ranging from 10-20 for the higher temperatures and 25 - 45 for temperatures close to T_{LL}. The induction stage ends with the stochastic formation of a critically sized ice nucleus that grows. Formation of the critically sized nucleus is the rate-limiting step in this crystallization process.

Fast Growth. Upon formation of a growing critical nucleus, the total energy drops sharply accompanying an increase in the size of the largest ice nucleus to more than 70% of the system. While multiple ice nuclei grow and dissolve simultaneously during the induction stage, growth of a critical nucleus during the fast growth stage quickly overtakes the entire system, typically growing to absorb all smaller nuclei that may also occupy the simulation cell. This ultimately results in a single crystallite that spans the entire system. The fast growth period is significantly shorter than the induction time, requiring less than 5 ns in simulations at temperatures above T_{LL}. This stage ends when the final ice nucleus reaches a size comparable to the size of the simulation cell.

Slow Growth. A third stage follows in which the energy decreases slowly while the crystal continues growing in the interstitial spaces. This process may require rearrangement of the system to eventually include all molecules into the ice structure. For this work, we focus on the timescales and mechanisms of nucleation and growth, not

rearrangement or recrystallization. Recording of the crystallization trajectories is stopped once 70% of the system is ice, typically at the onset of the slow growth stage.

In an analysis of a single crystallizing trajectory consisting of 512 TIP4P water molecules, Matsumoto et al.[25] distinguished an additional stage in the crystallization trajectory between induction and growth. The atomistic system presented a small dip in energy (about 2%) at the beginning of the growth process. We observe the same in crystallization simulations consisting of 512 mW water molecules (not shown): as the size of the critical ice nucleus is comparable to the total system size, its formation is accompanied with a small decrease in energy. This is not the case for the larger systems we report here, for which the critical nucleus contains less than 3% of the molecules in the simulation cell.

Temperatures below T_{LL}

Crystallization below T_{LL} shows significant differences when compared to higher temperatures: most noticeably, the induction time appears absent. For $T \leq T_{LL}$, the growth time becomes longer than the nucleation time of the system, signaling a change in kinetics. In this case, the rate-limiting step in the process of crystallization is no longer formation of the critical nucleus, but also includes how fast the ice nuclei can grow as the nucleation timescales and the growth timescales become coupled.

At T_{LL}, the energy appears stable for about 5 ns before decreasing, signaling crystallization, but during that apparent induction time the largest ice nucleus is growing in size, not maintaining a consistent average for more than a few nanoseconds (Figure 8.1 panel d). The energy starts its initial decrease quickly upon quenching to temperatures below T_{LL}. Growth of the largest nucleus is slow, but constant as multiple ice nuclei compete for largest nucleus in the system up to sizes of $n_{LN} = 0.30$, resulting in large fluctuations in the largest nucleus size in the early stages of growth. Eventually a

stage similar to the slow growth stage of the higher temperature crystallization is reached. For example, T = 195 K (Figure 8.1 panel b) reaches the slow growth stage at about 20 ns, where a relatively constant energy is found as the system makes slight rearrangements while progressing to the final crystal structure.

When comparing the largest nucleus size for trajectories above and below T_{LL}, in the temperature range below T_{LL} there are significant fluctuations in the largest nucleus size below n_{LN} = 0.30 (Figure 8.1 panel d). To illustrate the cause, we present snapshots of a system at 208 K and 192 K at 20% crystallized and 70% crystallized in Figure 8.4. Note that at 70% crystalline, we consider the crystallization complete and record the time required to reach this point as the crystallization time, τ_X.

For 208 K in Figure 8.4 panel a, at 20% crystallized there is one large growing ice nucleus (the nucleus has grown through the periodic boundary conditions, appearing to be in the top and bottom of the simulation cell, but is a single connected nucleus). This is characteristic of nucleation above $T_{LL,}$ in which a single critical nucleus develops and grows to include the entire system. At 70% crystallized, there is a crevice in the middle of the simulation cell, where the two sides of the ice crystal approached but are unable to join, due to misalignment of the growth planes. Within this crevice exists the remaining amorphous water (not shown).

For 193 K, Figure 8.4 b, at 20% crystalline, there exist multiple nuclei spread throughout the simulation cell. Each of these could potentially gain a few molecules and then be considered the largest nucleus or become connected (or disconnected) with a neighboring nucleus, resulting in a large increase (or decrease) in size. Crystallization below T_{LL} can be described as slow growth of many nuclei. By 70% crystallized, the nuclei have consolidated into a single large ice structure, though multiple crevices can be seen, a result of the growth through multiple initial sites of nucleation.

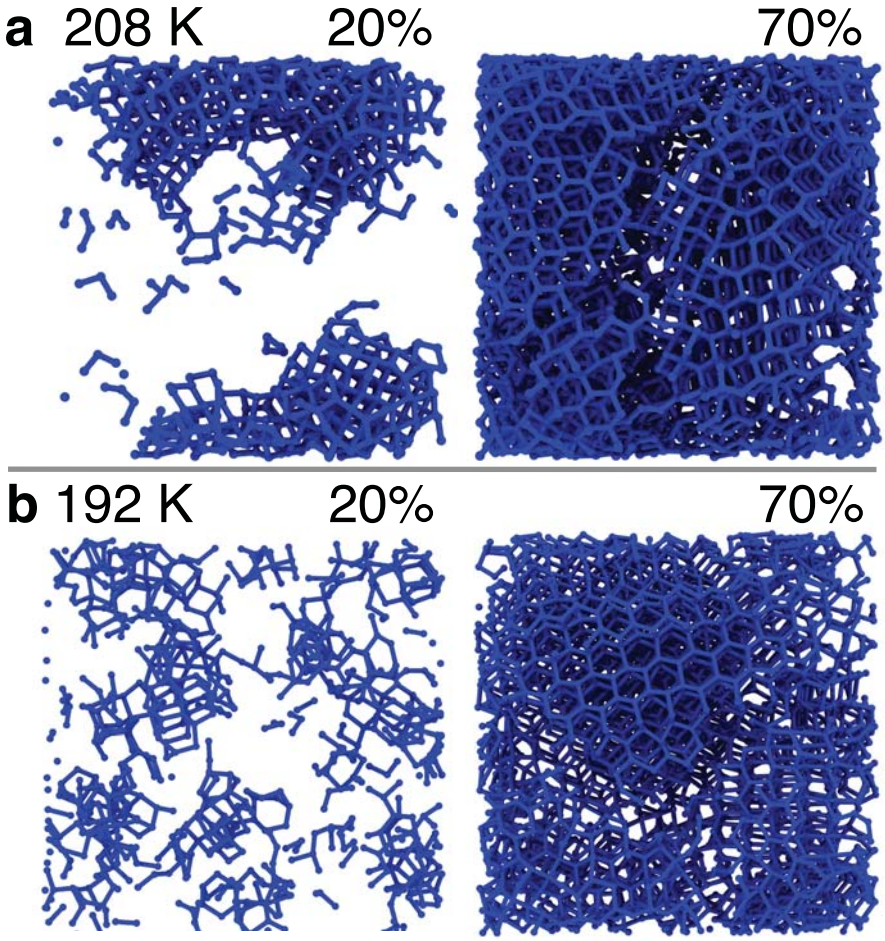

Figure 8.4. Ice Crystallization Above and Below T_{LL}
'Bonds' between molecules considered as ice (cubic, hexagonal and interfacial) are shown, with all other molecules invisible. Crystallization is shown at 208 K (panel a) and 192 K (panel b) for 20% and 70% ice content. Note that system is periodic, so in all cases crystals are continuous at the box edges.

The resulting crystallization mechanism below T_{LL} involves quick development of multiple nucleation sites, indication of a low (≤ kT) barrier to nucleation. This is evidence of spinodal decomposition, where the limit of stability of the liquid has been reached. While a thermodynamic spinodal is not reached in the mW model under the conditions of these simulations, at which point the critical nucleus size is one, the change in mechanism is likely due to reaching a kinetic spinodal. Above T_{LL} the existence of an induction time, during which the structure of water fluctuates while maintaining a consistent average provides evidence that the liquid structure has relaxed prior to onset of crystallization. For temperatures below T_{LL}, the lack of induction time is the result of crystallization occurring prior to relaxation of the liquid. A kinetic spinodal is the point where the lifetime of the liquid, the time to onset of crystallization, is comparable to the relaxation time of the liquid, precisely what we observe below T_{LL}. Kiselev,[31] using the IAPWS-95 equation of state and extrapolations of the surface tension, predicted the temperature of the kinetic spinodal to lie just below T_H, consistent with our results.

Critical Ice Nuclei

Each nucleation event is unique and relies upon random fluctuations within the liquid. A critically sized nucleus that grows in one system, leading to crystallization, may dissolve in another, meaning that it is not the characterization of a single critical nucleus that we seek, but an ensemble average for numerous nucleation events.

Size. In the temperature range from 200-208 K, the critical ice nucleus contains 100±30 molecules (0.7-1.0 nm radius if assumed to be spherically shaped). The critical size is insensitive to temperature within this range. Temperature independent critical nucleus sizes were also predicted for this temperature range by Kiselev[31] using Classical Nucleation Theory (CNT) and equations of state. In the temperature range T < 200 K, well into the growth-dominated crystallization domain, nucleation and growth

occur simultaneously, blending together the two timescales. This results in a MFPT without an inflection point from which to determine the critical nucleus size. The barrier to nucleation is decreasing upon cooling, as evidenced by the multiple nucleation sites that develop at short timescales (within a few nanoseconds), so the critical nucleus size is no larger than that obtained for the higher temperature range. Based on our estimate of the critical nucleus size for crystallization at 180 K (see chapter 6) the critical nuclei in the temperature range from 190 – 200 K likely contain 10 - 100 molecules.

Experimental results on freezing water droplets in emulsion[32,33] have been interpreted using CNT as indicating that the critical nucleus has a radius between 1-1.5 nm, consisting of 150-500 molecules near T_H. Huang and Bartell, using CNT and the rate of crystallization of water clusters containing 4,000-6,000 water molecules, derived critical nucleus sizes of 0.7 nm radius at 200 K .[32] Kiselev, using CNT and equations of state extrapolated into the metastable region,[31] obtained a critical nucleus size of 0.7-1.2 nm over the temperature range of 190-230 K.

In previous estimates of critical nucleus size, the following approximations are invoked within CNT to allow for quantitative determinations of nucleus size:[34,35]

- The forming ice nucleus is compact, typically considered spherical.[34,36] As we will show in the following section, elongated and non-spherical nuclei are also possible.
- The forming ice nucleus has a surface tension related to that of the macroscopic surface tension. It is not possible to quantitatively determine the surface tension far from the melting temperature, and at such small nucleus sizes, surface tension begins to lose meaning. [35,37]
- Equilibrium exists in which the critical ice nucleus forms through one-by-one addition of water molecules in consecutive equilibria. Instead, crystallization is non-equilibrium event and it is through random fluctuations that the critically sized ice nucleus appears. [36,38]

While consistent with experimental results and theoretical predictions both utilize approximations from CNT. This work provides the first direct measurement of the critical ice nucleus size from spontaneous nucleation events free of finite-size effects and is independent of any particular nucleation theory.

While nucleus size is an important factor in the process of nucleation, it is only one characteristic of the critical nuclei. The shape and local environment of nuclei also play a role in determining whether growth or dissolution will occur. Localized analysis of individual nuclei is not yet possible experimentally, and the necessary data is readily available from the simulations of crystallization presented here. In the following two sections, we describe the characteristic shape and local liquid environment from analysis of nearly half a million nuclei.

Shape. The critical nuclei are typically not compact or spherical in shape, but can be elongated and asymmetric. To determine the characteristic size regardless of shape, MFPT analysis was completed using as the reaction coordinate the radius of gyration, R_g a measure of the average distance between molecules in the ice nuclei. Note, the determination of the critical radius, R_g is independent of critical number of molecules, n^*. The critical R_g^* was found to be 1.1-1.2 nm over the temperature range 200-208 K. This is consistent with a non-compact critical nucleus size of n^* = 70-130 water molecules. The distribution of R_g found for nuclei of critical size, n^* is shown in Figure 8.5 panel a. Most of the critically sized nuclei have an R_g of 0.8-0.9 nm, slightly less than R_g^*, with the distribution broadening to include larger R_g values as the temperature is decreased.

A measure of compactness, the non-sphericity NS of the nuclei, defined as the ratio between the actual R_g and the R_g of a sphere containing the same number of molecules, was used to determine characteristic compactness of the critical nuclei. Smaller NS values correspond to nuclei that are more compact, with a nucleus having an

NS of 1 being spherical in shape. Figure 8.5 panel b shows the distribution of NS found for critically sized clusters, where NS values of 1.2-1.3 are most common, with a shift toward less compact nuclei at lower temperatures.

We now have defined three parameters capable of describing the critical nuclei, size of nuclei, n and R_g and a measure of the shape, NS. To help illustrate the variations of nuclei possible, Figure 8.6 shows a sample of nuclei of various size and shape taken from nine different crystallization trajectories at 205 K. Critically sized nuclei can be compact (Figure 8.6 top row), slightly elongated (Figure 8.6 middle row) or quite elongated (Figure 8.6, bottom row). Nuclei with greater amounts of constituent molecules tend to have larger R_g values, though a compact nucleus can contain more molecules than a nucleus with larger R_g. Notice that even the most compact nuclei (NS near 1) in Figure 8.6 is only roughly spherical, and is rare in the distribution of NS for all critically sized nuclei (Figure 8.5). Most critically sized nuclei have the slightly elongated shape shown in Figure 8.6 middle row.

If the critical nuclei are not spherical in shape, is NS a useful indicator of whether a nucleus has a higher or lower probability of leading to crystallization of the system? To answer this question we took individual configurations containing ice nuclei with a critical number of water molecules (90-100) and various NS (from the elongated NS of 1.72 to the more compact NS of 1.06) and ran two hundred simulations from the configuration containing each nucleus at 205 K, changing the velocities of all the molecules in the system at the beginning of each simulation so that every trajectory is unique. By determining the fraction of crystallization events, f_C resulting from the various nuclei we found that the more compact nuclei tend to have a higher probability of growth than the elongated, more string-like nuclei, though the ice nucleus does not have to be completely compact to have a greater than 50% chance of growth. The fact that nuclei with an NS of 1.65 and 1.4 can have crystallization NS values fractions

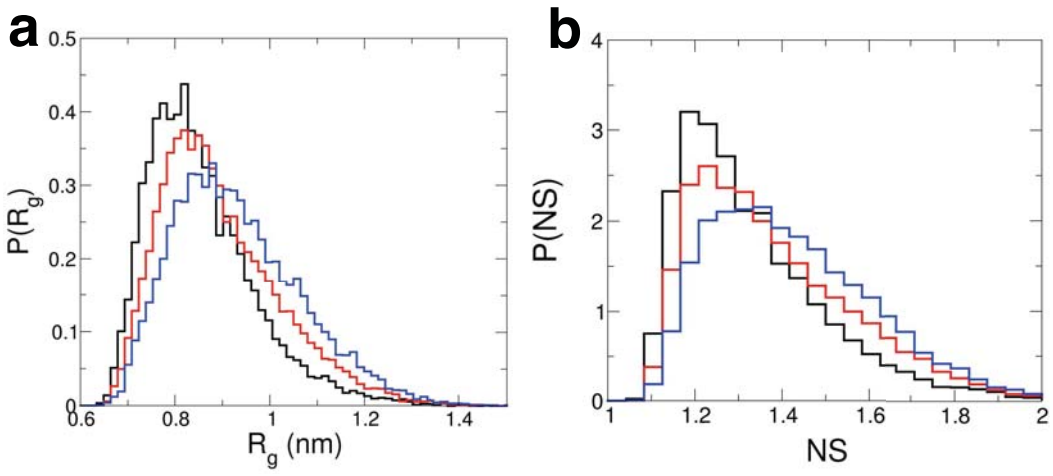

Figure 8.5. Distribution of R_g and NS for Critically Sized Nuclei
Panel a shows a histogram of the R_g values for all critically sized nuclei (70-130 water molecules) at three different temperatures, 205 K (black), 202 K (red) and 200 K (blue). For these same temperatures, panel b shows the histogram of the NS values for all critically sized nuclei.

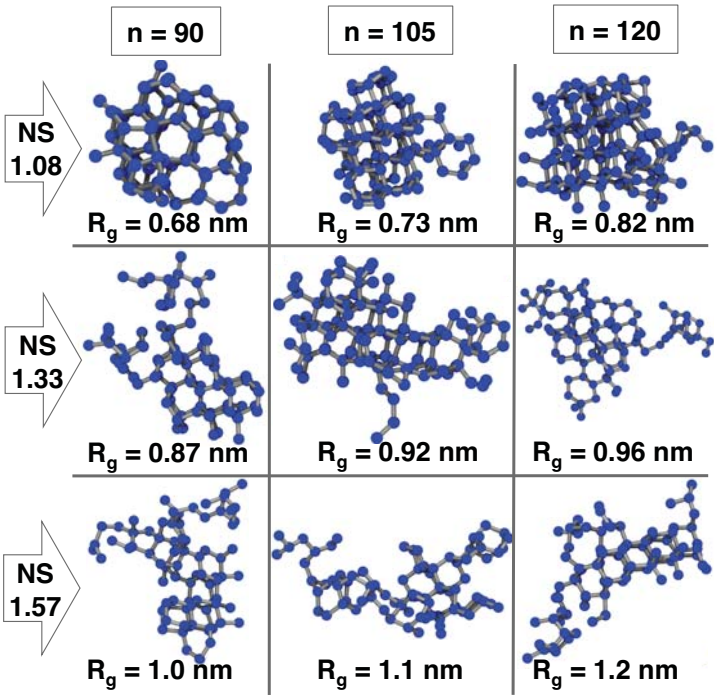

Figure 8.6. Examples of Critical Ice Nuclei at 205 K
Critical nuclei with various size, R_g and NS values are shown. The top row nuclei have the lowest NS values and are the most compact, the middle row of nuclei have intermediate and are slightly elongated. The lower row of nuclei have high NS values and are elongated.

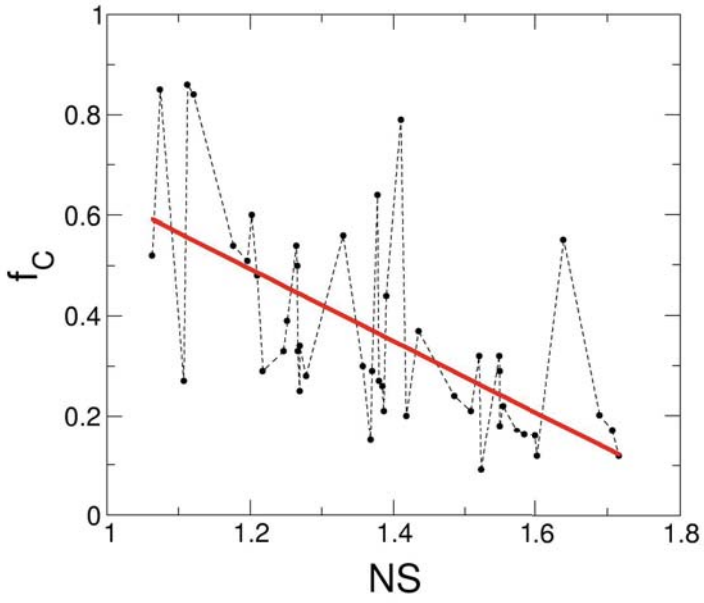

Figure 8.7. Effect of Nonsphericity on Crystallization Fraction
The fraction of simulations (out of 200 total) that result in crystallization from nuclei of size 90-100 molecules at 205 K with different compactness (NS) is shown. More compact nuclei typically result in a higher fraction of crystallization events. The solid red line is a linear fit to the data points shown.

comparable to much more compact nuclei shows the complexity in describing completely the critical nucleus.

Local Environment. The environment surrounding the forming ice nuclei consists of a dynamic exchange of water molecules from the disordered liquid and tetrahedrally ordered ice, creating a complex setting in which the ice nuclei form and dissolve. By analysis of the local liquid environment surrounding the ice nuclei, the characteristics of the liquid regions that give rise to nuclei are determined.

Prior to crystallization, the change from higher-coordinated to four-coordinated and from liquid local symmetry to ice local symmetry requires only slight changes in neighboring molecule alignment. The identity of water molecules as belonging to the liquid or the ice can change quickly (with transitions occurring in the picosecond to nanosecond timescales in these simulations), though typically the larger the region of ice

the longer the constituent molecules' classifications are maintained. The changing environment of liquid and ice is due to the inherently dynamic conditions of the highly supercooled liquid and is not an artifact of the method of structural classification.

From analysis of the liquid surrounding the critically sized nuclei, we observe twice as many four-coordinated molecules surrounding ice nuclei as higher-coordinated molecules (Figure 8.8). Even though the liquid environment becomes more four-coordinated on cooling, (Figure 8.2 panel b), the local liquid environment of the ice nuclei contain 30-70% more four-coordinated molecules surrounding the ice nuclei than would be expected based on the fraction of total four-coordinated and higher-coordinated molecules in each configuration. This demonstrates that the ice nuclei are preferentially wetted by four-coordinated molecules in the liquid phase. This result is found regardless of nucleus size, from pre-critical nuclei to nuclei containing 400 molecules.

To make certain that this result is independent of the structural classification from the CHILL algorithm, we reanalyzed the crystallization trajectories using a more relaxed variation of the CHILL algorithm. In this variation, less stringent structural requirements are used in determining the ice structures, which essentially allows for the (liquid) outer shell to be included as ice in the nuclei. The results are the same, more four-coordinated molecules surround the ice nuclei than would be expected from a random distribution.

The regions of four-coordinated liquid molecules are not sufficiently large to fully contain the critically sized ice nuclei. Once nuclei grow to sizes larger than 200 molecules, for temperatures above 200 K, crystallization is inevitable. The determination that the number of four-coordinated molecules in the liquid surrounding the critical nuclei is consistently two-thirds of the liquid environment up to and beyond critical sizes may indicate that once growth of the nucleus begins, cooperative fluctuations in the

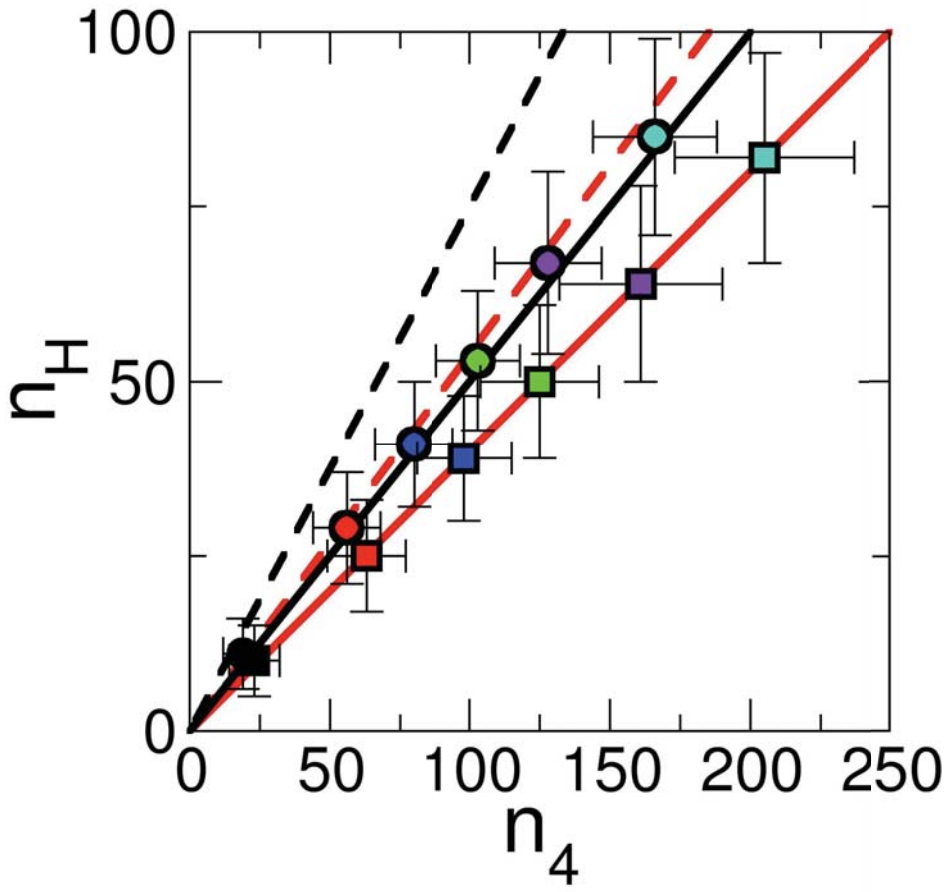

Figure 8.8. Ice Nuclei Local Environment
Amount of four-coordinated, n_4 and higher-coordinated, n_H molecules in contact with the ice nuclei at 205 K (circles) and 200 K (squares). Data is separated by nuclei sizes, for nuclei containing 10-50 molecules (black), 51-100 (red), 101-150 (blue), 151-200 (green), 201-300 (purple) and 301-400 molecules (turquoise). Line fit (solid black) to the 205 K data corresponds to x = 2y, while line fit (solid red) to 200 K data corresponds to y = 2.5x. The total amount of four-coordinated molecules found within the systems at 205 K, y = 0.75x is shown (dashed black) and 200 K, y = 0.54x, (dashed red). Each ice nucleus size averages at least twice as many four-coordinated molecules as higher-coordinated molecules, even though there are less than twice as many four-coordinated molecules as higher-coordinated molecules in total within the systems.

surrounding liquid aid in the fast growth of the nuclei. Lower temperatures have higher fractions of four-coordinated molecules wetting the ice nuclei.

Conclusions

In chapter 3, simulation studies using the mW water model showed a maximum in the density fluctuations of water at the liquid-liquid transformation temperature, T_{LL} = 202 ± 2 K. In this work, we have presented an analysis of the kinetics of ice crystallization at temperatures around T_{LL}. From more than a thousand simulations, we obtained hundreds of crystallization events allowing for analysis of the relative timescales of the crystallization process in two domains of crystallization. The temperature of greatest structural change in the liquid was found to coincide with maximum crystallization rate and the change in crystallization mechanism from nucleation-dominated to growth-dominated. This change from nucleation to growth dominance marks the kinetic spinodal.

Above T_{LL}, crystallization timescales are dominated by the nucleation process, with an induction period prior to nucleation ranging from one to hundreds of nanoseconds. Growth in this region is immediate, requiring only a few nanoseconds for a single critical nucleus to grow from less than 3% of the total number of molecules to 70% or more. Below T_{LL}, crystallization timescales are growth-dominated, with nucleation occurring quickly, typically less than a nanosecond, but with growth requiring significantly longer. In this low temperature region, the increasingly tetrahedral coordination of the water molecules effectively slows diffusion, contributing to the slow growth process.[39] Nucleation at this temperature occurs not through growth of a single critical nucleus, as found at higher temperatures, but through growth of multiple nuclei. The shorter time scales of nucleation compared to relaxation of the liquid (for which we

use the growth time) evidence that at T_{LL} supercooled liquid water reaches a kinetic spinodal, the kinetic limit of stability of the liquid phase.

The critical nuclei were characterized based on size and shape. The critical nuclei were found to contain about a 100 water molecules, and have a radius of gyration of 1.1-1.2 nm, consistent with theoretical and experimental determinations using classical nucleation theory, though determined in this work directly from the kinetics of the crystallization process without the aid of any nucleation particularly nucleation theory. Most critical nuclei were found to be slightly elongated, rather than compact spheres, though more compact nuclei typically had a greater probability of leading to crystallization. The liquid environment surrounding the nuclei was found to contain twice as many four-coordinated molecules as molecules with higher coordination.

The work presented here renders a complex picture of ice crystallization, with liquid water at temperatures higher than T_{LL} crystallizing after developing, through fluctuations in the liquid, ice nuclei that are preferentially wetted, though not encased, by patches of four-coordinated molecules. These nuclei are typically slightly elongated, and upon onset of growth, the liquid environment continues to be predominately four-coordinated with rapid growth leading to crystallization of the system. At lower temperatures, crystallization also occurs through development of nuclei preferentially wetted by four-coordinated molecules, though nucleation is rapid. The critical nuclei are typically more elongated than at higher temperatures, and found with more neighboring four-coordinated molecules in the surrounding liquid than critical nuclei at higher temperatures. With multiple nuclei developing in close proximity, and surrounded predominately by four-coordinated molecules, crowding occurs, slowing down the growth process.

Prior analysis of the effect of structural change in the liquid was studied with respect to the process of vitrification, how the liquid forms a glass.[15,16] In systems where

the local structure of the liquid favors symmetries inconsistent with the crystalline phase, vitrification occurs. Consistent with the fact that liquid water is a poor glass former, we find that the change in structure within liquid water upon cooling results in increased crystallization rates, until a kinetic spinodal is reached. At this point nucleation is occurring rapidly at multiple sites within the simulation cell. This work provides the first direct evidence from simulation studies of water of a connection between the structure of the liquid, the lowest temperature at which the liquid can be equilibrated and the kinetics of crystallization.

References

[1] S. Mossop, Proc. Phys. Soc. London, Sect. B **68**, 193 (1955); O. Mishima, Nature **384**, 546 (1996).

[2] B. J. Murray, S. L. Broadley, T. W. Wilson, S. J. Bull, R. H. Wills, H. K. Christenson, and E. J. Murray, Phys. Chem. Chem. Phys. **12**, 10380 (2010).

[3] E. B. Moore and V. Molinero, J. Chem. Phys. **132**, 244504 (2010); J. Webber, J. Dore, J. Strange, R. Anderson, and B. Tohidi, J. Phys. Condens. Matter **19**, 415117 (2007).

[4] C. Kim, B. Barstow, M. Tate, and S. Gruner, PNAS **106**, 4596 (2009).

[5] A. Soper, Mol. Phys. **16**, 2053 (2008); A. Botti, F. Bruni, A. Isopo, M. A. Ricci, and A. K. Soper, J. Chem. Phys. **117**, 6196 (2002).

[6] A. K. Soper, F. Bruni, and M. A. Ricci, J. Chem. Phys. **106**, 247 (1997).

[7] C. A. Angell, J. Shuppert, and J. C. Tucker, J. Phys. Chem. **77**, 3092 (1973); P. G. Debenedetti and H. E. Stanley, Phys. Today **56**, 40 (2003).

[8] P. G. Debenedetti, Journal of Physics-Condensed Matter **15**, R1669 (2003).

[9] R. Speedy and C. Angell, J. Chem. Phys. **65**, 851 (1976).

[10] W. Price, H. Ide, and Y. Arata, J. Phys. Chem. A **103**, 448 (1999).

[11] J. Schufle and M. Venugopalan, J. Geophys. Res. **72**, 3271 (1967).

[12] A. Soper, J. Phys. Condens. Matter **19**, 335206 (2007).

[13] G. Malenkov, J. Phys. Condens. Matter **21**, 283101 (2009).

[14] J. Finney, A. Hallbrucker, I. Kohl, A. Soper, and D. Bowron, Phys. Rev. Lett. **88**, 225503 (2002).

[15] H. Shintani and H. Tanaka, Nat. Phys. **2**, 200 (2006).

[16] H. Tanaka, Phys. Rev. Lett. **80** (1), 113 (1998).

[17] C. Angell, Annu. Rev. Phys. Chem. **34**, 593 (1983).

[18] L. Bosio, J. Teixeira, and H. Stanley, Phys. Rev. Lett. **46**, 597 (1981); Y. Xie, K. Ludwig Jr, G. Morales, and D. Hare, Phys. Rev. Lett. **71**, 2050 (1993).

[19] L. Bosio, J. Teixeira, and M. Bellissent-Funel, Phys. Rev. A **39**, 6612 (1989).

[20] C. Huang, T. Weiss, D. Nordlund, K. Wikfeldt, L. Petterson, and A. Nilsson, PNAS **133**, 134504 (2010).

[21] P. Debenedetti, J. Phys. Condens. Matter **15**, 1669 (2003).

[22] P. H. Poole, F. Sciortino, U. Essmann, and H. E. Stanley, Nature **360**, 324 (1992).

[23] S. Sastry, P. G. Debenedetti, and F. Sciortino, Phys. Rev. B: Condens. Matter **53**, 6144 (1996).

[24] D. Quigley and P. M. Rodger, J. Chem. Phys. **128**, 154518 (2008).

[25] M. Matsumoto, S. Saito, and I. Ohmine, Nature **416**, 409 (2002).

[26] R. Radhakrishnan and B. L. Trout, J. Am. Chem. Soc. **125**, 7743 (2003).

[27] S. Plimpton, J. Comput. Chem. **117**, 1 (1995).

[28] V. Molinero and E. B. Moore, J. Phys. Chem. B **113**, 4008 (2009).

[29] J. Wedekind, R. Strey, and D. Reguera, J. Chem. Phys. **126**, 134103 (2007).

[30] G. Chkonia, J. Wo lk, R. Strey, J. Wedekind, and D. Reguera, J. Chem. Phys. **130**, 064505 (2009).

[31] S. Kiselev, Int. J. Thermophys. **22**, 1421 (2001).

[32] J. Huang and L. S. Bartell, J. Phys. Chem. **99**, 3924 (1995).

[33] B. Krämer, O. Hübner, H. Vortisch, L. Wöste, T. Leisner, M. Schwell, E. Rühl, and H. Baumgärtel, J. Chem. Phys. **111**, 6521 (1999); H. R. Pruppacher and J. D. Klett, *Microphysics of clouds and precipitation*. (Kluwer Academic Publishers, Norwell, MA, 1997); J. Liu, Nicholson, C.E., Cooper, S.J., Langmuir **23**, 7286 (2006).

[34] P. G. Debenedetti, *Metastable Liquids: Concepts and Principles*. (Princeton University Press, Princeton, 1996).

[35] D. A. Hegg and M. B. Baker, Rep. Prog. Phys. **72**, 056801 (2009).

[36] J. McDonald, Am. J. Phys. **30**, 870 (1962).

[37] J. Merikanto, E. Zapadinsky, A. Lauri, and H. Vehkamäki, Phys. Rev. Lett. **98**, 4 (2007).

[38] J. P. Hansen and I. R. McDonald, *Theory of simple liquids*, 2nd. ed. (Academic Press, London ; Orlando, 1986).

[39] F. Sciortino, A. Geiger, and H. E. Stanley, Nature **354**, 218 (1991).